UNIVERSITÀ
DEGLI STUDI
DI BRESCIA

UNIVERSITÀ DEGLI STUDI DI BRESCIA

PHD IN

INGEGNERIA MECCANICA E INDUSTRIALE

ING-IND/09 SISTEMI PER L'ENERGIA E L'AMBIENTE

CYCLE

XXXIV

Advanced Carbon dioxide Thermodynamic Cycles for Power Production

Dottorando

Abubakr Ayub Sheikh

Matricola: 725714

SUPERVISOR'S NAME

Prof. Costante Mario Invernizzi

RIASSUNTO

L'aumento del riscaldamento globale e delle emissioni di CO_2 dovuto al consumo di combustibili fossili richiede anche nuove tecnologie per la produzione di energia che siano efficienti ed economicamente sostenibili. Aumentare l'efficienza energetica degli impianti di conversione di calore in energia elettrica è fondamentale per raggiungere l'obiettivo di ridurre l'impronta di carbonio e ridurre il costo dell'elettricità. Un possibile modo per produrre energia e raggiungere la sostenibilità è la conversione termodinamica della energia solare, ad esempio: in sistemi con collettori parabolici (PTC) oppure in impianti a concentrazione con torre centrale (CSP). Altre opportunità sono l'utilizzo del calore di scarto dei gas di scarico da processi industriali per produrre ulteriore energia elettruca oppure la realizzazione di sistemi combinati per la produzione di calore ed energia elettrica. I cicli termodinamici dell'anidride carbonica supercritica (sCO_2) per la produzione di energia sono una nuova tecnologia allo studio in vari gruppi di ricerca in tutto il mondo. L'anidride carbonica è un fluido di lavoro termicamente stabile e non infiammabile. I cicli termodinamici che la impiegano in condizioni supercritiche (sCO_2) hanno tendenzialmente elevate efficienze e, rispetto ai tradizionali cicli Rankine con vapore d'acqua, dimensioni ridotte di turbine e di scambiatori di calore. Essendo poi cicli termodinamici chiusi, hanno la capacità di utilizzare differenti sorgenti di calore disponibili a temperature massime anche molto variabili.

Tuttavia, i cicli sCO_2 presentano alcuni problemi tecnologici che, tendenzialmente, se utilizzati per recuperi di calore comportano elevati costi specifici. Per applicazioni in sistemi CSP, un problema termodinamico è la penalizzazione della efficienza del ciclo dovuto all'elevata temperatura dell'ambiente, tiopica delle località nelle quali questi tipi di impianto sono realizzati. Inoltre, le pressioni di esercizio naturalmente risultano elevate (da 200 a 400 bar) e notevole è l'impiego necessario di recuperatori/rigeneratori di grande potenza. Per affrontare le sfide di cui sopra, in questa tesi si propongono miscele binarie a base di CO_2 come fluidi di lavoro per migliorare le prestazioni termodinamiche dei cicli con sCO_2 per recupero del calore di scarto e da impiegare nelle centrali solari a concentrazione. In una prima fase, alcuni dopanti vengono selezionati sulla base della loro temperatura critica richiesta, della pressione critica, del peso molecolare, della complessità molecolare e della stabilità termica a lungo termine ad alta temperatura. Durante la selezione vengono considerati anche gli aspetti ambientali e tossicologici. In una seconda fase, le proprietà termodinamiche della miscela binaria selezionata a base di

CO_2 vengono calcolate utilizzando un'equazione di stato affidabile (EoS). L'accuratezza di EoS viene valutata confrontando, quando possibile, le proprietà termodinamiche calcolate con i dati sulle proprietà sperimentali disponibili in letteratura. Il principale fattore decisivo per selezionare la composizione della miscela adatta è il suo punto critico vapore-liquido risultante. Pertanto, è stato sviluppato un programma numerico in grado di calcolare tutti i punti critici vapore-liquido di una miscela binaria con ragionevole precisione a diversa composizione molare.

In una terza fase, si sono analizzate le prestazioni termodinamiche delle miscele binarie selezionate in cicli termodinamici con differenti configurazioni di impianto. Vengono considerate due applicazioni per fonti di calore: recupero del calore residuo ad alta temperatura (Tmax = 350℃) e energia solare concentrata (Tmax = 550℃ e 700℃).

Nell'ambito del recupero di calore ad alta temperatura, la miscela di CO_2-R134a [70% CO_2 molare] nel ciclo di alimentazione transcritico ha mostrato un'efficienza totale superiore di 4 punti percentuali rispetto al ciclo di alimentazione con sCO_2 (14,3% nel caso di CO2-R134a contro 10,8% in caso di CO_2) in semplice. L'efficienza risultante risulta sensibilmente superiore anche rispetto a configurazioni più complesse per cicli con anidride carbonica pura. Questi guadagni in termini di efficienza totale dimostrano il potenziale interesse delle miscele quali fluidi di lavoro in cicli termodinamici a base di CO_2 grazie alla maggiore efficienza totale e al layout del ciclo più semplice (che implicano costi di installazione inferiori) rispetto al tradizionale ciclo sCO_2. Nel caso dei recuperi termici considerati, rispetto a cicli di Rankine organico (ORC), si ottengono efficienze comparabili, selezionando opportunamente la composizione finale e il fluido dopante.

Per l'applicazioni CSP, cinque miscele binarie a base di CO_2 sono state analizzate e il guadagno in efficienza del ciclo è stato indagato con riferimento al ciclo con ricompressione di sCO_2 e al ciclo semplice di sCO_2. L'analisi viene eseguita per una temperatura minima del ciclo più elevata (Tmin = 50 °C) per simulare condizioni di temperatura ambiente tipicamente disponibili presso i siti degli impianti CSP. Con un semplice layout del ciclo di recupero, il fluido di lavoro CO2-TiCl4 [80% CO_2 molare] mostra un'efficienza del ciclo del 50,7%, che è vicina all'efficienza del ciclo ottimale del ciclo di ricompressione sCO_2 (cioè 50,8%) alla temperatura massima del ciclo di 700 ℃.

Altre tre miscele come CO_2-C6F6 [85% CO_2 molare], CO_2-CF3I [60% CO_2 molare] e CO_2-SO_2F_2 [40% CO_2 molare] comportano anche un non trascurabile guadagno nell'efficienza del ciclo rispetto al ciclo semplice di sCO_2. Ovvero: 2,7 punti di guadagno per la miscela CO_2-C_6F_6; 1,1 punti di guadagno nella miscela di CO_2-CF_3I e 1,5 punti di guadagno nella miscela di CO_2-SO_2F_2 con una temperatura massima del ciclo di 550 ℃.

Anche l'anidride solforosa (SO_2) è anche indagata come dopante per la miscela binaria a base di CO_2 . Essa è termicamente stabile ad alta temperatura (700 ℃), non infiammabile con un potenziale di distruzione dell'ozono stratosferico trascurabile. L'unico compromesso nella selezione dell'SO_2 è il suo rischio per la salute più elevato che può essere risolto nelle centrali elettriche controllando i problemi di perdita. Considerando la CO_2-SO_2 come fluido di lavoro, viene eseguita un'analisi termodinamica dettagliata per un blocco di potenza da 100 MW integrato con una torre solare a concentrazione avanzata con temperatura massima di ciclo di 700 ℃ e temperatura minima di 51 ℃. L'analisi a diversa composizione molare della miscela suggerisce una miscela di CO_2 molare all'85% come scelta ottimale per una buona efficienza del ciclo indipendentemente dal layout che si considera. L'efficienza del ciclo ottenuta mediante ciclo di ricompressione con miscela CO_2-SO_2 [85% CO_2 molare] è del 50,8% (2 punti percentuali in più rispetto al ciclo di ricompressione sCO_2) a T_{max} di 700 ℃ e P_{max} di 250 bar. Un altro vantaggio degno di nota dell'adozione della miscela CO_2-SO_2 è la riduzione della temperatura all'ingresso del riscaldatore primario con aumento della composizione molare di SO_2 nella miscela che porta a una maggiore differenza di temperatura attraverso il riscaldatore primario, e, conseguentemente, una potenziale riduzione delle portate di fluido termovettore nel campo solare. Inoltre, il CAPEX specifico ($/kWe) del blocco di potenza si riduce anche con l'aumento della composizione molare di SO_2 nella miscela, a causa dell'effetto collettivo della portata di massa relativamente inferiore del fluido di lavoro nel ciclo, delle dimensioni inferiori del riscaldatore primario e dei recuperatori e minor costo di pompaggio della miscela rispetto ai cicli di alimentazione sCO_2. Nel complesso, i cicli di alimentazione transcritici operanti con una miscela di CO_2-SO_2 risultano essere una scelta migliore per le centrali CSP in base ai vantaggi termodinamici ed economici rispetto ai cicli di alimentazione a sCO_2.

ABSTRACT

The increase in global warming potential and CO_2 emissions due to consumption of fossil fuels in conventional power plants is demanding new power production technologies which are efficient and economically sustainable. Increasing the energy efficiency of heat to power conversion plants is paramount to achieve the target of decreasing carbon foot print and reduction in cost of electricity. One possible way to produce power and achieve sustainability is by harnessing solar energy using advanced solar collectors, for example: parabolic trough collectors (PTC) and concentrated solar power (CSP). Another pathway of ample potential is utilizing exhaust gas waste heat from industries to produce power or to design combined heat and power system with the objective to reduce the environmental impact of exhaust gases.

Supercritical carbon dioxide (sCO_2) thermodynamic cycles for power production is a new technology under research and development in various research groups around the globe. Carbon dioxide is a thermally stable and non-flammable working fluid. The main attractive features of supercritical carbon dioxide power cycles are higher cycle efficiency, compact size of turbines and heat exchangers compared to conventional steam Rankine cycle and their integration capability with different heat sources ranging from low to high temperature.

However, there are some challenges of sCO_2 power cycles which includes lower heat recovery effectiveness and higher size foot print of cycle layouts which lead to higher specific cost when employed for waste heat recovery application. When the same sCO_2 power cycle technology is applied in CSP plant, the main problem arises is the drop in cycle efficiency due to high ambient temperature at CSP site making this technology less attractive compared to conventional steam Rankine cycle. Third main concern is the larger operating pressures (200 to 400 bar) and the need for larger heat transfer areas in recuperators since the heat exchange requirement is larger in recuperated cycle layouts.

To address the abovementioned challenges, this thesis proposed novel CO_2-based binary mixtures as working fluids to enhance thermodynamic performance of sCO_2 power cycles in waste heat recovery application and in concentrated solar power plants.

In a first step, dopants or additives are selected for CO_2-based binary mixture on the basis of required critical temperature, critical pressure, molecular weight, molecular

complexity and long-term thermal stability at high temperature. Other environmental and health hazards of additives are also considered during the selection. In a second step, thermodynamic properties of selected CO_2-based binary mixture are calculated using a reliable Equation of State (EoS). The accuracy of EoS is assessed by comparing the calculated thermodynamic properties with experimental property data available in the literature. The main deciding factor to select suitable mixture composition is the vapor-liquid critical point of a CO_2-based binary mixture. Therefore, a numerical program is developed which can compute all vapor-liquid critical points of a binary mixture with reasonable accuracy at different mixture molar composition.

In a third step, the selected CO_2-based binary mixtures are utilized as working fluids in carbon dioxide power cycles and thermodynamic performance is investigated. Two heat source applications are considered: high temperature waste heat recovery (T_{max}=350℃) and concentrated solar power (T_{max}=550℃ and 700℃).

In the topic of high temperature heat recovery, CO_2-R134a [70% molar CO_2] mixture in transcritical power cycle showed 4 percentage points higher total efficiency compared to sCO_2 power cycle (14.3% in case of CO_2-R134a versus 10.8% in case of CO_2) when simple cycle layout is considered. Moreover, the total efficiency of transcritical power cycle with CO_2-R134a [70% molar CO_2] mixture and simple cycle layout is also 1.5 percentage points higher than single flow split dual expansion sCO_2 cycle which is a complex cycle layout (14.3% versus 12.7%). These gains in total efficiency demonstrate promising potential of CO_2-based binary mixture working fluids owing to higher total efficiency and simpler cycle layout (that imply lower installation cost) compared to sCO_2 power cycle. Compared to organic Rankine cycle (ORC), comparable total efficiency is achieved in case of CO_2-R134a [70% molar CO_2] mixture but with only 30% molar R134a in the mixture that means smaller amount of R134a (an expensive fluid) is required to achieve the same total efficiency as obtained in ORC with 100% molar R134a as working fluid. In comparison to sCO_2 cycle and CO_2-R134a mixture power cycle, other working fluids in ORC like CH_3Cl, CH_2Cl_2, and CH_3OH demonstrated highest total efficiency (18% to 20%). However, they are flammable working fluids.

For application in CSP power block, five CO_2 based binary mixtures are considered as working fluids and the gain in cycle efficiency is studied with reference to sCO_2 recompression cycle and sCO_2 simple recuperative cycle. The analysis is performed for

higher cycle minimum temperature (T_{min} = 50 °C) to simulate higher ambient temperature conditions typically available at CSP plant sites. With a simple recuperative cycle layout, CO_2-$TiCl_4$ [80% molar CO_2] working fluid shows cycle efficiency of 50.7%, which is close to the optimum cycle efficiency of the sCO_2 recompression cycle (i.e. 50.8 percent) at cycle maximum temperature of 700℃. Other three mixtures like CO_2-C_6F_6 [85% molar CO_2], CO_2-CF_3I [60% molar CO_2] and CO_2-SO_2F_2 [40% molar CO_2] mixtures also brings about gain in cycle efficiency compared to sCO_2 simple recuperative cycle, that is 2.7 points gain in CO_2-C_6F_6 mixture, 1.1 points gain in CO_2-CF_3I mixture and 1.5 points gain in CO_2-SO_2F_2 mixture working fluid for cycle maximum temperature of 550℃.

Sulphur dioxide (SO_2) is also selected as dopant for CO_2-based binary mixture since it is thermally stable at high temperature (700℃), non-flammable with negligible ozone depletion potential. The only compromise in the selection of SO_2 is its higher health hazard which can be resolved in power plant by controlling leakage problems. Considering CO_2-SO_2 as working fluid, a detailed thermodynamic analysis is carried out for a 100 MW power block integrated with advanced concentrated solar power tower with cycle maximum temperature of 700 ℃ and minimum temperature of 51℃. Analysis at different molar composition of mixture suggests 85% molar CO_2 mixture as optimum choice owing to higher cycle efficiency irrespective of cycle layout. Cycle efficiency obtained by recompression cycle with CO_2-SO_2 mixture [85% molar CO_2] is 50.8% (2 percentage point higher than sCO_2 recompression cycle) at T_{max} of 700 ℃ and P_{max} of 250 bar. Another worth noting benefit of adopting CO_2-SO_2 mixture is the reduction in temperature at inlet of the primary heater with increase in molar composition of SO_2 in the mixture which leads to larger temperature difference across primary heater, as a result, lower size of thermal energy storage and solar receiver is required for constant thermal power input. Moreover, specific CAPEX ($/kWe) of power block also reduces with increase in molar composition of SO_2 in the mixture which is due to the collective effect of comparatively lower mass flowrate of working fluid in the cycle, lower size of primary heater and recuperators and lower pumping cost of the mixture compared to sCO_2 power cycles. Overall, transcritical power cycles operating with CO_2-SO_2 mixture turns out to be a better choice for CSP power plants based on thermodynamic and economic advantages compared to sCO_2 power cycles.

List of Publications

Journal publications

1. C. M. Invernizzi, **A. Ayub**, G. Di Marcoberardino, and P. Iora, "Pure and Hydrocarbon Binary Mixtures as Possible Alternatives Working Fluids to the Usual Organic Rankine Cycles Biomass Conversion Systems," *Energies*, vol. 12, no. 21, p. 4140, Oct. 2019, doi: 10.3390/en12214140.
2. G. Di Marcoberardino, C.M. Invernizzi, P. Iora, **A. Ayub**, D. Di Bona, P. Chiesa, M. Binotti, G. Manzolini, "Experimental and analytical procedure for the characterization of innovative working fluids for power plants applications," Appl. Therm. Eng., vol. 178, no. May, p. 115513, Sep. 2020, doi: 10.1016/j.applthermaleng.2020.115513.
3. **A. Ayub**, C. M. Invernizzi, G. Di Marcoberardino, P. Iora, and G. Manzolini, "Carbon Dioxide Mixtures as Working Fluid for High-Temperature Heat Recovery: A Thermodynamic Comparison with Transcritical Organic Rankine Cycles," *Energies*, vol. 13, no. 15, p. 4014, Aug. 2020, doi: 10.3390/en13154014.
4. F. Crespi, P. Rodríguez de Arriba, D. Sánchez, **A. Ayub**, G. Di Marcoberardino, C.M. Invernizzi, G.S. Martínez, P. Iora, D. Di Bona, M. Binotti, G. Manzolini, "Thermal efficiency gains enabled by using CO2 mixtures in supercritical power cycles," Energy, vol. 238, p. 121899, Jan. 2022, doi: 10.1016/J.ENERGY.2021.121899.
5. E. Morosini, **A. Ayub**, G. di Marcoberardino, C. M. Invernizzi, P. Iora, and G. Manzolini, "Adoption of the CO2 + SO2 mixture as working fluid for transcritical cycles: A thermodynamic assessment with optimized equation of state," *Energy Convers. Manag.*, vol. 255, p. 115263, Mar. 2022, doi: 10.1016/j.enconman.2022.115263.

Conference Publications

1. **A. Ayub**, G. Marcoberardino, C. Invernizzi, and P. Iora, "Advanced Thermodynamic Power Cycles Utilizing Carbon Dioxide Based Mixtures As Working Fluids For High Temperature Waste Heat Recovery," in *4th European sCO2 Conference for Energy Systems: March 23-24, 2021, Online Conference***, Mar. 2021**, pp. 58–67, doi: https://doi.org/10.17185/duepublico/73947.
2. F. Crespi, P. Rodríguez de Arriba, D. Sánchez, **A. Ayub,** G. Di Marcoberardino, C.M. Invernizzi, G.S. Martínez, P. Iora, D. Di Bona, M. Binotti, G. Manzolini, "Thermal efficiency gains enabled by using supercritical CO2 mixtures in Concentrated Solar Power applications," in *4th European sCO2 Conference for Energy Systems: March 23-24, 2021, Online Conference*, **Mar. 2021,** pp. 291–300, doi: 10.17185/DUEPUBLICO/73972.

List of Figures

List of Tables

Acknowledgements

First and foremost, I thank Allah Almighty, my creator and the creator of the entire world, for giving me life full of energy and abilities that allow me to carry out all of my daily activities.

I'd like to thank my supervisor, Professor Costante Mario Invernizzi, for considering me as a PhD student and patiently guiding me throughout my PhD work. Thank you for always removing technical errors in my Aspen Simulation work, editing and reviewing progress reports, and sharing new ideas with me. Many thanks also for resolving all other issues concerning my residence in Italy.

I am grateful to Professor Laura Depero (coordinator) and Fabiana Farro (Responsabile U.O.C. Dottorati di Ricerca) for providing student services, granting funds and scholarships, and being always available to assist international student like me during the difficult COVID-19 period.

I would also like to express my gratitude to Gioele Di Marcoberardino and Paolo Iora for providing feedback on my research work and for always being willing to share their knowledge and skills, which has helped me improve my practical knowledge. I had the pleasure of working with Ettore Morosini (Politecnico di Milano, Italy) and Francesco Crespi (University of Seville, Spain), and I hope to work with them again in the future.

I am forever thankful to my beloved parents, who constantly motivates and encourages me and always prays for my success in this life and the life to come.

Finally, I want to express my sincere gratitude to my beloved wife and my adorable little daughter for their immense love and prayers.

Nomenclature

Acronyms

CAPEX	Capital expenditure ($/kWel)
CSP	Concentrated solar power
Ds	Specific diameter of axial turbine
EoS	Equation of state
GERG-2008	Groupe Européen de Recherches Gazières 2008 EoS
GWP	Global warming potential
HTF	Heat transfer fluid
INTLAB	Interval laboratory tool box
INBM	Interval Newton Bisection Method
LCOE	Levelized cost of electricity, $/MWh
MAPE	Mean absolute percentage error
MITA	Minimum internal temperature approach, ℃
NFPA	National Fire Protection Association
N	Shaft speed
Ns	Specific speed of axial turbine
ODP	Ozone Depletion Potential
PC-SAFT	Perturbed-chain Statistical Associating Fluid Theory EoS
PCHE	Printed circuit heat exchanger
PHE	Primary heat exchanger
PHC	Partial heating cycle layout
REFPROP	Reference Fluid Thermodynamic and Transport properties
SFDE	Single flow split dual expansion cycle layout
SRC	Simple recuperative cycle layout
sCO_2	Supercritical CO_2
TES	Thermal energy storage
UA	Overall heat transfer times area of heat exchanger
VLE	Vapor-Liquid Equilibrium

Symbols

DP	Pressure drop
ΔT	Temperature difference, ℃
m	Segment number of fluid components for PC-SAFT EoS
$\dot{m}$	Mass flow rate, kg/s
β_T	Binary parameter of temperature reducing function for GERG-2008 EoS
β_v	Binary parameter of density reducing function for GERG-2008 EoS
γ_T	Binary parameter of temperature reducing function for GERG-2008 EoS
γ_v	Binary parameter of density reducing function for GERG-2008 EoS

γ_2	Rotor inlet flow velocity angle for axial turbine
ΔH_f^0	Standard enthalpy of formation of compound

Greek symbols

η_{cycle}	Power cycle thermodynamic efficiency
$w_{specific,cycle}$	Power cycle specific work, kJ/kg
ε/k	Characteristic segment energy parameter for PC-SAFT EoS, K
σ	Characteristic segment size parameter for PC-SAFT EoS
ω	Pitzer acentric factor
ϕ	Heat recovery effectiveness
ϕ_f	Flow coefficient in axial turbine
Λ	Degree of reaction of axial turbine
ψ	Blade loading coefficient
τ	Cycle temperature ratio, T_{max}/T_{min}

Subscripts

bub	Bubble point
cond	Condenser
cr	Critical point
dew	Dew point
el	Electrical
i,j	Fluid species
IN	Input
LM	Log-mean
m	Mean diameter
mix	mixture
wf	Working fluid

Chapter 1: Introduction

1.1 **Background**

The rise in demand of electricity and the global cause to reduce the consumption of fossil fuels suggests renewable energy sources as potential solution for power production. Among the various renewable energy sources, solar energy is the one which can be exploited using different solar concentration technologies. The intermittency of solar energy compared to fossil fuel-based energy pose additional challenge of energy storage to allow flexible operation of power plant.

Secondly, the valorization of industrial waste heat by utilizing waste heat for power production is also potential way of reducing carbon footprint of the industry and reduction of global warming [1].

Steam Rankine cycles, a mature technology has been used for decades for power production harnessing fossil fuels. Now, this technology is also adopted for power production from concentrated solar power and from waste heat recovery. The technology is economically feasible for large scale power production (>100 MW) owing to larger size and larger number of cycle components; requirement of larger feedwater heaters to enhance cycle efficiency and necessity of water purification system. Organic Rankine cycle is another power production technology which has been developed for small scale power production especially for off grid and remote areas [2]–[4]. However, the efficiency of technology is lower therefore it is only feasible economically for power production ranging from few kilowatts to maximum of 10 MW. Another challenge in organic Rankine cycle is the lower thermochemical stability of organic working fluids which limits the maximum temperature of power cycle (for most fluids, allowable T_{max} < 400℃) and thus limits the power production [5].

1.2 **Supercritical Carbon dioxide power cycles**

In the last decade, there has been renewed interest in using carbon dioxide (CO_2) as a working fluid in thermodynamic cycles for power generation. Supercritical carbon dioxide (sCO_2) power cycles, in particular, are being investigated using low, medium, and high temperature heat sources [6]–[8]. The main advantage of sCO_2 power cycle technology is its higher thermal efficiency and smaller size footprint when compared to conventional steam Rankine cycle technology. Because of the higher density in the

supercritical phase, the sCO_2 cycle requires approximately ten times smaller turbomachinery than the steam Rankine cycle for same power output.

When turbine inlet temperatures are greater than 650°C, Angelino [9] demonstrated that the CO_2 condensing cycle has a higher efficiency than the reheat steam Rankine cycle. For turbine inlet temperature less than 550°C, the cycle efficiency of condensing CO_2 cycle is lower than the steam cycle, however, it is still cost-effective due to the need of fewer cycle components (No need of large turbine stages and large number of feed-water heaters). Based on the cycle configurations presented in Angelino's work, Dostal *et* al [10] investigate the thermodynamic performance and design main cycle components of sCO_2 cycles for advanced nuclear reactors. The recompression layout was chosen because it showed higher cycle efficiency and lower power plant cost than the steam Rankine cycle.

Application in concentrated solar power (CSP) and associated challenges

Carbon dioxide, owing to higher thermochemical stability at temperature up to 700 ℃ allow its application in high temperature concentrated solar power plants (CSP). Considerable efforts are being made to study the thermodynamic performance and economic assessment of supercritical carbon dioxide cycles integrated with concentrated solar power. The main aim is to achieve higher cycle efficiency and lower levelized cost of electricity; the target value to approach in near future is 6 cents/kWh [11]. In this perspective, different cycle architectures (or layouts) are proposed like recompression cycle and partial cooling cycle to enhance power block thermodynamic efficiency and integration capability with CSP [12].

The operation of compressor of sCO_2 cycle near to critical point of CO_2 (T_{cr} = 31℃, P_{cr} = 7.14 MPa) results in lower compressor work and higher cycle efficiency owing to real gas effects [13]. However, the rise in compressor inlet temperature of CO_2 must occur with rise in temperature of cooling medium i.e. air in case of dry cooling. As a result of higher compressor inlet temperature, compression work enhances which brings about dramatic drop in cycle efficiency. The same effect happens in CSP sites, the temperature of air entering the dry cooler is normally high ranging from 30℃ to 50 ℃ and even higher during peak summer days. With such high temperature, the compressor inlet temperature also increases which negatively affects cycle efficiency [14].

To address this issue, authors in ref [15], modified the configuration of sCO_2 recompression cycle by introducing another low temperature recuperator before the recompressor in order to shift the recompression process near to critical point temperature and obtain reduction in work consumption of recompressor. As a result, the modified sCO_2 recompression cycle proved to be less sensitive to increase in compressor inlet temperature; it yields 1.92% higher efficiency than typical sCO_2 recompression cycle at compressor inlet temperature of 50℃.

Another real gas effect of supercritical CO_2 cycle is larger difference of heat capacity between cold and hot streams of recuperator which increases irreversibility in recuperator thus limits cycle efficiency. The issue of irreversibility is handled by adopting recompression cycle configuration and other split cycle configurations suggested by Angelino [9] in late 90s and Crespi *et* al [16] in recent article. However, the advanced layouts improve efficiency; they also increase the installation costs.

Application in waste heat recovery and associated challenges

In recent past, various works are also carried out to investigate potential of supercritical carbon dioxide cycles for waste heat recovery. In this regard, a brief overview of different waste heat recovery technologies and thermodynamic analysis of supercritical carbon dioxide cycles is presented in Chapter 4. The main challenge in supercritical carbon dioxide cycle is lower heat recovery effectiveness and larger specific costs of advanced cycle layouts [17].

1.3 Proposed Solution and Main Objectives

Instead of modifying cycle configuration or adjusting operating conditions to increase cycle efficiency of sCO_2 power cycles, another pathway is to alter the properties of CO_2 by using CO_2 based binary mixtures or CO_2 blends [18]. This new concept is recently explored in some scientific papers [19], [20] and patents [21]. The underlying idea is to shift the critical point of CO_2 to higher temperature by adding certain amount of carefully selected additive with critical temperature higher than CO_2. In this way, condensation cycle can be designed with compression inlet conditions lower than critical point temperature of the CO_2 mixture. The critical point temperature of the mixture and corresponding mixture compositions are decided depending upon the ambient temperature available for dry cooling. Using this concept, authors in ref [14] performed

the thermodynamic evaluation of power cycles operating with five different CO_2-based binary mixtures working fluids in recompression Brayton cycle incorporated with dry cooling. The study selected CO_2-cyclohexane, CO_2-propane, CO_2-butane, CO_2-isobutane and CO_2-H_2S as candidate working fluids and assessed the performance of the power cycle at different ambient temperatures based on energy and exergy analysis. It was found that power cycles operating with CO_2-based binary mixtures yield better efficiency under higher ambient temperature compared to sCO_2 Brayton cycle. However, the study showed important results pertinent to CO_2-based binary mixtures for dry cooling power cycles, but it didn't take into account the thermochemical stability of selected pure compounds and the binary mixtures at higher turbine inlet temperatures (550℃).

In ref [22], authors proposed CO_2-based binary mixtures for thermodynamic performance improvement of sCO_2 Brayton cycles integrated with molten salt solar power tower (SPT). Based on analysis on three different binary mixtures and four-cycle configurations, CO_2-Xenon binary mixture in intercooling power cycle was decided to be an effective way to enhance the system efficiency as compared to corresponding sCO_2 power cycles.

Table 1: Summary of recent scientific works on CO_2 mixtures working fluids in carbon dioxide power cycles

Authors	Objective	Working Fluids	Heat Source	Main Outcomes
Jeong *et al* [23] (2013)	To study the Improvement in performance of recompression Brayton cycle on adding different gases into CO_2.	CO_2/N_2 CO_2/O_2 CO_2/Helium CO_2/Argon	Sodium cooled fast Reactor (SFR)	Cycle efficiency enhanced by 1.73%
Bonalumi *et al* [24] (2018)	To improve the performance of CO_2 cycles in warm areas using optimum binary mixture of CO_2 and $TiCl_4$. To highlight the problems and challenges that arise during the selection of an optimum binary mixture for power production.	CO_2 $CO_2/TiCl_4$	Solar power tower	5% gain in efficiency is achieved in case of CO_2 $TiCl_4$ recuperative Brayton power cycle compared to recuperative CO_2 power cycle. 3% gain in efficiency is achieved in case of CO_2 $TiCl_4$ recompressed Brayton power cycle compared to

				recompressed CO_2 power cycle.
Manzolini *et al* (2019) [25]	To improve the thermal-to-power conversion efficiency and to reduce the levelized cost of electricity (LCOE) of solar tower power plants.	CO_2 N_2O_4 CO_2/N_2O_4 $CO2/TiCl_4$	Solar Power Tower	The suitable increase in critical temperature of CO_2 can be achieved by adding few molar percentages of N_2O_4 or $TiCl_4$. As a result of this addition, binary mixture is formed which proofs to be a better working fluid for Brayton cycles operating in warm and arid areas (like solar plants sites). The power cycles operating with the considered binary mixtures outperforms the conventional steam Rankine cycle both in terms of efficiency and LCOE.
Aqel *et* al (2021) [26]	Thermodynamic performance and turbine design of trancritical thermodynamic cycle for 100MW CSP power plant.	$CO_2/TiCl_4$ CO_2/NOD CO_2/C_6F_6	Solar power tower	Maximum efficiencies achieved by $CO_2/TiCl_4$, CO_2/NOD and CO_2/C_6F_6 are 49.5%, 46.5% and 42.3% respectively. Specific work of turbine increase with increase in fraction of NOD in the CO_2-NOD mixture.

Table 1 summarized main findings of some recent works which proposed different CO_2 mixtures as working fluids in carbon dioxide power cycles both in perspective of thermodynamics and economics.

The previous works, on one hand, showed potential benefits of CO_2 based binary mixtures as working fluids in thermodynamic power cycles, however, there are important aspects which require deeper study including: 1) determination of accurate vapor-liquid equilibrium and critical points of CO_2 mixtures using accurate property models, 2) optimization of property models using experimental data of CO_2 mixtures, 3) determination of maximum operating temperature for CO_2 mixtures using thermal stability tests and 4) selection of optimum composition of the mixture in perspective of thermodynamic performance, CAPEX and OPEX of power cycle.

To address aforementioned challenges and issues of sCO_2 cycles, this thesis proposed novel carbon dioxide mixtures as working fluids in carbon dioxide thermodynamic power cycles for concentrated solar power and waste heat recovery applications. In brief, the key objectives of adopting CO_2-based binary mixtures as working fluids are:

1. To improve cycle thermodynamic efficiency of power cycles operating under higher ambient temperature.
2. To improve heat recovery effectiveness and total efficiency in waste heat recovery.
3. To reduce the cycle maximum operating pressure in waste heat recovery power cycles.
4. To adopt simple cycle configuration/layout compared to Steam Rankine cycle.
5. To reduce the size of heat exchangers (i.e. UA of recuperators) in particular recuperators which are responsible for internal heat recovery.
6. To reduce the specific investment costs (CAPEX) of power block.

1.4 **Structure of the Thesis**

This chapter (Chapter 1) covers the background of supercritical carbon dioxide power cycles and their applications. The main challenges of sCO_2 cycles in CSP and waste heat recovery are discussed in section 1.2. The proposed solution is explained (in section 1.3) in which the main idea is to adopt carbon dioxide based binary mixture (or CO_2 blends) as working fluids to enhance thermodynamic performance, reduce size and CAPEX of sCO_2 power cycles.

Thermophysical properties of CO_2-based binary mixture working fluids

Before adopting novel CO_2 mixtures as working fluid in a power cycle, the first and foremost task is to define a reliable method for calculation of thermophysical properties of CO_2-based binary mixtures. Therefore, Chapter 2 is dedicated to explain different property models and equation of states; mathematical formulation of three equation of states (EoS) are described and procedure is developed to compute binary interaction parameter ($k_{1,2}$) required in the equation of state using the experimental vapor-liquid equilibrium data. There are many binary mixtures for which the experimental VLE data is not available to calculate $k_{1,2}$, for such mixtures a correlation is developed using the data of CO_2 mixtures with known value of $k_{1,2}$. Moreover, equations to compute enthalpy and entropy of a binary mixture are also explained for each EoS. The final section of the paper presented a step-by-step procedure for selecting an accurate equation of state model for any CO_2-based binary mixture using available experimental VLE data, because experimental data is necessary to assess the accuracy of different equations of states.

Vapor-liquid critical points of CO_2-based binary mixture

Prior to cycle thermodynamic analysis, it is necessary to calculate the critical points of CO_2-based binary mixture at different mixture composition. Information of vapor-liquid critical points is important in transcritical power cycle in order to decide suitable mixture composition of the working fluid. Given the importance of critical point, in Chapter 3, a numerical program is developed in MATLAB in conjunction with INTLAB toolbox to solve the system of equations of criticality conditions. The developed program is capable to compute stable, unstable and meta stable critical points of a binary mixture.

Thermodynamic potential of novel CO_2-based binary mixture working fluid in power cycle for waste heat recovery

Once the analytical procedure to compute thermodynamic properties and the critical points of a CO_2-based binary mixture is developed, the subsequent step is to perform cycle thermodynamic analysis. In Chapter 4, thermodynamic performance of three types of thermodynamic cycles is compared for application in high temperature waste heat recovery. The first section of the chapter considers sCO_2 power cycles and investigates the effect of different cycle operating conditions and cycle layouts on thermodynamic performance. The second part of Chapter 4 evaluated the thermodynamic performance of transcritical organic Rankine cycles using the same heat source. In the third phase of the chapter, transcritical power cycles with CO_2-based binary mixtures as working fluids are

proposed in order to improve thermodynamic performance and reduce power cycle size compared to sCO_2 technology. The advantages of using a CO_2-based binary mixture in a transcritical cycle are summarized in terms of thermodynamic cycle efficiency, total efficiency, axial turbine geometry and size, and benefits in heat exchange in the power cycle recuperator.

Thermodynamic potential of novel CO_2-based binary mixture working fluid in power cycle for concentrated solar power plant

The thermodynamic analysis of sCO_2 power cycles for concentrated solar power plant is presented in the Chapter 5. The effect of increase in cycle minimum temperature, cycle minimum pressure, cycle maximum temperature and cycle maximum pressure on thermodynamic cycle efficiency is evaluated. The optimum cycle efficiency of recompression sCO_2 is obtained at higher cycle minimum temperature (i.e. 50℃).

Additionally, CO_2-based binary mixtures are chosen as working fluids in Chapter 5 due to their favorable thermodynamic and environmental characteristics. Peng Robinson EoS is used to calculate the thermodynamic properties, and a simple cycle layout is chosen for the calculations. The goal is to increase cycle efficiency at higher minimum cycle temperatures than with sCO_2 cycles. The results demonstrate potential gain in cycle thermal efficiency and smaller recuperator size compared to sCO_2 power cycle are obtained by using CO_2-based binary mixture working fluids.

Chapter 6 delves deeper into the design of a transcritical power cycle for a CSP power plant using a CO_2-SO_2 mixture as the working fluid. First, the reason for using SO_2 is explained. The thermodynamic properties of a CO_2-SO_2 mixture are calculated using the PC-SAFT Equation of state because it is more accurate than the PR-EoS, as explained in Chapter 2. Finally, a thermodynamic and economic analysis of a transcritical power cycle operating with a CO_2-SO_2 mixture with a power block output of 100 MWel is performed.

Conclusion Chapter

The thesis concludes with Chapter 7, which summarizes the main conclusions of this work and outlines the main challenges and future work that needs to be done.

Chapter 2: Study of thermodynamic behavior of CO_2 based binary mixtures using Equation of state

2.1 Equation of state (EoS)

A reliable thermodynamic assessment of power cycles is strongly dependent on the accuracy of thermodynamic properties of a working fluid. Therefore, this chapter is focused on study of thermodynamic properties of CO_2 mixtures which includes vapor-liquid equilibrium (VLE), density, specific heat, enthalpy and entropy of the mixtures. The most important step is to identify appropriate thermodynamic property model which can predict properties with accuracy (or show good agreement with experimental property data).

Many equation of states (EoS) are formulated in literature for binary mixtures among which some are non-predictive and some are predictive ones. Non-predictive EoS requires experimental VLE data for optimization of binary interaction parameters while predictive EoS are capable to predict properties without the need of experimental VLE data.

Nevertheless, proper knowledge about mathematical formulation and behavior of EoS is important before selecting suitable EoS for any particular CO_2 based binary mixture. Therefore, next sections describe three EoS and the procedure for determination of binary interaction parameter.

Cubic Equations of state

Cubic equation of states are most common EoS among industry and scientist because of wide range of validity and simpler mathematical formulation. The first Cubic EoS is formulated by van der Waals (vdW) in 1873 to improve ideal gas model by taking into account volume of molecules and attractive forces of attraction between molecules. Mathematical form of this EoS is,

$$P = \frac{RT}{v - b} - \frac{a}{v^2}$$

Parameter ***a*** accounts for attractive forces between molecules and parameter ***b*** accounts for the volume of molecules. vdW EoS is the first EoS which describes all thermodynamic

phases of a fluid including gas, liquid and supercritical phase. Later on, Redlich-Kwong (RK) and Soave-Redlich-Kwong (SRK) EoS are introduced as a modified form of van der Waals EoS. Mathematical formulation of SRK EoS is,

$$P = \frac{RT}{v-b} - \frac{a(T)}{v(v+b)}$$

The major enhancement compared to van der Waals EoS is the substitution of temperature dependent parameter 'a'.

Peng-Robinson EoS

In 1975, cubic Peng-Robinson (PR) EoS is developed as a modification to enhance the predictive capability of SRK EoS. Firstly, this EoS was applied to study P-v-T behavior of some hydrocarbons. Later on, different modifications of PR EoS are proposed to enhance its applicability to polar compounds and binary mixtures. Compared to SRK EoS, PR EoS calculates vapor pressures and liquid densities more accurately and can also predicts properties near critical region (for Z_c =0.307). Moreover, PR EoS is also capable to estimate retrograde condensation in natural gas pipelines [27].

In the Chapter 4 of this thesis, standard form of PR-EoS in conjunction with van der Waals mixing rules is used to study thermodynamic properties of CO_2 based binary mixtures.

The standard PR EoS for pure fluid is expressed as,

$$P = \frac{RT}{v-b} - \frac{\alpha a}{v(v+b)+b(v-b)}$$

Where

$$\alpha = \left[1 + k(1-\sqrt{T_r})\right]^2$$

$$k = 0.37464 + 1.54226\omega - 0.26992\omega^2$$

$$a = 0.45724\frac{R^2T_c^2}{P_c}$$

$$b = 0.0778\frac{RT_c}{P_c}$$

The applicability of PR EoS can be extended to binary mixtures with the help of mixing rules. In literature [27], various formulations of mixing rules have been proposed; however, for sake of simplicity, this study adopted simpler formulation of mixing rules known as van der Waals mixing rules as shown below,

$$a_{mixture} = \sum_i \sum_j z_i \, z_j \, a_{i,j}$$

$$b_{mixture} = \sum_i \sum_j z_i \, z_j \, b_{i,j}$$

And,

$$a_{i,j} = \sqrt{a_i a_j}(1 - k_{i,j})$$

$$b_{i,j} = \frac{b_i + b_j}{2}$$

Hence, critical temperature and critical pressure of pure fluids (subscript ***i*** corresponds to fluid 1 and ***j*** corresponds to fluid 2), acentric factor along with accurate value of binary interaction parameter ($k_{i,j}$) are required to completely describe P-v-T behavior of a binary mixture using PR EoS.

Finally, residual enthalpy and residual entropy can be calculated using following equations as function of specific volume (v),

$$\Delta h_{residual} = \int_0^P \left(v - T \left(\frac{\partial v}{\partial T} \right)_P \right)_T dP$$

$$\Delta s_{residual} = \int_0^P \left(\frac{R_{gas}}{P} - \left(\frac{\partial v}{\partial T} \right)_P \right)_T dP$$

PC-SAFT EoS

PC-SAFT stands for perturbed chain statistical associating fluid theory; it is an EoS based on perturbation theory in which molecule is modeled as chain of freely joined spheres. Fundamentally, it describes total intermolecular forces into repulsive and attractive forces. Hard chain reference system is used to account for repulsive forces while attractive forces are divided into contributions from polar, dispersion and associating forces.

In PC-SAFT EoS, generalized ψ function is defined which is function of residual Helmholtz energy as shown below:

$$\psi = \frac{a_{res}}{RT} = \int_0^{\rho} Z - 1 \frac{d\rho}{\rho}$$

And,

$$\psi = \psi^{HC} + \psi^{polar} + \psi^{disp} + \psi^{assoc}$$

Where, a_{res} is the molar residual Helmholtz energy of mixtures, R is the gas constant, T is the temperature, ρ is the molar density, and Z is the compressibility factor. a_{res} is defined as difference of actual Helmholtz energy and ideal gas Helmholtz energy i.e. $a_{actual} - a_{ideal}$. There are separate models available in the works of Gross and Sadowski [28] to calculate all four terms. The modeling of these forces are out of the scope of this chapter. For more knowledge, reader is encouraged to read the works of Gross and Sadowski.

Table 2: Pure component parameters required in PC-SAFT EoS

Compounds	m	σ [Å]	ϵ/k [°C]	k_{AB}	ϵ_{AB}/k_B [°C]
CO_2	2.5692	2.5637	-121.05	Non-associating	
SO_2	2.8611	2.6826	-67.80		
C_6F_6	3.779	3.396	-51.50		
HCl	1.5888	2.9567	-66.09	0.00057172	766.8

For non-associating pure compounds, three pure fluid parameters are required in PC-SAFT EoS to compute hard chain and dispersive contributions of ψ. They are: segment number (m), segment diameter (σ) and segment-segment interaction energy (ϵ/k) parameter. For associating compounds, two additional parameters known as association volume (k_{AB}) and association energy (ϵ_{AB}/k_B) are also required. These pure fluid parameters are usually obtained by fitting experimental liquid density and vapor pressure data; these parameters are reported in Table 2 for CO_2 and some other compounds.

For binary mixtures, one binary interaction parameter ($k_{i,j}$)) is also required in addition to pure fluid parameters and it is determined using regression as described in section 2.2 .

Lastly, with a known value of ψ, the residual enthalpy and residual entropy can be calculated using following equations,

$$\Delta h_{residual} = RT\left[-T\frac{\partial \psi}{\partial T} + (Z-1)\right]$$

$$\Delta s_{residual} = R\left[-\psi + \ln(Z) - T\frac{\partial \psi}{\partial T}\right] - Rln\left(\frac{P}{P_{ref}}\right)$$

REFPROP method

REFPROP uses multi-parameter Helmholtz energy equation of state (also known as GERG-2008 EoS) to predict thermodynamic properties of pure fluids as well as binary mixtures. This EoS is proposed by Neumann *et* al [29] to predict thermodynamic properties of CO_2 rich binary mixtures.

Mathematical formulation of GERG-2008 EoS and comprehensive description of binary parameters are given in the thesis of Neumann [30]. In summary, four binary parameters ($\beta_{T,ij}, \beta_{V,ij}, \gamma_{T,ij}, \gamma_{V,ij}$) are needed to calculate temperature and density reducing functions. The values of these parameters are computed by curve fitting with experimental VLE data or molecular data. For few CO_2 mixtures, the values of these parameters are available in REFPROP software.

2.2 Determination of binary interaction parameter ($k_{i,j}$) for PR EoS and PC-SAFT EoS

As mentioned earlier, a single binary interaction parameter is also required for mixing rules In addition to pure fluid parameters in PR EoS and PC-SAFT EoS. The accurate value of binary interaction parameter ($k_{i,j}$) ensures accurate results of properties of a binary mixture. A well-known practice adopted in literature for determination of binary interaction parameter is by doing regression on experimental vapor-liquid equilibrium (VLE) data (P-xy or T-xy data).

In this work, Aspen plus software v11 is used to perform regression analysis using experimental VLE data (acquired from the literature) with selected EoS as thermodynamic model and $k_{i,j}$ as fitting parameter. Regression problem is defined as,

DATA: *Experimental VLE*

MODEL: *Peng-Robinson EoS with van der Waals mixing rule or PC-SAFT EoS*

FITTING PARAMETER: *Binary interaction parameter ($k_{i,j}$)*

OBJECTIVE FUNCTION OF REGRESSION: *Maximum Likelihood*

For all CO_2 mixtures considered in this thesis, regression approach described in this section is adopted to determine the value of binary interaction parameter ($k_{i,j}$) subject to availability of experimental VLE data of the mixture under investigation.

As previously mentioned, regression is not required for GERG-2008 EoS because binary parameters are already computed for each binary mixture and available in REFPROP software.

2.3 Binary interaction parameter for binary mixtures with No experimental VLE data

The original procedure to compute $k_{i,j}$ (or $k_{1,2}$ in case of binary mixture) as explained in the previous sections is by regression using the experimental VLE data of the binary mixture. The question arises, what if there is No available experimental VLE data for a particular mixture to compute $k_{1,2}$?

Considering the formulation of van der Waals mixing rules, the coefficient $a_{mixture}$ of the Peng Robinson EoS can be expressed as,

$$a_{mixture} = \sum_i \sum_j z_i \, z_j \, a_{i,j} = \; {z_1}^2 a_1 + 2 z_1 z_2 a_{1,2} + {z_1}^2 a_2$$

Where, z_1 and z_2 stands for the molar composition of pure fluid component 1 and component 2 respectively. The coefficient $a_{1,2}$ by definition can be expressed as,

$$a_{1,2} \equiv \sqrt{a_2}(1 - k_{1,2})$$

The parameters a_2 represents magnitude of intermolecular forces of attraction and corresponds to second pure component (or dopant) of CO_2 based binary mixture. The value of a_1 in CO_2 mixtures is constant since first component is CO_2. The value of a_2 for different fluids can be calculated as,

$$a_2 = \frac{27 R^2 T_{c,2}^2}{64 N_A^2 P_{c,2}} \quad \left[\frac{\mathrm{Jm}^3}{\mathrm{molecule}^2}\right]$$

Where, $T_{c,2}$ and $P_{c,2}$ are the critical point temperature and critical point pressure of second fluid component. $R=8.3143\ Jmol^{-1}K^{-1}$ is the gas constant and N_A is the Avogadro number.

A correlation is developed by collecting the values of $a_{1,2}$ and a_2 of 19 CO_2 mixtures for which the values of $k_{1,2}$ are known. The regression of data resulting correlation are shown in Figure 1. This correlation can be very helpful to provide first estimation of $a_{1,2}$ for binary mixtures with No experimental VLE data. Based on the estimated value of $a_{1,2}$, the value of $k_{1,2}$ can be determined.

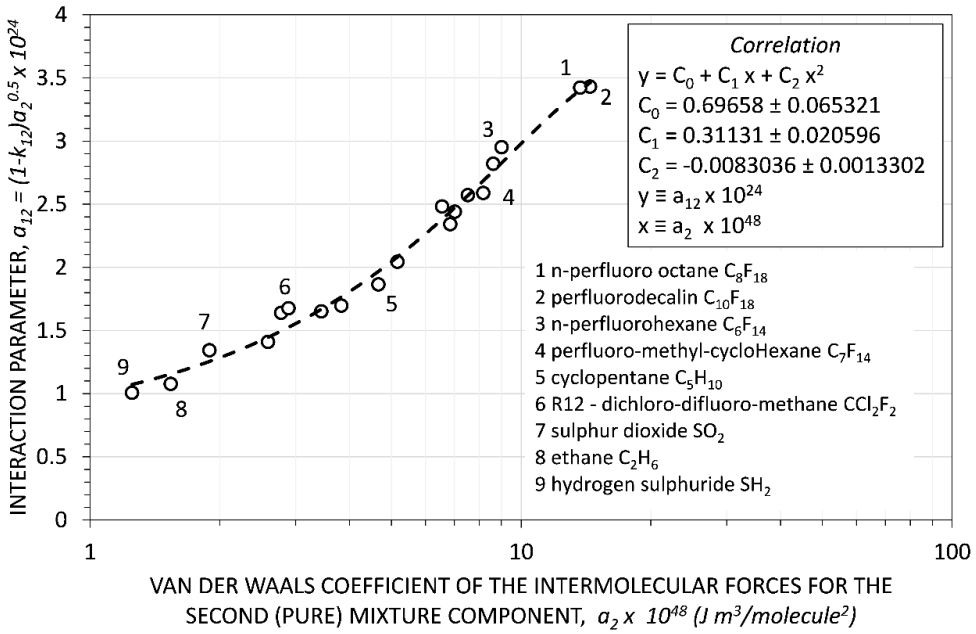

Figure 1: Regression of interaction parameter ($a_{1,2}$) for different CO_2 mixtures. Symbols corresponds to interaction parameter of 19 CO_2 mixtures with available experimental data. Dotted line shows the trend line and the Box represents resulting correlation and definition of coefficients.

2.4 CO_2-SO_2 binary mixture

This section presented a systematic procedure to select suitable thermodynamic model on the basis of accuracy for any CO_2-based binary mixture. However, the method is applicable only for CO_2-based mixtures for which experimental property data is available. As an example, CO_2-SO_2 binary mixture is selected to demonstrate the procedure because of availability of experimental property data for this mixture in literature. For this, the predictive capability of three EoS described in previous sections is tested. The main motivation is to identify suitable EoS for CO_2-SO_2 binary mixture on the basis of accuracy of EoS. Both thermodynamic and caloric properties are calculated and compared with experimental data followed by calculation of mean absolute percentage error (MAPE).

EoS which shows minimum deviation from experimental data or lowest MAPE is selected.

Following steps are followed;

a) Pure fluid parameters are gathered which include critical temperature (T_{cr}), critical pressure (P_{cr}), acentric factor (ω) for PR EoS and segment number (m), segment diameter (σ) and segment-segment interaction energy (ε/k) for PC-SAFT EoS. These pure fluid parameters are reported in Table 3 for pure CO_2 and pure SO_2.

b) PR and PC-SAFT EoS are calibrated and binary interaction parameter (ki,j) is calculated using experimental VLE data. Binary parameters for GERG-2008 EoS are already available in REFPROP (See Table 4), thus No calibration is necessary.

c) Accuracy of three EoS is evaluated in VLE, bubble and dew point densities, speed of sound, residual specific heat and Joule Thompson inversion pressures with reference to experimental data available in works of Gimeno *et* al [31] and Nazeri *et* al [32].

d) Average MAPE in different properties corresponding to each EoS is determined to choose one EoS with minimum MAPE.

Accuracy of EoS

Accuracy of EoS is assessed by computing mean absolute percentage error (MAPE) which indicates the closeness of prediction from EoS with experimental data. MAPE in any property *X* is expressed as,

$$\mathrm{MAPE_X} = \frac{1}{\mathrm{N}} \sum_{\mathrm{i=1}}^{\mathrm{N}} \left| \frac{\mathrm{X_{EoS}} - \mathrm{X_{experimental}}}{\mathrm{X_{EoS}}} \right| \mathrm{x}\ 100$$

Table 3: Pure component parameters required in Peng Robinson EoS and PC-SAFT EoS

Pure fluid	**T_{cr} (°C)**	**P_{cr}** (bar)	**ω**	**MW**	**PC-SAFT EoS parameters**		
					m	**σ**	**ε/k**
CO_2	31	73.8	0.2236	44.01	2.569	2.564	-121.05
SO_2	157.6	78.8	0.2454	64.06	2.861	2.683	-67.80

Table 4: Binary parameters for REFPROP v10 inbuilt EoS

CO_2 mixture	$\beta_{T,ij}$	$\beta_{V,ij}$	$\gamma_{T,ij}$	$\gamma_{V,ij}$
CO_2+SO_2	1.0201	0.8899	1.0080	1.0058

Calibration of PR-EoS and PC-SAFT EoS

The selected PR-EoS and PC-SAFT EoS are of non-predictive type which means that these EoS needs to be calibrated using the available experimental VLE data. The usual approach well documented in literature involves fitting EoS on the isothermal experimental VLE (P-x,y) data and finding the optimum value of binary interaction parameter (k_{ij}) as also explained in section 2.3. Coquelet *et* al [33] presented the experimental VLE data at temperatures of -10℃ and 60℃. This data can be exploited to correlate with EoS and determine the value of k_{ij}.

Therefore, to calibrate PR and PC-SAFT EoS, the regression analysis is carried out using the maximum likelihood method as optimization method. The experimental bubble pressure and dew composition (given by Coquelet *et* al) are fitted using the selected EoS as regression model. The result of regression analysis returns the optimized value of k_{ij} for best fit of selected EoS. Aspen plus v11 software is used to perform regression analysis.

Table 5 shows the optimized value of binary interaction parameter corresponding to each EoS along with MAPE in bubble pressure and dew composition with reference to experimental VLE data. Graphical representation of experimental VLE data and fitted EoS on P-xy plane are shown in Figure 2

Table 5: MAPE for different EoS in the VLE calculations with respect to experimental data reported in [33]

Equation of state	**Binary parameter**	**MAPE of P_{bub}**			**MAPE of y_{dew}**		
		-10℃	**60**℃	**Average**	**-10**℃	**60**℃	**Average**
PR EoS	0.0242	1.4%	0.6%	1.0%	0.3%	0.8%	0.5%
PC-SAFT	0.0121	0.8%	1.1%	0.9%	0.7%	1.7%	1.2%
REFPROP	Table 2	2.0%	1.3%	1.7%	0.5%	1.7%	1.1%

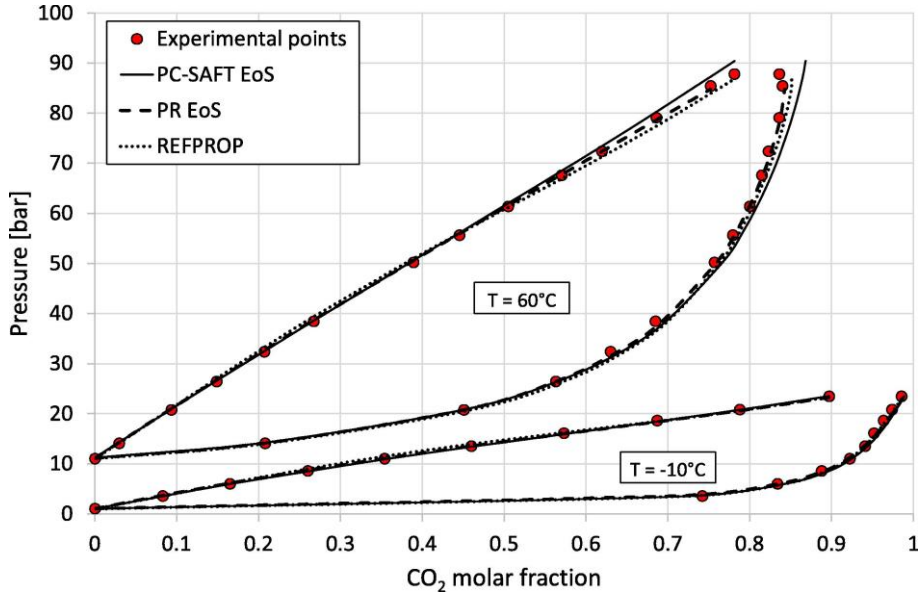

Figure 2: Comparison of predicted vapor-liquid equilibrium by three equation of states with experimental data at two temperatures. Experimental points (red points) are taken from [33].

Validation and assessment of predictive capability of three EoS

After calibration of EoS using experimental VLE data, this section focuses on validation of EoS with reference to experimental VLE density data (in $P-\rho-T$ form) and liquid densities from Gimeno *et* al [31] and densities, speed of sound, inversion curves and pseudo experimental residual specific heat from Nazeri *et* al [32].

This methodology allows to assess the predictive capability of the various EoS using MAPE as the benchmark variable. The EoS which brings about minimum MAPE is selected as the reference EoS to adopt for CO_2-SO_2 mixture.

Figure 3 and Figure 4 show $P-\rho-T$ data from Gimeno *et* al [31] compared to predicted values from the three EoS. Table 6 shows the corresponding MAPE in bubble and dew point properties for the three equations. All of the selected EoS predict bubble and dew point pressures and densities reasonably well. When the computed densities are compared, it is important to note that PR EoS has a good agreement in bubble point densities when compared to the values from PC-SAFT and REFPROP. To predict the bubble point density is critical for calculation of compression step in a thermodynamic cycle, which has a significant impact on cycle efficiency.

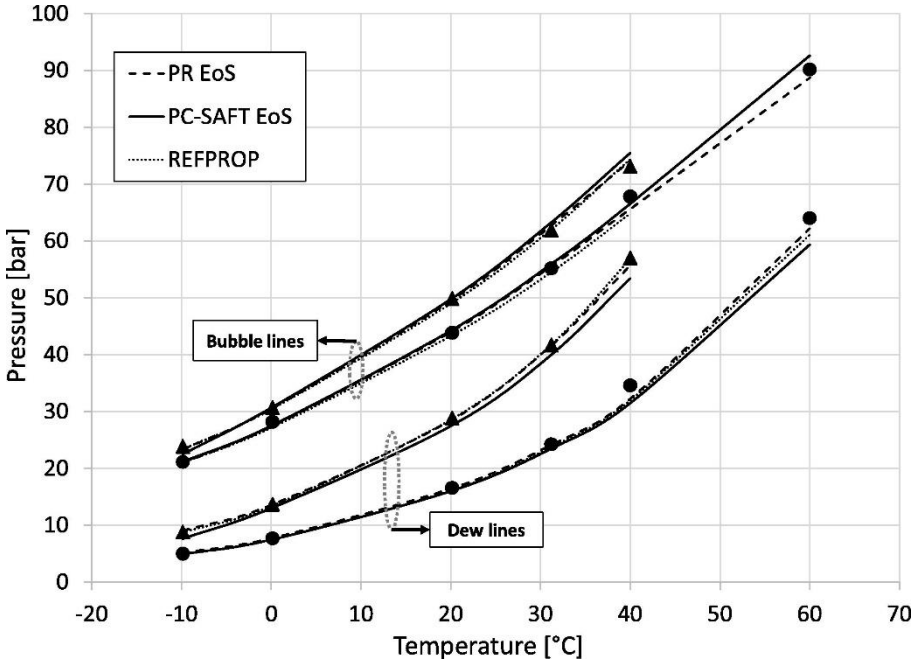

Figure 3: Comparison of bubble and dew point pressures among three EoS and experimental data. Triangles show experimental points for 90% molar CO2 mixture, Solid circles show experimental points for 80% molar CO2 mixture from [31]

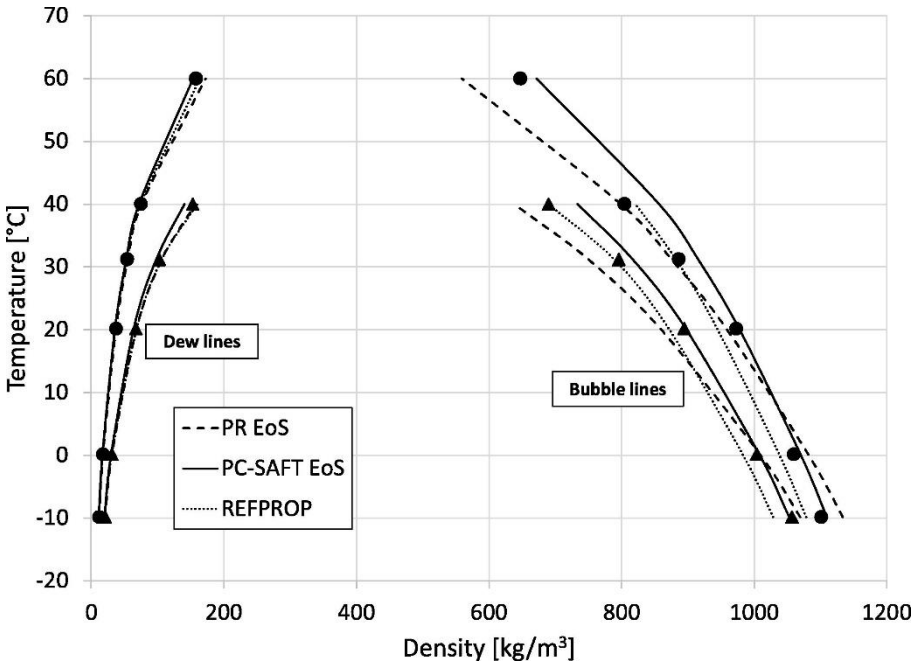

Figure 4: Comparison of bubble and dew point densities among three EoS and experimental data. Triangles show experimental points for 90% CO2 mixture, Solid circles show experimental points for 80% CO2 mixture from [31]

Table 6. MAPE of predicted bubble point pressures and bubble point densities of CO_2+SO_2 mixture with respect to experimental data from [31]

Equation of state	Molar Fraction	MAPE of bubble point		MAPE of dew point	
		Pressure	Density	Pressure	Density
PR EoS	80% CO_2	1.2%	3.7%	1.1%	2.4%
PC-SAFT		1.5%	2.6%	4.5%	3.7%
REFPROP		2.1%	1.9%	3.4%	2.5%
PR EoS	90% CO_2	1.2%	3.8%	1.3%	1.9%
PC-SAFT		2.3%	2.0%	6.6%	5.4%
REFPROP		1.3%	1.7%	0.6%	2.7%

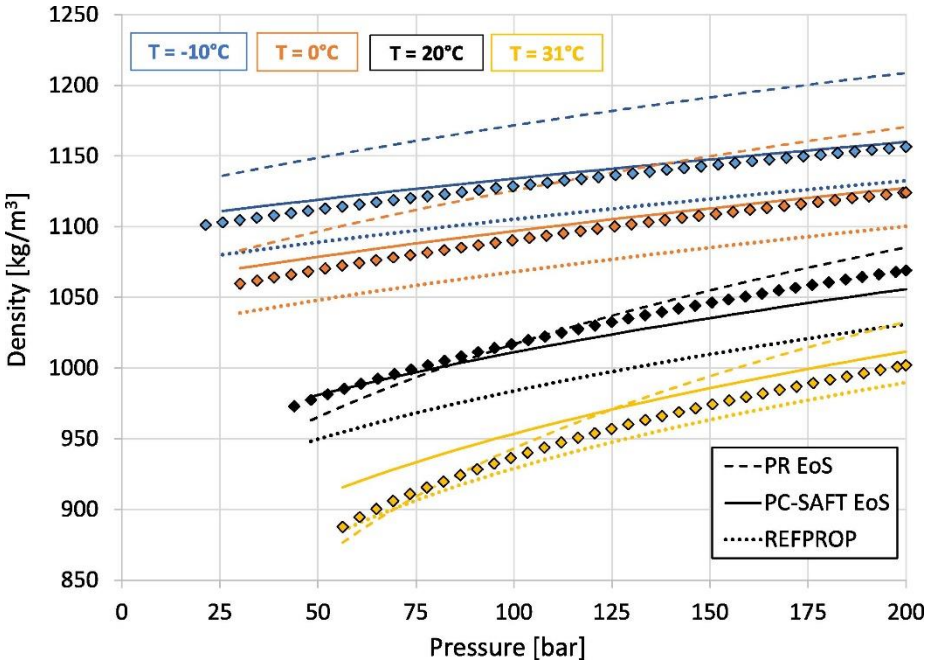

Figure 5: Comparison of predicted densities with experimental densities in the liquid region for the CO2+SO2 mixture (80% molar CO2). Experimental densities (scatter points) are taken from [31]

The graphical comparison of experimental liquid densities of the mixture from Gimeno *et* al and the predicted values by the EoS for a CO_2 molar composition of 80% is illustrated in Figure 5 and the corresponding MAPE for both 80% and 90% molar CO_2 mixture are reported in Table 7. Among the three models, PC-SAFT EoS shows the best accuracy in predicting liquid densities of the mixture. Moreover, a comparison with density data of

Nazeri *et* al for 95% molar CO_2 mixture also reveals minimum deviations for the PC-SAFT and the REFPROP EoS, as presented in Table 8.

Table 7: Mean absolute percentage error (MAPE) in predicted densities of CO_2+SO_2 mixture with reference to experimental data from [31]

Equation of state	**Molar fraction**	**MAPE of density**			
		-10°C	**0°C**	**20°C**	**31°C**
PR	80% CO_2	4.2%	3.8%	1.1%	1.8%
PC-SAFT		1.4%	1.6%	1.3%	1.6%
REFPROP		2.7%	2.8%	2.8%	1.2%
PR	90% CO_2	3.3%	2.1%	1.4%	2.5%
PC-SAFT		1.2%	0.6%	0.7%	1.9%
REFPROP		2.9%	2.2%	2.1%	2.1%

Table 8: Mean absolute percentage error (MAPE) in predicted densities of CO_2+SO_2 mixture with reference to experimental data from [32]

Equation of state	**Molar fraction**	**MAPE of density**					
		400 bar	**350 bar**	**300 bar**	**250 bar**	**200 bar**	**150 bar**
PR	95% CO_2	3.7%	3.1%	2.9%	2.7%	2.8%	2.7%
PC-SAFT		1.0%	1.1%	1.2%	1.3%	1.4%	1.1%
REFPROP		1.3%	1.2%	1.1%	1.0%	0.8%	1.1%

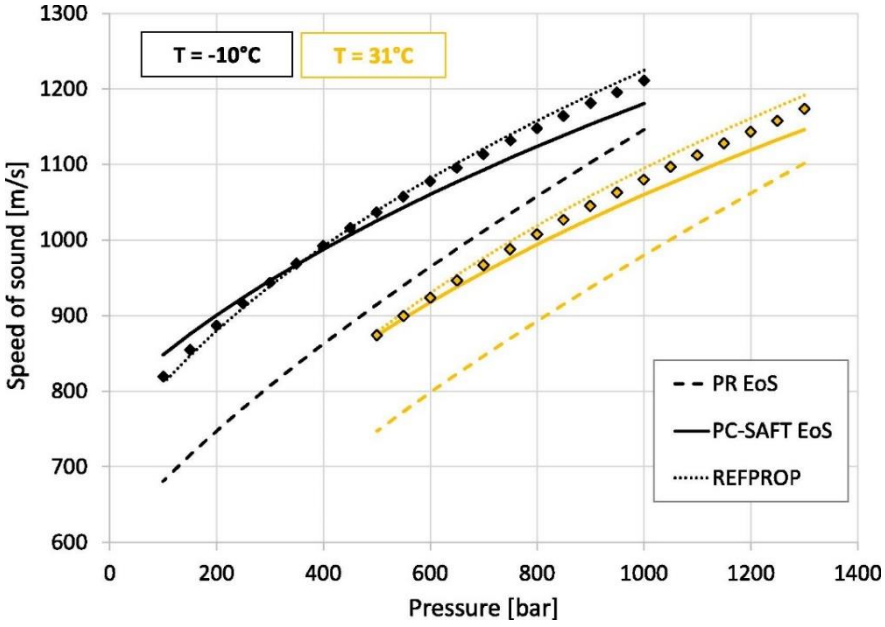

Figure 6: Comparison of predicted speed of sound with experimental speed of sound of the CO_2+SO_2 mixture (80% molar CO_2). Experimental values (scatter points) are taken from [31]

Calorimetric variables also plays key role in power cycle design particularly heat exchanger and turbine design. Therefore, calorimetric variables (speed of sound, inversion curves and the residual specific heats) are computed using selected EoS and values are compared with the reference experimental data from literature [31]. The analytical formulations of these quantities include various partial derivatives and are presented in Table 9 where the inversion point indicates the condition where the residual enthalpy ($\Delta h_{residual} = \int_0^P v - T \cdot \frac{\partial V}{\partial T} dP$) presents a minimum.

Table 9: Analytical formulations of properties which involves calorimetric variables

Speed of sound	**Residual C_P**	**Inversion point**
$c = \sqrt{\frac{C_p}{C_v}\frac{dP}{d\rho}}$	$\Delta C_{p,residual} = -\int_0^P T\left(\left(\frac{\partial^2 v}{\partial T^2}\right)_P\right)_T dP$	$\frac{v}{T} = \frac{\partial v}{\partial T}$

Figure 6 and Figure 7 compares the speed of sound and residual specific heat with experimental data, while the corresponding MAPE are reported in Table 10 and

Table 11, respectively.

Considering the speed of sound in the liquid region for 80% molar CO_2 mixture, the comparison reveals a large MAPE, around 10%, corresponding to PR EoS. The PC-SAFT and REFPROP EoS have instead MAPE lower than 2% at all temperatures.

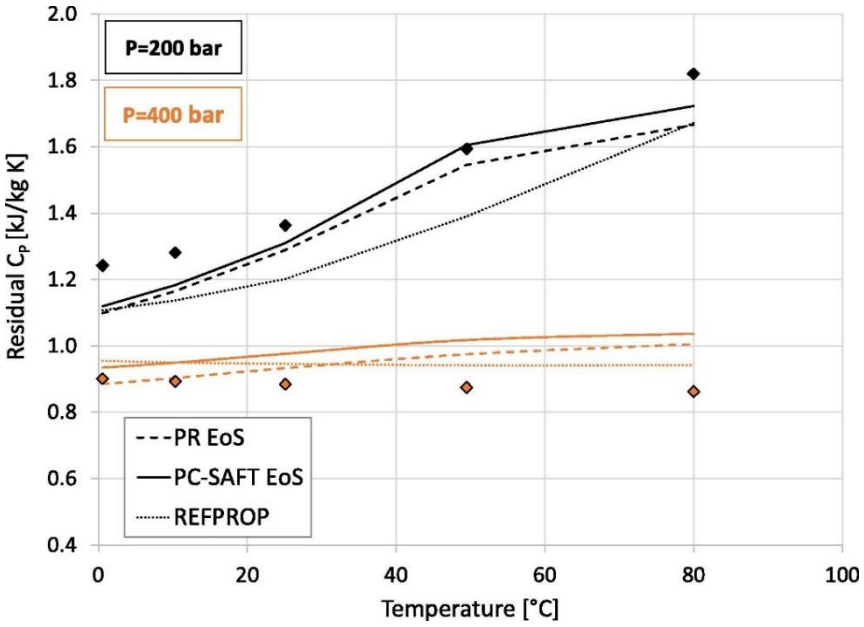

Figure 7: Comparison of predicted residual Cp with experimental residual Cp in the liquid region for the CO2+SO2 mixture (95.03% molar CO_2). Experimental data (scatter points) are taken from [32]

Table 10: Mean absolute percentage error (MAPE) in predicted speed of sound of CO_2+SO_2 mixture with reference to experimental data from [31]

Equation of state	**Molar fraction**	**MAPE of speed of sound**			
		-10°C	**0°C**	**20°**	**31°C**
PR	80% CO_2	11.2%	10.5%	10.1%	10.3%
PC-SAFT		1.7%	1.6%	1.5%	1.5%
REFPROP		0.6%	0.7%	1.0%	1.2%

Table 11: Mean absolute percentage error (MAPE) in residual specific heat of CO_2+SO_2 mixture with reference to experimental data from [32]

Equation of state	Molar fraction	MAPE of residual specific heat					
		400 bar	350 bar	300 bar	250 bar	200 bar	150 bar
PR	95% CO_2	7.3%	4.6%	4.1%	5.8%	7.5%	14.6%
PC-SAFT		11.4%	4.7%	4.2%	3.8%	5.5%	13.7%
REFPROP		7.2%	1.4%	3.3%	8.5%	11.0%	17.1%

Finally, the Joule Thompson inversion curve for a single temperature (at 0°C) and various mixture compositions is also computed and compared with the experimental data, reported in Figure 8. The REFPROP and PC-SAFT EoS show good agreement with experimental inversion pressures compared to PR EoS. Nevertheless, due to the limited number of experimental points and the single temperature reported, no MAPE is presented for these calculations. The interest in comparing the inversion curve with EoS lies in the characterization of the trend of enthalpies, a crucial step for the definition of the power balance and the efficiency of the cycle.

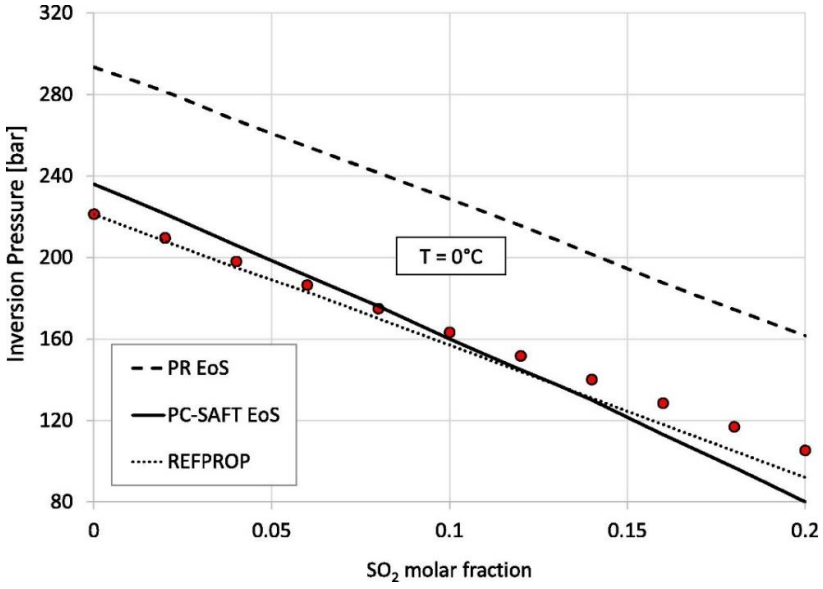

Figure 8: Inversion curve at 0°C for the CO_2+SO_2 mixture at different molar composition. Experimental data shown by solid circles is taken from ref [31]

Table 12: Overall MAPE in different set of thermodynamic properties

EoS	MAPE				
	VLE	**Density**	**Speed of sound**	**Residual specific heat**	**Average**
PR	1.1%	2.5%	10.4%	7.3%	5.3%
PC-SAFT	2.0%	1.4%	1.6%	7.2%	3.0%
REFPROP	1.5%	2.3%	0.9%	8.1%	3.2%

Table 13. Experimental uncertainties of the experimental data gathered for the analysis on this work

u_{VLE} [33]	$u_{Density}$ [32]	$u_{Density}$ [31]	$u_{SoundSpeed}$ [31]
0.2%	0.2%	0.05%	0.06%

Which EoS to adopt for CO_2-SO_2 mixture?

The final scope of this section is to identify the most accurate EoS to be adopted as reference EoS for CO_2-SO_2 mixture. The identification of the most suitable EoS is more challenging, since it can be difficult to combine all MAPEs at different temperatures and compositions for different set of properties and select the most accurate EoS. Therefore, the properties of the mixture are divided into four main categories: VLE, density, speed of sound and residual specific heat. A single MAPE indicator is computed for each set of property incorporating all the data points at different compositions, temperatures and pressures. Table 12 reports the overall MAPE for each category of experimental data fitted by the EoS, along with an average MAPE computed considering the four previous data. Considering the accuracy of PC-SAFT model in prediction of densities of CO_2-SO_2 mixture and comparatively lowest average MAPE indicator (see Table 12), this model is accepted as reference EoS for CO_2-SO_2 mixture.

It is worth mentioning that comparative analysis based on magnitude of MAPE is only meaningful if the magnitude of MAPE is higher than the experimental uncertainty of considered properties. If the experimental uncertainty and the MAPE computed with the

EoS on the experimental data are of the same magnitude, the comparison may be considered weak. Table 13 reports the average experimental uncertainty reported in the works of Coquelet [33], Gimeno [31] and Nazeri [32].

As evident, the magnitude of experimental uncertainties is below the computed MAPE by the EoS, thus the comparison between EoS based on the fitting capability with experimental data can be considered valid and meaningful.

2.5 **Phase diagram of CO_2-SO_2 mixture**

Finally, using the selected PC-SAFT EoS, the global phase diagram of the mixture is computed and reported. It includes mixture critical points and P-T envelope at different molar compositions as illustrated in Figure 9. Critical points in Figure 9 are computed using density marching method available in ASPEN plus v10.

The study of the behavior of the P-T envelop for a specific CO_2 mixture is important because it allows for the selection of suitable CO_2 mixture molar composition as working fluid for transcritical power cycle. The main requirement, particularly for transcritical CO_2 mixture power cycles, is to identify compositions with pump inlet temperatures that are lower than the critical temperature of the CO_2 mixture working fluid and must lie at the bubble line of the mixture. As a result, studying the P-T envelop diagram allows for the identification of mixture compositions that meet the required criteria. In addition, it also allows to study the impact of increment in mixture composition on the behavior of bubble and dew lines and vapor-liquid critical points.

In chapters 4, 5 and 6, P-T envelop of different CO_2 mixtures are studied to select suitable mixture composition as working fluid in transcritical power cycles. This entails certain criterion to be defined for temperature difference between pump inlet of power cycle and critical temperature of CO_2 mixture.

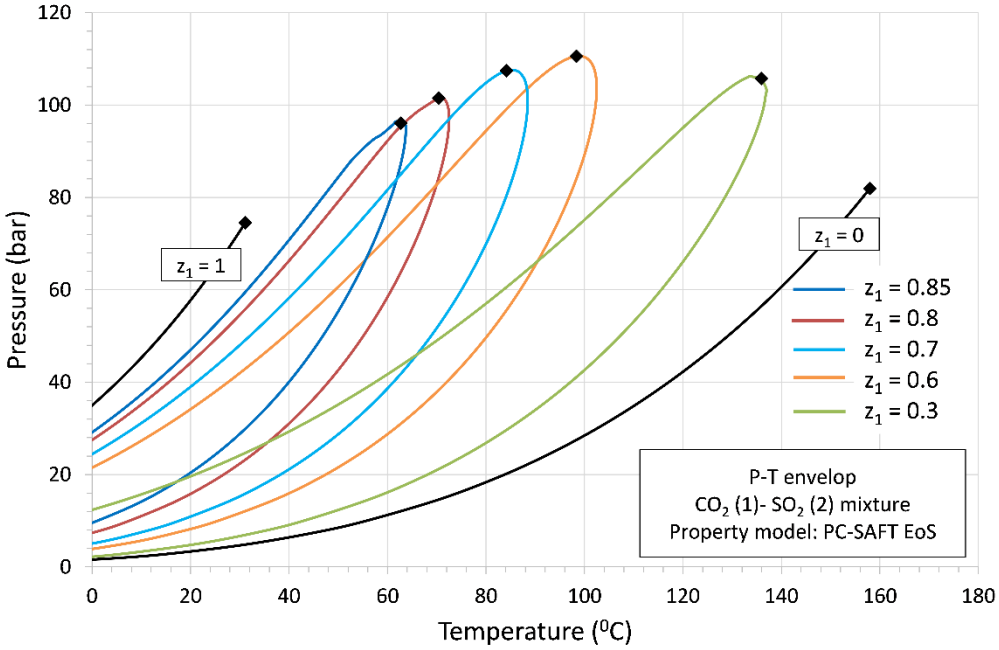

Figure 9: P-T envelopes of the CO_2+SO_2 mixture at various molar composition modelled with the PC-SAFT EoS. Vapor-Liquid critical points (Black rhombus shaped points) are calculated using density marching method available in Aspen plus v10.

2.6 **Chapter Summary**

Studying the phase behavior of CO_2 based binary mixtures and selection of accurate thermodynamic model for calculation of thermodynamic properties is pre-requisite to thermodynamic cycle analysis. This chapter covers this aspect by describing the mathematical formulation and significance of three Equation of States for study of phase behavior and thermodynamic properties of binary mixtures. They are: Peng Robinson EoS, PC-SAFT EoS and GERG EoS of REFPROP. The calculation of one binary interaction parameter ($k_{1,2}$) is also necessary for calculation of phase behavior of binary mixtures. Therefore, the method to calculate binary interaction parameter needed in PR EoS and PC-SAFT EoS is described. The method for calculation of binary parameters required in GERG EoS is not included because of very different nature of EoS and advanced regression methods are required to compute four binary parameters corresponding to one binary mixture which is out of the scope of this work.

For binary mixtures with known experimental vapor-liquid equilibrium data, the method presented in the chapter is to perform regression analysis using the available VLE data and compute the binary interaction parameter ($k_{1,2}$) considering PR EoS or PC-SAFT EoS as the regression model.

However, the scenario in which No experimental VLE data is known for a particular CO_2 mixture, a correlation between binary parameter ($a_{1,2}$) and a_2 (parameter of intermolecular forces of attraction) of dopant is developed by regression analysis using the known $a_{1,2}$ values of 19 CO_2 mixtures as the regression data. This developed correlation allows to predict preliminary value of $a_{1,2}$ although with uncertainty which in turn allows to develop preliminary thermodynamic analysis of some new CO_2 mixtures. The correlation is used in Chapter 5 to predict $a_{1,2}$ for carbon dioxide-sulfuryl fluoride (CO_2-SO_2F_2) mixture. The predicted parameter is incorporated in PR EoS with van der Waals mixing rules to calculate and study phase diagram of CO_2-SO_2F_2 mixture and evaluate thermodynamic performance of the power cycle.

The last section of the chapter discusses the accuracy of three EoS in describing the VLE behavior and calculation of densities, specific heat and speed of sound for CO_2-SO_2 mixture as an example. Among the selected three EoS, the EoS which show good agreement with experimental thermodynamic properties is chosen as reference EoS for thermodynamic cycle calculations. Based on the comparison of mean absolute percentage error (MAPE), PC-SAFT EoS is found to be the accurate EoS for CO_2-SO_2 mixture. The same approach presented in this chapter can be adopted for other CO_2 mixtures to select the most suitable EoS which shows minimal error provided that the experimental densities, specific heat data and speed of sound data of the mixture are available. In Chapter 6, PC-SAFT EoS with binary interaction parameter obtained in this chapter is considered for cycle thermodynamic analysis with CO_2-SO_2 mixture as working fluid in transcritical power cycle.

Chapter 3: Computation of true critical points of CO_2-based binary fluid mixtures

3.1 Introduction

To predict complete vapor-liquid phase behavior of a binary mixture, determination of true critical points is fundamental. There are many industrial processes which require information of critical point of a binary mixture at certain composition. For example, to study phenomenon of retrograde condensation in hydrocarbon processing industry. Another useful application is design of thermodynamic power cycles operating with binary mixtures as working fluids [13], [34]. In supercritical and transcritical power cycles, compression process occurs close to critical point of working fluid, thus, it is critical to compute critical points to decide safe operating conditions for compression process.

Regarding study on CO_2-based binary mixtures, it is important to have knowledge of vapor-liquid critical points at different molar composition because the main purpose is to design thermodynamic power cycle with compression process occurring at temperature and pressure in vicinity of critical point of the mixture.

For pure fluid, critical point is the highest temperature and highest pressure at which vapor and liquid phases merge or coexist. Another definition of critical point of a pure substance is '*It is a thermodynamic state at which the volumes of liquid and vapor are equal and that occurs between stable and unstable states of the pure fluid'* [35].

In case of binary mixture, vapor-liquid critical point is the point at which two phase boundaries (bubble line and dew line) merge and vapor and liquid phases become indistinguishable in terms of chemical properties [36]. According to numerical formulation of Heidemann and Khalil [37], critical point of a mixture is a thermodynamic state at which fugacities of each component in each phase become equal and higher order derivatives of fugacities of a mixture become zero.

There are also liquid-liquid critical points in binary mixture at which two liquid phases of a mixture become indistinguishable in terms of their chemical properties [38]. Compressibility of liquid-liquid critical point is lower and density is higher than vapor-liquid critical point.

The locus of critical points of a binary mixture does not always lie in between the critical point values of the pure components. The different trends of critical locus in binary mixtures occurs due to occurrence of different types of phase transitions. The six main types of critical locus behaviors studied in detail by Van Konynenburg and Scott [39] and summarized in ref[38] are shown in Figure 10. There can be a possibility of No critical point at some compositions in a binary mixture.

The theoretical criteria to define stable critical point of a binary mixture was first developed by Gibbs. Various attempts are done in literature to solve Gibbs criteria of critical point using cubic equation of state to determine critical points. Peng and Robinson used PR EoS to solve the criticality conditions of Gibbs and develop a numerical strategy to calculate critical points of binary and even larger mixtures [40]. An alternative way to reduce computation costs is presented by Heidemann and Khalil [37]; they expressed the critical point criteria of Gibbs in the form of Helmholtz free energy and developed a simple computational algorithm in conjunction with cubic-two constant equation of state for critical point search of multicomponent mixtures. The method of Heidemann and Khalil is very reliable to locate high temperature vapor-liquid critical point, but it requires a reasonable guess to locate other critical points of a mixture. Later on, Michelson *et* al [41] improved the model of Heidemann and Khalil and expressed it in the form of two complex non-linear system of equations, the roots of these equations gives critical temperature and critical volume of a binary mixture. The method of Michelson *et* al can be applicable to any cubic-two constant equation of state like Redlich Kwong Soave EoS and Peng-Robinson EoS. Following the formulation of Michelson *et* al, Panagiotis *et* al[42], [43] proposed damped Newton-Raphson method and computed the critical points of 44 multicomponent mixtures. Nevertheless, the authors validated the results with experimental data, but the method is initial guess dependent and it cannot locate L-L critical points.

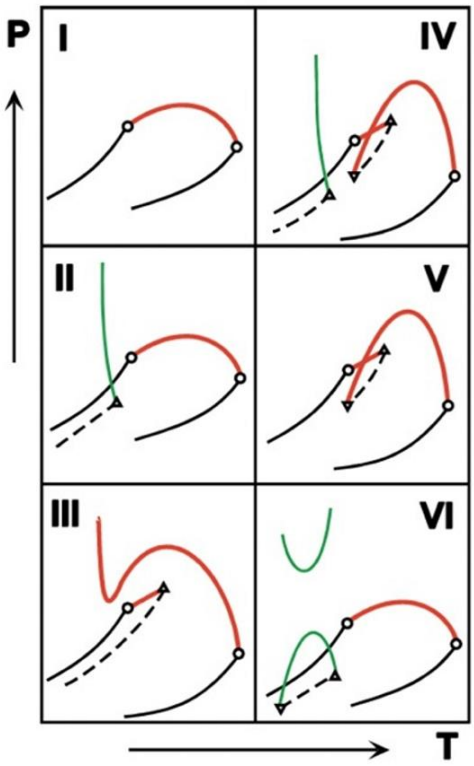

Figure 10: Six different behaviors of critical locus classified by Konynenburg and Scott [4]. Red and green lines shows vapor-liquid critical locus and liquid-liquid critical locus respectively. Figure taken from ref [36].

Stradi *et* al[44], [45] developed a numerical method known as interval-Newton bisection method which can compute all the critical points and also guarantee if there is No critical point for given composition of a mixture without a need of initial guess. However, the authors didn't compute critical points of different types of binary mixtures to ensure validity of the numerical method. Henderson *et* al[46] used differential evolution algorithm to compute more than one critical point of several petroleum fluid mixtures. Hoteit *et* al[47] presented a hybrid method based on combination of one-dimensional search methods and proved that their method is more robust than the approach of Stradi *et* al.

The aim of this chapter is to develop a numerical code which can compute efficiently all the stable, meta-stable and unstable critical points of a binary mixture. The numerical approach proposed by Stradi *et* al is adopted and implemented in MATLAB using the interval laboratory toolbox known as INTLAB toolbox; this advanced toolbox significantly reduces the computational effort since it includes inbuilt functions for interval arithmetic calculations. The main intent is to develop an accurate numerical code

which can compute true critical points of different types of binary mixtures, in particular, the CO_2-based binary mixtures for thermodynamic analysis of power cycles.

3.2 **Critical point criteria and practical formulation**

The first condition for a critical point to lie on stability limit (spinodal curve) is the determinant of quadratic form (second derivative of Helmholtz energy) must be zero [37],

$$\mathrm{Det(Q)=0} \qquad \text{Eq. 1}$$

Or, it can also be written as

$$\mathrm{Q.\Delta n = 0} \qquad \text{Eq. 2}$$

Where, Δn is the vector of mole number differences:

$$\mathrm{\Delta n = (\Delta n_1, \Delta n_2, \Delta n_3, ...\Delta n_C)^T} \qquad \text{Eq. 3}$$

And for Δn to be non-negative,

$$\mathrm{\Delta n^T.\Delta n = 1} \qquad \text{Eq. 4}$$

The elements of quadratic form matrix Q are,

$$Q_{i,j} = \left(\frac{\partial^2 \mathrm{A}}{\partial n_i \partial n_j} \right)_{T,\mathrm{V,n}} \qquad \text{Eq. 5}$$

Heidemann and Khalil represents the elements of quadratic form in terms of fugacity with temperature (T), volume (V) and mole numbers (n) as independent variables as shown,

$$Q_{i,j} = \left(\frac{\partial^2 \mathrm{A}}{\partial n_i \partial n_j} \right)_{T,\mathrm{V},\mathrm{n_{k,k\neq i\ or\ j}}} = RT \left(\frac{\partial \ln \widehat{f}_\mathrm{i}}{\partial n_j} \right)_{T,\mathrm{V},\mathrm{n_{k,k\neq j}}} \qquad \text{Eq. 6}$$

So that, Eq. 1 can be described as follows,

$$Q = RT \begin{vmatrix} \left(\frac{\partial \ln \hat{f}_1}{\partial n_1}\right)_{T,\mathrm{V,n}} & \cdots & \left(\frac{\partial \ln \hat{f}_1}{\partial n_C}\right)_{T,\mathrm{V,n}} \\ \vdots & \ddots & \vdots \\ \left(\frac{\partial \ln \hat{f}_C}{\partial n_1}\right)_{T,\mathrm{V,n}} & \cdots & \left(\frac{\partial \ln \hat{f}_C}{\partial n_C}\right)_{T,\mathrm{V,n}} \end{vmatrix} = 0 \qquad \text{Eq. 7}$$

The second condition for a stable point to be a critical point requires the cubic form (i.e. third order derivative of Helmholtz energy) equals to zero [37], [41] as follows:

$$C = \sum_{i=1}^{C}\sum_{j=1}^{C}\sum_{k=1}^{C} C_{i,j,k}\Delta \mathrm{n}_i \Delta \mathrm{n}_j \Delta \mathrm{n}_k = 0 \qquad \text{Eq. 8}$$

The elements of cubic form in terms of Helmholtz free energy and fugacity can also represented as follows:

$$C_{i,j,k} = \left(\frac{\partial^3 \mathrm{A}}{\partial n_i \partial n_j \partial n_k}\right)_{T,\mathrm{V},\mathrm{n}_{l,l\neq \mathrm{i\ or\ j\ or\ k}}} = RT\left(\frac{\partial^2 \ln \hat{f}_\mathrm{i}}{\partial n_j \partial n_k}\right)_{T,\mathrm{V},\mathrm{n}_{l,l\neq \mathrm{j\ or\ k}}} \qquad \text{Eq. 9}$$

The first condition known as quadratic form as defined in Eq. 1 and Eq.7 is the necessary condition for a point to be a stable point (lie on spinodal curve), whereas, the second condition known as cubic form as defined in Eq. 8 is the necessary condition for a stable point to be a critical point. In above equations, *C* is the total number of components in a mixture, *n* is the number of moles, subscripts *i*,*j* and *k* show the *ith* component, *jth* component and so on. *R* is the gas constant and $\hat{f}_i$ is the fugacity of *ith* component.

To solve both conditions of critical point, Heidemann and Khalil calculated the fugacity of component using SRK EoS and derived the expressions of both criticality conditions. Then, these expressions are solved using Newton Raphson technique in a nested loop; the results of which are critical point temperature and volume. Eventually, the critical pressure is computed using SRK EoS using the calculated critical temperature and volume. The numerical algorithm of Heidemann and Khalil is described in detail in ref [38].

Subsequently, Michelson *et* al[41] formulated the generalized expressions of criticality conditions which can be applicable to cubic PR and SRK EoS. These expressions as shown in Eqs. 10-12 are rigorous in variables and solution of these provides the critical

volume and critical temperature and corresponding mole numbers at given composition of a mixture.

$$\frac{RT_c}{n}\left(\frac{\Delta n_i}{y_i}+F_1\left(\beta_i\bar{N}+\bar{\beta}\right)+\beta_i F_1^{\,2}\bar{\beta}\right) + \frac{a}{bn}\left(\beta_i\bar{\beta}F_3-\frac{F_5}{a}\sum_{j=1}^{C}(a_{ij}\Delta n_j)+F_6(\beta_i\bar{\beta}-\alpha_i\bar{\beta}-\bar{\alpha}\beta_i)\right)=0, \quad \text{where } i=1....C \qquad \text{Eq. 10}$$

$$\frac{RT_c}{n^2}\left(-\sum_{i=1}^{C}\frac{\Delta n_i^{\,2}}{y_i^2}+3\bar{N}(\bar{\beta}F_1)^2+2(\bar{\beta}F_1)^3\right) + \frac{a}{bn^2}\left(3\bar{\beta}^2(2\bar{\alpha}-\bar{\beta})(F_3+F_6)-2\bar{\beta}^3F_4-3\bar{\beta}\bar{a}F_6\right)=0 \qquad \text{Eq. 11}$$

$$\sum_{i=1}^{C}\Delta n_i^{\,2}-1=0 \qquad \text{Eq. 12}$$

Where, Eq. 10 is generalized expression of criticality condition 1 i.e. quadratic form, Eq.11 is generalized expression of condition 2 i.e. cubic form and Eq.12 confirms the non-negative nature of mole number change Δn . In these equations, T_c is the critical point of mixture, n is the total number of moles in a mixture and y_i is the mole fraction of *ith* component in a mixture. Other variables $a, b, a_{ij}, \bar{a}, F_1, F_2, F_3, F_4, F_5, F_6, \beta_i, \bar{\beta}, \alpha_i$ and $\bar{\alpha}$ are computed using the selected cubic equation of state. The definitions of these variables are given in refs [41], [43] for both PR and SRK EoS. It is important to mention that these equations are implicit in critical volume v_c. For any mixture, the total number of equations to solve depends on the number of components (C) in a mixture (binary or ternary or larger). Altogether, there are C+2 equations and C+2 variables to compute for any mixture. For instance, there are 2 equations (Eq. 10 for two components) + 2 equations (Eq. 11 and Eq. 12) corresponds to 4 variables ($T_c, v_c, \Delta n_1$ and Δn_2) to calculate for a binary mixture.

3.3 **Computation Method**

The critical point model equations (Eqs. 10-12) are multivariate non-linear system of equations implicit in critical volume. There is possibility of one or more solutions (critical points) to these equations or it can be No solution. Therefore, an efficient and robust numerical method is needed rather than conventional numerical methods like Newton

Raphson, Bisection and secant methods to solve this model, since these methods are initial guess dependent and consumes a lot of computational time to solve multivariate system of equations.

Since, the aim is to find all critical points of a binary mixture, the most suitable numerical method is interval Newton-Bisection method (INBM) previously adopted by Stradi *et* al. This numerical method is based on a concept of Mathematics known as interval analysis; basic idea is to find solution for a system of equations in the form of precise intervals or bounds of real numbers rather than real numbers. Stradi *et* al implemented INBM using INTBIS library along with programming in FOTRAN. The method proved to be accurate, but it took significant time (84.8 seconds to compute three critical points at 0.97/0.03 mole fraction of CO_2-$nC_{16}H_{34}$ binary mixture).

Finding critical points using INTLAB root finding function

In this work, INTerval LABoratory (INTLAB) toolbox version 11 is used to solve system of equations of critical point. This robust toolbox is developed in MATLAB by Siegfried Rump [48] for solving mathematical problems using interval arithmetic approach. The toolbox significantly makes computational effort smaller and generates results faster.

INTLAB has an inbuilt routine known as *verifynlss* for finding all roots of multi variable non-linear system of equations. This routine works on the concept of Interval Newton-Bisection method (INBM). It can compute all roots of a non-linear system of equations without a requirement of initial guesses. Though, it is important to first understand the algorithm of *verifynlss* routine but it is out of scope of this work to explain all the numerical steps involved in the algorithm. To gain understanding of the algorithm, readers are encouraged to read ref [44] and ref[45].

However, the steps to solve critical point equations using *verifynlss* are described as follows:

1. As input information, the routine requires intervals for each unknown variable, the given interval for an unknown variable should be large so that the routine can find all the possible roots of system of equations. The required input intervals for each variable are as follows:

$$\frac{T_c}{800} \in [0.1 \;\; 1]\text{K},$$

$$\frac{v_c}{5b} \in [0.22 \;\; 1],$$

$$\Delta n_1 \in [0 \quad 1],$$

$$\Delta n_2 \in [-1 \;\; 1].$$

The use of scaled interval is convenient and proved to be effective in finding roots.

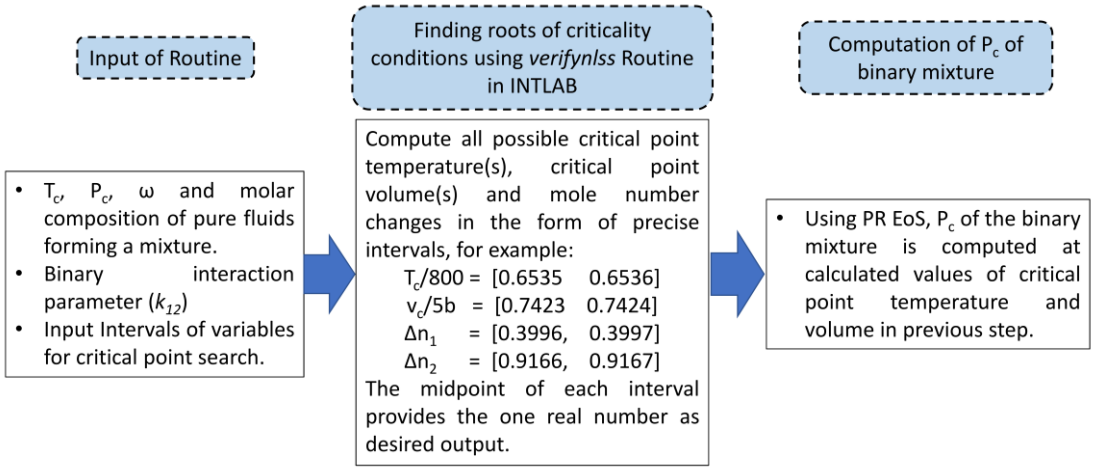

Figure 11: Flow diagram of MATLAB program for computation of critical points of a binary mixture.

2. Pure fluid critical temperature, critical pressure, acentric factor (ω), mole fractions of each component of a binary mixture and binary interaction paramater (*kij*) are also required as an input to the program.
3. The system of equations of criticality conditions to solve are Eqs. 10-12.
4. The *verifynlss* routine outputs the critical temperature(s) T_c, critical volume(s) v_c and mole number changes in the form of very precise intervals; midpoint of the each interval is taken in order to get one real number for T_c and v_c.
5. Finally, the computed T_c and v_c are used to calculate P_c of binary mixture using PR EoS.
6. Steps from 1 to 5 are repeated for each molar composition of mixture.

The main steps of the MATLAB routine are illustrated in Figure 11.

3.4 **Results**

This last section is dedicated to calculation of complete critical point locus of different types of binary mixtures. The purpose is to validate the results from the MATLAB routine using experimental as well as numerical critical point data of binary mixtures available in literature. Critical locus of eight main types of binary mixtures are studied, they are:

1. Carbon dioxide + alkane
2. Carbon dioxide + perfluorocarbon
3. Carbon dioxide + tetrachloride
4. Carbon dioxide + polar compound
5. Carbon dioxide + sulphur compound
6. Alkane + Alkane
7. CO_2-H_2O
8. NH_3-H_2O

Pure fluid properties and binary interaction parameter of these mixtures are taken from Aspen databank. Subsequent sections presented the results and comparison with experimental data for 11 different binary mixtures.

Table 14: Binary interaction parameter ($k_{1,2}$) of different binary mixtures required for computation of vapor-liquid critical points.

Binary mixture	$k_{1,2}$	**Source**
CO_2-C_3H_8	0.1241	Aspen databank
CO_2-SO_2	0.02431±0.00117	Regression of experimental VLE data
CO_2-C_6F_{14}	0.01757±0.00277	Regression of experimental VLE data
CO_2-C_4F_{10}	0.10114±0.0038	Regression of experimental VLE data
CO_2-C_6F_6	0.04381± 0.01167	Regression of experimental VLE data
CO_2-$TiCl_4$	0.07907±0.04564	Regression of experimental VLE data
CO_2-CH_2Cl_2	0.06637± 0.01244	Regression of experimental VLE data
C_6H_{14}-C_3H_8	0.0007	Aspen databank
CO_2-C_8H_{18}	0.10543±0.001	Regression of experimental VLE data
NH_3-H_2O	-0.2589	Aspen databank
CO_2-H_2O	0.1697	Reference [49]

Carbon dioxide-Propane (CO_2-Propane)

Table 15: Vapor-liquid critical points of CO_2-C_3H_8 binary mixture computed using critical point code at different molar composition

Molar Composition of CO_2 (z_1)	Number of Roots of criticality conditions	Tc [^{0}C]	Pc [bar]	Nature of critical point
1		31.06	73.83	Vapor-Liquid
0.95	1 root	30.56	70.31	Vapor-Liquid
0.9	1 root	31.35	67.98	Vapor-Liquid
0.8	1 root	36.14	65.94	Vapor-Liquid
0.7	1 root	43.64	65.46	Vapor-Liquid
0.6	1 root	52.29	64.81	Vapor-Liquid
0.5	1 root	61.15	63.12	Vapor-Liquid
0.4	1 root	69.64	60.26	Vapor-Liquid
0.3	1 root	77.48	56.46	Vapor-Liquid
0.2	1 root	84.58	52.04	Vapor-Liquid
0.1	1 root	90.96	47.31	Vapor-Liquid
0		96.83	42.48	Vapor-Liquid

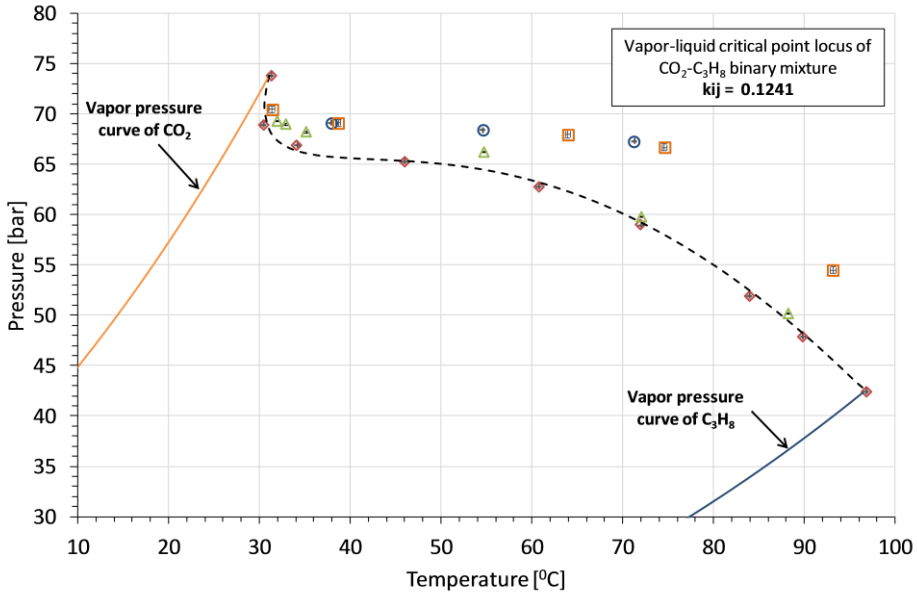

Figure 12: Vapor pressure of pure fluid components (solid lines) and vapor liquid critical point locus of CO_2-C_3H_8 binary mixture computed using critical point code (black dashed line). Scatter points show experimental data from literature; Poettmann et al (box)[50]*, Reamer et al (circle)*[51]*, Roof et al (triangle)*[52] *and Juntarachat et al (diamond)*[53].

Carbon dioxide-Sulphur dioxide (CO_2-SO_2)

Table 16: Vapor-liquid critical points of CO_2-SO_2 binary mixture computed using critical point code at different molar composition

Molar Composition of CO_2 (z_1)	Number of Roots of criticality conditions	Tc [^{0}C]	Pc [bar]	Nature of critical point
1		31.06	73.83	Vapor-Liquid
0.95	1 root	39.83	78.91	Vapor-Liquid
0.9	1 root	48.26	83.66	Vapor-Liquid
0.8	1 root	64.32	91.77	Vapor-Liquid
0.7	1 root	79.51	97.48	Vapor-Liquid
0.6	1 root	93.82	100.43	Vapor-Liquid
0.5	1 root	107.13	100.71	Vapor-Liquid
0.4	1 root	119.34	98.76	Vapor-Liquid
0.3	1 root	130.42	95.12	Vapor-Liquid
0.2	1 root	140.43	90.32	Vapor-Liquid
0.1	1 root	149.45	84.78	Vapor-Liquid
0		157.6	78.84	Vapor-Liquid

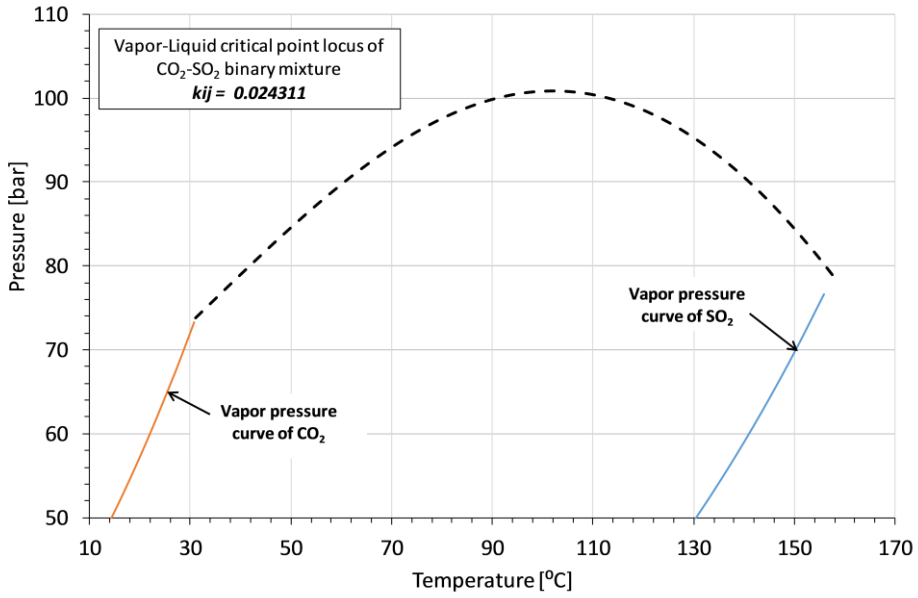

Figure 13:Vapor pressure of pure fluid components (solid lines) and vapor-liquid critical point locus of CO_2-SO_2 binary mixture computed using critical point code (black dashed line).

Carbon dioxide-Perfluorohexane (CO_2-C_6F_{14})

Table 17: Vapor-liquid critical points of CO_2-C_6F_{14} binary mixture computed using critical point code at different molar composition

Molar Composition of CO_2 (z_1)	Number of Roots of criticality conditions	Tc [^{0}C]	Pc [bar]	Nature of critical point
1		31.06	73.83	Vapor-Liquid
0.95	1 root	46.52	77.09	Vapor-Liquid
0.9	1 root	63.54	79.61	Vapor-Liquid
0.8	1 root	93.17	76.37	Vapor-Liquid
0.7	1 root	115.63	67.33	Vapor-Liquid
0.6	1 root	132.21	57.27	Vapor-Liquid
0.5	1 root	144.62	48.02	Vapor-Liquid
0.4	1 root	154.11	39.99	Vapor-Liquid
0.3	1 root	161.57	33.14	Vapor-Liquid
0.2	1 root	167.56	27.3	Vapor-Liquid
0.1	1 root	172.46	22.31	Vapor-Liquid
0		176.55	18.02	Vapor-Liquid

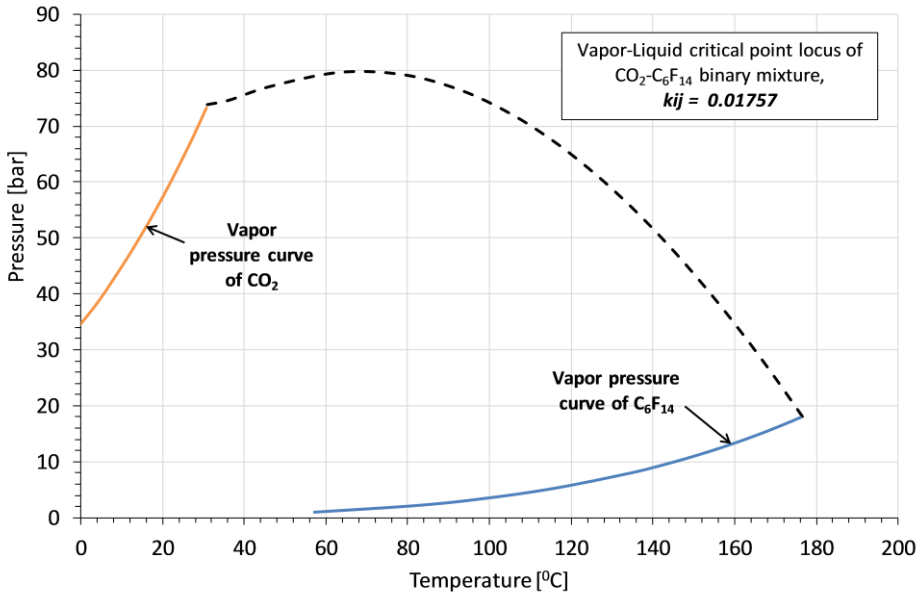

Figure 14: Vapor pressure curve of pure fluid components (solid lines) and vapor-liquid critical point locus of CO_2-C_6F_{14} binary mixture computed using critical point code (black dashed line).

Carbon dioxide-Decafluorobutane (CO_2-C_4F_{10})

Table 18: Critical points of CO_2-C_4F_{10} binary mixture computed using critical point code at different molar composition

Molar composition of CO_2 (z_1)	Number of roots of criticality conditions	Tc [^{0}C]	Pc [bar]	Nature of CP
1		31.25	73.74	
0.98	1 root	30.05	69.85	Vapor-Liquid
0.9	3 roots	-44.28	-122.79	Meta stable
		-44.23	-164.55	Meta stable
		33.86	63.52	Vapor-Liquid
0.88	3 roots	-44.67	-166.16	Meta stable
		-33.905	83.20	Not sure
		36.13	63.1	Vapor-Liquid
0.87	2 roots	-45.75	-169.64	Meta stable
		37.34	62.94	Vapor-Liquid
0.85	2 roots	-48.77	-180.41	Meta stable
		39.93	62.71	Vapor-Liquid
0.8	2 roots	-58.88	-220.36	Meta stable
		46.77	62.09	Vapor-Liquid
0.7	1 root	60.44	59.45	Vapor-Liquid
0.6	1 root	72.59	54.8	Vapor-Liquid
0.5	1 root	82.79	49.12	Vapor-Liquid
0.4	1 root	91.23	43.23	Vapor-Liquid
0.3	1 root	98.22	37.57	Vapor-Liquid
0.2	1 root	104.06	32.33	Vapor-Liquid
0.1	1 root	108.98	27.54	Vapor-Liquid
0		113.2	23.23	

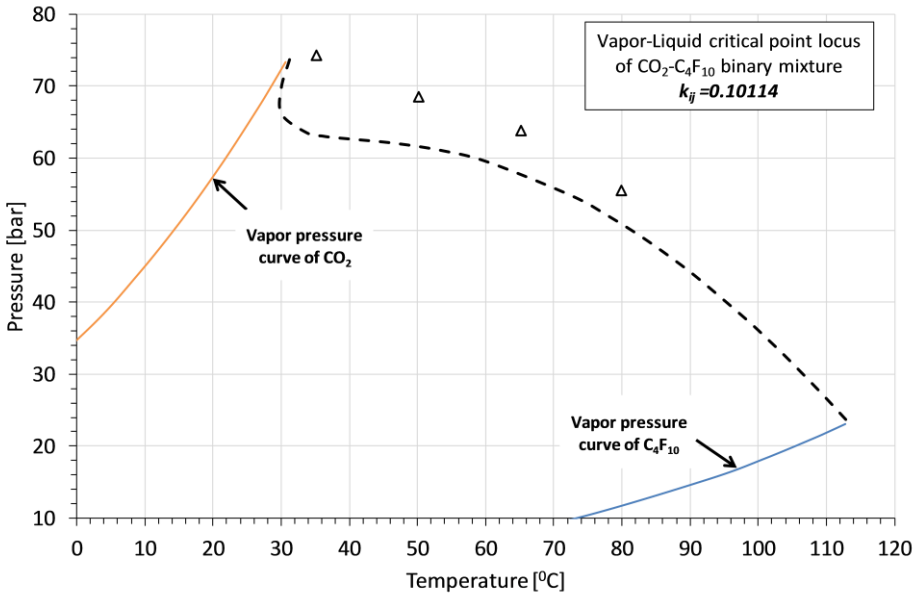

Figure 15: Vapor pressure curves of pure fluid components (Solid lines) and vapor-liquid critical point locus of CO_2-C_4F_{10} binary mixture computed using critical point code (black dashed line). Scatter points (triangles) show experimental data from literature [54]

Carbon dioxide-Perfluorobenzene (CO_2-C_6F_6)

Table 19: Vapor-liquid critical points of CO_2-C_6F_6 binary mixture computed using critical point code at different molar composition

Molar Composition of CO_2 (z_1)	Number of Roots of criticality conditions	Tc [^{0}C]	Pc [bar]	Nature of critical point
1	1 root	31.06	73.83	Vapor-Liquid
0.9	1 root	78.59	111.48	Vapor-Liquid
0.85	1 root	100.34	121.44	Vapor-Liquid
0.8	1 root	120.65	124.57	Vapor-Liquid
0.75	1 root	138.67	122.42	Vapor-Liquid
0.7	1 root	154.27	117.01	Vapor-Liquid
0.65	1 root	167.63	109.90	Vapor-Liquid
0.6	1 root	179.07	102.12	Vapor-Liquid
0.5	1 root	197.42	86.56	Vapor-Liquid
0.4	1 root	211.32	72.44	Vapor-Liquid
0.3	1 root	222.13	60.16	Vapor-Liquid
0.2	1 root	230.75	49.61	Vapor-Liquid
0.1	1 root	237.76	40.55	Vapor-Liquid
0	1 root	243.58	32.73	Vapor-Liquid

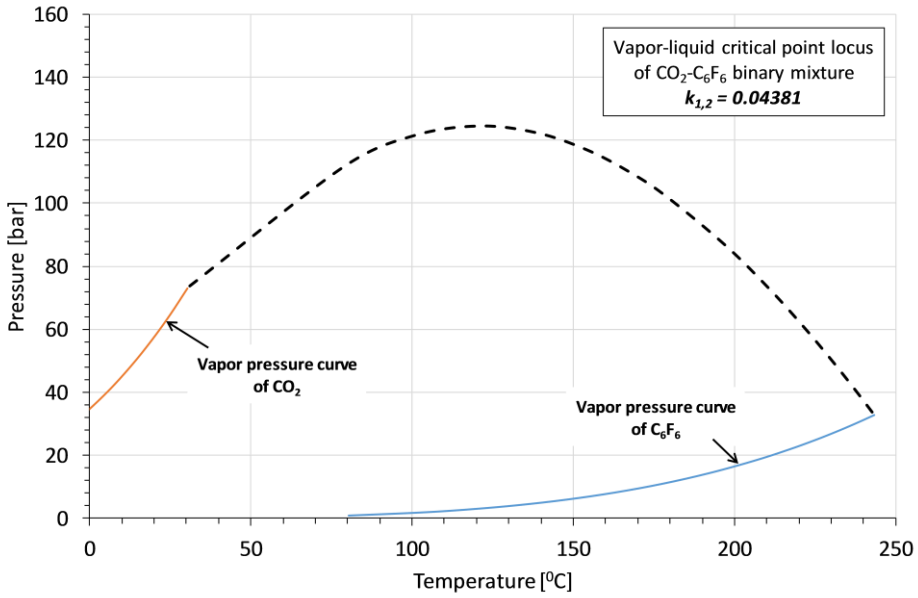

Figure 16:Vapor pressure curve of pure fluid components (solid lines) and vapor-liquid critical point locus of CO_2-C_6F_{14} binary mixture computed using critical point code (black dashed line).

Carbon dioxide-Titanium tetrachloride (CO_2-$TiCl_4$)

Table 20: Critical points of CO_2-$TiCl_4$ binary mixture computed using critical point code at different molar composition

Molar Composition of CO_2 (z_1)	Number of Roots of criticality conditions	Tc [^{0}C]	Pc [bar]	Nature of critical point
1		31.06	73.83	Vapor-Liquid
0.96	1 root	49.28	96.56	Occurrence of Liquid-Liquid critical points.
0.95	1 root	49.14	96.26	
0.93	1 root	45.79	88.59	
0.92	1 root	43.53	82.78	
0.9	1 root	42.38	79.62	
0.8	1 root	149.56	243.65	Vapor-Liquid
0.7	1 root	224.44	232.47	Vapor-Liquid
0.6	1 root	269.89	191.42	Vapor-Liquid
0.5	1 root	299.76	153.42	Vapor-Liquid
0.4	1 root	320.71	122.32	Vapor-Liquid
0.3	1 root	336.14	97.31	Vapor-Liquid
0.2	1 root	347.96	77.05	Vapor-Liquid
0.1	1 root	357.29	60.44	Vapor-Liquid
0.02	1 root	363.44	49.18	Vapor-Liquid

0		364.85	46.61	Vapor-Liquid

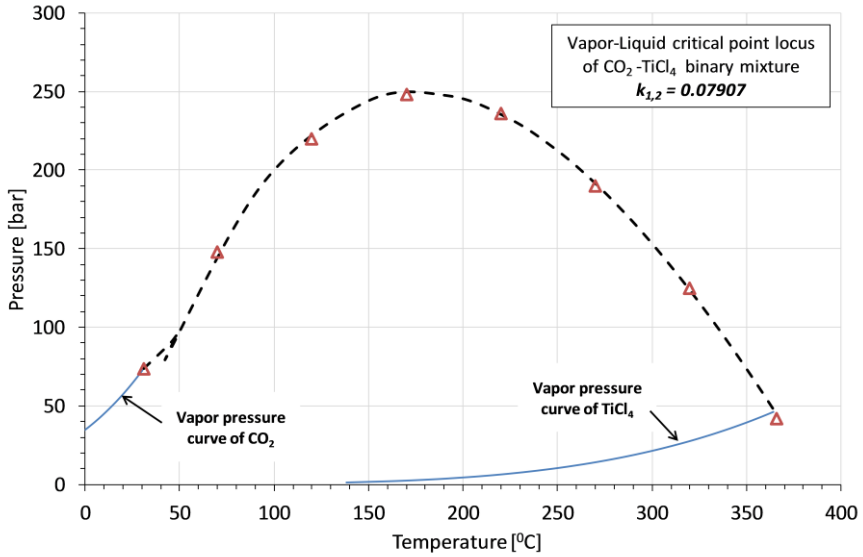

Figure 17: Vapor pressure curve of pure fluid components (solid lines) and vapor-liquid critical point locus of CO_2-$TiCl_4$ binary mixture computed using critical point code (black dashed line). Scatter points (triangle) show critical point calculated in reference [55].

Carbon dioxide-Methylene chloride (CO_2-CH_2Cl_2)

Table 21: Vapor-liquid critical points of CO_2-CH_2Cl_2 binary mixture computed using critical point code at different molar composition

Molar Composition of CO_2 (z_1)	Number of Roots of criticality conditions	Tc [^{0}C]	Pc [bar]	Nature of critical point
1	1 root	31.06	73.83	Vapor-Liquid
0.95	1 root	47.04	85.91	Vapor-Liquid
0.9	1 root	61.58	97.96	Vapor-Liquid
0.8	1 root	90.07	119.85	Vapor-Liquid
0.7	1 root	119.92	132.48	Vapor-Liquid
0.6	1 root	147.37	132.17	Vapor-Liquid
0.5	1 root	170.42	123.37	Vapor-Liquid
0.4	1 root	189.25	110.88	Vapor-Liquid
0.3	1 root	204.64	97.43	Vapor-Liquid
0.2	1 root	217.33	84.29	Vapor-Liquid
0.1	1 root	227.91	72.03	Vapor-Liquid
0	1 root	236.85	60.8	Vapor-Liquid

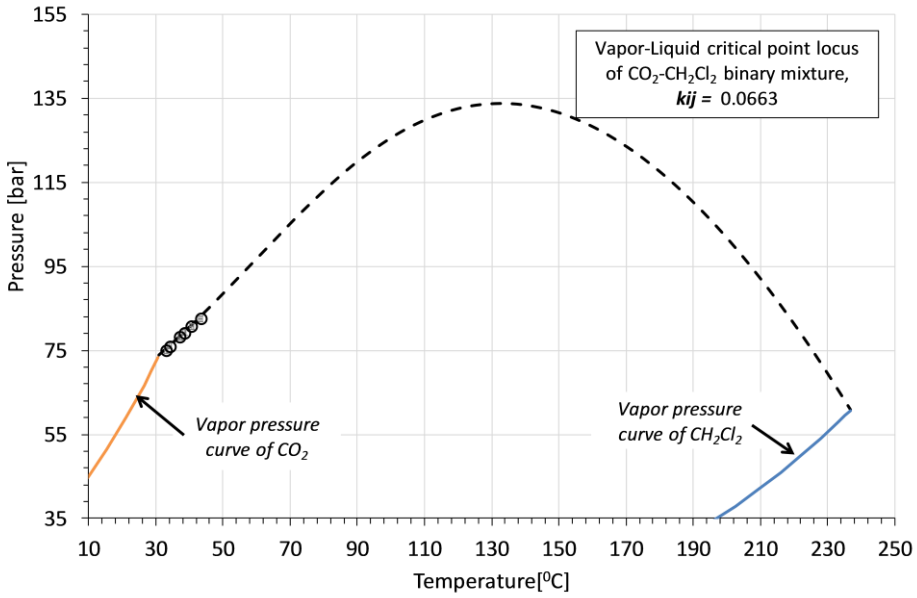

Figure 18: Vapor pressure curve of pure fluid components (solid lines) and vapor-liquid critical point locus of CO_2-CH_2Cl_2 binary mixture computed using critical point code (black dashed line). Scatter points show experimental data from literature [56]

Hexane-Propane (C_6H_{14}-C_3H_8)

Table 22: Vapor-liquid critical points of C_6H_{14}-C_3H_8 binary mixture computed using critical point code at different molar composition

Molar Composition of Hexane (z_1)	Number of Roots of criticality conditions	Tc [^{0}C]	Pc [bar]	Nature of critical point
0	1 root	96.96	42.55	Vapor-Liquid
0.1	1 root	122.52	47.95	Vapor-Liquid
0.2	1 root	143.55	50.02	Vapor-Liquid
0.3	1 root	161.39	49.8	Vapor-Liquid
0.4	1 root	176.67	48.15	Vapor-Liquid
0.5	1 root	189.83	45.66	Vapor-Liquid
0.6	1 root	201.24	42.72	Vapor-Liquid
0.7	1 root	211.18	39.58	Vapor-Liquid
0.8	1 root	219.9	36.4	Vapor-Liquid
0.9	1 root	227.6	33.27	Vapor-Liquid
1	1 root	234.37	30.27	Vapor-Liquid

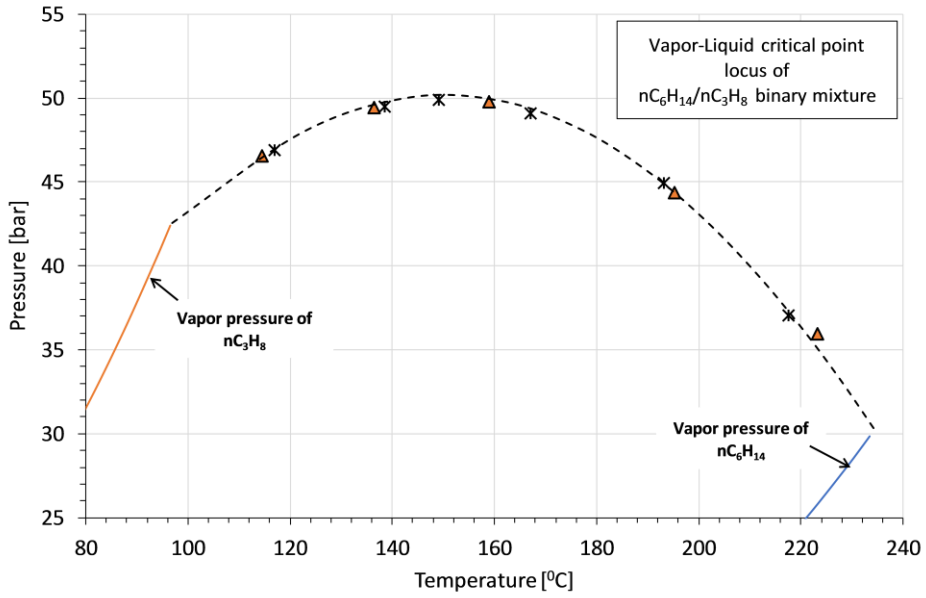

Figure 19: Vapor pressure curve of pure fluid components (solid line) and vapor-liquid critical point locus of propane-hexane binary mixture computed using critical point code (black dashed line). Scatter points show experimental data from literature [57]

Carbon dioxide-Octane (CO_2-C_8H_{18})

Table 23: Critical points of CO_2-C_8H_{18} binary mixture computed using critical point code at different molar composition

Molar Composition of CO_2 (z_1)	Number of Roots of criticality conditions	Tc [^{0}C]	Pc [bar]	Nature of critical point
0.1	1 root	290.57	32.39	Vapor-Liquid
0.2	1 root	284.23	41.46	Vapor-Liquid
0.3	1 root	276.22	52.54	Vapor-Liquid
0.4	1 root	265.82	66.26	Vapor-Liquid
0.5	1 root	251.79	83.54	Vapor-Liquid
0.6	1 root	231.94	105.33	Vapor-Liquid
0.7	1 root	202.04	131.62	Vapor-Liquid
0.8	1 root	153.53	154.09	Vapor-Liquid
0.85	1 root	118.4	151.11	Vapor-Liquid
0.86	3 roots	-24.76	-105.07	Metastable
		-21.23	-132.21	Metastable
		110.56	147.82	Vapor-Liquid
0.87	3 roots	-21.23	-28.73	Metastable

		-18.01	-123.89	Metastable
		102.62	143.52	Vapor-Liquid
0.872	3 roots	-17.61	-122.64	Metastable
		-20.1	-7.12	Liquid-Liquid
		101.04	142.52	Vapor-Liquid
0.875	3 roots	-17.16	-121.16	Metastable
		-18.09	31.89	Liquid-Liquid
		98.65	140.88	Vapor-Liquid
0.878	3 roots	-16.96	-120.61	Metastable
		-15.51	83.39	Liquid-Liquid
		96.28	139.19	Vapor-Liquid
0.88	3 roots	-16.87	-120.29	Metastable
		-13.4	127.81	Liquid-Liquid
		94.72	138.03	Vapor-Liquid
0.9	2 roots	-20.73	-135.23	Metastable
		80.13	125.15	Vapor-Liquid
0.95	1 root	56.64	98.1	Vapor-Liquid
0.999	1 root	31.8	74.14	Vapor-Liquid

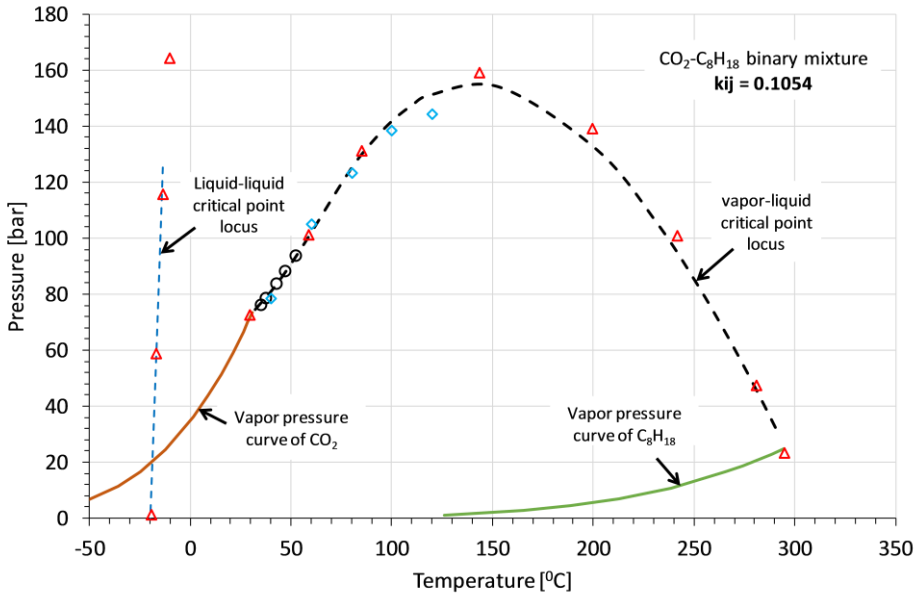

Figure 20: Vapor pressure curves of pure fluid components (solid lines), vapor liquid critical point locus (black dashed line) and liquid-liquid critical point locus (blue dashed line) of CO_2-C_8H_{18} binary mixture computed using critical point code. Scatter points show experimental data from literature; Gurdial et al (Black circles) [25] *, Sun et al (diamonds)* [59], *Heidemann et al (triangles)* [37]

Ammonia-Water (NH_3-H_2O)

Table 24: Vapor-liquid critical points of NH_3-H_2O binary mixture computed using critical point code at different molar composition of water

Molar Composition of water (z_1)	Number of Roots of criticality conditions	Tc [^{0}C]	Pc [bar]	Nature of critical point
1		374.096	220.64	Vapor-Liquid
0.95	1 root	367.68	219.42	Vapor-Liquid
0.9	1 root	361.03	218.54	Vapor-Liquid
0.8	1 root	346.92	217.65	Vapor-Liquid
0.7	1 root	331.51	217.71	Vapor-Liquid
0.6	1 root	314.48	218.35	Vapor-Liquid
0.5	1 root	295.37	218.85	Vapor-Liquid
0.4	1 root	273.53	217.92	Vapor-Liquid
0.3	1 root	248.02	213.02	Vapor-Liquid
0.2	1 root	217.49	199.22	Vapor-Liquid
0.15	1 root	199.87	186.4	Vapor-Liquid
0.1	1 root	180.53	168.05	Vapor-Liquid
0		132.5	112.8	Vapor-Liquid

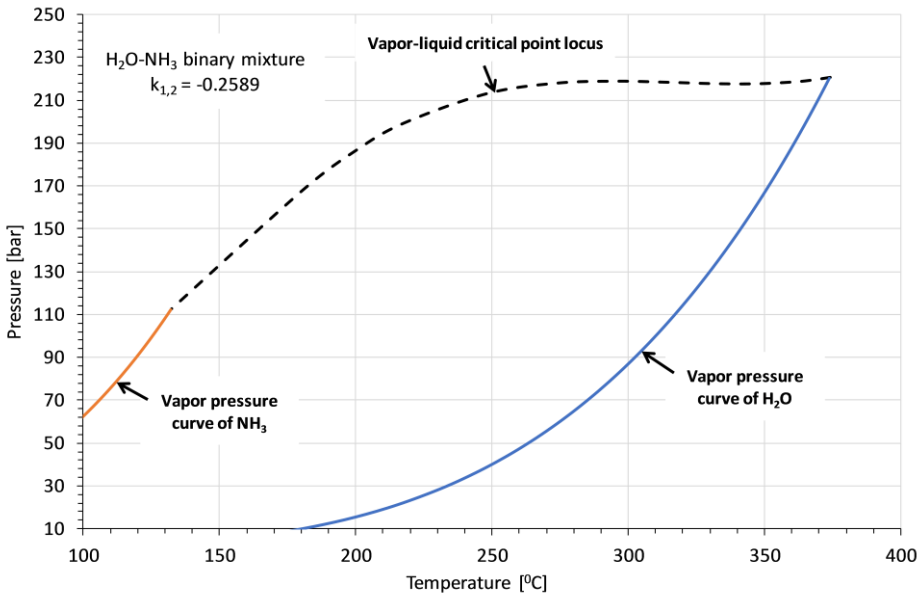

Figure 21: Vapor pressure curves of pure fluid components (solid lines) and vapor-liquid critical point locus of NH_3-H_2O binary mixture computed using critical point code (black dashed line).

Carbon dioxide-water (CO_2-H_2O)

Table 25: Vapor-liquid critical points of CO_2-H_2O binary mixture computed using critical point code at different molar composition of CO_2

Molar Composition of CO_2 (z_1)	Number of Roots of criticality conditions	Tc [^{0}C]	Pc [bar]
0.98	1 root	35.96	77.5
0.95	1 root	43.39	84.45
0.9	no root		
0.8	no root		
0.7	no root		
0.6	no root		
0.5	no root		
0.4	no root		
0.35	no root		
0.3	1 root	318.86	1360.45
0.25	1 root	327.59	723.47
0.2	1 root	339.61	493.33
0.15	1 root	350.27	379.97
0.1	1 root	359.35	309.59
0.08	1 root	362.62	287.76
0.05	1 root	367.19	259.43
0.02	1 root	371.43	235.11

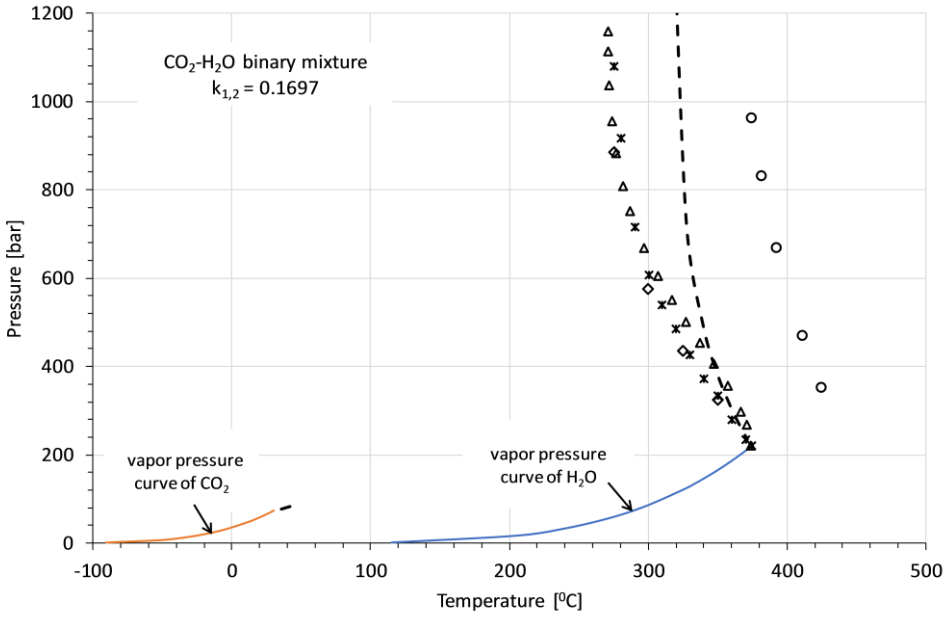

Figure 22: Vapor pressure curves of pure fluids (solid lines) and computed critical points locus of CO_2-H_2O mixture (black dashed line). Scatter points show experimental critical point data from takenouchi et al [60]*(diamonds), todheide et al* [61] *(crosses), Gallagher et al* [62] *(triangles) and Alain et al* [63]*(circles).*

3.5 **Chapter Summary**

This chapter addressed the problem of computation of critical points of binary mixtures by developing a numerical code which can calculate all possible critical points of a binary mixture at given molar composition and pure fluid properties. Numerical code is written in MATLAB together with INTLAB toolbox (version 11) to solve criticality conditions. The methodology adopted is known as interval Newton-bisection method and this approach is proposed earlier by Stradi *et* al to calculate critical points of binary as well as ternary mixtures. The salient features of the numerical code are:

1. Accurate computation of critical points of binary mixture at all compositions.
2. All critical points including stable, unstable and metastable can be computed.
3. No initial guess is required to search for critical point.
4. Both Vapor-Liquid and Liquid-Liquid critical points can be determined.

In subsequent chapters, numerical code developed in this chapter is used to study critical locus of carbon dioxide mixtures.

Chapter 4: CO_2 based binary mixtures as working fluid in transcritical thermodynamic power cycles for high temperature waste heat recovery: Comparison with supercritical CO_2 cycles and ORC

4.1 Introduction

The exhaust gas waste heat from industrial processes carries ample amount of energy at different temperature levels. The recovery of waste heat is important in order to decarbonize industrial sector and to meet the energy demand in efficient way. The total theoretical waste heat potential in the EU is estimated to be 918 TWh, which accounts for waste heat from low, medium, and high temperature rejected by various types of industries [64]. While, high temperature flue gases at temperatures above 270°C share approximately 30% of waste heat potential [65]. In general, some useful ways to recover and valorize waste heat is by using preheaters in industry to heat air or steam, heat pumps for district heating, vapor absorption systems to fulfil cooling needs, and thermodynamic power cycles to generate electrical power.

One of the highest energy consumptive industry and the main contributor of CO_2 emissions is cement production plant. For production of one ton of cement, energy of 4 to 5 GJ is required along with waste heat carrying CO_2 emissions of around 0.8 kg CO_2/kg of cement [66]. In particular, two main sources of flue gases at different temperatures and mass flow in cement plant are exhaust of Kiln preheaters and clinker coolers. It is extremely important to recover heat from flue gases of cement plant in order to produce electricity and to reduce the flue gases temperature. Depending upon the temperature of flue gases, up to 30% of total energy demand of cement plant can be meet by heat recovery power system. As an alternative, heat recovery can also possibly contribute in fulfilling heating demand of the industry or nearby district.

Other significant sources of high temperature waste heat are flue gases from glass manufacturing industry (750 to 1650℃), iron and steel production (900 to 1500 ℃) and chemical processes which includes fluid catalyst cracking (for example, 700 to 800℃).

Corrosion in the tubes of the heat recovery heat exchanger, however, is a challenge due to the presence of sulphur compounds in dusty flue gases. This problem is addressed by

keeping the flue gas outlet temperature above the acid dew point temperature or by using corrosion-resistant materials.

The choice of thermodynamic cycle for power generation is a critical part of heat recovery. Steam Rankine cycles (SRC), Kalina cycles (KC), and organic Rankine cycles (ORC) are among the developed technologies in the market. Steam Rankine cycle technology is primarily competitive for power production greater than 10 MW owing to higher footprint of the power cycle. Organic Rankine cycles, on the other hand, function well at power levels of around 1MW because they use working fluids with a lower evaporation temperature. There are numerous studies in the literature that examine ORC performance with a focus on organic working fluid selection and cycle thermodynamic and economic analysis.

Scaccabarozzi *et* al [67] investigated over 40 organic working fluids, including pure and binary mixtures in ideal ORC engines, using waste heat from heavy duty diesel engines. The mechanical efficiency of ORC was found to be in the range of 16-19% when the flue gas temperature was 245°C and 20-24% when the flue gas temperature was 354°C. The study also emphasizes the necessity of experimental thermodynamic properties and thermal stability data for some new working fluids (like Novec 649 and HFO1233zde) that theoretically showed maximum efficiency in organic Rankine cycles.

Aziz *et* al [68] optimized the thermodynamic efficiency of an ORC employing flue gases from biomass combustion as a heat source at 450°C and considered three working fluids (m-xylene, decane, and Propylcyclohexane). The study selected m-xylene as a potential fluid owing to lower overall size of heat exchanger and higher exergy efficiency. Ref [69] provides a very brief overview of organic working fluids and their selection for subcritical and supercritical cycles.

Bombarda *et* al [70] investigated the potential of the Kalina cycle and ORC in heat recovery of a diesel engine (exhaust temperature of 346°C) to increase power output. The comparison of the Kalina cycle and the ORC cycle reveals that the ORC cycle is a better choice due to its lower operating pressure, smaller heat exchanger size, and simpler cycle layout.

Because of the thermal stability limit imposed by organic working fluids, it is obvious from the vast amount of research that ORCs cannot operate at heat source temperatures beyond 450℃. Thus, the primary energy sources for ORCs are between 100 and 450℃, such as waste heat of internal combustion engines [71], geothermal heat [72], biomass

heat [73], waste heat from micro-gas turbines[74] and parabolic trough solar collectors [75]. As a result, the power size of ORCs is around few kilowatts to tens of megawatts (<1-10 MW), with first law efficiency ranging from 10-30% depending upon the operating conditions.

Nevertheless, ORC research continues to progress in the direction of selecting thermally stable working fluids, which necessitates thermal stability testing at various temperatures and with various container materials [5]. Moreover, the selection of the best working fluid is based on the working fluid's thermodynamic and environmental properties, power cycle boundary conditions, site conditions, and required electrical power. It's difficult to draw a line suggesting optimal working fluid without first knowing the required operating conditions and working fluid properties.

In the last decade, there has been renewed interest in use of carbon dioxide (CO_2) as a working fluid in thermodynamic cycles for power generation. Supercritical carbon dioxide (sCO_2) power cycles, in particular, are being investigated using low, medium, and high temperature heat sources [76]. The main advantage of sCO_2 power cycle technology is its higher thermal efficiency and smaller size footprint when compared to conventional steam Rankine cycle technology. Because of the higher density in the supercritical phase, the sCO_2 cycle requires approximately ten times smaller turbomachinery than the steam Rankine cycle for same power size [77].

There is a lot of research and projects underway with the goal of designing and deploying a cost-effective heat recovery solution. sCO_2 cycles, without a doubt, can be a viable candidate for power generation by utilizing a wide range of heat recovery sources such as waste heat from gas turbines, waste heat from the glass manufacturing industry, and so on. For waste heat recovery of cement plants, Kizilkan *et* al. [66] compared the thermodynamic performance of the sCO_2 cycle and the Steam Rankine cycle. According to the analysis, the sCO_2 cycle outperformed the steam Rankine cycle in terms of energy and exergy efficiency; the sCO_2 cycle demonstrated around 3 percentage points higher energy efficiency and around 7 percentage points higher exergy efficiency than the steam Rankine cycle.

Astolfi *et* al. [78] compared ORC and CO_2 cycles (supercritical and transcritical cycles) at heat source temperatures ranging from 200 to 600°C, focusing on both air cooled and water cooled heat sinks. For heat source temperatures greater than 350°C, the study suggested a transcritical CO_2 cycle with a water-cooled condenser as an efficient cycle.

ORC, on the other hand, is recommended as an efficient cycle for heat sources that are less than 350°C.

For heat recovery from a glass furnace with a flue gas temperature of 450 °C, a comparison was made among ORC, sCO_2 cycle, and Air Brayton cycle. In terms of higher power output, the study proved sCO_2 cycle as a promising heat recovery solution when compared to the ORC and Air Brayton cycles [79]. Marchionni *et* al [80] carried out the study on eight different sCO_2 cycle layouts in order to determine a competitive cycle layout using flue gases at 650°C as a heat source. Similarly, Manente *et* al [17] compared traditional and novel sCO_2 cycle layouts for a wide range of waste heat sources from 400 to 800℃. Based on heat recovery efficiency and plant cost, the study recommended single flow split and dual flow split with dual expansion layouts as the best possible compromise for waste heat recovery.

Why CO_2 mixtures for heat recovery power cycles?

Despite the fact that sCO_2 cycles show promising cycle efficiency and compact size of the turbomachinery and heat exchangers, there are some challenges that must be overcome in order to obtain a cost-effective heat recovery cycle:

1. *Complex cycle layout versus total efficiency*: The sCO_2 cycle layouts which showed higher heat recovery total efficiency are complex with larger size foot print which imply higher specific investment costs ($/kWel) compared to simple recuperative cycle layout.
2. *High turbine inlet pressure:* Maximum operating pressure (250 to 400 bar) in sCO_2 cycles are higher than ORCs, necessitating the use of specialized materials to withstand higher pressure.

Adopting CO_2-based binary mixtures, which involve doping CO_2 with organic or inorganic additives, can be a very useful way to deal with the aforementioned challenges of sCO_2 cycles in waste heat recovery. Doping can cause the CO_2 critical point to shift to a higher temperature and lower pressure, allowing for the possibility of a condensation cycle. Lower cycle minimum pressure below the critical point can provide a degree of freedom to increase the cycle's pressure ratio while also maintaining a lower turbine inlet pressure. As a result of the high-pressure ratio, the cycle can produce more power, improving total efficiency while maintaining the same cycle layout. Second, due to liquid phase compression in the condensation cycle, with compression starting at a temperature below the critical point temperature of the CO_2 mixture, less compression power consumption is achievable as compared to sCO_2 cycle. A recent work [81] compared the

ratio of compression power and turbine power ($\dot{W_{comp}}/\dot{W}_{turbine}$) for sCO_2 cycle and transcritical CO_2-propane cycle. In case of CO_2-propane cycle, the value of ratio is 19% lower compared to sCO_2 cycle at constant cycle maximum temperature and minimum temperature (i.e. 550℃ and 51℃). This shows how CO_2-based binary mixtures can be used to reduce compression power and enhance thermodynamic efficiency.

In lieu of above discussion, the thermodynamic evaluation of CO_2 power cycles using CO_2-based binary mixtures as working fluids for heat recovery application is discussed in this chapter.

4.2 **Scope of this Chapter**

This chapter deals with thermodynamic analysis and comparison of transcritical ORCs, sCO_2 cycles and transcritical CO_2 mixture based power cycles. The heat source temperature is assumed as 450℃ because this temperature represents wide range of applications like waste heat from cement plant, waste heat from internal combustion engines and glass furnaces.

The main focus is on the following two aspects:

1. Compare the thermodynamic performance of benchmark heat recovery power cycle technologies (sCO_2 vs ORCs) and choose the best conditions and working fluid to improve the heat recovery system's overall efficiency.
2. Propose CO_2-based binary mixtures as working fluids in transcritical cycles to demonstrate benefits in total efficiency and overall power plant size compared to sCO_2 cycle and ORCs.

The structure of this Chapter is divided into three main sections:

1. Heat recovery using supercritical CO_2 power cycles
2. Heat recovery using transcritical Organic Rankine cycles
3. CO_2 mixtures working fluid in transcritical power cycles

4.3 **Method**

Power cycle operating parameters and assumptions

Table 26 shows the properties of flue gases as a heat source for heat recovery. The dew point temperature of the gases, which is 51°C, is the minimum possible cooling temperature of flue gases. In the literature, the typical minimum temperature of gases is assumed to be 150 to 180°C to avoid condensation of suphur compounds and the production of sulphuric acid in the pipes of a heat recovery heat exchanger [79]. Because the flue gas composition assumed in this study lacks sulphur compounds, the calculated dew point temperature is quite low.

Table 26: Characteristics of flue gases from an industrial process

T_{flue} [°C]	P_{flue} [bar]	T_{dew} [°C]	$\dot{m}_{flue}$ [kg/s]	Thermal power $\dot{Q}_{available}$ [MW]	Molar composition of flue gas			
					CO_2	N_2	O_2	H_2O
450	1.01	51	100	44.27	0.28	0.58	0.03	0.11

The general assumptions for thermodynamic analysis of power cycles are listed in Table 27. The minimum temperature difference approach (MITA) is used to model heat exchangers (recuperators, radiators, condensers, and primary heat exchangers), the values of which are shown in Table 2. The efficiencies of turbomachinery (compressors, pumps, and turbines) are also derived from best practices in the literature.

The critical pressure of the working fluid determines the minimum pressure (P_{min}) of the cycles. The minimum pressure in supercritical CO_2 cycles is optimized using range of pressure values slightly above the critical point of CO_2. Whereas, the minimum pressure in transcritical cycles is less than the critical pressure; in fact, it is the bubble pressure at the calculated cycle minimum temperature (P_{sat} @T_{min}).

Table 27: Operating parameters and common assumptions for thermodynamic simulation of sCO_2 power cycles.

Parameter	Value
P_{min} [bar]	P_{sat} @ T_{min} for transcritical cycle Optimum value for supercritical cycle
P_{max} [bar]	Optimum value
T_{max} [°C]	300,350,400
$MITA_{PHE}$ [°C]	50

$MITA_{radiator}$ [℃] / $MITA_{condenser}$ [℃]	20
$MITA_{recup}$ [℃]	20
Air coolant inlet/outlet [℃]	15/35
$\eta_{isent,comp}/\eta_{mech,comp}$	0.8 / 0.98
$\eta_{isent,turb}/\eta_{mech,turb}$	0.85/0.95

Furthermore, the cycle maximum pressure (P_{max}) should be always greater than the critical pressure of the working fluid as this is the primary requirement for supercritical and transcritical cycles. For each working fluid and cycle layout, the optimal value of P_{max} is calculated. Regarding cycle maximum temperature (or turbine inlet temperature), three values are considered; 300℃, 350℃ and 400℃ and optimum value for each cycle layout is computed. Pressure losses in heat exchangers are neglected for simplicity.

4.4 **Thermodynamic modeling**

To evaluate the thermodynamic performance of heat recovery system, following performance indicators are defined:

Cycle total efficiency

$$\dot{W}_{net} = \dot{W}_{turbine} - \dot{W}_{comp/pump} \quad \text{Eq. 13}$$

$$\dot{W}_{elec} = \eta_{mech,turb} * \dot{W}_{turbine} - \frac{\dot{W}_{comp/pump}}{0.98} \quad \text{Eq. 14}$$

$$\eta_{cycle} = \frac{\dot{W}_{elec}}{\dot{Q}_{PHE}} \quad \text{Eq. 15}$$

The symbol $\dot{W}_{net}$ indicates the gross work output of the power cycle and cycle efficiency (η_{cycle}) represents the ability of cycle to convert thermal power exchanged in primary heat exchanger (required input) into gross work output (desired output). Normally, large heat exchange in PHE brings about reduction in cycle efficiency of the power cycle but on other hand it also results in more cooling of flue gases. As a result, it is preferable to define a composite indicator for a heat recovery power cycle that considers both the capacity of cycle to cool flue gases and its efficiency. Total efficiency (η_{total}) as expressed in **Eq. 16** is rather more inclusive indicator because it is a multiple of heat recovery effectiveness and cycle efficiency. It refers to the power cycle's ability to convert flue gas thermal power (available input) into gross work output (desired output).

$$\phi_{recovery} = \frac{\dot{Q}_{PHE}}{\dot{Q}_{available}} \quad \text{Eq. 16}$$

$$\eta_{total} = \eta_{cycle}\, \phi_{recovery} = \frac{\dot{W}_{net}}{\dot{Q}_{available}} \quad \text{Eq. 17}$$

$$\dot{Q}_{available} = \dot{m}_{flue}(h_{flue,in} - h_{flue,dp}) \quad \text{Eq. 18}$$

Where, $\dot{Q}_{available}$ represent the maximum thermal power available in flue gases which is the multiple of enthalpy difference and mass flow of flue gases.

Exergy or second law efficiency

Analysis of entropic losses and evaluation of exergy efficiency provides the location of thermodynamic losses in a thermodynamic power cycle and also helps in systematic comparison of different power cycles on consistent bases i.e. maximum obtainable power from the available heat source.

$$\eta_{II} = \frac{\eta_{total}}{\eta_{carnot}} \quad \text{Eq. 19}$$

$$\eta_{carnot} = 1 - \frac{T_o}{T_H^*} \quad \text{Eq. 20}$$

$$T_H^* = \frac{h_{flue,in} - h_{flue,dp}}{s_{flue,Iin} - s_{flue,dp}} \quad \text{Eq. 21}$$

Where, T_0 is the ambient air temperature (or dead state temperature) of 15℃, T_H^* is the temperature of sensible heat source (flue gases). The definition of T_H^* depends on the inlet and minimum possible cooling temperature of flue gases i.e. dew point temperature (*dp*). For a thermodynamic power cycle, the total efficiency in terms of exergy losses can be expressed as,

$$\eta_{total} = \eta_{carnot} - \eta_{loss} \quad \text{Eq. 22}$$

$$\eta_{loss} = \frac{T_0 \sum_{i=1}^{N} \dot{S}_G}{\dot{Q}_{available}} \quad \text{Eq. 23}$$

$T_0 \sum_{i=1}^{N} \dot{S}_G$ represents the exergy losses (or loss of available power) occurring due to entropy generation in cycle components, exergy loss due to cooling of residual exhaust gases to dew point temperature (stack losses) and due to heating of air in the radiator.

The entropy generation rate for each process in the components of the power cycles are computed as follows,

$$\dot{S}_{G,comp/pump} = \dot{m}_{wf} * (s_{outlet} - s_{inlet}) \quad \text{Eq. 24}$$

$$\dot{S}_{G,turbine} = \dot{m}_{wf} * (s_{outlet} - s_{inlet}) \quad \text{Eq. 25}$$

$$\dot{S}_{G,PHE} = \dot{m}_{wf} * \left(s_{cold,outlet} - s_{cold,inlet}\right) - \dot{m}_{flue} * \left(s_{flue,in} - s_{flue,out}\right) \quad \text{Eq. 26}$$

$$\dot{S}_{G,recuperator} = \dot{m}_{wf} * \left[\left(s_{cold,outlet} - s_{cold,inlet}\right) - \left(s_{hot,inlet} - s_{hot,outlet}\right)\right] \quad \text{Eq. 27}$$

$$\dot{S}_{G,radiator/condenser} = \frac{\dot{m}_{air} * \left(h_{air,out} - h_{air,in}\right)}{T_0} - \dot{m}_{wf} * \left(s_{hot,inlet} - s_{hot,outlet}\right) \quad \text{Eq. 28}$$

Moreover, entropy generation rate due to residual flue gases from outlet of PHE cooled down to dew point is calculated as,

$$\dot{S}_{G,stackloss} = \frac{\dot{m}_{flue}*(h_{flue,out}-h_{flue,dp})}{T_0} - \dot{m}_{flue} * (s_{flue,out} - s_{flue,dp}) \quad \text{Eq. 29}$$

Summing up all the losses terms and inserting in **Eq. 22** gives the total efficiency of the power cycle. Finally, the second law efficiency or exergy efficiency can be computed using **Eq. 19**.

Taking into account the above-mentioned operating conditions and thermodynamic model, next sections present the thermodynamic results of three power cycle technologies for heat recovery:

1. Supercritical carbon dioxide power cycles
2. Transcritical Organic Rankine cycles
3. Carbon dioxide mixtures transcritical power cycles

4.5 **Supercritical CO_2 power cycles**

Cycle Layouts

As shown in Figure 23, the first sCO_2 power cycle layout considered for heat recovery is a simple recuperative sCO_2 power cycle. In this design, CO_2 is heated to its maximum temperature in a primary heat exchanger before being expanded in a turbine. Following expansion, there is one recuperator that recovers the available thermal power at the turbine outlet in order to raise the temperature of the CO_2 coming from the compressor at high pressure. The amount of heat exchange in the recuperator is determined by the compressor pressure ratio and the mass flow rate of CO_2. After the recuperator, the cooled CO_2 is further cooled to cycle minimum temperature while passing through a radiator.

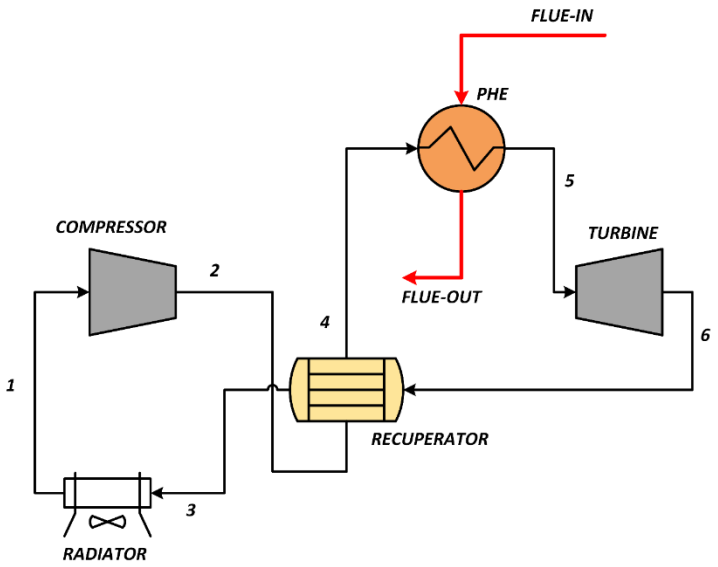

Figure 23: Layout diagram of sCO_2 simple recuperative cycle

The Partial heating cycle was chosen as the second layout. As shown in *Figure 24*, this cycle scheme includes a mass split and another heat recovery heat exchanger in addition to a simple recuperative cycle layout. Because of the split in mass flow rate after compression, some CO_2 mass flows to the heat exchanger for heat recovery, while the remaining flows to the recuperator, depending on the specified value of mass split. After being heated by the heat exchanger and recuperator, the two CO_2 streams are combined and heated in the primary heat exchanger to achieve the required turbine inlet temperature. The turbine expands to the minimum cycle pressure, then cools the CO_2 stream in the recuperator and through the radiator to the minimum cycle temperature.

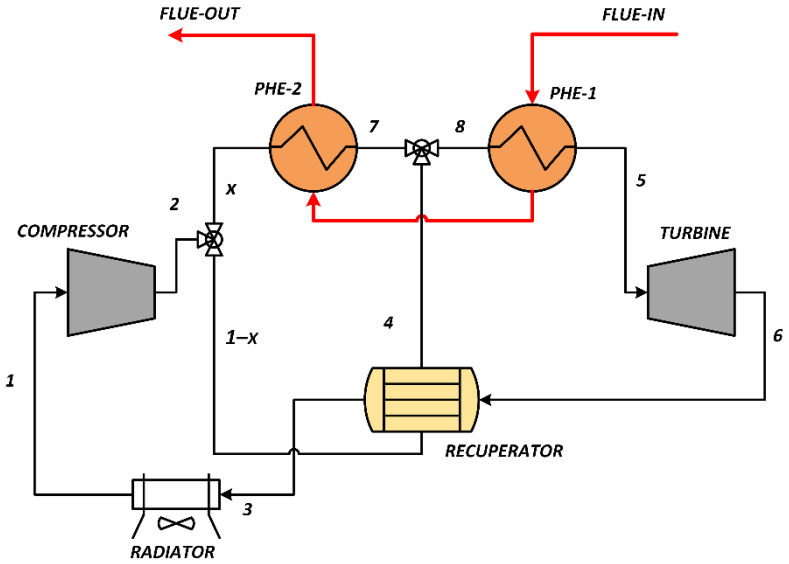

Figure 24: Layout diagram of sCO_2 partial heating cycle

Figure 25 depicts the third layout, known as the single flow split dual expansion cycle. The cycle components in this configuration are larger than in the Partial heating cycle due to the addition of one low temperature (LT) turbine. CO_2 is compressed in the main compressor before being split into two streams. One stream is heated in PHE before being expanded in a high temperature (HT) turbine. While the other stream is heated in the LTR and HTR before being expanded in the LT turbine. In order to achieve a better thermal match, the different mass flow in recuperators balances the heat capacities between hot and cold streams inside the recuperators. Finally, CO_2 is cooled to the minimum cycle temperature in the radiator. This cycle configuration is known as a cascade cycle in the literature [6].

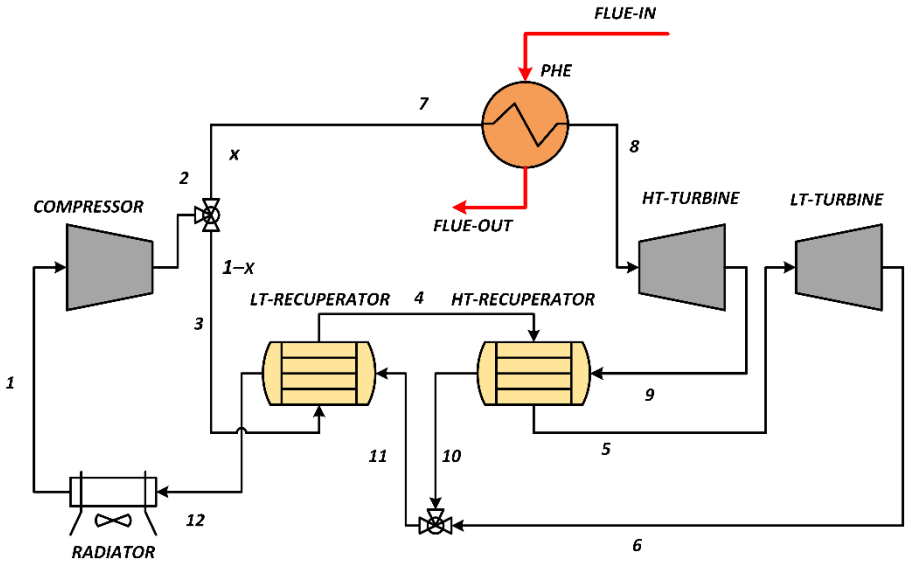

Figure 25: Layout diagram of sCO_2 single flow split-dual expansion cycle

4.6 **Thermodynamic cycle results of sCO_2 cycles**

Simple recuperative cycle (SRC)

To find optimum point based on total efficiency, the cycle thermodynamic performance is investigated at different minimum pressures (P_{min}), pressure ratio (P_R) and maximum temperature (T_{max}). Figure 26 shows the effect of different P_R and P_{min} on total efficiency ($\eta_{th} * \phi$) for cycle maximum temperature of 350 ℃ and 400℃. The maximum efficiency obtained at T_{max} = 350 ℃ is almost the same compared to one obtained at T_{max} = 400 ℃ with optimum pressure ratio smaller for T_{max} = 350 ℃. The optimum total efficiency is obtained at P_{min} = 100 bars, T_{max} = 400 ℃ and P_R of 4.

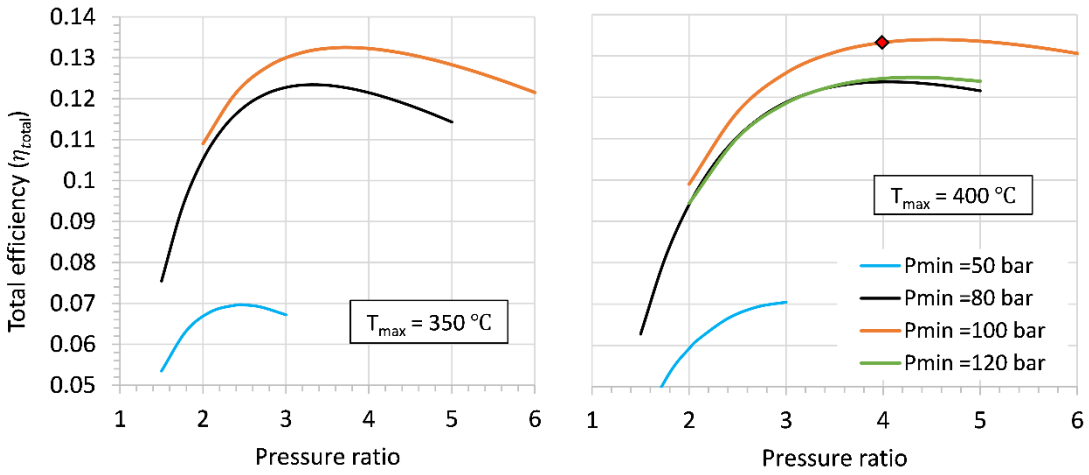

Figure 26: Trend of cycle total efficiency with variation in pressure ratio and cycle minimum pressure (Pmin) for sCO2 simple recuperative cycle at Tmax of 350℃ and 400℃

With a higher P_{min}, such as P_{min} = 120 bars as shown in Figure 26, heat recovery in the recuperator increases, resulting in a higher temperature available at the inlet of the heat recovery heat exchanger (state 4), limiting the effective utilization of waste heat and resulting in lower cycle heat recovery effectiveness and total efficiency. Figure 27 and Figure 28 show optimal cycle results in the T-s and T-Q planes, respectively.

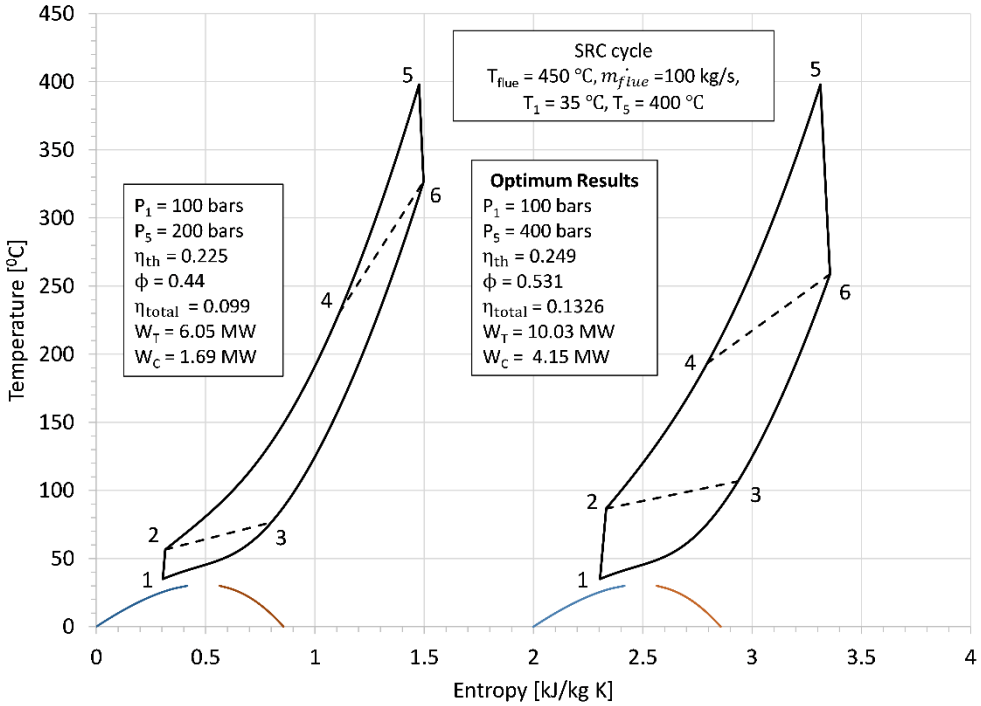

Figure 27: Thermodynamic results of sCO_2 simple recuperative cycle in T-s plane.

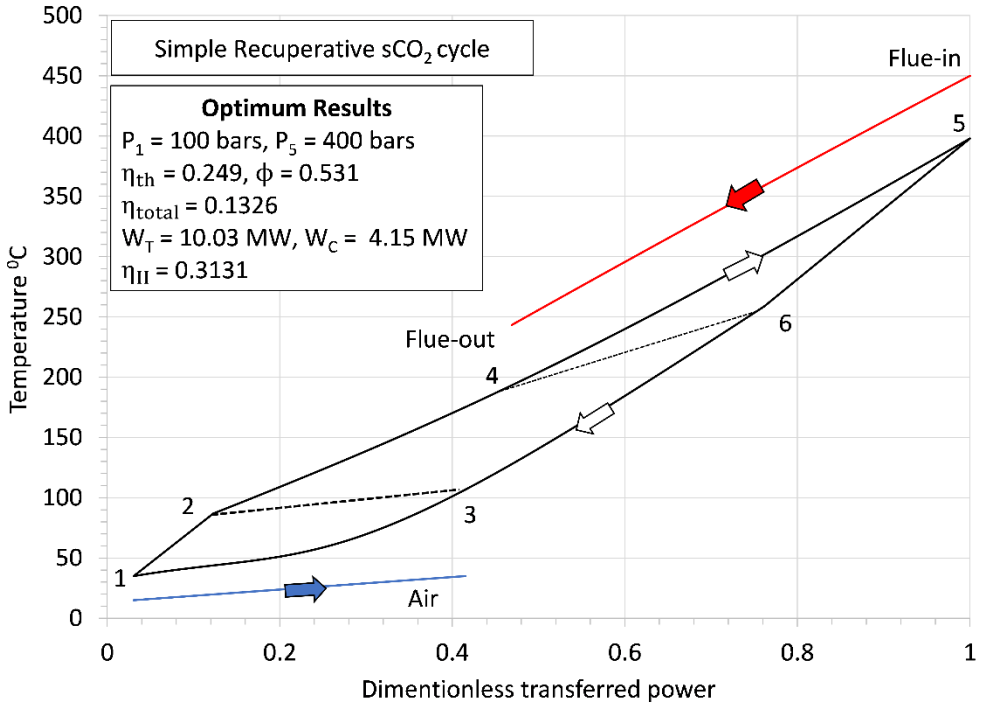

Figure 28: Thermodynamic process diagram at optimum point of sCO_2 simple recuperative cycle on temperature-dimensionless heat transferred plane.

Partial heating cycle (PHC)

Figure 29 shows the influence of cycle minimum pressure and maximum temperature (or T_5) on total efficiency at mass split x of 0.5. The optimum performance is achieved at P_R = 3, P_{min} = 100 bars and T_{max} = 350°C. At constant P_{min}, the total efficiency at T_{max} = 350°C

is better than at T_{max} = 400℃. This is due to the fact that as T_{max} decreases, the temperature at the primary heat exchanger's entry decreases, resulting in more utilization of heat from flue gases and more cooling of flue gases. The greater cooling of flue gases improves heat recovery effectiveness and, as a result, total cycle efficiency.

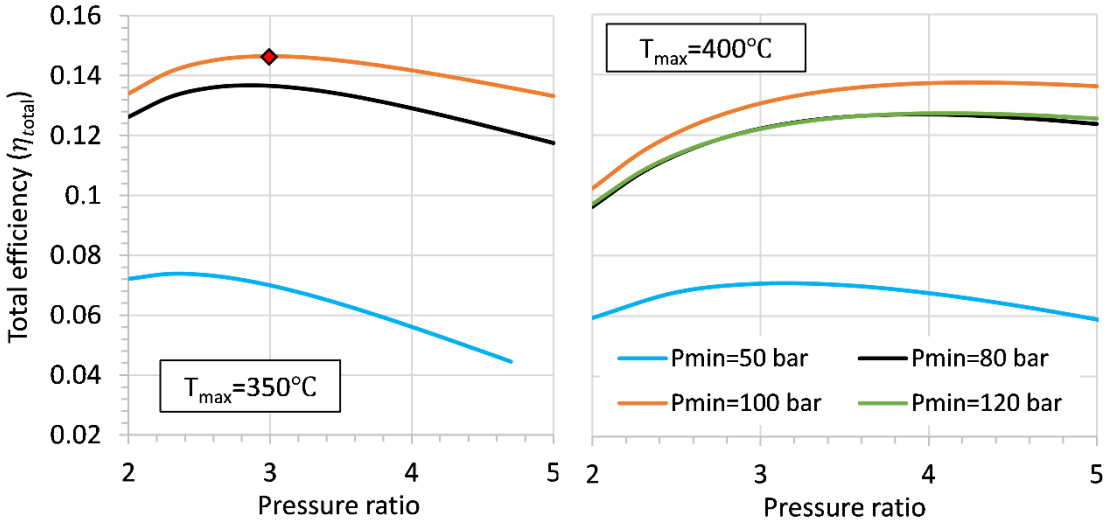

Figure 29: Total efficiency at different minimum cycle pressures versus pressure ratio for sCO_2 partial heating cycle at Tmax of 350℃ and 400℃. Mass split x is 0.5. Red mark shows the optimum performance point.

At optimum T_{max}, P_R and P_{min}, the cycle performance is studied at different mass split in order to decide the optimal as shown in Figure 30 . As shown in red marks, x=0.3 is decided as optimum mass split since it results in both higher cycle thermal efficiency and total efficiency. At x<0.3, the rise in total efficiency is due to rise in heat recovery effectiveness, since, the effect on thermal efficiency is negligible. However, thermal efficiency drops with increase in x>0.3 and effectiveness keep on increasing which results in uniform total efficiency.

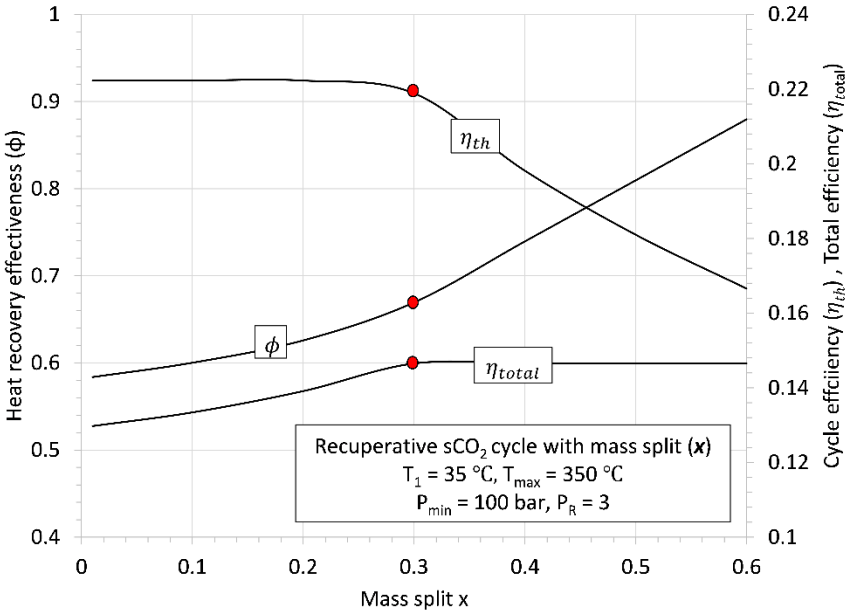

Figure 30: Trend of heat recovery effectiveness, cycle efficiency and total efficiency versus mass split (x) at optimum Pmin, P_R and Tmax.

The trend of cycle efficiency with variation in mass split can be comprehensible by analyzing the temperature differences between cold and hot streams inside the recuperator. The cycle thermal efficiency is linked to the log mean temperature difference (LMTD) inside the recuperator. Lower the LMTD implies better thermal match between the cold and hot streams which results in larger recuperation and higher cycle efficiency. Moreover, lower LMTD bring about lower exergy losses and vice versa. Figure 31 shows the relationship between LMTD and exergy losses in the recuperator at different mass split. It can be easily noticed that, there exists a minimum log mean temperature difference (LMTD) in the recuperator at which the thermal efficiency is maximum and exergy losses are minimum. LMTD increases at x>0.3 which contributes to drop in cycle efficiency and increase in the exergy loss. Finally, the cycle optimum results are shown in Figure 32 and Figure 33 on T-s plane and T-Q plane respectively.

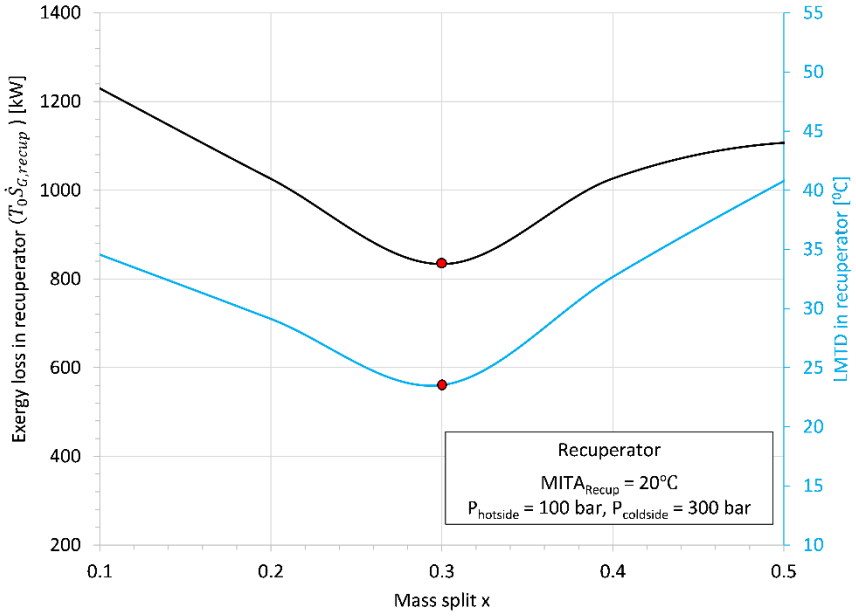

Figure 31: Exergy loss and log mean temperature difference inside the recuperator for different mass split x. The red mark shows optimum x.

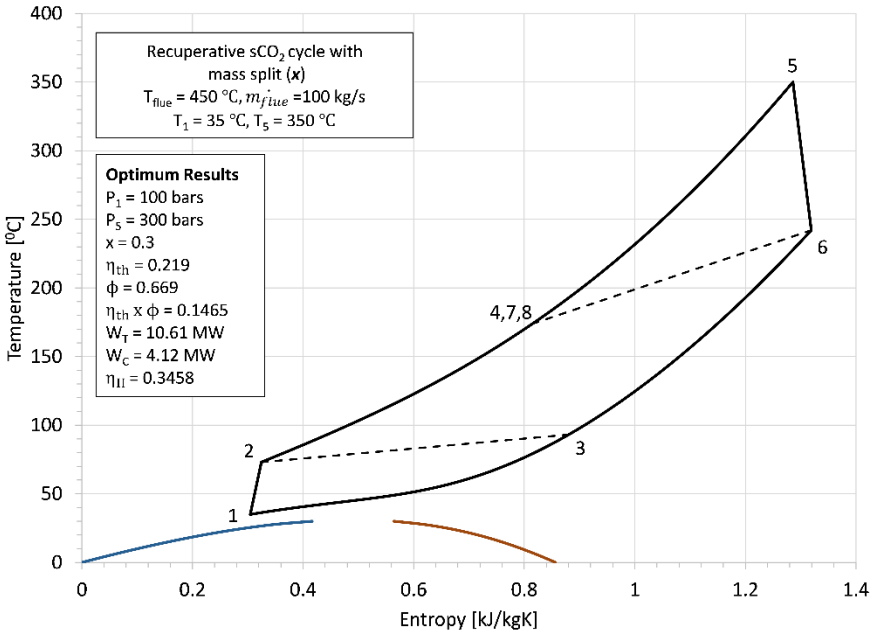

Figure 32: Optimum thermodynamic results of sCO_2 partial heating cycle in T-s plane.

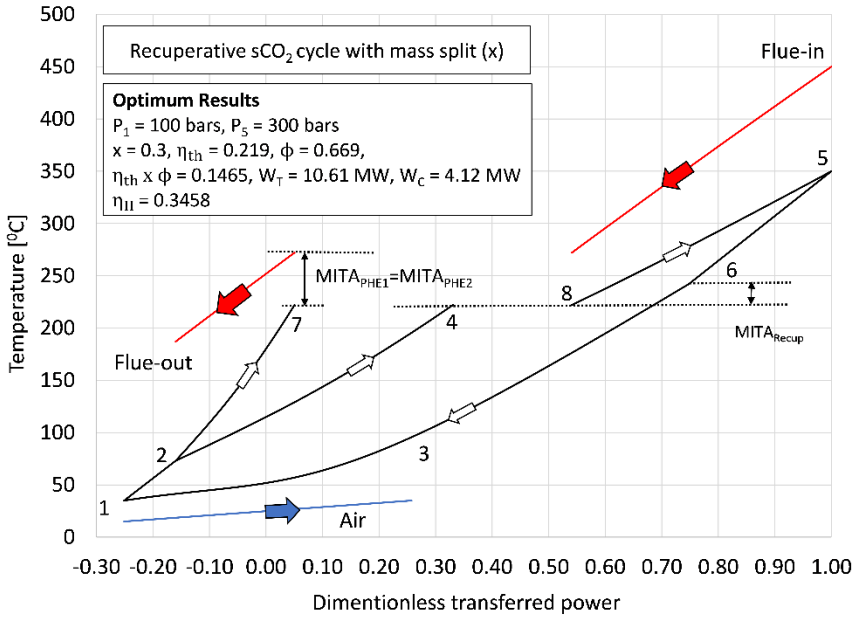

Figure 33: Thermodynamic process diagram at optimum point of sCO_2 partial heating cycle on temperature-dimensionless heat transferred plane.

In the following, performance of Partial heating cycle is compared with results of more advanced cycle layout in literature. Dario *et* al [82] proposed and analyzed the recompression with mass split cycle layout for heat recovery from flue gases at 50 kg/s and 550 ℃. The cycle performance of PHC is computed using the same cycle design assumptions and conditions mentioned in the reference. Firstly, the optimum T_{max}, mass split 'x' and P_R are obtained using sensitivity analysis at varying T_{max} and 'x' according to the method discussed earlier. Afterwards, the results of PHC at optimum conditions are compared with optimum results of recompression with mass split cycle (given in the reference). Table 28 illustrates the cycle conditions and comparison of results. As evident, the optimum total efficiency and cycle efficiency of PHC are comparable to more complex cycle layout, although, with higher cycle maximum pressure.

Table 28: Comparison between optimum results of recuperative cycle with mass split and complex cycle with recompression and mass split of literature [82].

Parameter	Value
	Cycle design assumptions and operating conditions
P_{min} **(bars)**	80
T_{min} **(℃)**	33
$T_{exh,\ in}$ **(℃)**	550
$\dot{m}_{exh}$ **(kg/s)**	50
$MITA_{PHE}$ **(℃)**	25
$MITA_{recup}$ **(℃)**	10
$\eta_{isent,comp}/\eta_{mech,comp}$	0.8 / 0.964
$\eta_{isent,turb}/\eta_{mech,turb}$	0.9 /0.964

Results		
	This study (Recuperative cycle with mass split layout)	**Literature (Recompression cycle with mass split layout)**
P_{min} ***(bars)***	80	81.2
P_{max} ***(bars)***	240	181.3
Mass split 'x'	0.3	0.174
T_{max} (℃)	350	346.6
η_{th}	0.262	0.269
ϕ	0.911	0.839
η_{total}	0.238	0.226
$\dot{m}_{CO_2}$***(kg/s)***	105.2	140.2

Single flow split-dual expansion cycle (SFDE)

As in the analysis of previous cycle configurations, the performance study of SFDE cycle also involves the sensitivity of cycle total efficiency at different T_{max}, P_R and P_{min}. The role of mass split in SFDE configuration is to enhance the turbine inlet temperature in LT turbine to improve the cycle efficiency. Besides, it is also essential to achieve same temperatures at mixer inlet (i.e. $T_6 \approx T_{10}$) to reduce mixing losses and in turn maintain higher cycle efficiency. On the other side, the temperature at the inlet of PHE (T_7) depends on the compressor outlet temperature, in other words, the pressure ratio (P_R).

In cycle thermodynamic calculations, optimum mass split ***x*** is calculated at which the total efficiency is higher. In addition, optimum point is also decided considering the sensitivity of cycle total efficiency at different compressor inlet pressure (P_{min}). To ensure the accuracy of cycle thermodynamic model, cycle calculations are carried out at same conditions as given by Manente *et* al [17] and the results are compared. Table 29 illustrates the cycle conditions and comparison of results. The optimum mass split, cycle efficiency and total efficiency calculated using present approach are the same as computed by Manente *et* al as evident form the Table 29.

Table 29: Comparison of results with literature for SFDE sCO_2 cycle [17].

Parameter	**Value**
Cycle design assumptions and operating conditions	
P_{min} ***(bars)***	76.3
P_{max} ***(bars)***	200
T_{min} ***(℃)***	32
T_{max} (℃)	450
$T_{exh,\ in}$ ***(℃)***	500

$\dot{m}_{exh}$ *(kg/s)*	9.37	
$MITA_{PHE}$ *(℃)*	50	
$MITA_{recup}$ *(℃)*	8 in HTR, 5 in LTR (corresponds to recuperator's effectiveness of 95%)	
$\eta_{isent,comp}/\eta_{mech,comp}$	0.8 / 0.98	
$\eta_{isent,turb}/\eta_{mech,turb}$	0.85 /0.95	
Results		
	This study	**Manente *et* al**
Mass split 'x'	0.4	0.4
η_{th}	0.2310	0.2363
η_{total}	0.2019	0.19
$T_{exh,\ out}$ *(℃)*	122	114

Focusing on the design conditions of present study, the performance of SFDE cycle at different turbine inlet temperature (T_{max}) of HT turbine and constant compressor inlet pressure (P_{min}) of 100 bars are shown in Figure 34. The increase in pressure ratio and T_{max} improves both the total efficiency and the optimum mass split x. Also, the optimum mass split values are lower for higher T_{max} keeping constant pressure ratio.

The influence of different compressor inlet pressure (P_{min}) and T_{max} on total efficiency are presented in Figure 35. Maximum total efficiency is obtained at T_{max} = 400℃, P_{min} = 100 bars and P_R of 2.9. Total efficiency is smaller at both P_{min} of 120 bars and 80 bars. At P_{min} = 80 bars, the temperature at entry of PHE (i.e.T_7) enhances which bring about reduction in heat recovery effectiveness as shown in Figure 36. Whereas, in case of P_{min} = 120 bars, there is very slight improvement in heat recovery effectiveness due to T_7 as compared to P_{min} = 100 bars, so the decrease in total efficiency at this pressure is more attributed to lower cycle efficiency. Figure 37 and Figure 38 illustrates the optimum results in T-s and T-Q plane.

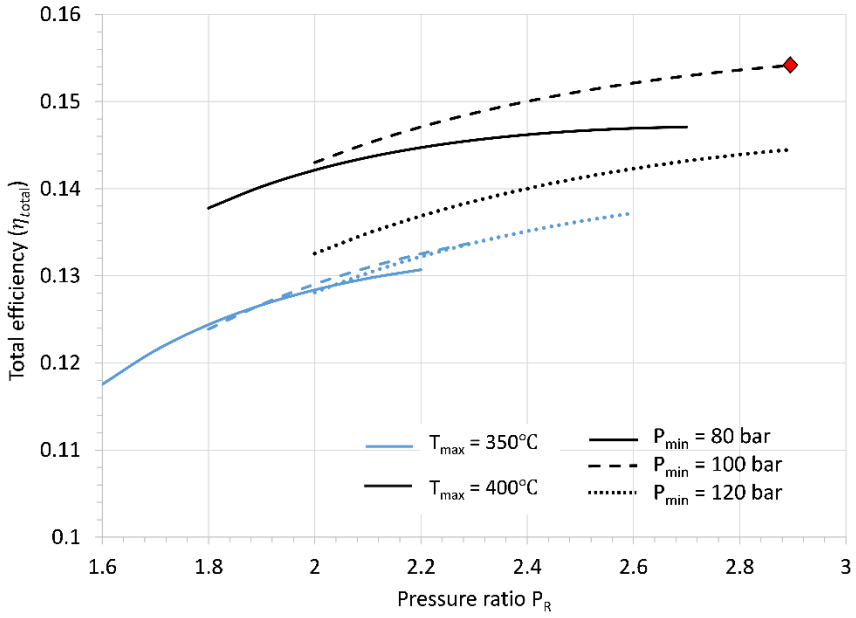

Figure 34: Effect of cycle minimum pressure and maximum temperature on total efficiency of SFDE cycle. Red mark shows the optimum performance point.

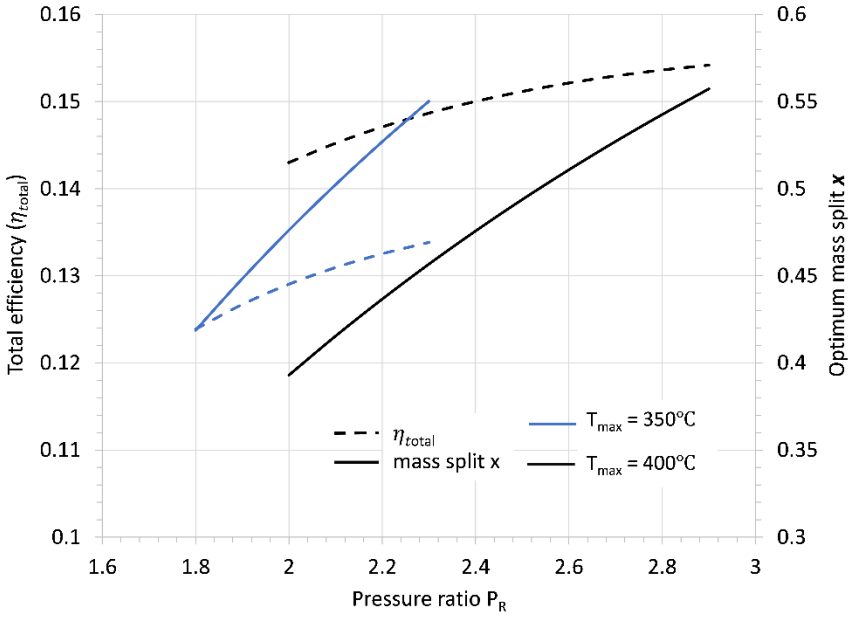

Figure 35: Effect of pressure ratio and cycle maximum temperature on total efficiency and optimum mass split x for single flow split dual expansion cycle.

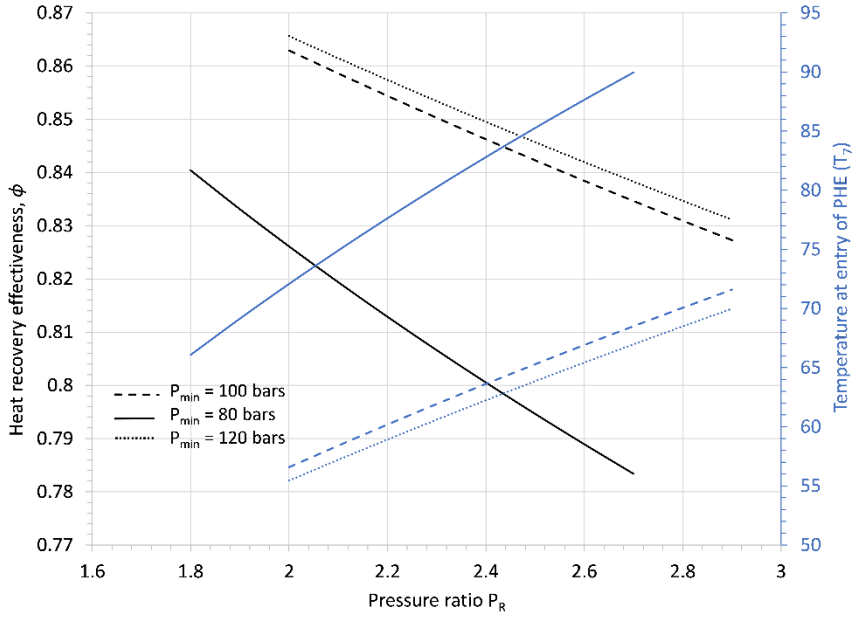

Figure 36: Trend of heat recovery effectiveness and PHE inlet temperature versus pressure ratio at different Pmin and Tmax=400℃ for SFDE cycle

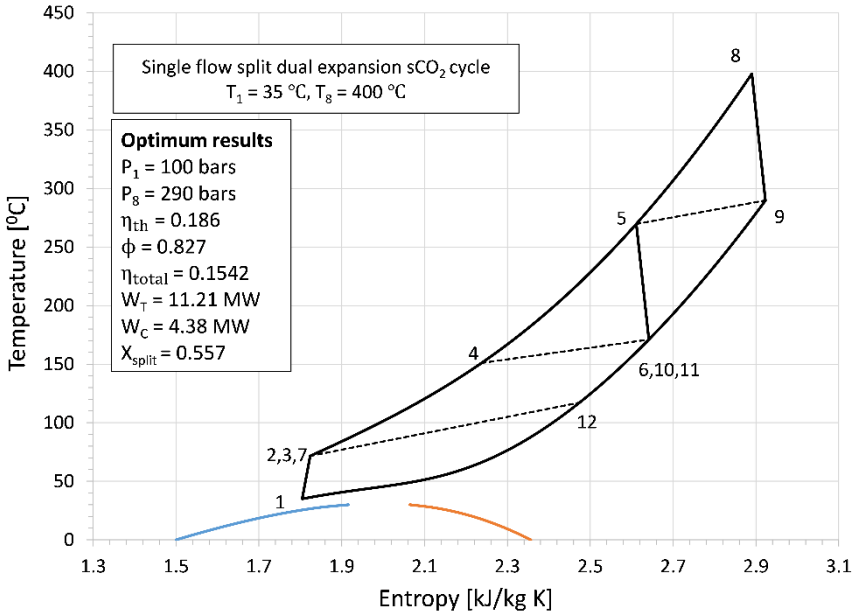

Figure 37: Optimum thermodynamic results of single flow split dual expansion sCO2 cycle in T-s plane.

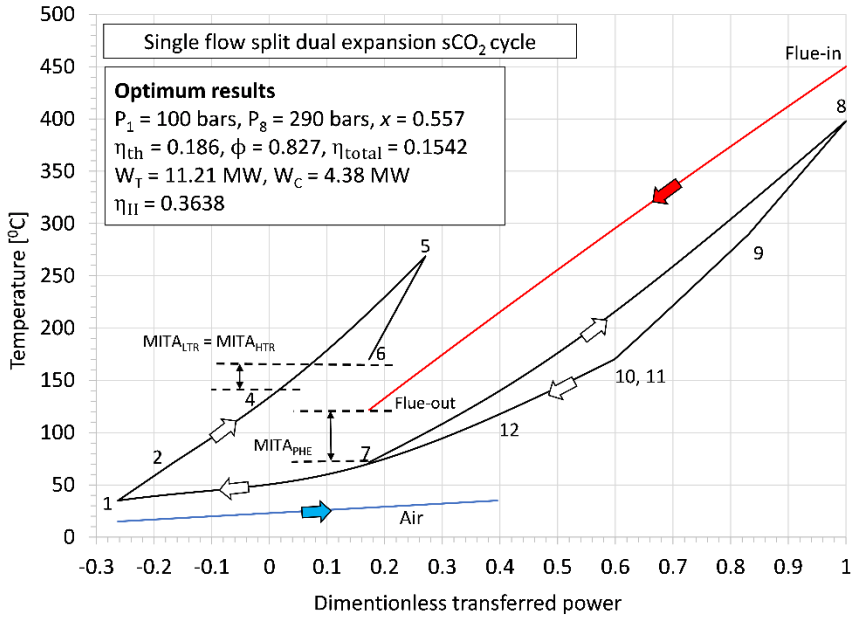

Figure 38: Thermodynamic process diagram at optimum point of single flow split dual expansion sCO_2 cycle on temperature-dimensionless heat transferred plane.

Comparison of optimum results of sCO_2 power cycles

The optimum results of the three sCO_2 power cycles are summarized in Table 30.

Simple recuperative cycle (SRC) shows the highest cycle efficiency but lowest total efficiency because of lowest heat recovery effectiveness. While, partial heating cycle and single flow split dual expansion shows higher heat recovery effectiveness and total efficiency than SRC besides not good in terms of cycle efficiency. Exergy efficiency of PHC and SFDE cycles are 3 percentage points and 5 percentage points higher than exergy efficiency of SRC respectively.

Figure 39 shows the bar chart representation of efficiency losses ($\frac{T_0 \sum_{i=1}^{N} \dot{S}_G}{\dot{Q}_{available}}$) in each process of the power cycles at optimum conditions. SRC shows higher total efficiency losses; the main source of which is associated to high temperature residual flue gases (stack losses). The losses corresponding to heat addition and heat rejection in PHC and SFDE are higher as compared to SRC and that's the main reason behind comparatively lower cycle efficiency of PHC and SFDE cycles. The higher losses in heat addition and heat rejection of PHC and SFDE cycles are correlated to greater log mean temperature differences LMTDs in PHE and radiator as given in Table 31.

Table 30: Summary of efficiency losses, total efficiency and exergy efficiency of three sCO_2 heat recovery power cycles at optimum conditions.

Power cycles	**SRC**	**PHC**	**SFDE**
T_{max} [°C]	400	350	400
P_R	4	3	2.9
$\dot{m}_{CO2}$[kg/s]	81.13	116.59	130.1
$\dot{m}_{air}$ [kg/s]	840.7	1111.7	1438.34
split fraction x	-	0.3	0.56
$\dot{Q}_{available}$ [kW]	44279.2	44279.2	44279.2
η_{carnot}	0.423	0.423	0.423
$W_{specific}$ [kJ/kg]	79.9	61.14	57.68
η_{cycle}	0.249	0.219	0.186
ϕ	0.532	0.669	0.827
η_{total}	0.132	0.146	0.154
$\dot{W}_{max}$ or $\dot{E}_{x,input}$ [kW]	18764.5	18764.5	18764.5
$\dot{E}_{x,losses}= T_0 \sum_{i=1}^{N} \dot{S}_G$ [kW]	12281.66	11636.03	11260.16
$\eta_{loss} = \frac{T_0 \sum_{i=1}^{N} \dot{S}_G}{\dot{Q}_{available}}$	0.277	0.262	0.254
$\dot{W}_{gross}$ [kW]	6482.87	7128.51	7504.38
$\dot{W}_{elec}$ [kW]	5873.74	6487.62	6826.44
η_{II}	0.313	0.345	0.363

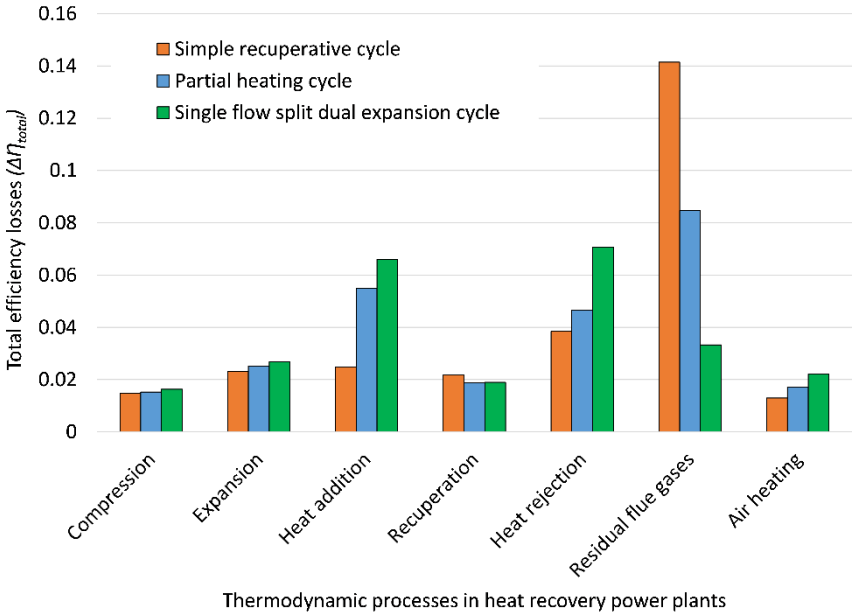

Figure 39: Total efficiency losses in power cycle processes for simple recuperative cycle (red bars), partial heating cycle (blue bars) and single flow split dual expansion cycle (green bars) at optimum conditions.

Table 31: Log mean temperature differences and UA of heat exchangers for three power cycles under study.

Heat exchangers	SRC	PHC	SFDE
		LMTD (℃)	
PHEs	55.11	74.14 (PHE1), 83.12 (PHE2)	68.42
Recuperator	37.37	23.52	22.42 (HTR), 31.85 (LTR)
Radiator	30.97	28.98	32.64
		UA (kW/K)	
PHEs	426.57	274.27 (PHE1), 111.98 (PHE2)	535.38
Recuperator	410.54	923.24	459.82(HTR) 282.35 (LTR)
Radiator	549.73	776.85	892.239
Total UA	**1386.84**	**2086.34**	**2169.79**

To gain better understanding about the size of the heat exchangers which play key role in size footprint of the power cycle, Table 31 also shows the heat transfer coefficient times area (UA) of heat exchangers. It is noticed that, the sum of UA of two PHEs in PHC is comparable to UA of single PHE in SRC. Whereas, recuperator and radiator of PHC shows higher UA values than of SRC owing to larger mass flow rates.

Although SFDE has higher total heat exchanger UA values, it is better at cooling flue gases and operating at lower cycle maximum pressures. Furthermore, the SFDE cycle is more complex, owing to the dual expansion process, which does not result in a significant increase in power output and exergy efficiency.

Overall, it is discovered that sCO_2 cycles with higher total efficiency or heat recovery effectiveness do not perform well in terms of cycle efficiency and the number of components in the cycle layout increases. The choice of an efficient and cost-effective cycle layout for converting available thermal power into electric power output necessitates a compromise solution. PHC appears to be a compromise solution based on the results of this section, as it has a higher total efficiency with a nominal power cycle size (lower complexity).

4.7 **Transcritical Organic Rankine cycles**

Selection and Properties of Organic fluids

In this section, organic Rankine cycles are adopted as power block for heat recovery. Total of 11 working fluids are considered and cycle efficiency and total efficiency are evaluated considering simple regenerative cycle configuration. The main thermodynamic properties and environmental properties of the working fluids are listed in Table 32 and Table 33 respectively.

Table 32: Main physical properties of dopants selected for CO_2 mixtures. Physical properties for Novec fluids are taken from [83].

Working fluid	T_{cr} *(°C)*	P_{cr} *(bars)*	*Boiling point (°C)*	*Molecular weight*	*Molecular Complexity* [84]	*Acentric factor* ω
CO_2	31.1	73.8	-78.4	44.1	-9.340	0.2236
R134a	101.1	40.5	-25.9	102.1	-2.429	0.3268
C_3H_8	96.6	42.4	-42.1	44.1	-2.409	0.152
C_4F_{10}	113.2	23.2	-1.3	238.1	13.37	0.366
NH_3	132.5	112.8	-33.4	17.1	-9.231	0.255
CH_3Cl	143.1	66.8	-24.2	66.8	-7.115	0.151
CH_2Cl_2	236.8	60.8	39.7	84.9	-4.793	0.198
CH_3OH	239.3	80.8	64.7	32.1	-10.63	0.557
$C_5F_{10}O$	146	21.4	26.5	266.1	17.145	0.429
$C_6F_{12}O$	168.6	18.6	49.1	316.1	28.165	0.471
HFO1234yf	94.7	33.8	-28.8	114.1	-1.017	0.282
HFO1234ze(E)	109.3	36.6	-18.2	114.1	0.046	0.323

Table 33: Safety and environmental impact characteristics of new refrigerants selected for CO_2 mixtures [85], [86].

Working fluid	*ODP* [87]	*GWP in 100 years* [87], [88]	*Flammability* [89]	*Health* [89]	*Instability* [89]
CO_2	0	1	0	2	0
R134a	0	1370	0	1	1
C_3H_8	0	≈20	4	2	0
C_4F_{10}	0	8600	0	1	0
NH_3	0	1	1	3-COR	0
CH_3Cl	0.02	13	4	2	0
CH_2Cl_2	n.a.	10	1	2	0
CH_3OH	n.a.	3	3	1	0
$C_5F_{10}O$	0	1	1	3	0
$C_6F_{12}O$	0	1	0	3	1
HFO1234yf	0	< 4.4	4	2	0
HFO1234ze(E)	0	6	n.a.	n.a.	n.a.

Critical temperature (T_{cr}) of a working fluid describes the type of the power cycle. When the critical temperature of a working fluid is close to the heat source temperature, the ideal cycle represents a subcritical ORC, whereas, when the critical temperature is lower than the heat source temperature, the ideal cycle represents a transcritical ORC with heat addition process above the critical temperature of the working fluid.

In subcritical and transcritical power cycles, critical pressure represents the highest and lowest benchmark for maximum cycle pressure, respectively.

Fluids with a critical temperature lower than the heat source temperature and moderate critical pressure values are preferred for transcritical heat recovery cycles.

Another useful information required are the molecular complexity and molecular weight of the working fluid. Molecular complexity is directly correlated with the molar specific heat of the working fluid. It is calculated by computing slope of saturated vapor curve (dew line) of the working fluid at reduced temperature of 0.7. Fluids with complex molecular structure (like Novec 649 and C_4F_{10}) possess higher values of molar specific heat and in turn positive values of the slope while on other hand fluids with simple molecular structure like (NH_3 and CH_2Cl_2) possess lower values of molar specific heat and lower the slope of the dew line (more negative or close to zero).

Secondly, the isentropic expansion exponent ($^{\gamma - 1}/_{\gamma}$) is lower for fluids with higher molecular complexity, as a result, the reduced cooling of fluid is achieved in the expansion process compared to fluids with lower molecular complexity at fixed expansion pressure ratio.

For the purpose of heat recovery, lower values of molecular complexity of organic fluid is desirable to obtain more cooling in expansion process and to reduce the duty of recuperator.

The high molecular weight of organic fluid implies reduction in isentropic enthalpy drop in expansion process which reduces the number of turbine stages and enhances mass flow rates for a fixed input of thermal power. However, due to the small enthalpy drop in the turbine, a large recuperator is required to cool the hot fluid from the turbine, which

increases the cycle size footprint. As a result, moderate molecular weight values are preferred.

Thermal stability, also known as thermo-chemical stability, is an important parameter to consider. At high temperatures, organic fluid should be thermally stable, at least at the turbine inlet temperature. The experimental determination of thermal stability temperature involves many considerations such as material of test container/vessel (e.g. stainless steel and Inconel), corrosion issue, nature of contaminants, reaction period, evaluation of decomposition level and safe temperature range for a working fluid.

The maximum operating temperatures of some working fluids determined by thermal stability tests with associated containing material are summarized in Table 34. The presence of different materials has a different effect on the thermal stability of the working fluid, as in the case of Dichloromethane (CH_2Cl_2), which decomposes at 350°C in stainless steel and at 450°C in Quartz. The same is true for contaminants; different contaminants can have an impact on the thermal stability temperature.

Table 34: Experimental thermal stability temperatures and corresponding material for some fluids.

Fluid	**Maximum operating temperature**	**Literature Reference and Containing material**
R134a	368℃	Stainless steel [90]
R1234yf	200-250 ℃	stainless steel (AISI-316) [91]
R1234ze(E)	180 ℃	stainless steel (SS316) [92]
CH_2Cl_2	350 ℃	stainless steel (AISI 430F) [93]
	450℃	Quartz [94]
$C_6F_{12}O$	475℃	Stainless steel [95]

The thermochemical stability of working fluid is strictly correlated to chemical stability of working fluid in an inert environment.

The amount of heat released/absorbed during the formation of a compound is given by the parameter standard enthalpy of formation (ΔH_f^0). It can be used as a relative indicator to assess the thermal stability of various working fluids. Fluids with more negative ΔH_f^0 values are generally more chemically stable than fluids with standard enthalpy of formation values close to zero or positive. The thermal decomposition of a working fluid occurs as a result of a series of chemical reactions, with the activation energy of the

reactions playing an important role. Thus, there are compounds that appear chemically unstable (with a positive value of (ΔH_f^0) but are chemically stable, such as Benzene. Despite this exception, the standard enthalpy of formation can provide a useful indication of the relative thermal stability of working fluids, as well as helps in the preliminary classification of working fluids.

Figure 40 depicts the standard enthalpy of formation per bond ($\Delta H_f^0/n_B$) of the selected working fluids in comparison with enthalpy of formation per bond of carbon dioxide which is a chemically stable working fluid. In the figure, all flammable compounds have standard enthalpy of formation close to zero.

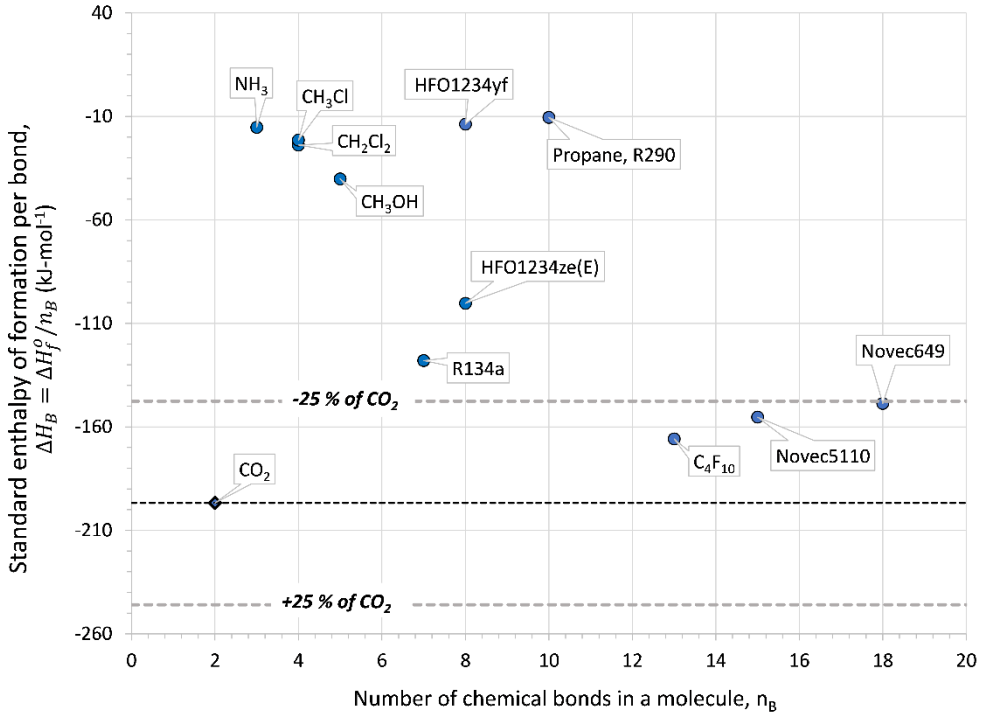

Figure 40: Standard enthalpy of formation of some working fluids for transcritical organic Rankine cycles versus number of bonds in an organic compound.

4.8 **Thermodynamic cycle results of transcritical ORCs**

The considered organic working fluids are analyzed in transcritical cycles to evaluate the thermodynamic performance at different condition and determine the optimum point for each working fluid based on total efficiency of the cycle. Cycle maximum temperature is assumed to be 350℃ as it is a reasonable thermal stability limit for all considered fluids except HFO1234ze(E) and HFO1234yf fluids (being thermally less stable these two fluids are excluded from the analysis).

Figure 41 shows cycle efficiency and Figure 42 shows total efficiency of transcritical cycles. For comparison, the curve of sCO_2 cycle is also shown in the Figures. As evident, the cycle efficiency and total efficiency of transcritical organic Rankine cycles are higher than sCO_2 cycle.

$C_5F_{10}O$ (Novec5110) and $C_6F_{12}O$ (Novec649) demonstrated the highest cycle efficiency, but the lowest heat recovery effectiveness and total efficiency. Figure 43 depicts the thermodynamic states of two cycles using Novec fluids in a temperature-dimensionless heat transferred plane. Because of the higher molecular complexities of Novec fluids, the expansion in the turbine results in less cooling of the fluid at the turbine exit, necessitating the use of recuperator with large heat duty and size. Consequently, the temperature rise on the cold side of the recuperator is also higher (T_4=224.5℃), resulting in a reduction in heat recovery effectiveness and total cycle efficiency.

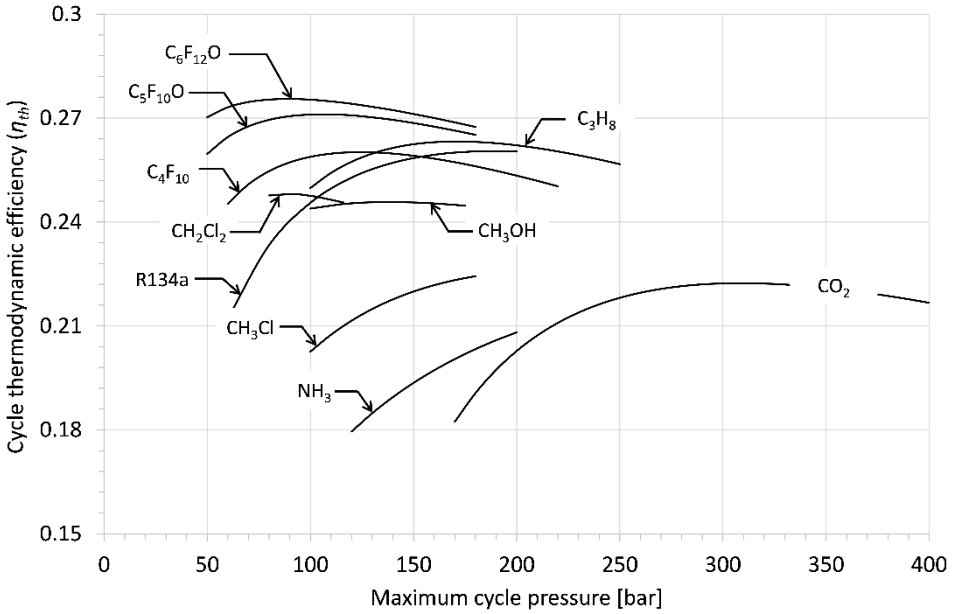

Figure 41: Cycle efficiency of transcritical organic Rankine cycles with different working fluids compared to sCO_2 cycle

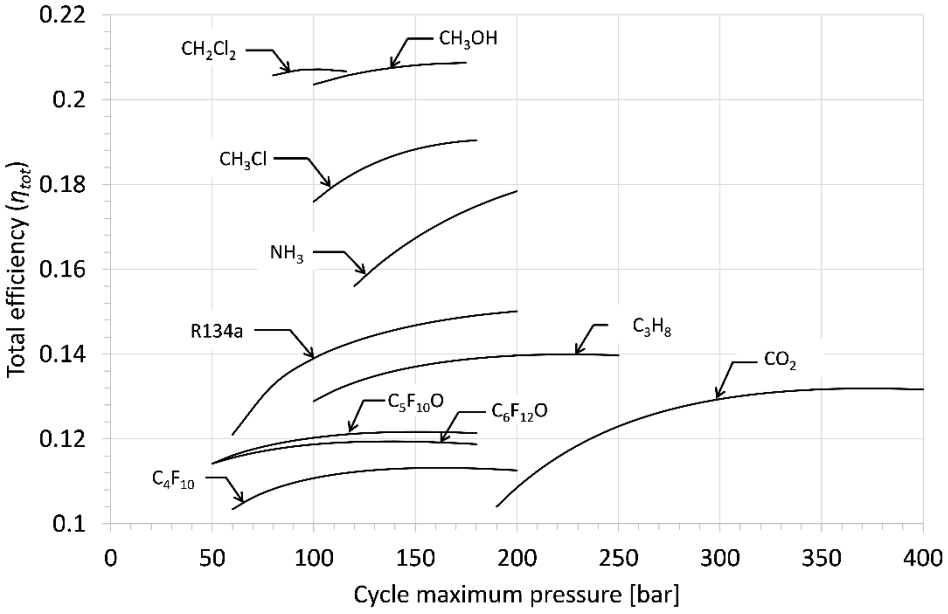

Figure 42: Total efficiency of transcritical organic Rankine cycles with different working fluids compared to sCO_2 cycle

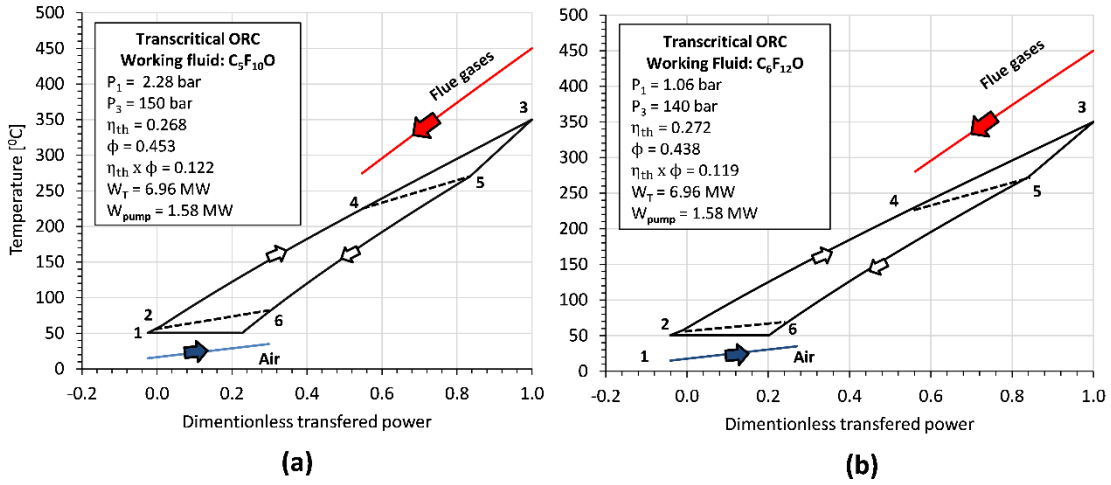

Figure 43: Cycle T-Q diagram of transcritical power cycle operating with (a) $C_5F_{10}O$ and (b) $C_6F_{12}O$ working fluids at optimum point.

Four fluids which demonstrate higher total efficiency are CH_3Cl, CH_2Cl_2, CH_3OH and NH_3. Figure 44 shows the optimum results of these four fluids in T-s plane. Due to lower molecular complexity of these fluids, the expansion in turbine is higher which results in lower temperature at exit of the turbine. The exit of turbine is in two-phase region for CH_3OH with vapor quality of 0.9. Thus, there is No need for a recuperator to cool the working fluid, resulting in smaller size of power cycle with higher heat recovery effectiveness than sCO_2 cycle.

The optimum results of working fluids which show higher cycle efficiency involving R134a, C_3H_8, C_4F_{10} and $C_6F_{12}O$ are shown on T-s plane in Figure 45. There is requirement of recuperator for these fluids owing to higher temperature available at the turbine exit.

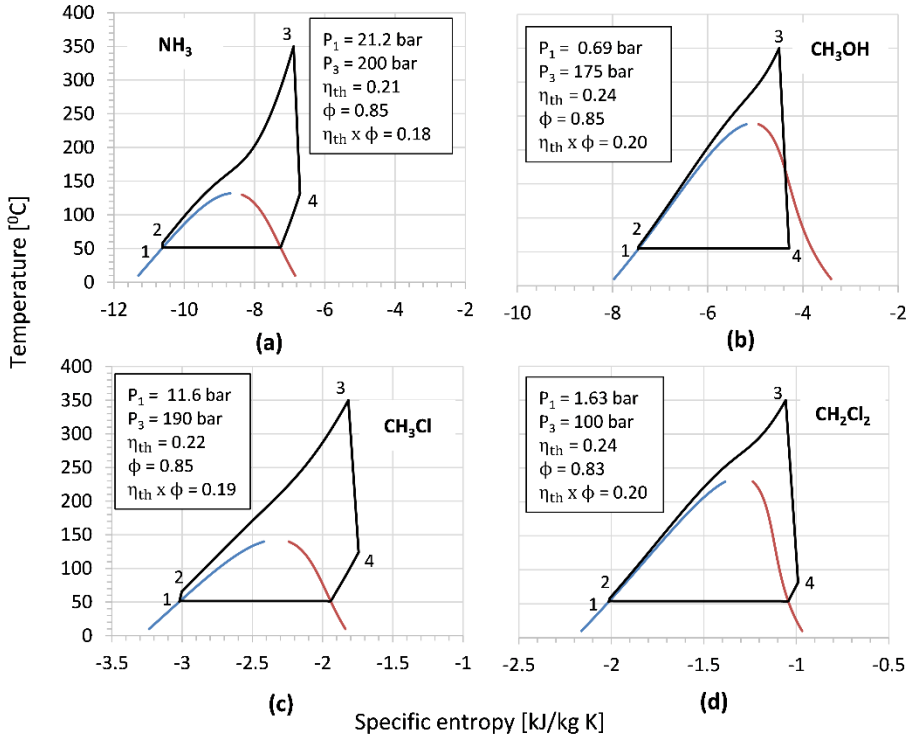

Figure 44: Cycle T-s diagram of transcritical organic Rankine cycles with (a) NH_3 (b) CH_3OH, (c) CH_3Cl and (d) CH_2Cl_2 working fluids at optimum conditions.

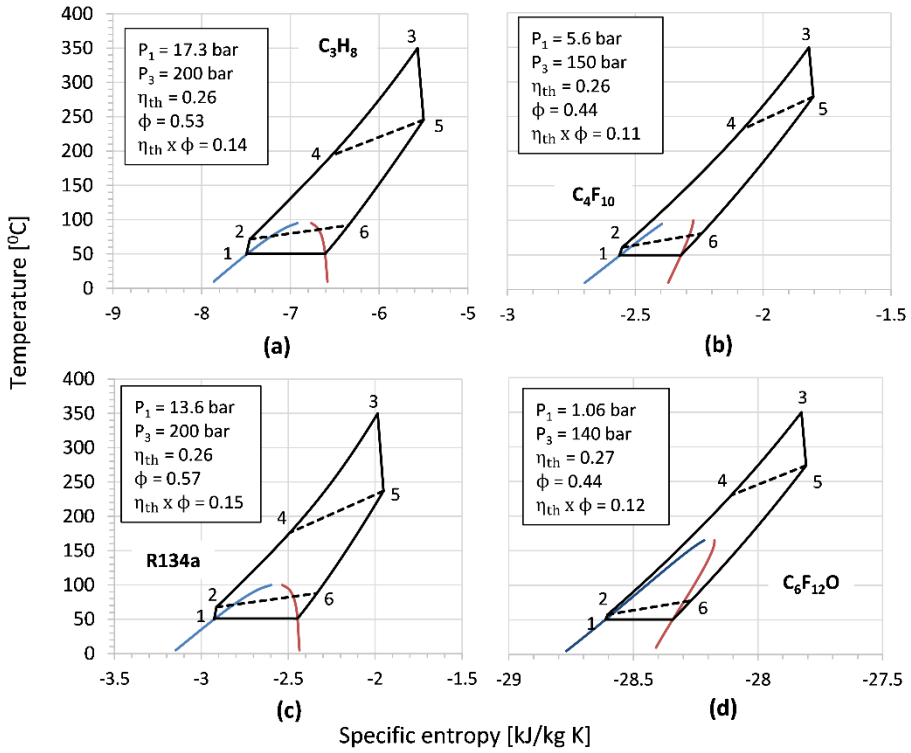

Figure 45: Cycle T-s diagram of transcritical organic Rankine cycles with (a) C_3H_8 (b) C_4F_{10} (c) R134a and (d) $C_6F_{12}O$ working fluids at optimum conditions.

Figure 46 compared the thermodynamic cycle states of two fluids with different properties in T-Q plane. Cycle with CH_2Cl_2 achieved more cooling of flue gases ($T_{flueout}$ = 119°C), larger power output and larger total efficiency without the requirement of a recuperator. Perfluorobutane (C_4F_{10}), on other hand, achieved less cooling of flue gases ($T_{flueout}$ = 282°C), smaller power output and lower total efficiency with the need of large recuperator to cool the working fluid before condenser.

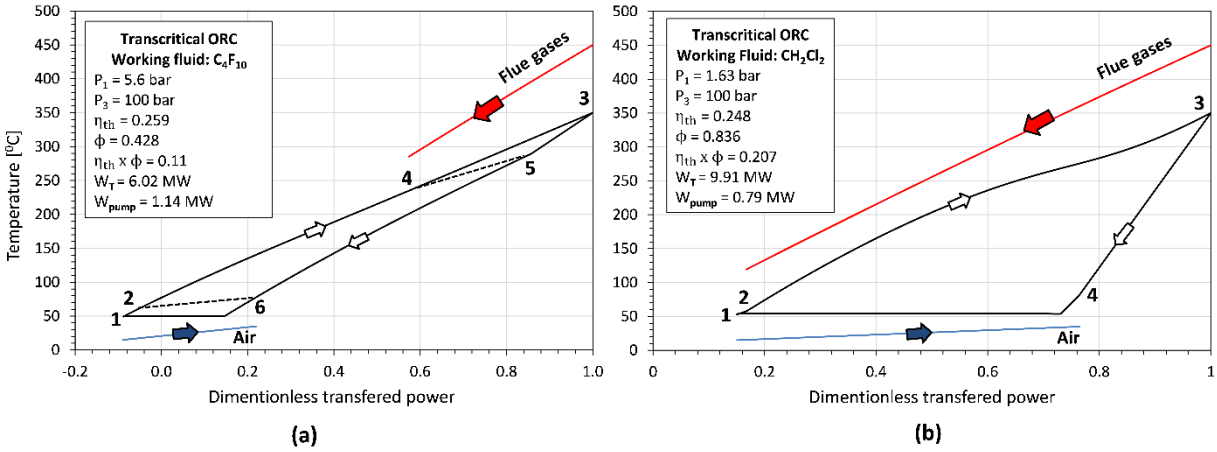

Figure 46: Cycle T-Q diagram of transcritical power cycle operating with (a) C_4F_{10} and (b) CH_2Cl_2 working fluids at optimum point.

Overall, it is discovered that transcritical organic Rankine cycles are preferable at a maximum temperature of 350℃ due to higher total efficiency in the range of 0.13 to 0.21 when compared to the sCO_2 simple recuperative cycle, which has a total efficiency of less than 0.13.

Novec fluids have good environmental properties and thermal stability at high temperatures, but they are not a good choice for heat recovery because of their lower total efficiency, which is due to their higher molecular complexity. Novec fluids, on the other hand, are a good choice in terms of cycle efficiency.

It should be noted that the fluids with the highest total efficiency are flammable, which necessitates the use of sophisticated sealing technology in the closed cycle to prevent working fluid leakage.

Considering cycle performance as well as working fluid thermal stability, R134a and C_3H_8 working fluids provide a good compromise for heat recovery power cycles. The following section designs novel CO_2 mixtures using R134a and C_3H_8 as dopants in CO_2 based mixtures. The aim is to enhance the total efficiency CO_2 power cycles utilizing the benefits of organic Rankine cycles while keeping the power cycle layout simpler in order to reduce the cycle cost.

4.9 CO_2 mixture based transcritical power cycles

As presented in section 4.6, the total efficiency achieved in case of single flow split dual expansion sCO_2 cycle is the maximum compared to partial heating sCO_2 cycle and simple recuperative sCO_2 cycle but with the expense of larger cycle components (cycle complexity) and comparatively larger size of recuperators (UA). Similar to this, Manente *et* al. [17] also came to the conclusion in their recent work that the complex cycle layout with dual flow split and dual expansion showed highest heat recovery total efficiency but with a trade-off of cycle complexity and larger specific investment cost.

To cope with this problem, one alternative way is to adopt CO_2-based binary mixture as working fluid for improving the total efficiency of sCO_2 cycles without increasing the complexity of the cycle layout.

Variation in the critical point of the working fluid can be achieved with the addition of dopant in CO_2 which results in new thermodynamic and thermophysical properties of the working fluid. As a result, novel mixtures can be designed based on the required properties and boundary conditions of the power cycle [96]. In heat recovery power cycles, for example, increasing the expansion pressure ratio is required to achieve higher power output. Furthermore, it is crucial to keep the maximum cycle pressure lower than sCO_2 cycle in order to reduce mechanical stresses caused by higher pressure. Therefore, a criterion is defined for the selection of dopant for CO_2 mixture in context of heat recovery.

The desired properties of dopant for CO_2 mixture are:

- Lower molecular complexity (value close to zero),
- Higher critical temperature than CO_2
- Lower critical pressure than CO_2
- Thermo-chemically stable at cycle maximum temperature (i.e. 350 ℃)
- Lower GWP and ODP

Two dopants: one hydrocarbon C_3H_8 and one refrigerant R134a are selected considering the lower molecular complexity, lower critical pressure, higher critical temperature and higher thermal stability of these compounds. However, higher flammability of C_3H_8 and higher GWP of R134a are two compromises in the selection. Both the dopants have zero ozone depletion potential (ODP). Other fluids can also be selected like toluene, benzene and some refrigerants as followed in some papers [2], [3]. Nonetheless, the goal here is to demonstrate the effect of two different classes of dopants on the properties of the CO_2

mixture and the thermodynamic performance of the power cycle. Another factor worth noting is the availability of experimental vapor-liquid equilibrium data, density and specific heat data of selected CO_2 mixtures. Experimental property data is helpful to optimize the binary parameters of equation of state (EoS) and to measure the accuracy of the EoS or other property model.

Thermodynamic properties of CO_2 based binary mixtures

In this chapter, thermodynamic properties of CO_2-R134a and CO_2-C_3H_8 are calculated at different mixture molar composition using standard Peng-Robinson Equation of state (PR-EoS) with van der Waals mixing rules.

As described in Chapter 2, one binary interaction parameter ($k_{1,2}$) is required in van der Waals mixing rules to compute the parameters of PR-EoS for a binary mixture. The $k_{1,2}$ is computed using regression analysis considering the experimental vapor-liquid equilibrium data of the mixtures and using the maximum likelihood function for curve fitting.

For CO_2-C_3H_8 mixture, value of $k_{1,2}$ is available in Aspen databank thus No regression is required to compute $k_{1,2}$. For CO_2-R134a mixture, experimental VLE data from literature are incorporated in regression to determine optimum value of $k_{1,2}$. All thermodynamic calculations using PR-EoS and regression analysis to fit experimental data for calculation of $k_{1,2}$ are carried out in Aspen Plus V11 software.

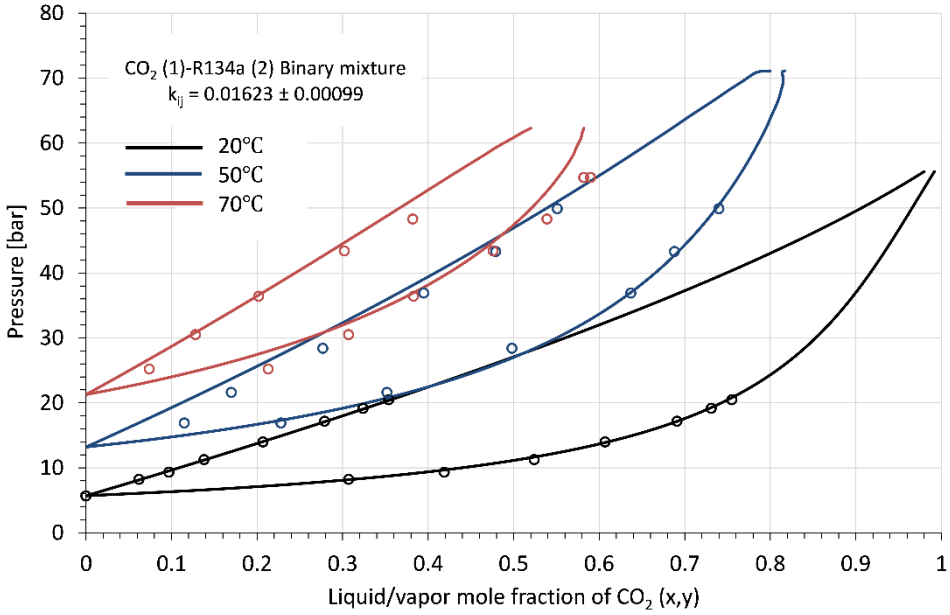

Figure 47: Vapor-liquid equilibrium (VLE) of CO_2-R134a mixture at different temperatures. Solid lines represent calculated VLE using PR-EoS with van der Waals mixing rules. Scatter point data show experimental VLE points from ref [97], [98]

Figure 47 shows the vapor-liquid equilibrium phase diagram of CO_2-R134a mixture at different temperatures. Experimental VLE data for this mixture are available in ref [97], ref [98] and ref [99] at temperatures from -20 to 80 ℃ and pressures up to 73 bar.
In regression analysis, experimental data of ref [99] is acquired to calculate the value of binary interaction parameter with minimum standard deviation. As evident from Figure 47**,** the calculated $k_{1,2}$ value brings good agreement between PR-EoS and experimental VLE data points.
The global phase diagram of CO_2-R134a and CO_2-C_3H_8 mixtures at different mixture molar composition are computed using PR-EoS and shown in Figure 48 and Figure 49 respectively. These phase diagrams show behavior of bubble line, dew line and vapor-liquid critical point of the CO_2 mixture at different mixture molar compositions.

The vertical dashed line shows the minimum cycle temperature (T_{min}) or pump inlet temperature require in a thermodynamic power cycle. The bubble point pressure (or pump inlet pressure) corresponding to T_{min} varies with the molar composition of the mixture; for example, for CO_2-R134a, the bubble pressure is 50 bar at z_1 = 0.7 (70% molar CO_2) and 25 bar at z_1=0.3 (30% molar CO_2). The addition of a dopant in CO_2 causes a transition from the supercritical cycle to the transcritical cycle, which has a lower condensation pressure. Figure 50 and Figure 51 depict the effect of increasing dopant composition on the temperature-specific entropy plot of the CO_2 mixtures. Temperature glide at constant pressure in the phase change region is also visible in CO_2 mixtures, which can affect the design of recuperator and condenser of the cycle since phase change process on hot side of recuperator and condenser occur at variable temperature rather than uniform temperature as in the case of pure fluids.

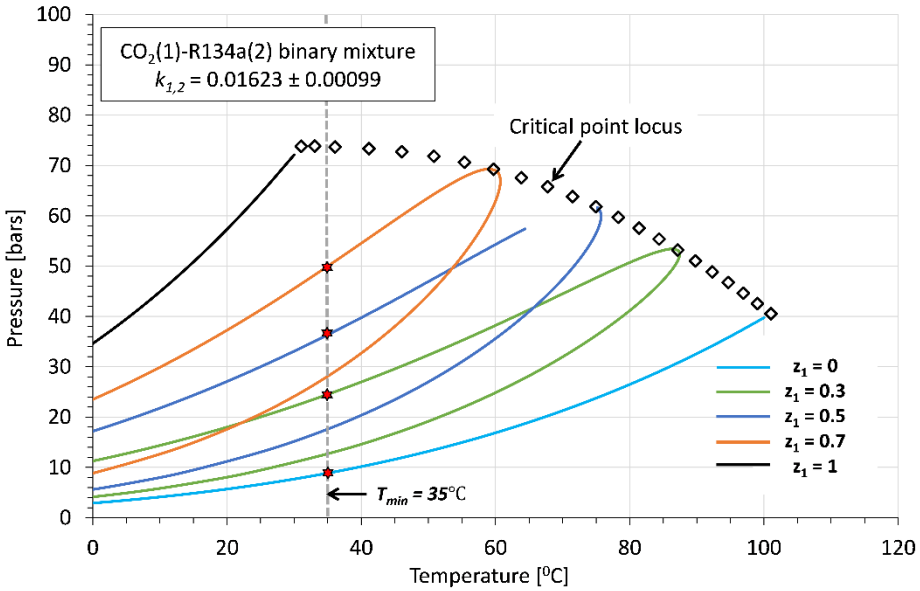

Figure 48: Global phase diagram of CO_2-R134a mixture showing bubble line, dew line and vapor liquid critical points at different mixture molar composition. Vapor liquid critical points are computed using the MATLAB program developed in Chapter 3.

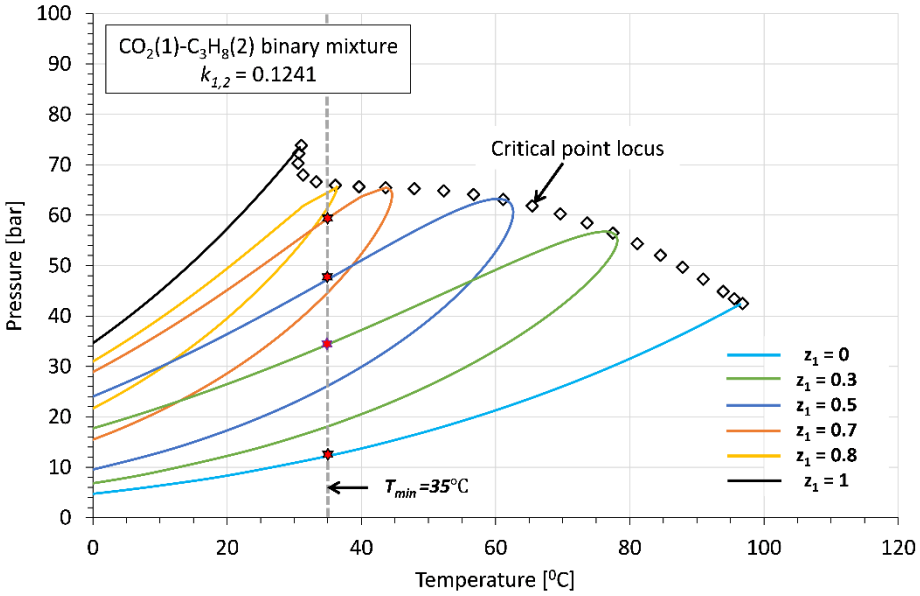

Figure 49: Global phase diagram of CO_2-C_3H_8 mixture showing bubble line, dew line and vapor liquid critical points at different mixture molar composition. Vapor liquid critical points are computed using the MATLAB program developed in Chapter 3.

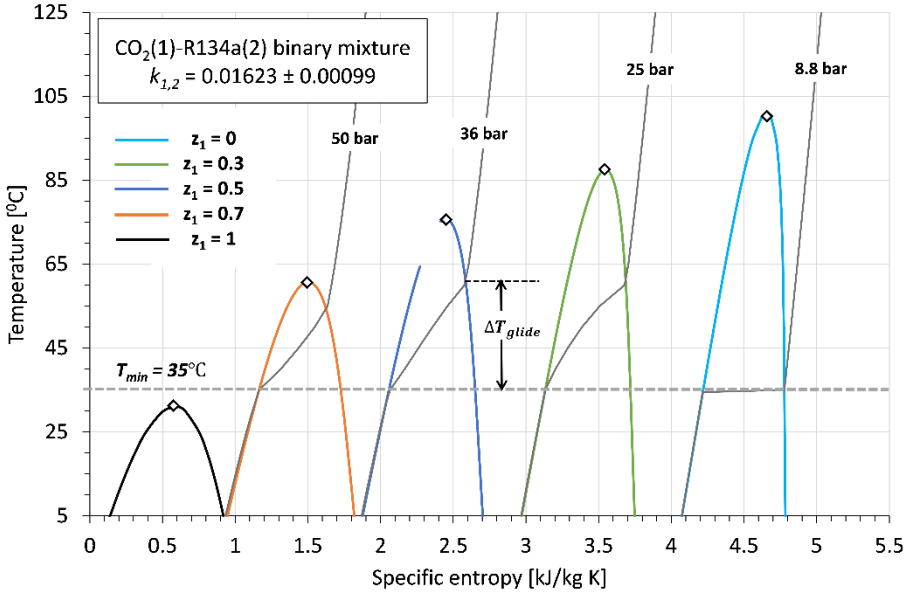

Figure 50: Bubble and dew lines of CO_2-R134a mixture for different mixture molar composition in temperature-entropy plane.

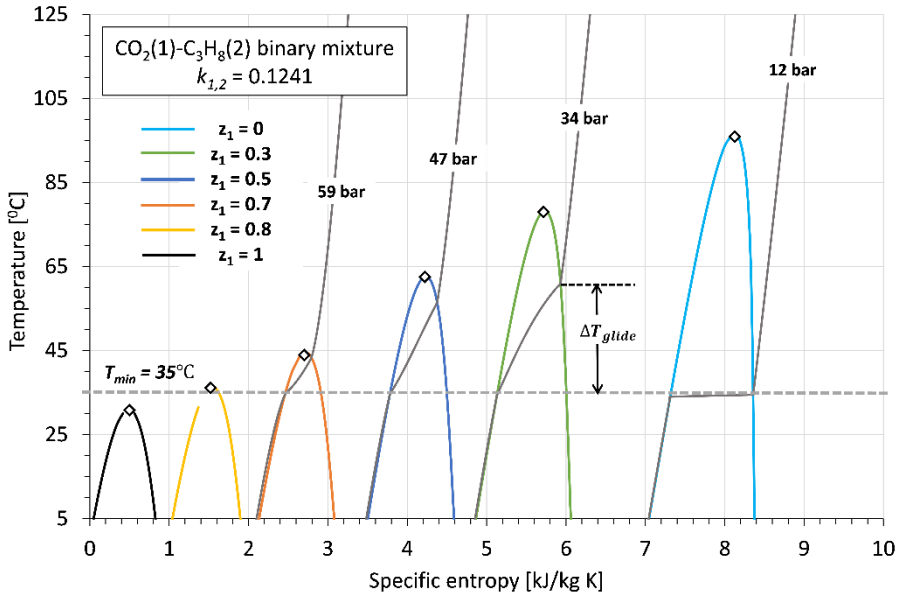

Figure 51: Bubble and dew lines of CO_2-C_3H_8 mixture for different mixture molar composition in temperature-entropy plane.

4.10 **Thermodynamic results of transcritical CO_2 mixtures power cycles**

Figure 52 and Figure 53 show the effect of different molar compositions of mixtures on cycle thermodynamic efficiency for CO_2-R134a and CO_2-C_3H_8 mixtures, respectively. In the Figures, z1 represents the molar composition of CO_2 in the mixture. Cycle efficiency improves as the molar composition of CO_2 in the mixture decreases for both mixtures. In comparison to the sCO_2 cycle, cycle efficiency of both CO_2-R134a and CO_2-C_3H_8 mixture are higher than sCO_2 simple recuperative cycle.

Regarding total efficiency, CO_2-R134a mixture shows higher values than sCO_2 cycle at all mixture compositions. At cycle maximum pressure of 200 bar, total efficiency of sCO_2 cycle (z1=1) is 0.108, for R134a transcritical cycle (z1=0) it is 0.15 and for CO_2-R134a mixture (z1=0.7) the value is 0.143. It means that adding 30% (molar composition) of R134a dopant to the CO_2 mixture results in a 3.5 percentage point rise in total efficiency compared to simple recuperative sCO_2 cycle. For CO_2-C_3H_8 mixture (z1=0.7), total efficiency of 0.134 is achieved at maximum pressure of 200 bar and this value is 2.6 percentage points higher than sCO_2 simple recuperative cycle.

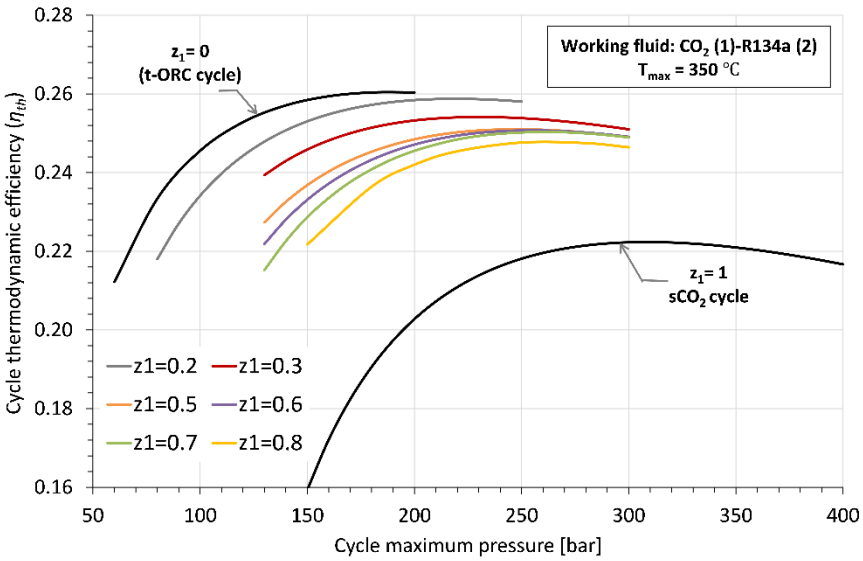

Figure 52: Cycle efficiency of CO2-R134a mixture at different molar compositions and cycle maximum pressure.

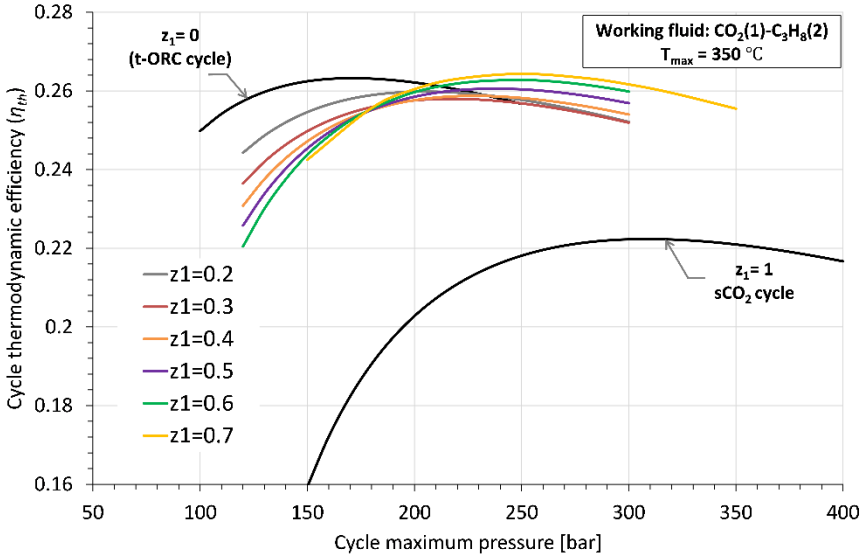

Figure 53: Cycle efficiency of CO_2-C_3H_8 mixture at different molar compositions and cycle maximum pressure.

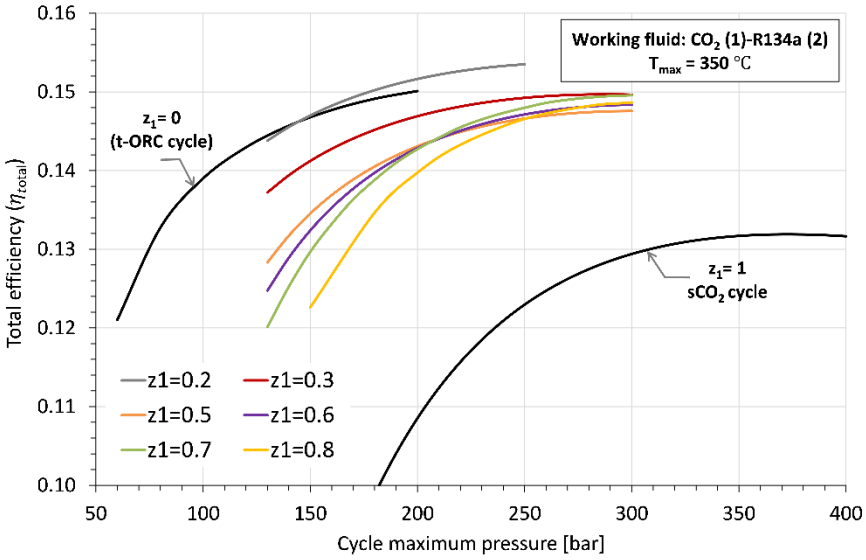

Figure 54: Total efficiency of CO2-R134a mixture at different molar compositions and cycle maximum pressure.

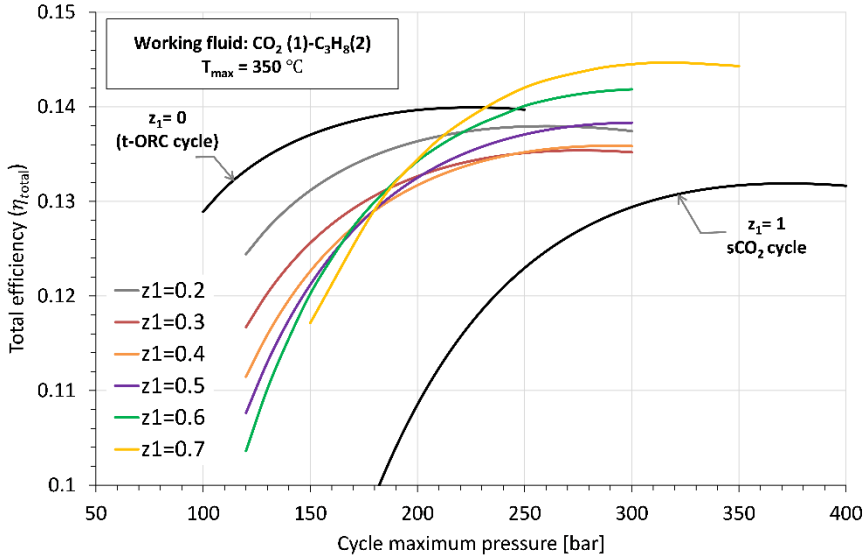

Figure 55: Total efficiency of CO_2-C_3H_8 mixture at different molar compositions and cycle maximum pressure.

For both selected CO_2 mixtures, mixture compositions with lower molar content of dopant are chosen because larger molar content of dopant can affect the cost of working fluid being R134a an expensive fluid with larger GWP.

In Figure 56, a comparison of total efficiency among CO_2 mixtures transcritical cycles and sCO_2 cycles is shown at three cycle maximum pressures (150 bar, 200 bar and 250 bar). Transcritical cycles show higher total efficiency and the gain in efficiency is appreciable at lower cycle maximum pressures.

For all cycles shown in Figure 56, total efficiency is improving with increase in cycle maximum pressure. However, one result quite notable is the higher total efficiency of

CO_2-R134a and CO_2-C_3H_8 mixtures compared to complex layout of sCO_2 cycle i.e. single flow split dual expansion cycle (SFDE). Therefore, gain in total efficiency at different P_{max} compared to SFDE cycle is computed in percentage points and reported in *Table 35*.

$$\Delta\eta_{total}(\%) = \left(\eta_{total,mixture} - \eta_{total,sCO2}\right) * 100$$

Transcritical cycles with CO_2 mixture show larger performance gain at lower cycle maximum pressures as well as with simple cycle configuration compared to complex configuration of the sCO_2 cycle.

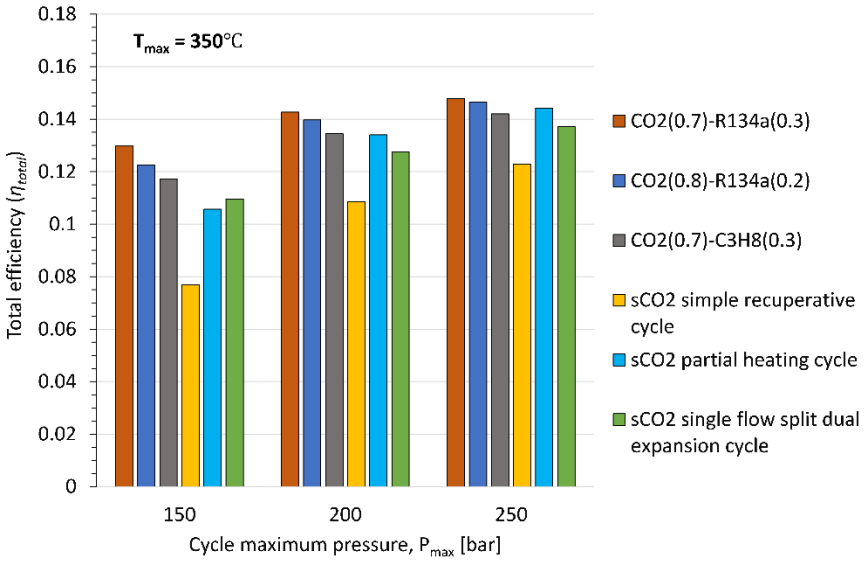

Figure 56: Comparison of total efficiency of supercritical CO_2 cycles and transcritical CO_2 mixture power cycles at cycle maximum temperature of 350℃

Table 35: Total efficiency gain in percentage points of three CO_2 mixtures transcritical cycles with reference to sCO_2 single flow split dual expansion cycle

Pmax [bar]	**CO_2 (0.7)-R134a (0.3)**	**CO_2 (0.8)-R134a (0.2)**	**CO_2 (0.7)-C_3H_8 (0.3)**
150	2.01%	1.3%	0.76%
200	1.52%	1.22%	0.69%
250	1.08%	0.94%	0.49%

Comparison between transcritical ORC with R134a and transcritical CO_2 (0.7)-R134a (0.3) mixture power cycle is illustrated in Figure 57 for cycle maximum pressure of 200 bar and cycle maximum temperature of 350°C. Total efficiency in case of the CO_2-R134a mixture is slightly lower than transcritical ORC (0.143 versus 0.15) however the expansion ratio (P_3/P_1) is half that of the ORC cycle. Similarly, in case of CO_2(0.7)-C_3H_8(0.3) mixture (as shown in Figure 58), total efficiency is close to total efficiency of transcritical ORC with C_3H_8 (0.134 versus 0.139) and the expansion ratio is less than half in the mixture power cycle.

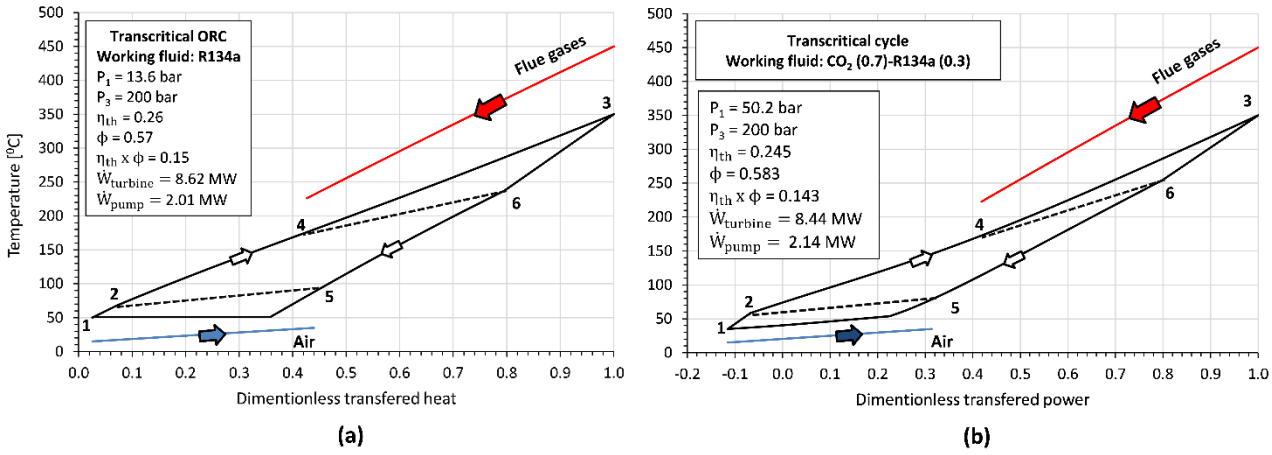

Figure 57: Thermodynamic cycle diagram in T-Q plane with (a) R134a and (b) CO_2(0.7)-R134a(0.3) mixture as working fluids.

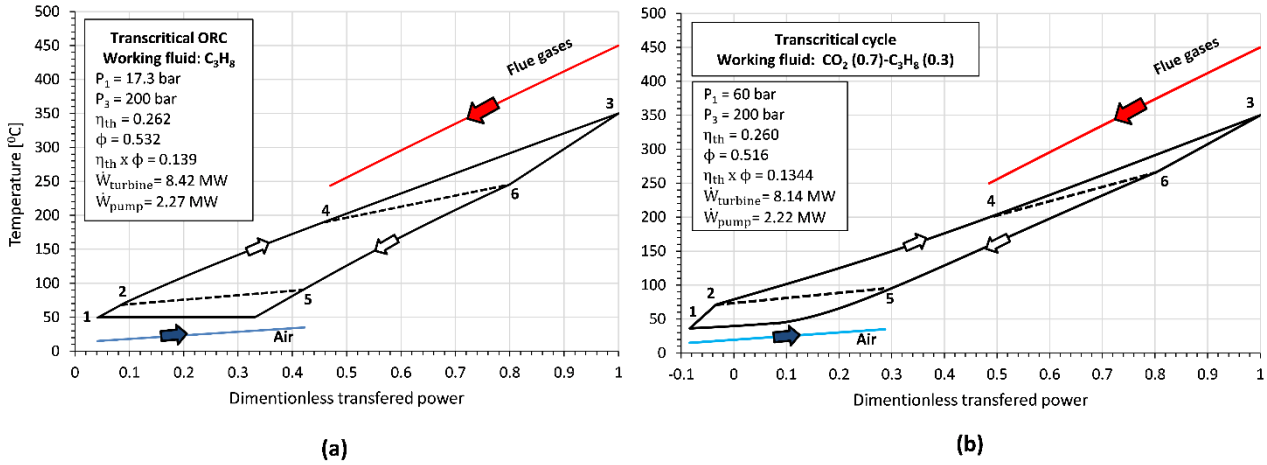

Figure 58: Thermodynamic cycle diagram in T-Q plane with (a) C_3H_8 and (b) CO_2 (0.7)-C_3H_8(0.3) mixture as working fluids.

Table 36 summarizes the thermodynamic results of all power cycles considered in this chapter for heat recovery at P_{max} of 200 bar and T_{max} of 350 °C. In addition to total

efficiency, which has already been discussed in previous sections of the chapter, important indicators related to turbine size and efficiency are also reported. These indicators include the isentropic enthalpy drop in the turbine (delta Hs), the volume flow ratio (VFR), and the size parameter (SP).

The definitions of these indicators are:

$$\Delta H_{isent} = h_{inlet} - h_{outlet,isent}$$

$$VFR = \frac{\dot{V}_{outlet}}{\dot{V}_{inlet}}$$

$$SP = \frac{\sqrt{\dot{V}_{outlet}}}{\Delta H_{isent}^{0.25}}$$

Table 36: Thermodynamic results of supercritical and transcritical power cycles at cycle maximum pressure of 200 bar and cycle maximum temperature of 350 ℃. The main assumption in cycle analysis are given in section 4.3.

Working fluid	Cycle configuration	P_{min} [bar]	η_{total}	$\dot{m}_{wf}$ [kg/s]	$\dot{m}_{air}$ [kg/s]	Turbine ΔH_{isen} [kJ/kg]	VFR	SP [m]
Supercritical CO_2	Simple recuperative	100	0.108	115	912.8	74.63	1.687	0.0645
	Partial heating	100	0.134	142	1223.7	74.63	1.687	0.0717
	Single flow split dual expansion	100	0.127	89.37	1578	74.63	1.687	0.0542
				81.22		55.01	1.641	0.0524
R134a	Simple	13.5	0.15	94.7	905.3	112.75	11.478	0.0896
C_3H_8	Simple	17.3	0.139	44.7	833.5	233.09	9.643	0.0694
CO_2 (0.7)-R134a (0.3)	Simple	50.2	0.143	102.4	937.1	102.02	3.145	0.0649
CO_2 (0.8)-R134a (0.2)	Simple	59.7	0.139	104.9	935.1	99.37	2.664	0.0641
CO_2 (0.7)-C_3H_8 (0.3)	Simple	60	0.134	80.32	809.5	125.5	2.718	0.0598

Isentropic enthalpy drop is a deciding factor for number of stages of a turbine; larger enthalpy drop implies increase in number of turbine stages. Volume flow ratio also gives information about density variations in turbine and larger values of this parameter means larger aerodynamic losses and requirement of multi-stage turbine to accommodate larger density variations. Size parameter of turbine is linked with VFR and ΔH_{isent}; it indicates the approximate size of a turbine and it is a quite useful parameter to compare sizes of turbine operating with different working fluids. Turbines with low SP are more likely to suffer with tip leakage losses therefore larger values of SP are desirable.

As evident from the Table 36, transcritical ORCs show highest values of ΔH_{isent} and VFR while supercritical CO_2 cycles show lower values. In case of CO_2 mixtures, the values of ΔH_{isent} and VFR lies in between the values of sCO_2 and ORC cycles. Overall, single stage axial turbine is enough for all considered cycles since the values of ΔH_{isent} and VFR are reasonable with corresponding isentropic power of turbines are around 9 MW (see Figure 57 and Figure 58).

However, values of SP are smaller which can pose challenges in turbine design to cater leakage losses. The mass flow rates of CO_2 mixture working fluid and mass flow rate of air in condenser are lower than sCO_2 cycles, which is beneficial in economic point of view since lower mass flow rates indicate lower size of cycle components.

4.11 **Preliminary single stage axial-turbine design**

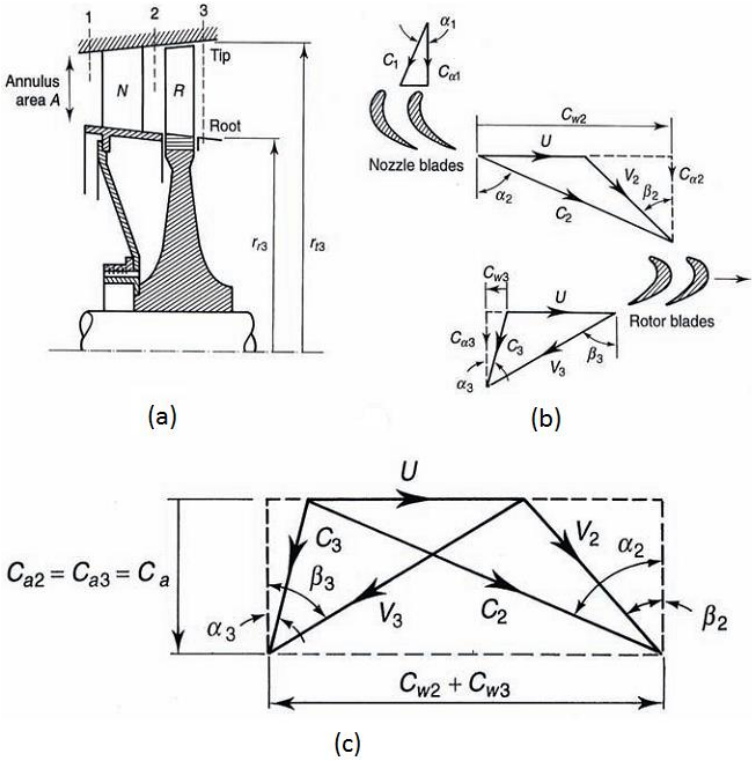

Figure 59: Single stage axial turbine: (a) cross sectional view, (b) top view with velocity diagram at each section, (c) Combined velocity diagram. Figure reproduced from Chapter 7 of ref [100]

A well-developed approach practiced in literature for estimation of turbine efficiency as well as geometry of blades is mean-line design method [101]. In this method, flow velocities are calculated at mean diameter of turbine rotor thus it shows average picture of variation in flow velocities along the annulus of the turbine. Mean line analysis is valid

on condition that blade heights are not very large (i.e. r_{tip}/r_{root} is lower). For larger heights, the blade speed (U) varies and it is then important to account for change in velocity triangles along the blade height.

The fundamental theory of an axial turbine is described in ref [100] . The reader is advised to start with this reference to gain a basic understanding of the operation of the nozzle and rotor in an axial turbine. Figure 59 depicts velocity triangles from the inlet of a nozzle to the outlet of a turbine rotor to help understand different velocities and gas angles in a single stage of an axial turbine.

Mean line design program of isentropic single stage-axial turbine

In this chapter, preliminary mean line design code of single stage axial turbine is also developed in MATLAB R2016b environment. Thermodynamic properties of the working fluid are obtained from Aspen plus v11 by linking with MATLAB using Active X automation server. The main goal is to investigate the geometry and efficiency of an axial turbine operating with pure CO_2 and CO_2-based binary mixture working fluids. The link between Aspen plus and MATLAB has the advantage of allowing different pure fluids and binary mixtures to be studied, as well as the effect of different property models on the turbine design.

The design code starts with input parameters from cycle thermodynamic analysis. Input parameters include turbine inlet total temperature (T_{01}), turbine inlet total pressure (P_{01}), outlet static pressure (P_3) and mass flowrate of working fluid ($\dot{m_{wf}}$). The assumptions in design procedure are:

1. Isentropic expansion ($\eta_{tt} = 1$); as preliminary phase in order to achieve approximate values of turbine geometry and performance parameters,
2. Constant axial flow velocity ($C_{a,1} = C_{a,2} = C_{a,3}$),
3. Repeating stage i.e. stage exit flow velocity is equal to inlet flow velocity i.e. $C_3 = C_1$,
4. Rotor inlet flow velocity angle ($\gamma_2 = 20°$).

Design objectives

The design code developed in this work, degree of reaction at mean diameter (Λ_m) and revolution speed (N) are two independent parameters which are varied to obtain feasible design with reasonable values of specific speed (N_s), specific diameter (D_s) and rotor

blade height to mean diameter ratio (h/D_m). As per Balje's chart [102], the optimal range of N_S and D_s should be 40-300 and 0.5 to 2 respectively (in English unit system) to obtain total to static efficiency (η_{t-s}) greater than 80%. The target value of h/D_m is decided to be close to 0.15.

Turbine design for CO_2-R134a mixture working fluid

In this section, the turbine design program described earlier is adopted to design single stage isentropic axial turbine operating with CO_2-R134a mixture [70% molar CO_2] as working fluid. Thermodynamic properties of the mixture are retrieved from Aspen plus v11 using an ActiveX automation server to link Aspen plus to a MATLAB program. Property model employed in Aspen plus is standard Peng-Robinson EoS with binary interaction parameter ($k_{1,2}$) value of 0.01623 (same value as determined in section 4.9).

The main question to address is: *Is there substantial difference in turbine geometry and efficiency when subject to CO_2-R134a mixture instead of sCO_2 working fluid?* To answer this question, turbine design is performed using input conditions derived from the cycle design point analysis presented earlier in section 4.10. These input conditions for CO_2-R134a mixture and sCO_2 are reported in Table 37.

Table 37: Input conditions for axial turbine design operating with CO2-R134a mixture and sCO2 as working fluid

Specification	***CO_2-R134a [70% molar CO_2]***	***sCO_2***
Inlet total pressure, P_{01} [bar]	200	200
Inlet total temperature, T_{01} [℃]	350	350
Outlet static pressure, P_3 [bar]	50.2	100
Mass flow rate, $\dot{m}$ [kg/s]	102.4	115
Rotor inlet flow angle, γ_2	20°	20°
Blade height to width ratio, h/W	3	3
Shaft speed, N [rpm]	15000 -50000	15000-50000
Degree of reaction at mean diameter, Λ_m	0.25-0.5	0.25-0.5
Blade loading coefficient, ψ_m	0.01-5	0.01-5

Design calculations are performed using fixed rotor inlet flow angle (i.e. angle of velocity C_2 at inlet of rotor) for both working fluids. Moreover, blade height to width ratio (h/W) is assumed to be 3; the purpose of this assumption is to determine stage length and stage flare angle.

Table 38: Mean line design results of isentropic single stage axial turbine

Turbine Parameter	***CO_2-R134a [70% molar CO_2]***	***CO_2***
Λ_m	0.5	0.5
N [rpm]	42,000	35,000
η_{ts}	0.937	0.937
η_{tt}	1	1
ψ_m	2	2
Power (MW)	9.79	8.049
$\phi_{f,m}$	0.364	0.363
N_s	121.17	117.23
D_s	0.894	0.924
D_m *[mm]*	140.6	144
h/D	0.150	0.159
h [mm]	21.1	23

In MATLAB program, the blade loading coefficient at mean diameter (ψ_m) is varied from 0.01 to 5 to maximize total to static efficiency for given revolution speed (N) and degree of reaction (Λ_m). Table 38 shows the results at mean diameter for degree of reaction of 0.5. In order to achieve blade height to mean diameter ratio of 0.15, revolution speed is varied. For CO_2-R134a mixture, revolution speed is higher, specific speed is higher and specific diameter is slightly lower than sCO_2 turbine. Overall, the axial turbine with mixture produces 1.7 MW higher power output together with slightly the same turbine rotor dimensions and the same degree of reaction. Table 39 shows the variation of absolute and relative velocities from the rotor root to the rotor tip calculated using free

vortex theory for both working fluids. Flow velocities are higher in the CO_2-R134a mixture, indicating a higher Mach number at the rotor outlet than in the sCO_2 turbine. Finally, the degree of reaction is positive at the blade root for both fluids, which is a requirement for a viable turbine rotor.

Table 39: Flow velocities at rotor inlet and outlet for isentropic single stage axial turbine with CO_2-R134a mixture and sCO_2 working fluids

Mean line		
Parameter	***CO_2-R134a [70% molar CO_2]***	***CO_2***
U_m *(m/s)*	309.29	264.57
C_a *(m/s)*	112.57	96.29
C_2 *(m/s)*	329.14	281.55
V_2 *(m/s)*	112.57	96.29
C_3 *(m/s)*	112.57	96.29
V_3 *(m/s)*	329.14	281.55
Root and Tip		
$C_{2,root}$ *(m/s)*	399.4	336.9
$C_{2,tip}$ *(m/s)*	282.66	243.9
$C_{3,root}$ *(m/s)*	112.57	96.29
$C_{3,tip}$ *(m/s)*	112.57	96.29
Λ_{root}	0.23	0.25
Λ_{tip}	0.65	0.64

4.12 **Characteristics of heat exchanger**

For turbulent flow in a long continuous tube of any cross-section (rectangular, circular etc.), heat transfer power per unit of surface area for one kelvin temperature change (or heat transfer coefficient 'h') can be expressed as [103],

$$h = \frac{\mu c}{Pr^{2/3}} \frac{1}{4r_h} Re\phi_h \qquad \text{Eq. 30}$$

Also, friction power per unit of surface area for a long continuous tube of any cross-section can be expressed as [103],

$$E = \frac{1}{2}\frac{\mu^3}{\rho^2}\left(\frac{1}{4r_h}\right)^3 Re^3 \phi_f \quad \text{Eq. 31}$$

Friction power represents power associated to pressure drop in a heat exchanger per unit of surface area. For a known value of ϕ_h and ϕ_f, hydraulic diameter, Reynolds number and fluid properties, Eq 30 and Eq 31 provides values of heat transfer power and friction power per unit of surface area.

It is quite useful to calculate ratio of h and E for different fluids and different type of surfaces (i.e. ϕ_h and ϕ_f). The higher value of the ratio demonstrates higher heat transfer power than friction power for a given heat exchange. On contrary, the lower values of the ratio (lower than 1) is undesirable since it represents a heat exchange with more expenditure of friction power than heat transfer power hence larger pumping work is required to overcome loss of power due to pressure drops.

The ratio h/E is derived from Eq 30, Eq 31 and using the definition of Reynolds number and Prandtl number. The final formulation is as shown in Eq.32,

$$\frac{h}{E} = \frac{c^{1/3}k^{2/3}}{\mu^{2/3}}\frac{\phi_h}{\phi_f} 2A^2 \left(\frac{\rho}{\dot{m}}\right)^2 \quad \text{Eq. 32}$$

For same type of surfaces, cross-sectional area and the mass flow rate, the ratio becomes only function of properties of fluid in a heat exchanger as shown below.

$$\frac{h}{E} \propto \frac{c^{1/3}k^{2/3}}{\mu^{2/3}}(\rho)^2 \quad \text{Eq. 33}$$

In this work, this ratio is selected as a rationale to compare heat transfer characteristics of two working fluids i.e. pure CO_2 and CO_2-R134a mixture. The purpose is to study effect of change in working fluid in a heat exchanger with same type of surfaces, cross-sectional area and fluid mass flow rate on the ratio h/E for large range of temperature and pressures. Therefore, h/E ratio for pure CO_2 and CO_2-R134a mixture are calculated using Eq 33 for temperatures higher than dew point temperatures and considering four pressure values (typical recuperator in carbon dioxide power cycle operate at these pressure values as discussed in previous chapters). Thermal conductivity and viscosity are computed using Chung-Lee starling method while specific heat and density are calculated using standard Peng-Robinson EoS with the same value of binary interaction parameter for CO_2-R134a

mixture as determined in the section 4.9. Similarly, the same property method applied to pure CO_2. Aspen plus V10 is used to calculate density, viscosity and thermal conductivity.

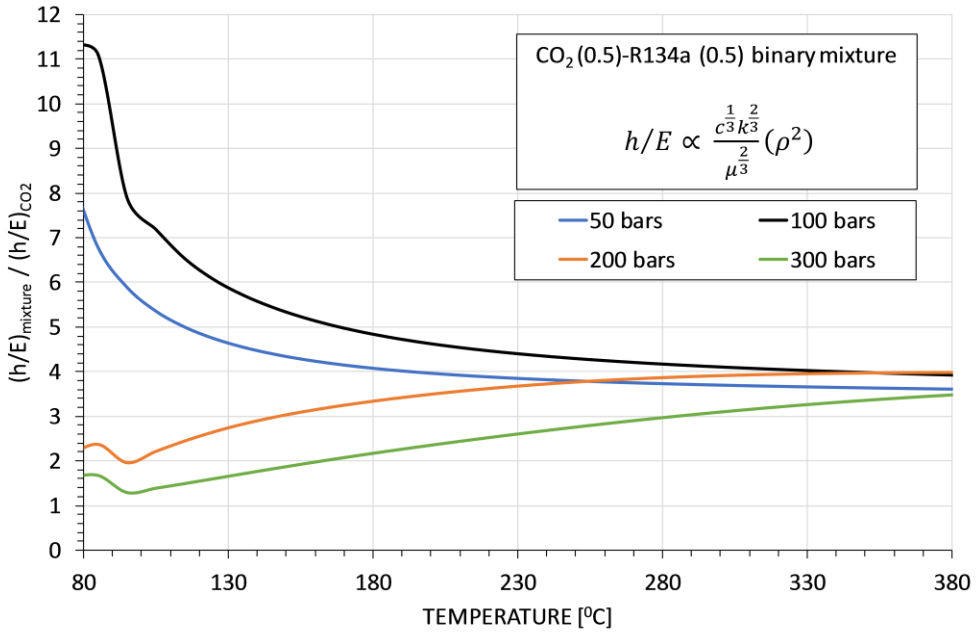

Figure 60: h/E ratio of CO_2 [0.5]-R134a [0.5] mixture and pure CO_2 for varying temperature and pressure

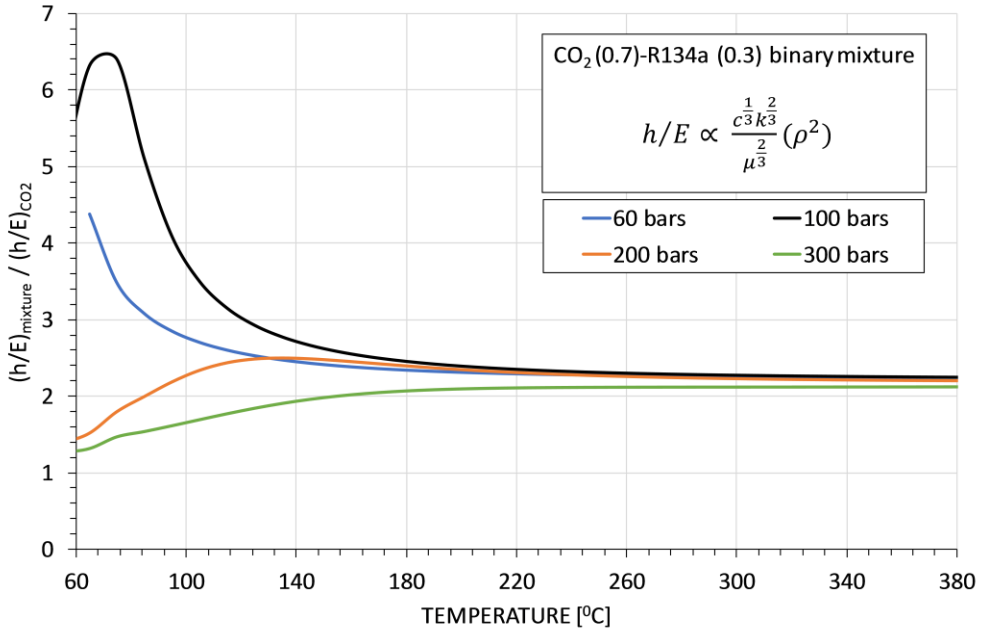

Figure 61: h/E ratio of CO_2 [0.7]-R134a [0.3] mixture and pure CO_2 for varying temperature and pressure

Figure 60 and Figure 61 illustrates the effect of different temperature and pressure isobars on the ratio between h/E for CO_2-R134a mixture and h/E for pure CO_2 i.e. $\left(h/E\right)_{CO2-R134a} \Big/ \left(h/E\right)_{CO2}$ for the two mixture compositions.

Following points are evident from the Figure 60 and Figure 61:

- At lower temperatures (close to dew point temperature), the ratio h/E in case of mixture is higher than pure CO_2; around 10 to 11 times higher at pressure of 100 bar for 50% CO_2-R134a mixture.
- For higher temperatures, the trend at each pressure converge to value of around 4 in case of 50% molar CO_2-R134a mixture and 2 in case of 70% molar CO_2-R134a mixture. In other words, h/E is four times higher than pure CO_2 when 50% molar CO_2-R134a mixture is adopted as working fluid assuming same heat transfer surfaces and mass flowrate. In similar way, h/E ratio is 2 times higher than pure CO_2 when 70% molar CO_2-R134a mixture is adopted as working fluid under the same assumption.

These results are very useful for heat exchanger design because it shows that CO_2-R134a mixture has a better heat transfer characteristic than CO_2. In a heat exchanger, a CO_2-R134a mixture can transfer heat with less friction power (or smaller pressure drops) than CO_2 if the same heat transfer surfaces, cross sectional area and fluid mass flow rate is considered.

Note: *The comparison of h/E is performed for the same mass flow rate and pressures for CO_2-R134a and pure CO_2, but this is not the actual scenario because mass flow rate and pressures differ for both working fluids in a thermodynamic power cycle and can result in slightly different results. However, the comparison presented is still useful in understanding the advantages of using the CO2-R134a mixture working fluid.*

Chapter 5: Advanced Carbon dioxide power cycles for high temperature heat sources: Analysis of supercritical CO_2 recompression cycle and proposal of CO_2 mixture based transcritical power cycles

5.1 Introduction

Among the high temperature heat sources, concentrated solar power technology is a clean energy source which can reach maximum temperature of 565℃ and even higher temperature of 720℃ using molten salts and advanced ternary salts respectively as thermal energy storage medium. Steam Rankine cycle are employed as power block in present available CSP power plants. A state-of-the-art steam cycle with one reheat and multiple feed water heaters is capable to achieve cycle efficiency of 47% when cycle maximum temperature is 550 ℃ and ambient temperature is 15℃.

In recent past, supercritical carbon dioxide (sCO_2) power cycle are introduced as power block in CSP plant. The key benefits of sCO_2 cycle over steam Rankine technology are simpler and compact cycle layout, comparatively higher cycle efficiency at medium to high cycle maximum temperatures i.e. 550 to 700 ℃ and acceptance to operate at higher maximum temperature owing to higher thermal stability of CO_2.

Nevertheless, as elaborated in Chapter 1, the cycle efficiency of supercritical carbon dioxide power cycle is sensitive to rise in compressor inlet temperature. To fully exploit the benefits of real gas effects near critical point (that are lower compressibility factor and lower compression work), it is essential to keep compressor inlet temperature close to critical point of CO_2 (i.e. 31 ℃) but this require cold medium like water to cool CO_2 near to its critical point temperature. In concentrated solar power (CSP) plants, usually installed in arid areas with higher ambient air temperature necessitate the use of dry coolers in spite of cooling towers.

This chapter considers supercritical CO_2 cycle for power production from high temperature heat sources (for instance: CSP). The idea is to study the effect of variation in compressor inlet temperature, compressor inlet pressure, cycle maximum pressure and cycle maximum temperature on cycle efficiency and to find the operating conditions to

obtain maximum cycle efficiency. The main aim is to study the effect of rise in compressor inlet temperature (due to rise in ambient temperature) on the cycle efficiency of recompression sCO_2 cycle.

To enhance the thermodynamic performance of sCO_2 cycle at high compressor inlet temperature, this chapter proposed five CO_2-based binary mixtures as working fluids. Effect of variation in mixture composition on cycle efficiency is investigated and comparison with recompression sCO_2 cycle and simple recuperative sCO_2 cycle is performed. In addition, the impact of change in working fluid on cycle specific work, temperature difference in primary heat exchanger and relative size of recuperators are also studied to understand the thermodynamic potential of CO_2-based binary mixtures.

The main objectives of this chapter are:

- Study of cycle efficiency of recompression sCO_2 power cycle with rise in compressor inlet temperature, cycle maximum temperature, cycle minimum pressure and cycle maximum pressure.
- To select appropriate additives for CO_2 based binary mixtures based on critical point properties, environmental characteristics, thermal stability and required compressor inlet temperature.
- Selection and optimization of thermodynamic property model to calculate thermodynamic properties of CO_2 based binary mixtures
- Apply CO_2 based binary mixtures as working fluids in power cycles and compare thermodynamic performance with simple recuperative sCO_2 cycle and recompression sCO_2 cycle.

5.2 Reference supercritical carbon dioxide (sCO_2) power cycle

This section analyzes thermodynamic cycle efficiency of recompression sCO_2 power cycle. Recompression sCO_2 cycle configuration is state-of-the-art cycle in the field of high temperature carbon dioxide cycles. At first this cycle was proposed by Angelino [9] for CO_2 condensing cycles. Angelino proposed recompression cycle configuration with the purpose to reduce irreversibility in recuperators which occurs due to large difference of heat capacities between cold and hot streams. Later on, different research works found recompression cycle as the one which shows higher efficiency in high temperature applications like nuclear power plants and solar power tower plants.

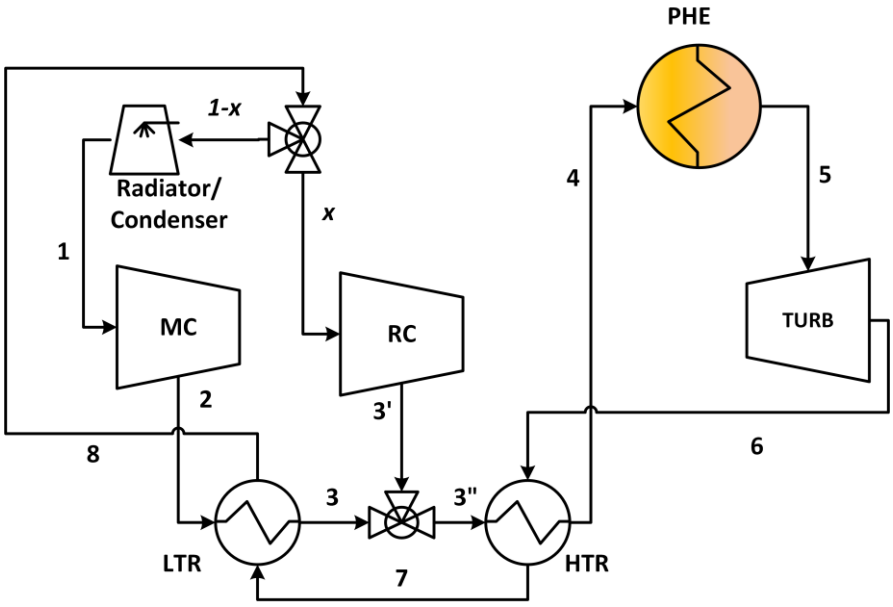

Figure 62: Plant layout of supercritical carbon dioxide (sCO_2) recompression power cycle

In recompression configuration (see Figure 62), there is a mass split after low temperature recuperators (LTR). After mass split, one stream known as 'x' goes to recompressor and other stream '1-x' goes to condenser. The stream from condenser is compressed in main compressor and then heated in LTR to temperature T_3. On other side, stream from recompressor also heated to temperature T_3. Two stream mixed together in mixer and gain heat from high temperature recuperators (HTR). After that, primary heat exchanger (PHE) raised the temperature of stream to maximum cycle temperature (T_{max}). This is followed by expansion in turbine and cooling of hot stream in HTR and LTR. The distinctive feature of this cycle is difference of mass flow through LTR, which balances heat capacities between high pressure (cold stream) and low pressure (hot stream) sides of LTR. In this way, more heat recuperation and smaller temperature differences are achieved in LTR with improvement in cycle efficiency. However, smaller temperature differences in recuperators possibly leads to larger heat transfer area and investment cost.

The required cycle assumptions and boundary conditions for design point analysis are shown in Table 40. Recuperators (LTR and HTR) are modeled using minimum internal temperature difference approach (MITA), the value of which is assigned as 5℃. Turbine and compressors are modeled using isentropic efficiencies; the values of efficiencies are aligned with recently available turbomachinery.

Cycle thermodynamic analysis is carried out at different turbine inlet pressure (P_{max}), turbine inlet temperatures (T_{max}), main compressor inlet pressures (P_{min}) and main compressor inlet temperature (T_{min}), the ranges of these variables are also given in Table 40. The main purpose is to study the sensitivity of cycle efficiency with change in cycle parameters and find the optimum efficiency point. Mass flow rate of CO_2 is considered to be 1 to develop a base design which can be translated to design with large power sizes.

Table 40: Operating parameters and common assumptions for design point analysis

Parameter	Value
P_{min} or P_1(bars)	74 to 120
P_{max} (bars)	150 to 400
T_{max} (℃)	500 to 700
T_{min} (℃)	$1.03T_{cr}$ to $1.1T_{cr}$
$\dot{m}_{CO_2}$ (kg/s)	1
$MITA_{recup}$ (℃)	5
$\eta_{isent,comp}/\eta_{mech,comp}$	0.89/ 0.99 [104]
$\eta_{isent,turb}/\eta_{mech,turb}$	0.93/0.99 [104]

Validation of thermodynamic model is also performed to ensure the accuracy of cycle model. Thermodynamic cycle efficiency is compared considering the operating parameters and assumptions of the literature. Table 41 shows the comparison of calculated and literature values. The difference of values between literature and calculated are due to pressure drops considered in literature works. For the sake of simplicity and to study the benchmark efficiency, pressure drops in cycle components are neglected in the thermodynamic model of this chapter.

Table 41: Comparison of thermodynamic efficiency of sCO_2 recompression cycle with literature values.

Operating conditions Binotti *et* al [105]	**Cycle thermodynamic efficiency (η_{th})**	
	Calculated value (No pressure drops)	**Literature value Binotti *et* al** [105] **(With pressure drops)**
T_{max} = 700 ℃, T_{min} = 51 ℃ P_{min} = 100 bars, P_{max} = 250 bars η_c= 89%, η_{turb}= 93% $MITA_R$ = 5℃	50.41%	48%

Effect of compressor inlet pressure (P_{min})

Figure 63 shows the trend of cycle thermodynamic efficiency (η_{th}) of the recompression sCO_2 cycle at different P_{min} and P_{max} with T_{max} = 700℃. Cycle efficiency is increasing with rise in P_{min} from 74 bars (P_{cr} of CO_2) to 120 bars. Since T_{min} of 50℃ is higher than critical temperature of CO_2, the cycle efficiency is lower even though P_{min} is close to critical temperature of CO_2. This is because of increase in compressibility factor of CO_2 with increase in T_{min}; this reason is elaborated in later sections. Moreover, it is quite notable that drop in efficiency is less sensitive to increase in P_{max} for P_{min} = 100 bars and 120 bars. The optimum cycle efficiency (η_{th}= 50.8%) is reached at P_{max} = 250 bars and P_{min} =100 bars. The maximum efficiency point (η_{th}= 51.2%) at P_{min} = 120 bars is not practically feasible to consider since it is occurring at rather higher P_{max} of 350 bars.

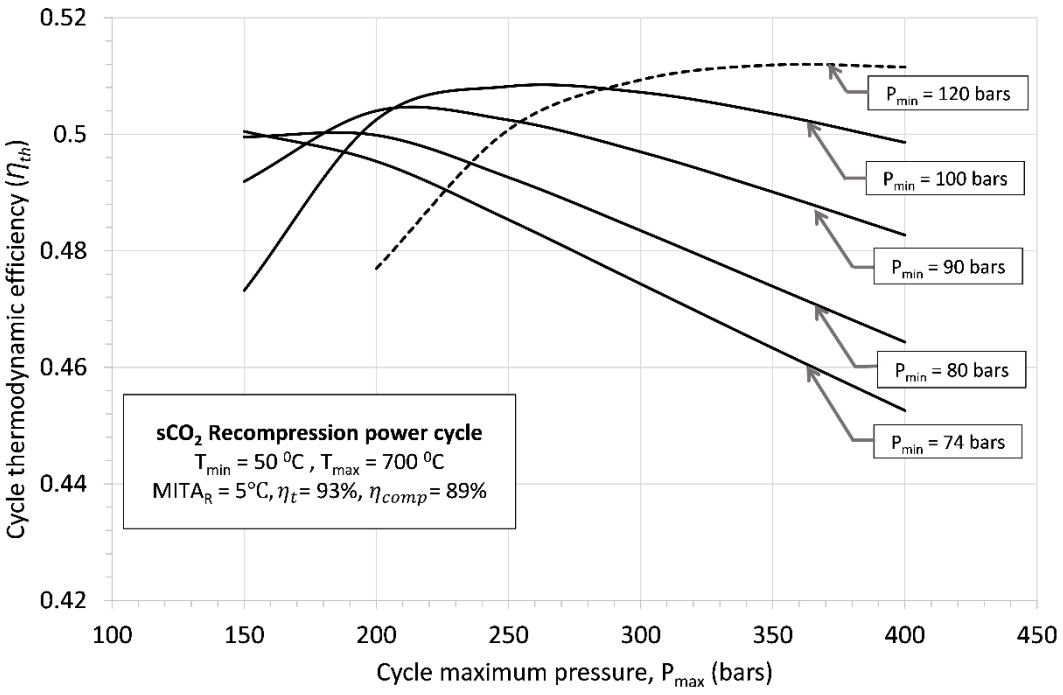

Figure 63: Influence of turbine inlet pressure (P_{max}) and compressor inlet pressure (P_{min}) on cycle thermodynamic efficiency

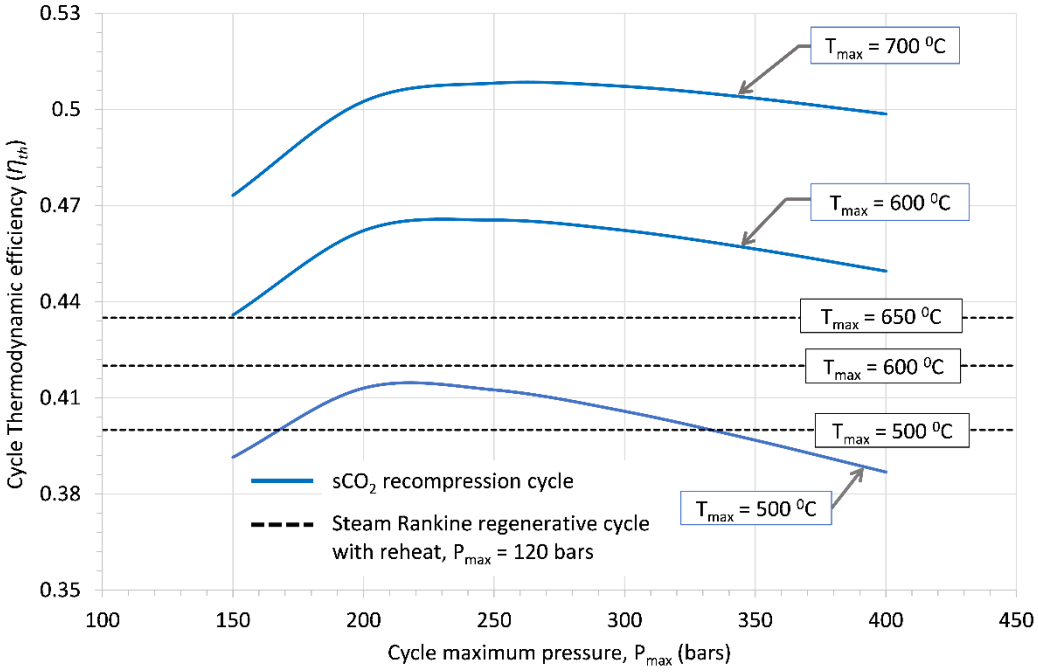

Figure 64: Influence of turbine inlet pressure (Pmax) and turbine inlet temperature (Tmax) on cycle thermodynamic efficiency of sCO2 recompression cycle. Horizontal dotted lines shows the efficiency of steam Rankine regenerative cycle with reheat at cycle maximum pressure of 120 bars taken from reference [106]*. Cycle minimum temperature for all cases is 50℃.*

Effect of turbine inlet pressure (P_{max}) and temperature (T_{max})

With P_{min} = 100 bars as the optimum pressure for T_{min} = 50℃, the cycle efficiency at different turbine inlet temperatures (T_{max}) are presented in Figure 64**.** Comparison with conventional steam Rankine cycle is also carried out in order to highlight the advantages of the sCO_2 cycle. The steam Rankine regenerative cycle with reheat, condensation temperature of 50℃ and turbine inlet pressure of 120 bars taken from ref [106] is chosen as the standard cycle for comparison. In Figure 64, the dotted lines at different turbine inlet temperatures shows the efficiency of the steam cycle at constant turbine inlet pressure of 120 bars. It is evident that cycle efficiency of recompression sCO_2 cycle remain higher than standard steam cycle; the gain in efficiency is more significant at turbine inlet temperatures higher than 600℃. The cycle process diagram of the sCO_2 cycle at optimum conditions in temperature-entropy plane is demonstrated in Figure 65

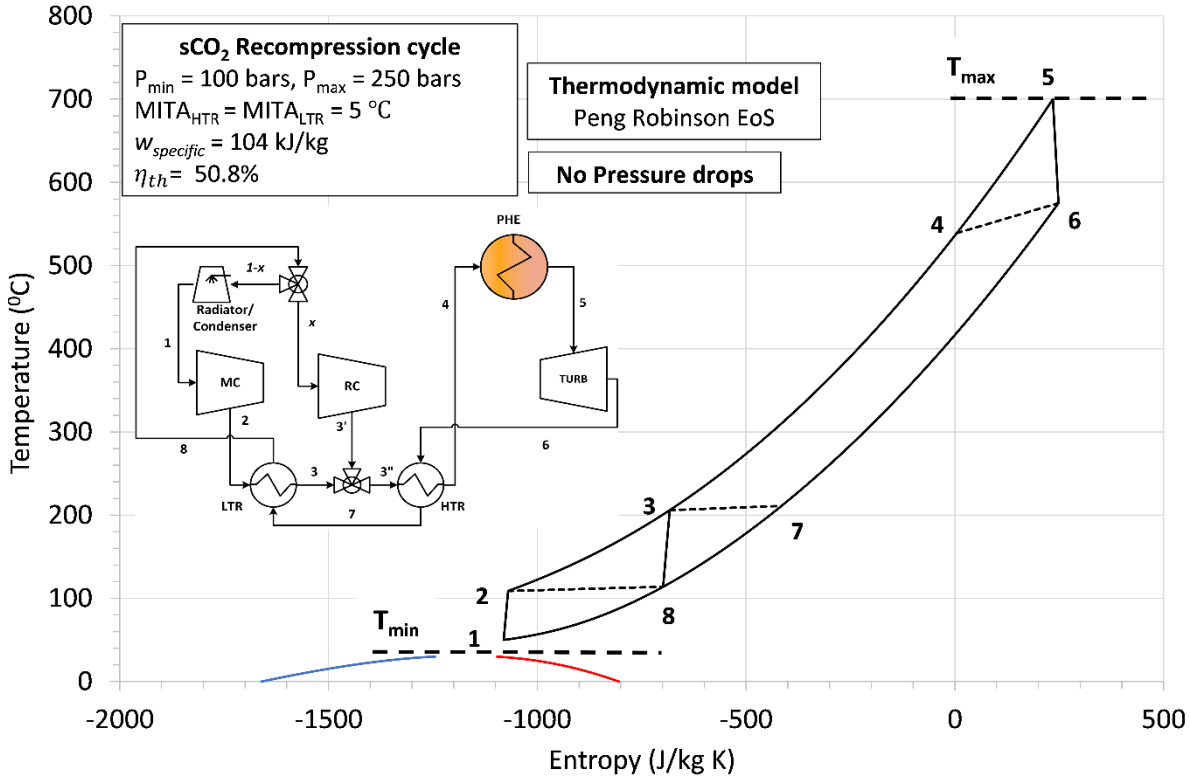

Figure 65: sCO_2 recompression cycle process diagram in T-s plane at optimum conditions

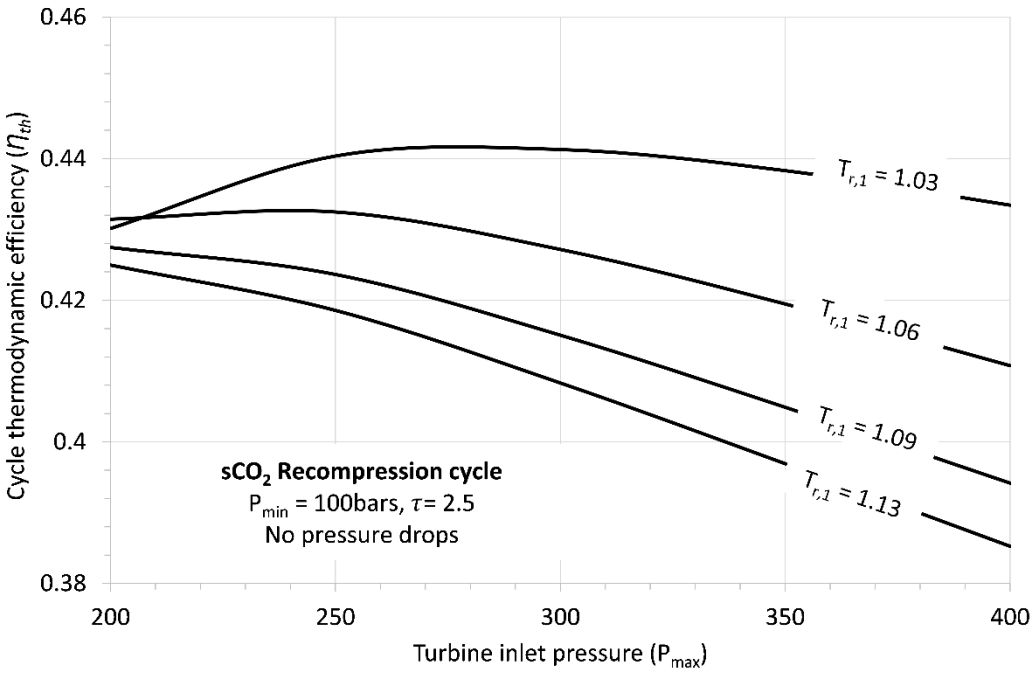

Figure 66: Influence of rise in reduced compressor inlet temperature on cycle thermodynamic efficiency of recompression sCO_2 power cycle

Effect of compressor inlet temperature (T_{min})

The influence of compression inlet temperature (T_{min}) on thermodynamic cycle efficiency is also assessed. Figure 66 demonstrates the effect of reduced compression inlet temperature ($T_{1,r} = T_{min}/T_{cr}$) on thermodynamic cycle efficiency at cycle temperature ratio (T_{max}/T_{min}) of 2.5. As evident, the efficiency is decreasing with rise in $T_{1,r}$ from 1.03 to 1.13. At P_{max} of 250 bars, efficiency drops from 0.44 to 0.42. Moreover, at P_{max} of 300 bars, there is 3 points drop in efficiency that is from 0.41 to 0.43. The underlying reason of this drop in efficiency is compressibility factor at inlet of compression which starts increasing at temperatures greater than critical temperature as shown in Figure 67.

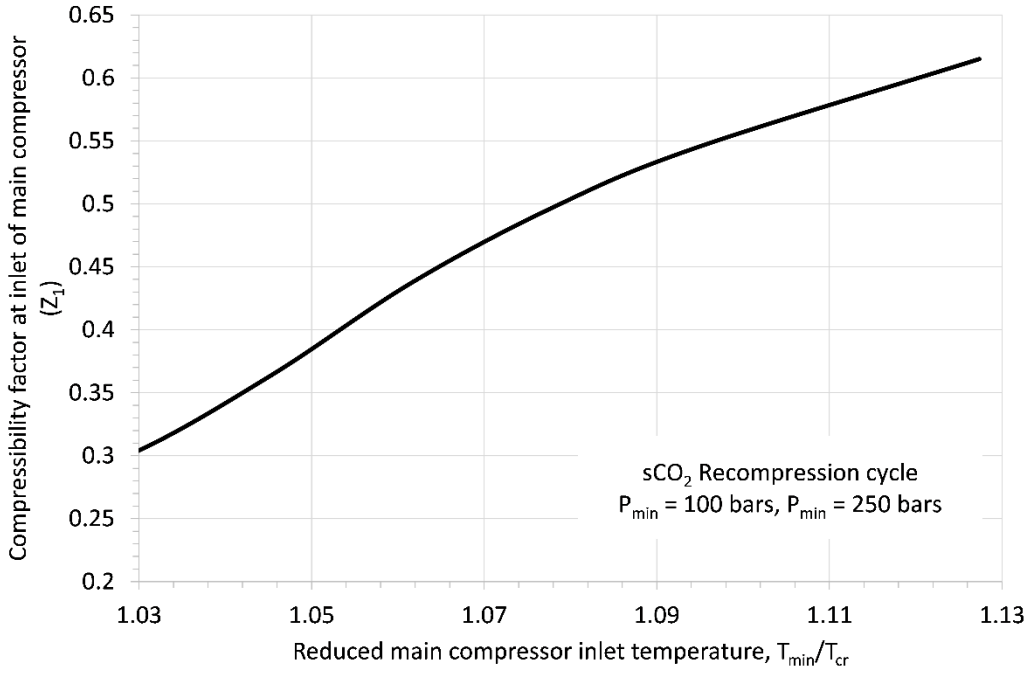

Figure 67: Influence of rise in reduced compressor inlet temperature on compressibility factor at inlet of main compressor of sCO_2 recompression cycle

The increase in value of compressibility factor implies increase in compression work which reduces cycle efficiency. It is important to note that in this analysis constant temperature ratio ($\tau = T_{max}/T_{min}$) or constant Carnot efficiency is assumed rather than constant T_{max} in order to investigate solely the effect of departure from critical point temperature on cycle thermodynamic efficiency.

The effect of different temperature ratios (τ) on cycle efficiency is presented in Figure 68. It can be observed that the decrease in efficiency is significant at lower temperature

ratios. At higher temperature ratios, efficiency of sCO_2 cycle is less sensitive to increase in compression inlet temperature (T_{min}).

In addition, If T_{max} is also kept constant which is typically the case of solar integrated power block, the ratio T_{max}/T_{min} of cycle decreases with rise in compressor inlet temperature (T_{min}) which brings about appreciable decrease in cycle efficiency. Figure 69 shows the trend of drop in cycle efficiency at constant T_{max}. There is 6 points drop in cycle efficiency for rise in reduced compressor inlet temperature from T_{cr} to 1.1 times T_{cr} for T_{max} of 700℃ and compressor inlet pressure of 7.4 bar.

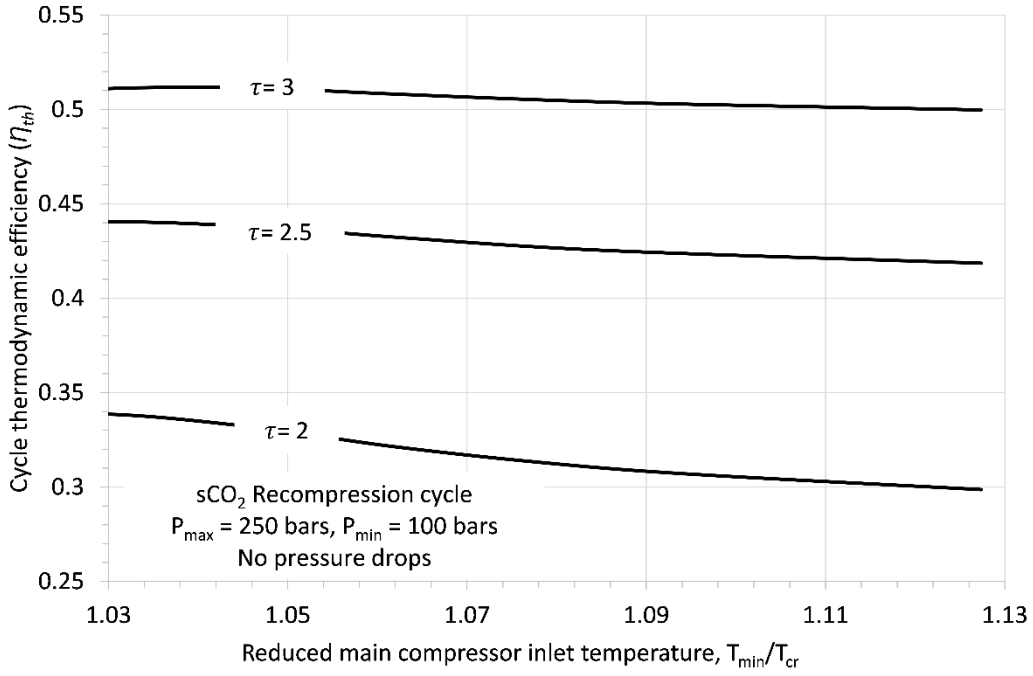

Figure 68: Influence of rise in reduced main compressor inlet temperature on cycle thermodynamic efficiency of recompression sCO_2 power cycle at different temperature ratios (τ)

In summary, the reduction in cycle efficiency at higher cycle T_{min} (or compressor inlet temperature) is associated to two reasons,

1) Rise in compressibility factor at inlet of compression which enhances compression work,

2) Decrease in ratio T_{max}/T_{min} when T_{max} is maintained constant.

In the light of above discussion, following points can be concluded from the thermodynamic analysis of recompression sCO_2 power cycle:

1. For power block operating at higher ambient temperature typical of solar power tower site, the design cycle minimum temperature or compressor inlet temperature is decided to be 50 ℃. Sensitivity analysis suggests values of 250 bars and 100 bars as optimum values for P_{max} and P_{min} respectively.
2. sCO_2 recompression power cycle yields higher cycle efficiency than steam Rankine cycle at turbine inlet temperatures of 500, 600 and 700℃ given the assumption that pressure drops are neglected in the model of the sCO_2 cycle.
3. The increase in compressor inlet temperature from critical temperature to 1.13 times critical temperature causes drop in cycle efficiency by 2 to 3 points. Furthermore, the drop in efficiency is more significant at lower cycle temperature ratios (τ) which shows that the cycle efficiency is more sensitive to compressibility effects at lower temperature ratios (τ).
4. From technological point of view, cycle maximum temperature (T_{max}) is maintained constant. In such scenario, profound negative impact on cycle efficiency is obtained; cycle efficiency drops from 0.52 to 0.46 (6 points) for increase in reduced compressor inlet temperature from 1 to 1.1 when the compressor inlet temperature is 74 bar (equal to Pcr of CO_2)

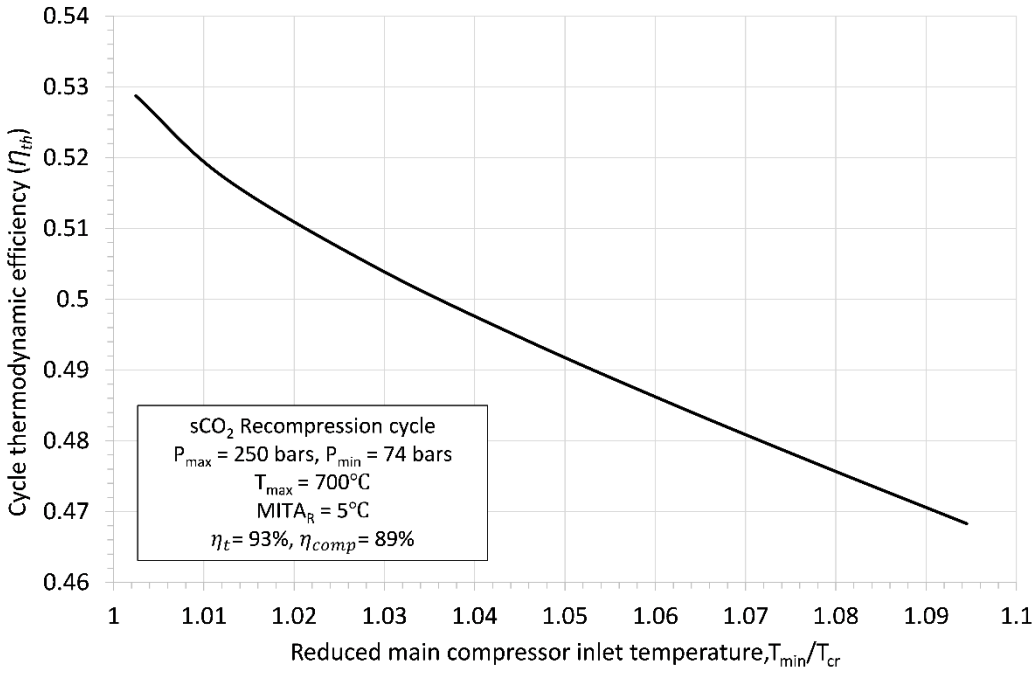

Figure 69: Influence of rise in reduced main compressor inlet temperature on cycle thermodynamic efficiency of recompression sCO_2 power cycle at constant T_{max}.

5.3 **Transcritical power cycles utilizing CO_2-based binary mixtures working fluid**

Previous section shows that maximum efficiency of recompression sCO_2 cycle is 50.8% at T_{max} of 700 ℃, P_{max} of 250 bar, P_{min} of 100 bar and T_{min} of 50 ℃ when Peng Robinson EoS is used as property model to calculate thermodynamic properties and pressure drops in the cycle are ignored.

In this section, carbon dioxide based binary mixtures are introduced as working fluid in transcritical power cycle considering the same temperature ratio of T_{max} and T_{min} i.e. 700 ℃/50 ℃. Transcritical cycle allows liquid phase compression with cycle T_{min} lower than critical temperature of the CO_2-based mixture and minimum cycle pressure is also lower than sCO_2 cycle. The compression below critical point implies less compression work and improvement in cycle efficiency. In this perspective, five CO_2-based binary mixtures are identified based on particular criteria of additive selection, thermodynamic properties are calculated, and thermodynamic performance of transcritical power cycle is performed.

Selection of additive for CO_2-based binary mixture

The key parameters to take into account in choice of additives for CO_2 based binary mixtures in case of high temperature power cycles are:

1. Thermal stability of additive;
   It should be higher than maximum operating temperature (T_{max}) of the power cycle. In the scenario of solar power plant, the required stability temperature is 400 to 700℃. (or maximum possible)

   Note: thermal stability of a working fluid is strictly correlated to materials and contaminants, for example the widely adopted materials for thermal stability testing are Inconel and stainless steel.

2. Critical temperature (T_{cr});
   Critical temperature higher than critical temperature of CO_2 is crucial so that to enable compression below critical point of the CO_2 mixture.

3. Critical Pressure (P_{cr});
   Lower critical pressure of additive is desirable compared to P_{cr} of CO_2 to reduce mechanical stress in cycle components.

4. Molecular complexity;

   The higher molecular complexity of compound implies lower difference of heat capacities between hot and cold streams in recuperator of the power cycle which results in more effective heat exchange. Therefore, additive with higher molecular complexity is adequate.

5. Environmental impact and safety;

   It is primarily important to select additive with lower harmful impact on the environment. So, lower values of ODP and GWP are needed. Moreover, additive should be safe to handle which suggests less toxic and non-flammable compounds.

Table 42: Main physical properties of new compounds selected for CO_2 mixtures.

Working fluid	T_{cr} (℃)	P_{cr} (bars)	Boiling point (℃)	Molecular weight	Molecular Complexity [84]	Acentric factor Ω	Thermal stability
CO_2	31.06	73.83	-78.45	44.01	-9.340	0.2236	>700 ℃ [10]
SO_2	157.6	78.84	-10	64.06	-8.239	0.2454	>700 ℃ [107]
C_6F_6	243.58	32.73	80.26	186.05	12.612	0.3953	480 ℃ [108]
$TiCl_4$	364.85	46.61	136.5	189.69	1.919	0.2837	>550 ℃ [109]
SO_2F_2	91.85	51.17	-55.4	102.06	-3.291	0.0746	n/a.
CF_3I	123.29	39.53	-21.8	195.911	-2.64	0.1763	n/a.

Practically, it is quite difficult to find an additive which meet all the above-mentioned criteria. However, criteria numbers 1,2 and 3 regarding thermal stability, T_{cr} and P_{cr} together with criteria number 5 regarding environmental impact of working fluid are considered foremost priority during screening of different chemical compounds. Table 42 shows the main thermodynamic properties of potential candidate compounds which are selected as additive for CO_2 mixtures. The environmental and safety characteristics of these compounds are shown in Table 43

Table 43: Safety and environmental impact characteristics of new compounds selected for CO_2 mixtures.

Working fluid	*ODP* [87]	*GWP in 100 years* [87], [88]	*Flammability* [89]	*Health* [89]	*Instability* [89]
CO_2	0	1	0	2	0
SO_2	0	n/a.	0	3	0
C_6F_6	n/a.	n/a.	3	1	0
$TiCl_4$	0	0	0	3	2
SO_2F_2	0	4780	0	3	1

CF_3I	<0.09	n/a.	0	2	0

Experimental thermal stability data of SO_2F_2 and CF_3I are not available. For such compounds, preliminary assessment of chemical stability is carried out by using standard enthalpy of formation per bond relative to standard enthalpy of formation per bond of pure CO_2. Considering the fact that, in general, more negative value of standard enthalpy of formation (ΔH_f^o) implies more stable compound. Figure 70 shows the parameter ($\Delta H_B = \Delta H_f^o / n_B$) with respect to number of chemical bonds in the molecule of additive fluid. CO_2 is considered as reference fluid for comparison owing to its well established higher chemical stability. The parameter value ΔH_B of both SO_2F_2 and CF_3I are closer to value of pure CO_2 which indicates that chemical stability of SO_2F_2 and CF_3I are close to chemical stability of pure CO_2. Nevertheless, the right approach to assess thermal stability of fluid is by performing long hour tests in a static cell at different temperatures and different containment materials as explained in refs [110], [111].

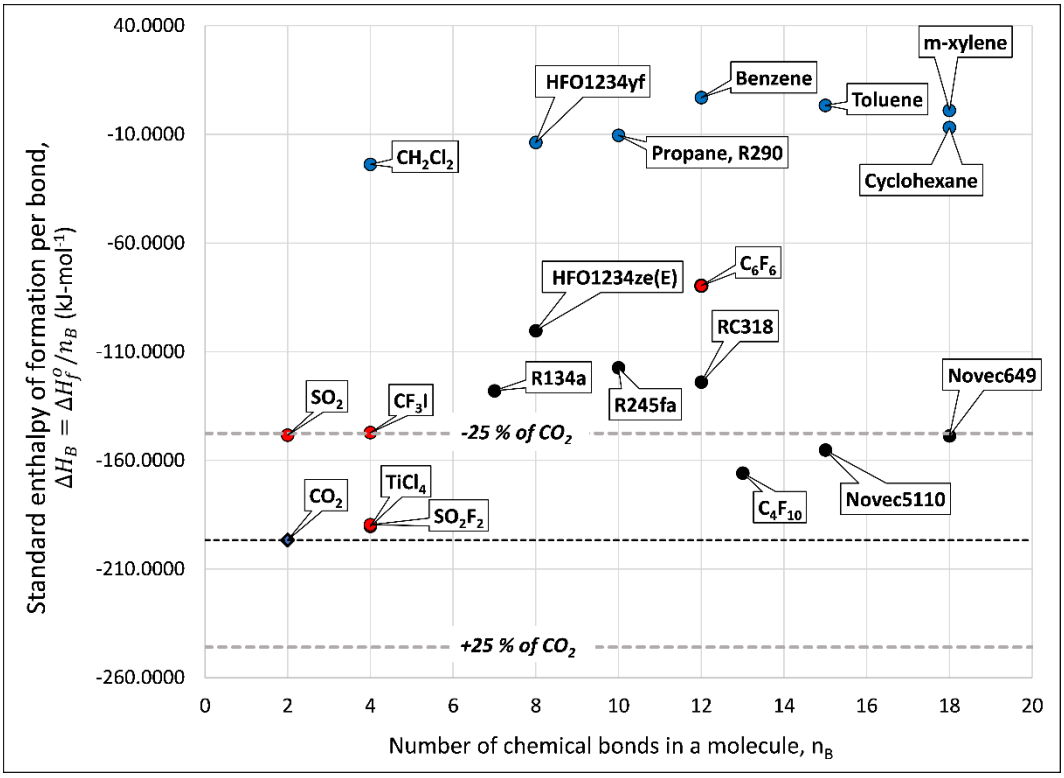

Figure 70: Standard enthalpy of formation per bond of some working fluids with respect to number of bonds in a molecule. CO_2 is considered as reference fluid for comparison owing to its higher chemical stability.

Thermodynamic properties of CO_2 mixtures

After selection of appropriate additive with desirable thermodynamic and environmental properties for CO_2 binary mixtures, the subsequent step is to analyze the fluid behavior of CO_2 mixture at different molar composition. This requires an accurate property calculation model; activity coefficient models or equation of state (EoS) depending on the range of temperatures and pressure in which the properties are needed. In this chapter, cubic Peng Robinson equation of state (PR EoS) with van der Waals mixing rules also known as standard PR EoS is selected because of its applicability both at low pressures and higher pressures greater than critical point.

Standard PR EoS is adopted by numerous studies in literature and it requires critical point temperature and pressure (T_{cr}, P_{cr}), acentric factor (ω) of pure fluid components and binary interaction parameter ($k_{1,2}$) to completely describe the thermodynamic properties of a binary mixture (read section 2.1 about cubic PR EoS). The pure fluid properties for both CO_2 and the additive compound are reported in Table 42. Secondly, in van der Waals mixing rule for a binary mixture, one binary interaction parameter ($k_{1,2}$) is also needed to determine interaction coefficient $a_{1,2}$ as shown,

$$\boldsymbol{a_{1,2} = \sqrt{a_1 a_2}\left(1 - k_{1,2}\right)} \qquad \textbf{Eq. 34}$$

Where, a_1 and a_2 are pure component parameters.

The usual approach well documented in literature to calculate the optimum value of $k_{1,2}$ is by regression analysis using available experimental vapor-Liquid equilibrium (VLE) data. The regression analysis is carried out using the maximum likelihood method as optimization method. Once optimum value of $k_{1,2}$ is determined, the PR-EoS is used to calculate pressure-temperature envelop at different mixture composition, mixture densities, enthalpies and entropies at different isobars from subcritical to supercritical phases. All the thermodynamic property calculations for pure fluids and CO_2 mixtures are carried out in Aspen Plus V10 simulation software [112].

The accuracy of EoS is assessed by computing mean absolute percentage error (MAPE) which indicates the deviation of prediction from EoS with experimental data. MAPE in any thermodynamic property is computed using following relation**,**

$$\mathrm{MAPE_X} = \frac{1}{\mathrm{N}} \sum_{\mathrm{i=1}}^{\mathrm{N}} \left| \frac{\mathrm{X_{EoS} - X_{experimental}}}{\mathrm{X_{EoS}}} \right| \mathrm{x}\ 100 \qquad \textbf{Eq. 35}$$

In next sections, the binary interaction parameter ($k_{1,2}$) is computed for each selected CO_2 mixture by regression using experimental VLE data. In addition, saturation curves (or limit curves) and vapor-liquid critical points are calculated at different mixture molar compositions. The feasible mixture compositions based on specific criteria of transcritical power cycle are decided. Finally, variation of density and entropy of CO_2 mixture with change in temperature and pressure are studied for selected mixture compositions to evaluate the behavior of these properties in different phases.

CO_2-SO_2 binary mixture

For CO_2-SO_2 mixture, experimental VLE data presented by Coquelet *et* al [33] is exploited in regression analysis to compute optimum value of $k_{1,2}$. Figure 71 shows isothermal VLE at three temperatures (-10, 60 and 80℃) computed using PR EoS with optimized $k_{1,2}$. It is evident that the VLE from PR-EoS closely matched the experimental VLE data; MAPE in bubble pressures is found to be 1.3% and 0.41% at -10 ℃ and 60℃ respectively. However, MAPE in vapor composition of CO_2 (Y) is found to be 0.59% and 0.72% at -10 ℃ and 60℃ respectively. The final obtained value of $k_{1,2}$ with standard deviation is 0.02431 ± 0.00117.

P-T phase diagram at different mixture composition is shown in Figure 72. Critical point temperature increases from 31℃ to 157℃ for increase in molar fraction of SO_2 (z_2) in the mixture. Whereas, critical pressure first rises from 74 bars to 100 bars with increase in molar composition of SO_2 from 0 to 0.5. Then, there is drop in critical pressure till 78 bars for SO_2 molar fraction of 0.5 to 1 in the mixture.

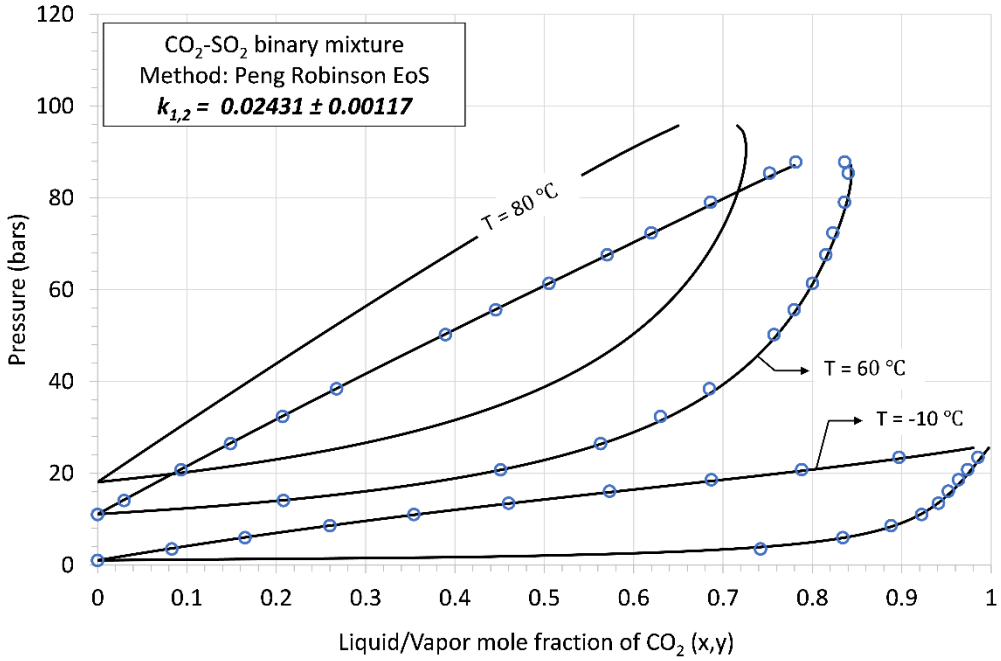

Figure 71: Vapor-Liquid equilibrium (VLE) phase diagram of CO_2-SO_2 binary mixture at three temperatures (-10 ℃, 60 ℃, 80 ℃). Scatter points show experimental data from literature [27].

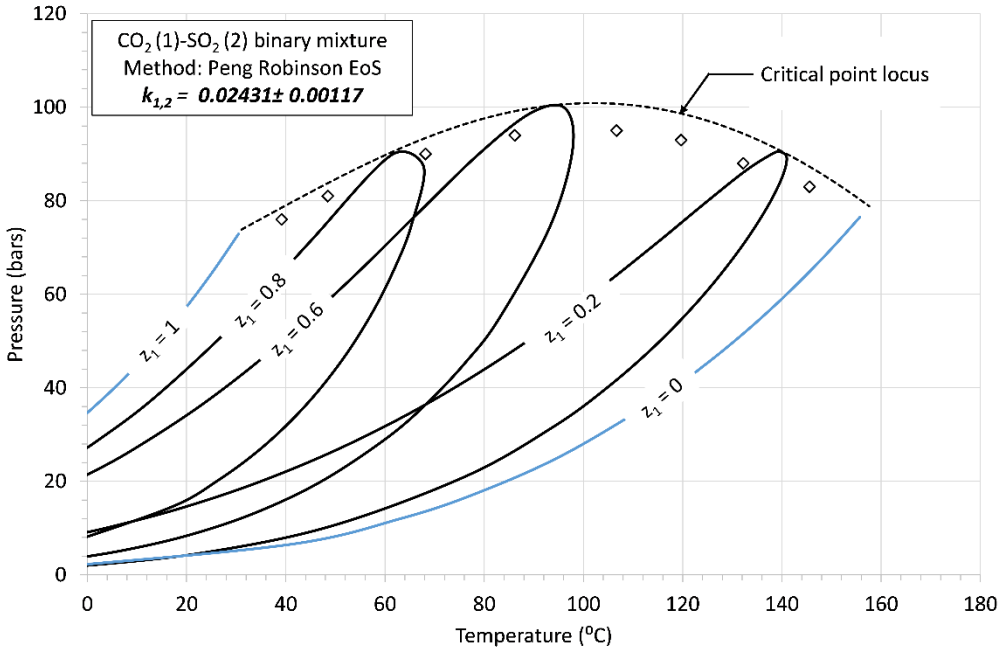

Figure 72: Pressure-temperature phase diagram of CO_2-SO_2 binary mixture at different molar composition. Diamond shape points show experimental critical points from literature [113]*. Dotted line shows calculated critical point locus.*

Definition of mixture composition for transcritical cycle

P-T phase diagram is very helpful in finding pump inlet pressure (P_1) corresponding to required pump inlet temperature (T_{pump}). In cycle design point analysis, the main goal is

to design condensation cycle which involves compression at temperature lower than critical point temperature of the mixture ($T_{cr,mix}$). In this context, the mixture molar composition of interest is decided based on criteria that the critical temperature of the mixture should be at the minimum 15 ℃ higher than pump inlet temperature (i.e. $T_{cr,mix} - T_{pump} \geq 15℃$) in order ensure compression phase below critical point of the mixture and to avoid operation of pump very close to critical point at which thermodynamic properties are difficult to compute.

The mixture critical point temperature ($T_{cr,mix}$), difference between $T_{cr,mix}$ and T_{pump} and pump inlet pressure (P_{pump}) are recorded in Table 44 for different molar composition of CO_2-SO_2 mixture. The mixture of CO_2-SO_2 which meet the above-mentioned criteria are 0.8 CO_2, 0.75 CO_2 and 0.7 CO_2 mixture by molar composition. Composition greater than 0.8 CO_2 for example 0.9 CO_2 is not feasible to study since critical temperature at that composition is 48 ℃ which is less than required pump inlet temperature of 50℃. Also, molar composition lesser than 0.7 CO_2 like 0.6 CO_2 or 0.5 CO_2 (or higher SO_2 content) are not suitable to adopt considering the effect of severe toxicity of SO_2 on the mixture. Temperature-density (T-ρ) plot and temperature-specific entropy (T-s) plot of 80% CO_2 mixture are shown in Figure 73 and Figure 74 respectively. In these plots, two isobars near pump inlet pressure (P_1) and two isobars corresponding to turbine inlet pressure are calculated and plotted.

Table 44: Critical temperature, difference between $T_{cr,mix}$ and T_{pump}, critical pressure ($P_{cr,mix}$) and pump inlet pressure (P_{pump}) for different molar compositions of CO_2-SO_2 mixture

Molar composition of CO_2	$T_{cr,mix}$ (℃)	$T_{cr,mix} - T_{pump}$	$P_{cr,mix}$ (bars)	P_1@ T_1=50 ℃ (bar)
0.9 CO_2	48.26	-1.74	83.66	Not applicable
0.85 CO_2	56.41	6.41	87.98	82
0.8 CO_2	64.32	14.32	91.77	77.5
0.75 CO_2	72.02	22.02	94.96	73
0.7 CO_2	79.51	29.51	97.48	69
0.65 CO_2	86.78	36.78	99.3	64.5

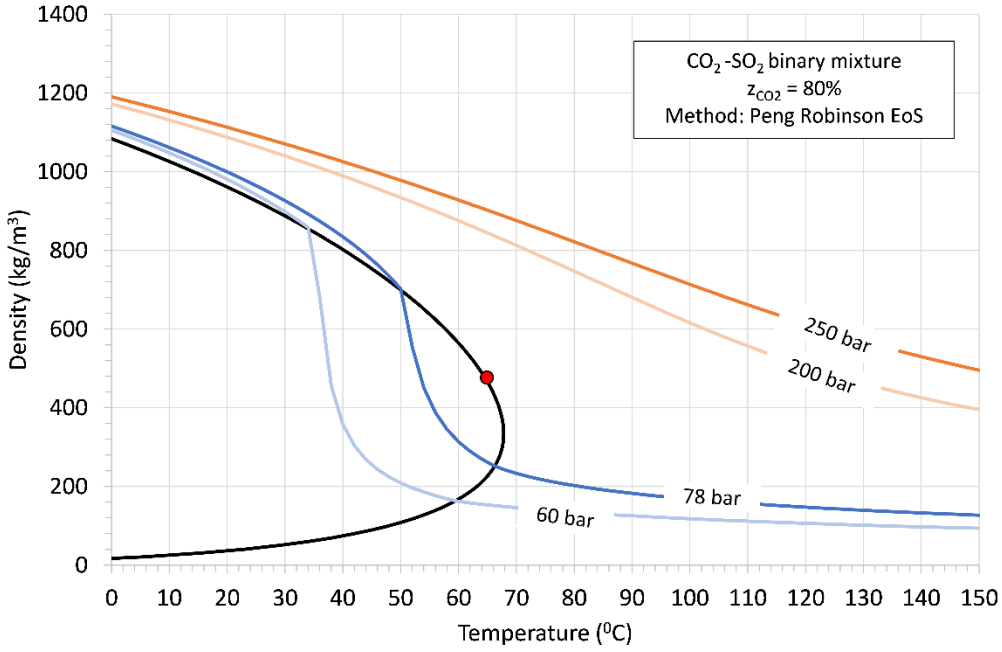

Figure 73: Density-temperature behavior of 80%CO_2+20%SO_2 mixture. Black line shows liquid vapor saturation line. Red point shows the critical point.

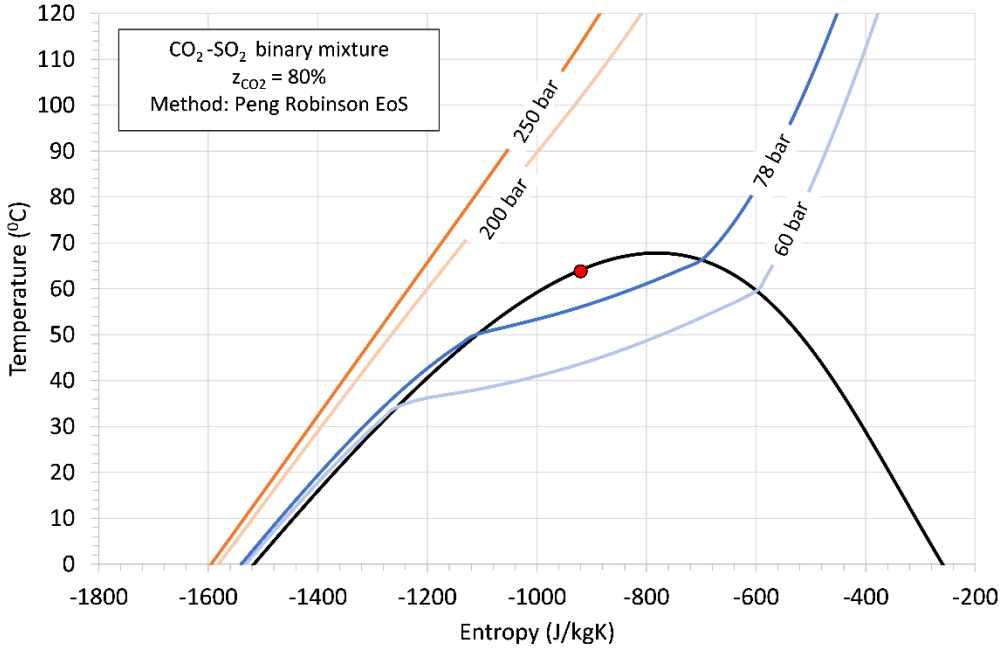

Figure 74: Temperature-specific entropy behavior of 80%CO_2+20%SO_2 mixture. Black line shows liquid vapor saturation line. Red point shows the critical point.

CO_2-C_6F_6 binary mixture

For CO_2-C_6F_6 mixture, the same Peng-Robinson EoS with van der Waals mixing rule is adopted as thermodynamic model. Following the same approach described earlier, the binary interaction parameter ($k_{1,2}$) is obtained using the experimental bubble points data of Dias *et* al [114] and new experimental VLE data (not-published yet) taken from LEAP laboratories.

The VLE behavior at 70℃ and 90℃ are shown in Figure 75 with solid lines representing the calculated VLE and scatter points show experimental data. Moreover, both experimental and calculated bubble points at temperatures from 20℃ to 60℃ are shown in the Figure 76. The MAPE in bubble point pressures and dew point composition are reported in Table 45. Finally, the value of $k_{1,2}$ obtained from regression analysis is 0.04381 ± 0.01167.

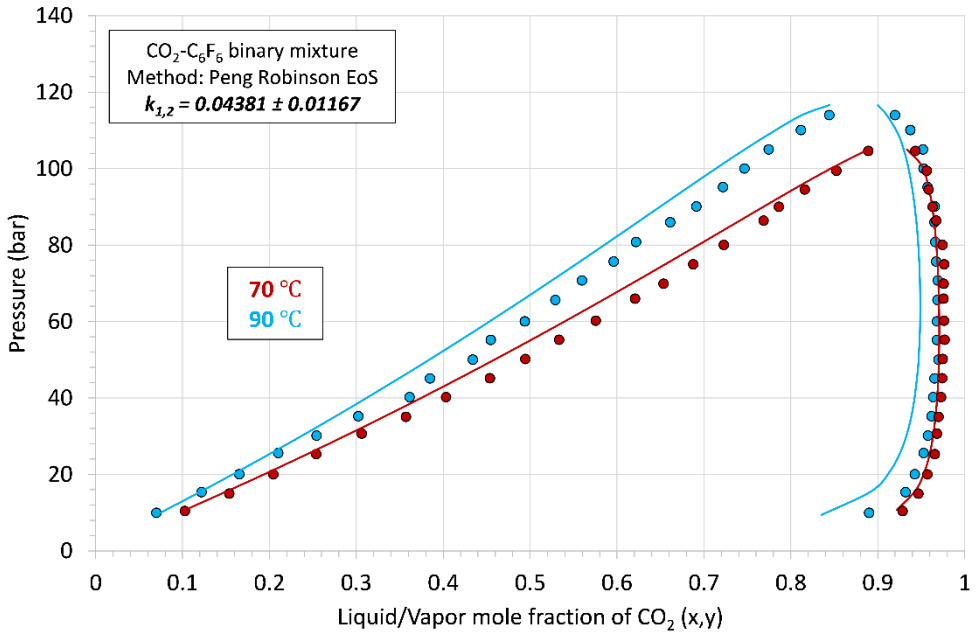

Figure 75: Vapor-Liquid equilibrium (VLE) phase diagram of CO_2-C_6F_6 binary mixture at two temperatures (70 ℃ and 90 ℃). Scatter points show new experimental data (not-published)

Table 45: MAPE in bubble pressure and dew composition of CO_2-C_6F_6 mixture at different temperature.

Literature reference	**LEAP laboratory**		**Dias *et* al** [114]
Quantity	**Bubble pressure (P_{bub})**	**Dew composition of CO_2 (Y_{CO2})**	**Bubble pressure (P_{bub})**

Temperature	70°C	90°C	70°C	90°C	20°C	30°C	40°C	50°C	60°C
MAPE	5.3%	7.2%	0.5%	2.3%	4.5%	3.3%	2.8%	2.4%	3.2%

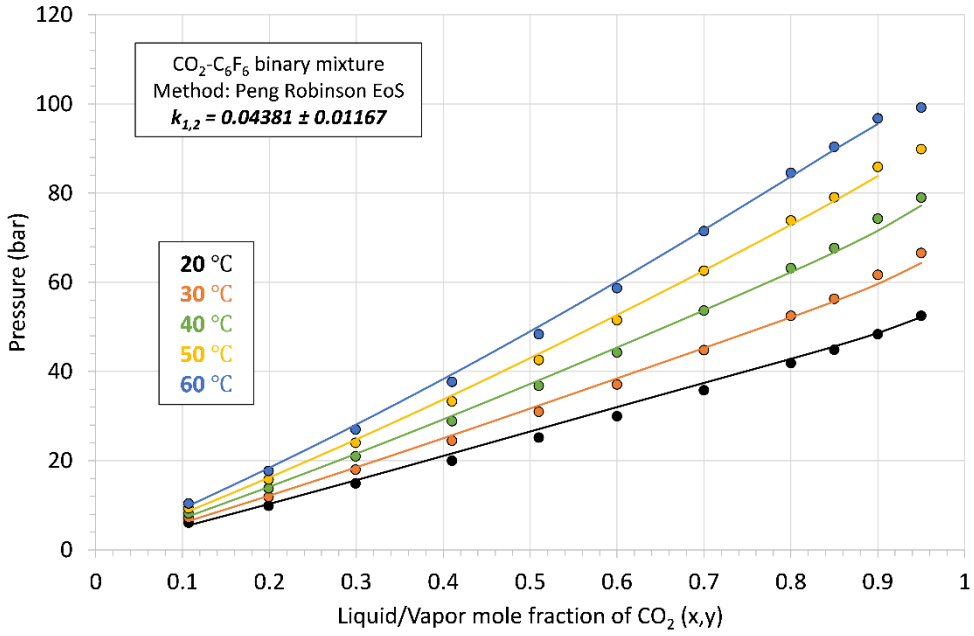

Figure 76: Bubble points of CO_2-C_6F_6 binary mixture at five temperatures (20 ℃, 30 ℃, 40 ℃, 50 ℃ and 60 ℃). Scatter points show experimental data from literature [114].

The thermodynamic behavior in P-T plane and calculated vapor-liquid critical points at different composition are shown in Figure 77. The difference between $T_{cr,mix}$ and T_{pump} is higher than 15℃ for mixture compositions from 0.9 CO_2 to 0.5 CO_2. Therefore, the compositions relatively rich in CO_2 which are 0.85 CO_2, 0.9 CO_2 and 0.8 CO_2 are selected for thermodynamic analysis of the power cycle. The temperature-density and temperature-entropy behavior of CO_2-C_6F_6 mixture with 0.8 CO_2 are shown in Figure 78 and Figure 79 respectively.

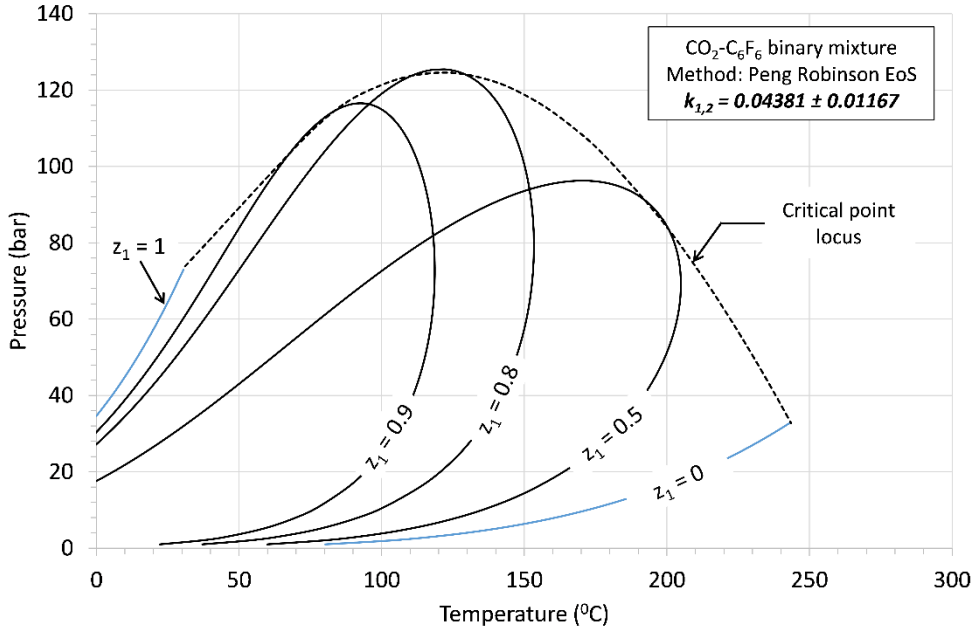

Figure 77: Pressure-temperature phase diagram of CO_2-C_6F_6 binary mixture at different mixture molar composition. Dotted line shows calculated critical point locus.

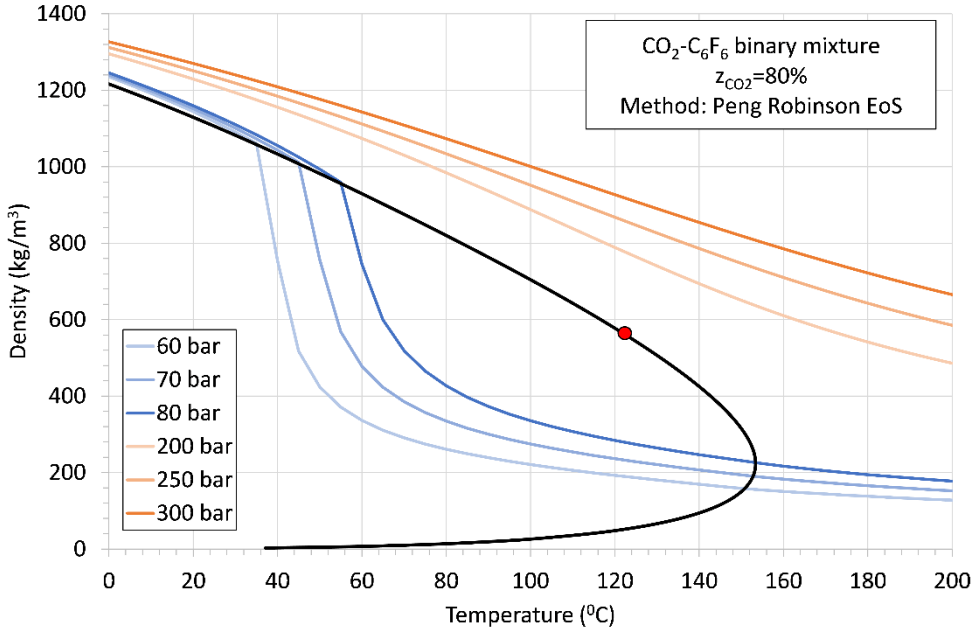

Figure 78: Density-temperature behavior of 0.8 CO_2-0.2 C_6F_6 mixture. Black line shows liquid vapor saturation line. Red point shows the critical point.

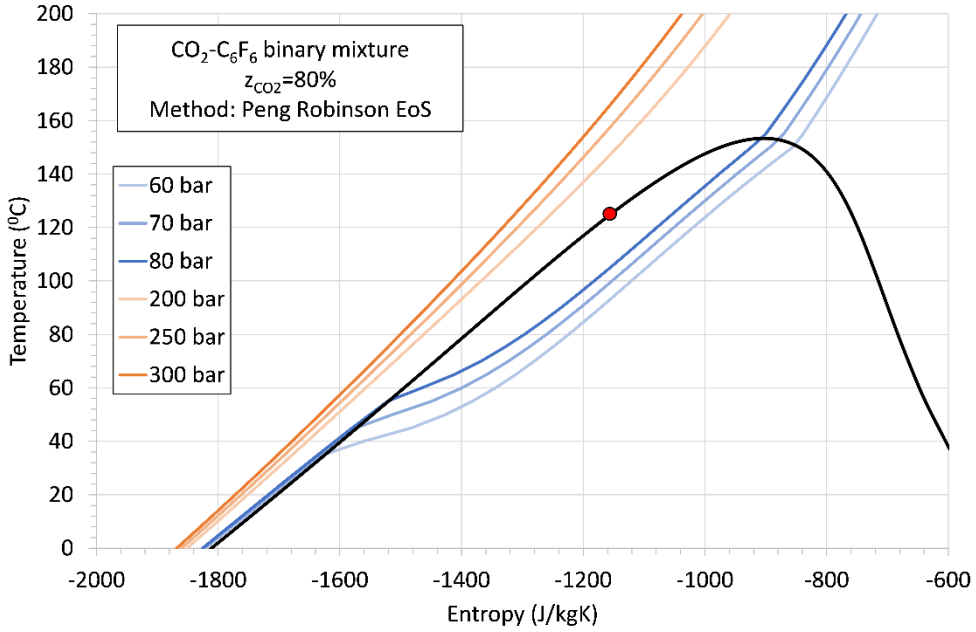

Figure 79: Temperature-specific entropy behavior of 0.8 CO_2-0.2 C_6F_6 mixture. Black line shows liquid vapor saturation line. Red point shows the critical point.

CO_2-$TiCl_4$ binary mixture

For CO_2-$TiCl_4$ binary mixture, the experimental VLE data is scarce; only two VLE points are available to calibrate the thermodynamic model. This limited data is exploited in regression analysis with Peng Robinson EoS as the thermodynamic model and the usual binary interaction parameter ($k_{1,2}$) is computed as described in previous section. The graphical representation of the VLE and the calculated value of $k_{1,2}$ are depicted in Figure 80. Using the regressed value of $k_{1,2}$, the behavior of this mixture in P-T plane at different mixture composition is calculated and plotted in Figure 81. The mixture is characterized by higher critical temperatures and very high critical pressures (close to typical maximum cycle pressure of CO_2 cycles i.e. 200 bars). Temperature glide between bubble and dew point are also greater for this mixture compared to other selected CO_2-mixtures. Besides all, this mixture is very promising for high temperature power cycles owing to higher thermo-chemical stability of $TiCl_4$.

The mixture compositions for which the difference between $T_{cr,mix}$ and T_{pump} is higher than 15 ℃ are those with CO_2 molar composition lower than 0.85. Therefore, 0.8 CO_2, 0.75 CO_2 and 0.7 CO_2 mixtures are selected for thermodynamic analysis of the power cycle. Behavior of density and entropy of the CO_2-$TiCl_4$ mixture for 0.8 CO_2-0.2 $TiCl_4$ composition are plotted in the Figure 82 and Figure 83 respectively.

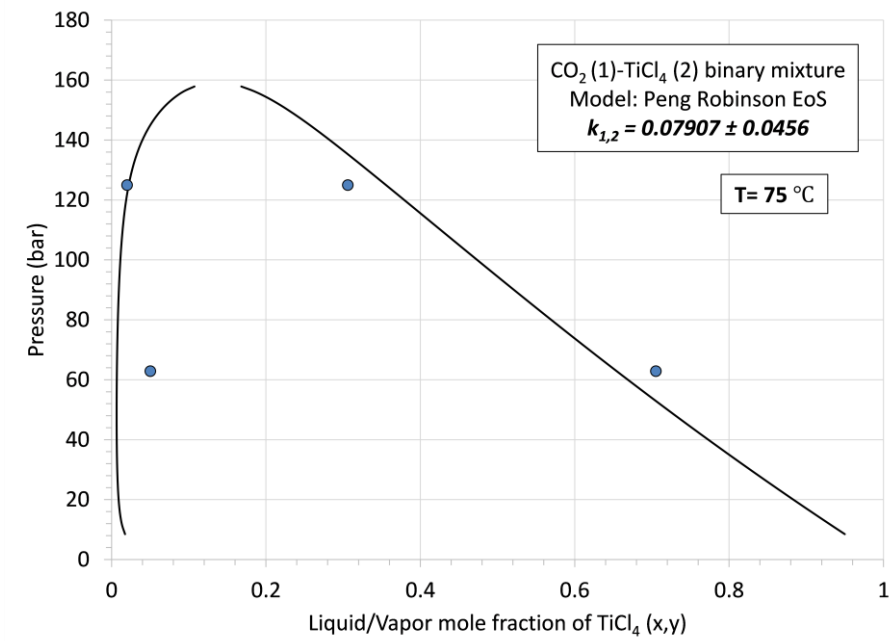

Figure 80: Vapor-Liquid equilibrium (VLE) phase diagram of CO_2-$TiCl_4$ binary mixture at 75 ℃. Scatter points show new experimental data.

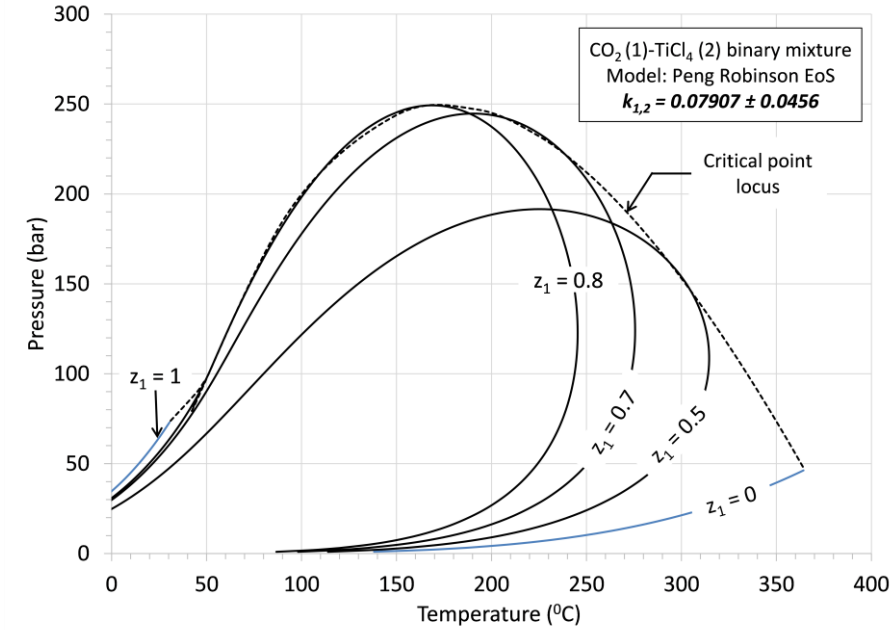

Figure 81: Pressure-temperature phase diagram of CO_2-$TiCl_4$ binary mixture at different molar composition. Dotted line shows calculated critical point locus.

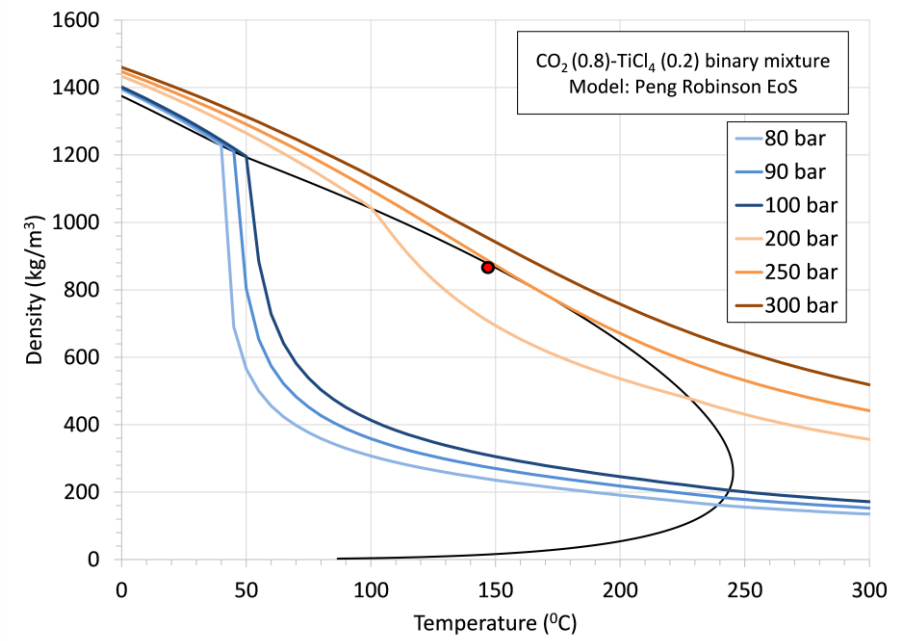

Figure 82: Density-temperature behavior of 0.8 CO_2-0.2 $TiCl_4$ mixture. Black line shows liquid vapor saturation line. Red point shows the vapor-liquid critical point.

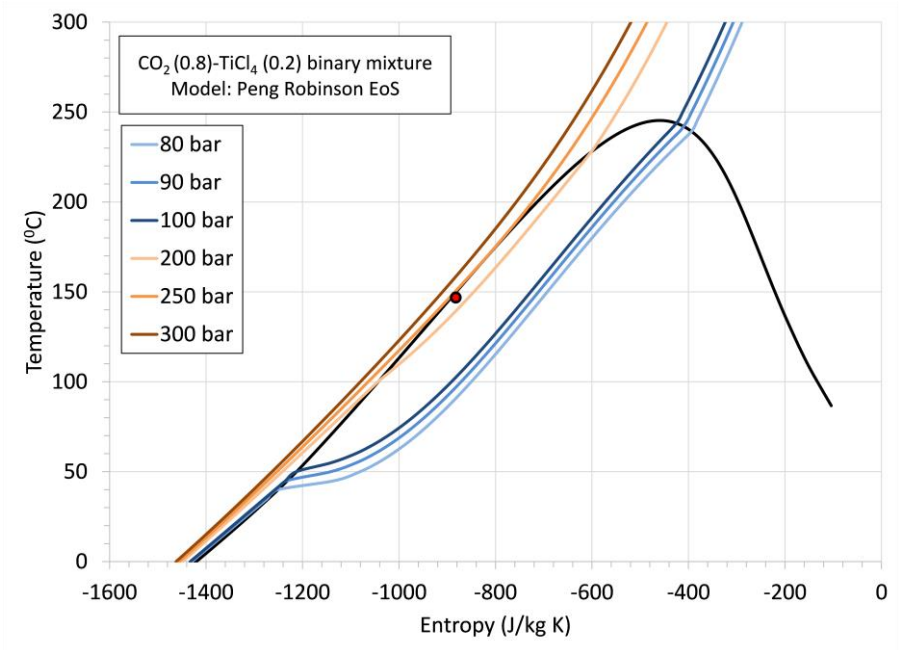

Figure 83: Temperature-entropy behavior of 0.8 CO_2-0.2 $TiCl_4$ mixture. Black line shows liquid vapor saturation line. Red point shows the vapor-liquid critical point.

CO_2-CF_3I binary mixture

Tri-fluoroiodomethane (CF_3I) is recently studied as a refrigerant in refrigeration and air-conditioning cycles. Its positive characteristics are low GWP, low ODP and non-flammability. The mixture of CF_3I and CO_2 is studied as insulation medium in electrical equipment to replace SF_6 gas.

Experimental VLE data for CO_2-CF_3I mixture available in literature is for very low temperatures (ranging from -30°C to 0°C) only relevant to refrigeration application. Additional VLE measurements at high temperature and experimental data of density and caloric properties are needed to calibrate EoS and ensure accuracy in thermodynamic cycle calculations. Regarding thermochemical stability, there is no information available about stability of CF_3I at higher temperatures (around 500°C).

To calculate properties of CO_2-CF_3I mixture, PR EoS is adopted and calibrated using available experimental VLE data. As a result of regression with VLE data, the value of $k_{1,2}$ is computed. The calibrated EoS is then used to compute thermodynamic behavior of the mixture, to compute critical points, density, enthalpy and entropy of the mixture at different molar composition.

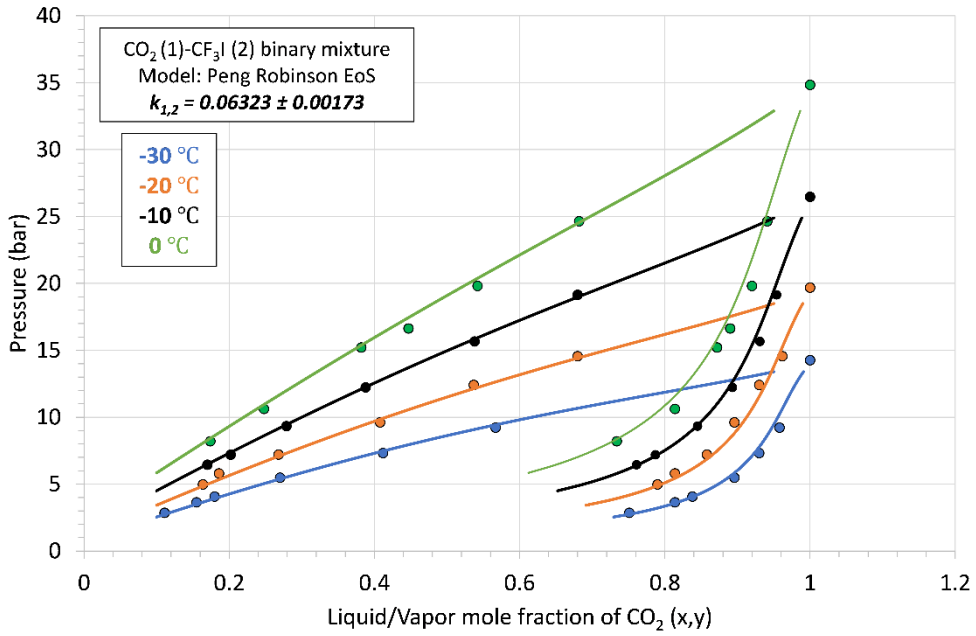

Figure 84: Vapor-Liquid equilibrium (VLE) phase diagram of CO_2-CF_3I binary mixture at four temperatures (0 °C,-10 °C, -20 °C and -30 °C). Scatter points show experimental data from ref [115].

Figure 84 shows the experimental and calculated VLE data at four temperatures. Peng-Robinson EoS represents good agreement with experimental data. The behavior of bubble and dew point pressures and critical points at different molar composition of the mixture are shown on P-T plane in Figure 85. Lastly, the behavior of density and entropy of the mixture in subcritical and supercritical phases for 0.6CO2-0.4CF3I mixture are calculated and illustrated in Figure 86 and Figure 87 respectively.

As decided earlier in thus section. to select mixture composition for cycle thermodynamic analysis, the criteria for transcritical power cycle is the difference $T_{cr,mix}$-T_{pump} should be greater than 15℃. Therefore, three mixture compositions are selected which meet the criteria; they are 0.65 CO_2, 0.6 CO_2 and 0.55 CO_2 mixtures.

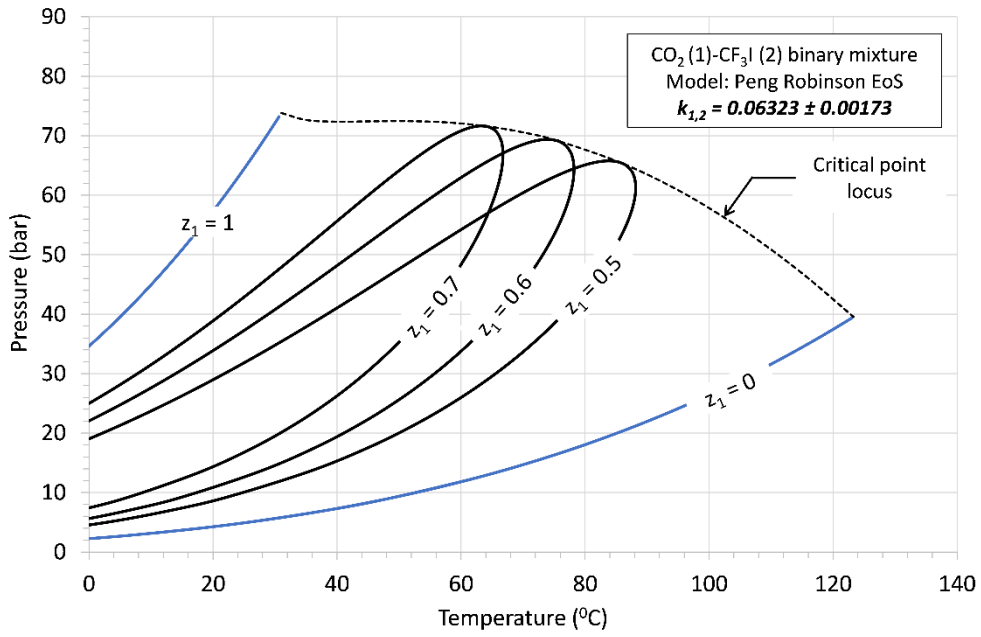

Figure 85: Pressure-temperature phase diagram of CO_2-CF_3I binary mixture at different mixture molar composition. Dotted line shows calculated critical point locus.

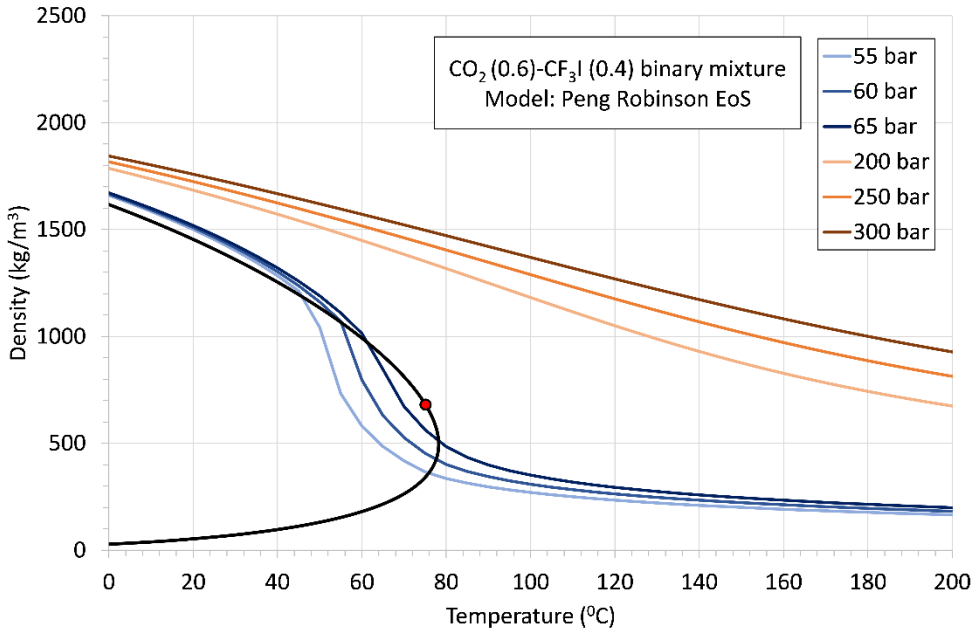

Figure 86: Temperature-entropy behavior of 0.6 CO_2-0.4 CF_3I mixture. Black line shows liquid vapor saturation line. Red point shows the vapor-liquid critical point.

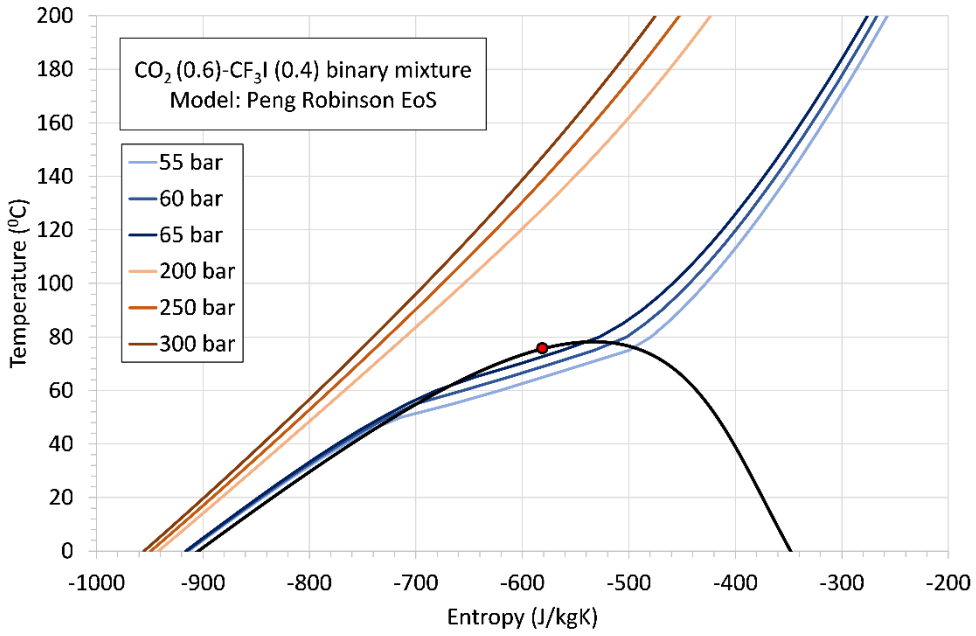

Figure 87: Temperature-entropy behavior of 0.6 CO2-0.4 CF_3I mixture. Black line shows liquid vapor saturation line. Red point shows the vapor-liquid critical point.

CO_2-SO_2F_2 binary mixture

Sulfuryl fluoride (SO_2F_2) also called as sulphonyl-difluoride gas is a colorless and odorless gas usually used in industry as reagent and in many other fields as a fumigant gas. When dry, the gas is stable up to 400°C. The long-term exposure of this gas is harmful

for human being. Moreover, the atmospheric life time of the gas is larger i.e. 36 years and a very high global warming potential i.e. 4800 according to recent estimation. Because of higher thermal stability and enthalpy of formation per bond value close to CO_2, this gas is identified as an additive for CO_2 mixtures.

In open literature, there is No experimental vapor-liquid equilibrium or density data available for CO_2-SO_2F_2 binary mixture. For such type of mixtures, a correlation is developed in Chapter 2 (section 2.3) to estimate binary interaction parameter ($k_{1,2}$) using the data of CO_2 mixtures with known values of $k_{1,2}$. This approach is explained in detail in Chapter 2.

Binary interaction parameter of CO_2-SO_2F_2

For mixture of CO_2-SO_2F_2, the interaction parameter $a_{1,2}$ is estimated using the correlation developed in Chapter 2 (section 2.3). The estimated value with uncertainty is,

$$a_{1,2} = 1.311 \pm 0.0784,$$

And using Eq.30 and uncertainty propagation rules the value of $k_{1,2}$ is determined as,

$$k_{1,2} = 0.0932 \pm 0.0542$$

This value of $k_{1,2}$ is incorporated in van der Waals mixing rules with Peng Robinson EoS and thermodynamic behavior is calculated at different mixture molar composition. Figure 88 shows isothermal vapor-liquid equilibrium for three temperatures (20℃, 40℃ and 50℃). The behavior of vapor-liquid critical points and saturation lines at different molar composition are shown in Figure 89. From these phase diagrams, it can be noticed that mixture with CO_2 molar composition greater than 50% are not feasible for transcritical cycle with T_{min} = 50 ℃ because critical temperature of the mixture is lower than 50℃ and the criteria of composition selection (i.e. $T_{cr,mix} - T_{pump} \geq 15$℃) is not satisfied for these compositions. Therefore, one composition with 40% CO_2 and 60% SO_2F_2 mixture is decided to consider in thermodynamic power cycle. At selected composition, the behavior of density and entropy are studied at different temperatures and pressures. Figure 90 and Figure 91 depicts the density-temperature and temperature-entropy diagrams of the mixture.

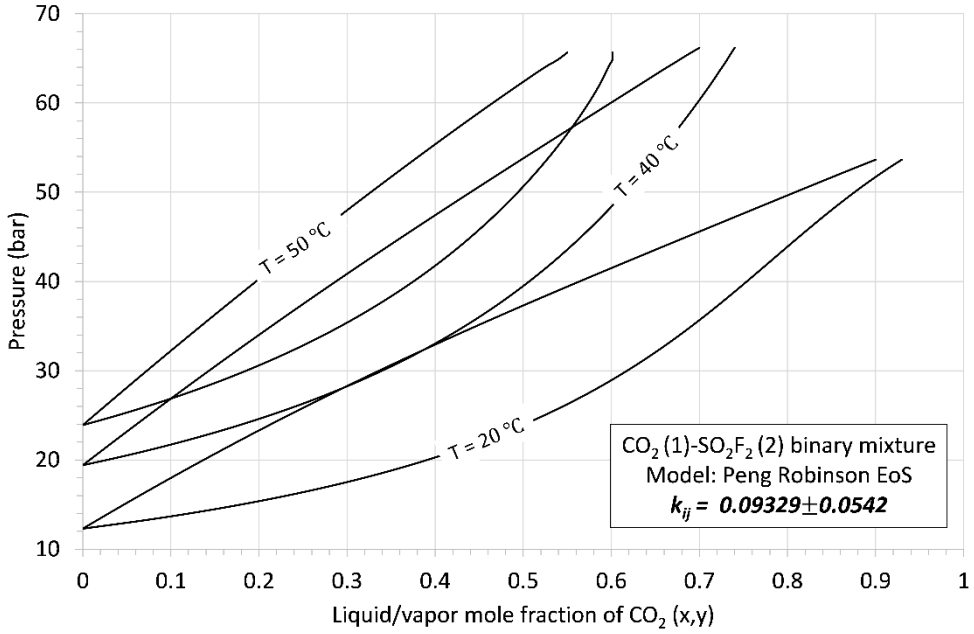

Figure 88: Vapor-liquid equilibrium of CO_2-SO_2F_2 binary mixture at three temperatures.

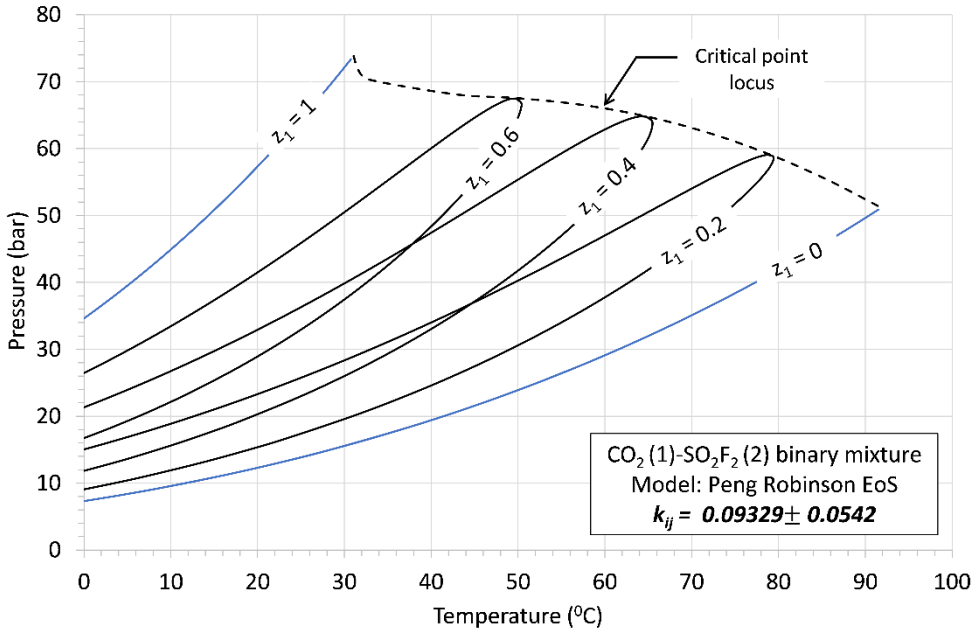

Figure 89: Vapor-liquid saturation lines and critical points of CO_2-SO_2F_2 binary mixture for different mixture compositions

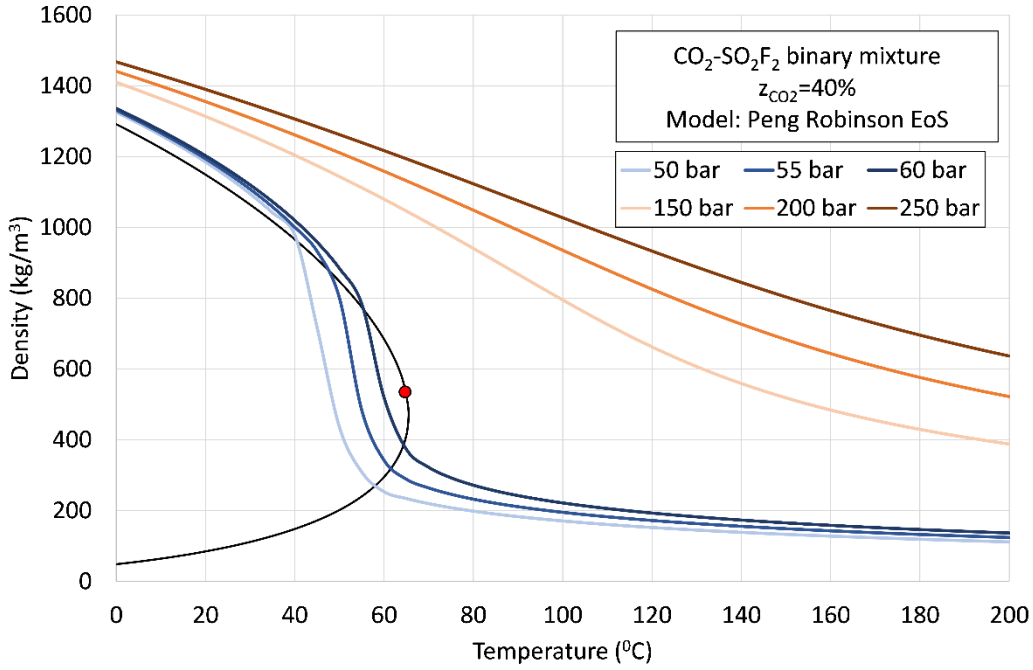

Figure 90: Temperature-density behavior of 40%CO_2-60%SO_2F_2 mixture. The red point represents vapor-liquid critical point of the mixture

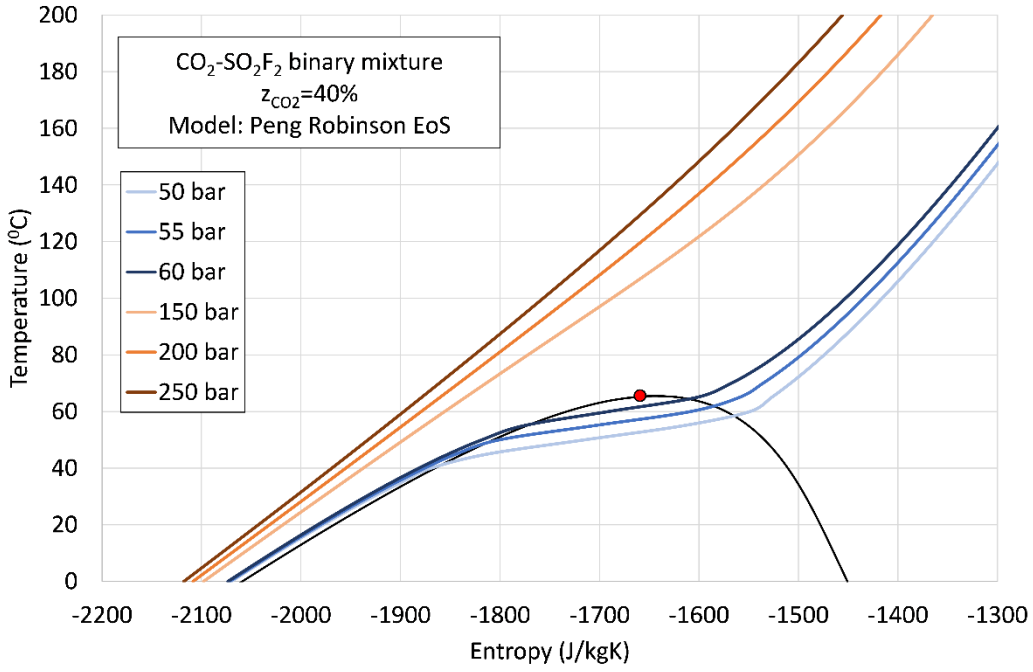

Figure 91: Entropy-temperature behavior of 40%CO_2-60%SO_2F_2 mixture. The red point represents vapor-liquid critical point of the mixture.

In summary, the binary interaction parameter ($k_{1,2}$) of the studied CO_2 mixtures are reported in Table 46 along with associated standard deviation and source of experimental VLE data acquired in regression analysis to compute $k_{1,2}$. The important thermodynamic properties of selected mixtures are reported in Table 47.

Table 46: Binary interaction parameters ($k_{1,2}$) of CO_2 mixtures with standard deviation and literature source of experimental data.

CO_2 mixture	**$k_{1,2}$**	**Standard deviation**	**Source of experimental VLE data**
CO_2- SO_2	0.024312	0.00117	[33]
CO_2- C_6F_6	0.043816	0.01167	[114] and new data by LEAP laboratory
CO_2- $TiCl_4$	0.07907	0.0456	[116]
CO_2- CF_3I	0.06323	0.00174	[115]
CO_2- SO_2F_2	0.09329 ± 0.05424 (determined using correlation developed in Chapter 2)		No experimental data

Table 47: Main thermodynamic properties of selected CO_2 mixtures

CO_2 mixture	**% mole composition of CO_2**	**$T_{cr,mix}$ [°C]**	**$P_{cr,mix}$ [bar]**	**MW_{mix} [g/mol]**	**P_{min} [bar]**
CO_2-SO_2	70%mol	79.5	97.5	50.03	69.6
	80%mol	64.3	91.7	48.02	78.6
CO_2-C_6F_6	80%mol	120.6	124.6	72.42	73.4
	85%mol	100.3	121.4	65.32	78.8
	90%mol	78.6	111.5	58.21	84.4
CO_2-$TiCl_4$	70%mol	224.4	232.5	87.71	91.2
	75%mol	192.1	247.1	80.43	95.5
	80%mol	149.6	243.6	73.15	98.7
CO_2-CF_3I	50%mol	86.1	65.4	119.96	48.3
	60%mol	75.5	69.2	104.77	56.5
	70%mol	64	71.6	89.58	64.9
CO_2-SO_2F_2	40%mol	64.8	64.8	78.84	56.2

5.4 **Thermodynamic cycle results and comparison**

This section presented the thermodynamic efficiency (η_{th}) of power cycles with selected CO_2 mixtures as working fluids. The motivation is to determine the sensitivity of main thermodynamic parameters on cycle thermodynamic efficiency (or cycle efficiency) and to find the optimum mixture composition which shows higher gain in cycle efficiency. In solar integrated power cycle, it's important to achieve higher cycle efficiency since it indicates the lower size of heat storage and solar field and also implies lower LCOE.

The cycle thermodynamic efficiency is defined as,

$$\eta_{th} = \frac{\dot{W}_{turbine} - \dot{W}_{comp/pump}}{\dot{Q}_{PHE}} \quad \text{Eq. 36}$$

Where, $\dot{W}_{turbine}$ gives power produced by turbine(s), $\dot{W}_{comp/pump}$ provides the compression work of pump or compressor (i.e. compressor in case of supercritical cycles and pump in case of transcritical cycles) and $\dot{Q}_{PHE}$ gives thermal power exchanged in primary heat exchanger. For comparison, the cycle boundary conditions for CO_2 mixtures are the same as considered in the case of pure sCO_2 recompression cycle (see Table 40). The only exception is the compression phase isentropic efficiency which is 88% for CO_2 mixtures (89% for pure CO_2) since the cycle is transcritical cycle with pump instead of compressor [117]. The minimum cycle pressure (or pump inlet pressure) in CO_2 mixtures is the bubble pressure corresponding to cycle minimum temperature of 50℃. Whereas, maximum cycle pressure (P_{max}) is decided to be higher than critical pressure ($P_{cr,mix}$) of the CO_2 mixture at given molar composition. For preliminary simulation, pressure drops in heat exchangers are ignored.

In the next chapter, all types of non-idealities in cycle calculations are taken into account including the pressure drops in heat exchangers and electromechanical efficiency of turbomachinery for more realistic calculation of cycle efficiency.

Moreover, for preliminary calculations in this chapter, the cycle configuration selected for CO_2 mixtures is simple recuperative transcritical cycle. For pure CO_2, simple recuperative and recompression cycle configurations are selected as the lower and the upper benchmarks respectively to evaluate cycle efficiency of different working fluids.

Cycle efficiency at different P_{max} and mixture molar composition (z_1) are illustrated in Figure 92 to Figure 96 for all CO_2 mixtures selected in this chapter. Considering CO_2-

C_6F_6 mixture at T_{max} of 550℃, the efficiency of transcritical recuperative cycle is higher than sCO_2 simple recuperative cycle at all P_{max} and mixture compositions. Moreover, the cycle efficiency is closer to efficiency of sCO_2 recompression cycle. Maximum cycle efficiency is obtained at 85% molar composition of CO_2 in the mixture that is 42.1% at P_{max} of 250 bar. While, the efficiency of sCO_2 cycle at P_{max} of 250 bar are 39.4% and 44.1% for simple recuperative cycle and recompression cycle respectively.

CO_2-SO_2 mixture as working fluid does not show higher cycle efficiency than sCO_2 cycles as evident from Figure 93. The reason of this is lower molecular complexity and lower molar mass of SO_2 than other dopants. Due to lower molecular complexity, the difference of specific heat between hot and cold streams of recuperator tends to increase which results in larger temperature differences and lower effectiveness of the recuperator and finally the lower cycle efficiency. The heat exchange in recuperator with different CO_2 mixtures is further elaborated in Figure 99**.**

CO_2-$TiCl_4$ also provides higher cycle efficiency with rise in molar composition of CO_2 from 70% to 80%. The potential gain is obtained for 80% CO_2 mixture at which cycle efficiency is close to recompression sCO_2 cycle (50.7% versus 50.8% at P_{max} of 250 bars).

For CO_2-CF_3I mixture, gain in efficiency is enabled compared to sCO_2 simple recuperative cycle but the values are lower than sCO_2 recompression cycle. The trend shows increase in cycle efficiency with increase in the molar composition of CF_3I in the mixture. Similarly, the cycle efficiency is higher than the sCO_2 cycle in case of CO_2-SO_2F_2 but with the expense of larger amount of SO_2F_2 in the mixture (i.e. 60% molar SO_2F_2).

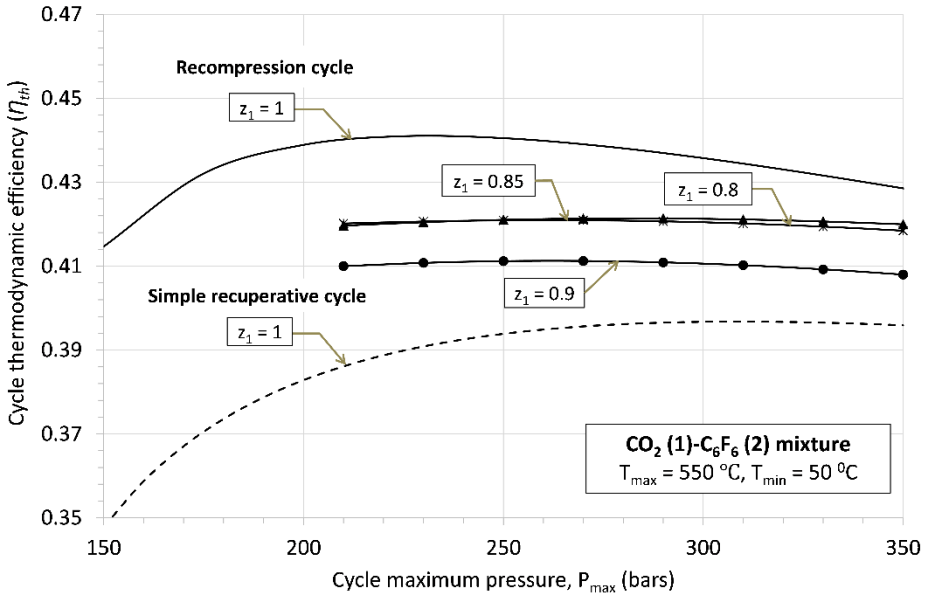

Figure 92: CO_2-C_6F_6 mixture cycle efficiency at varying cycle maximum pressure and mixture composition.

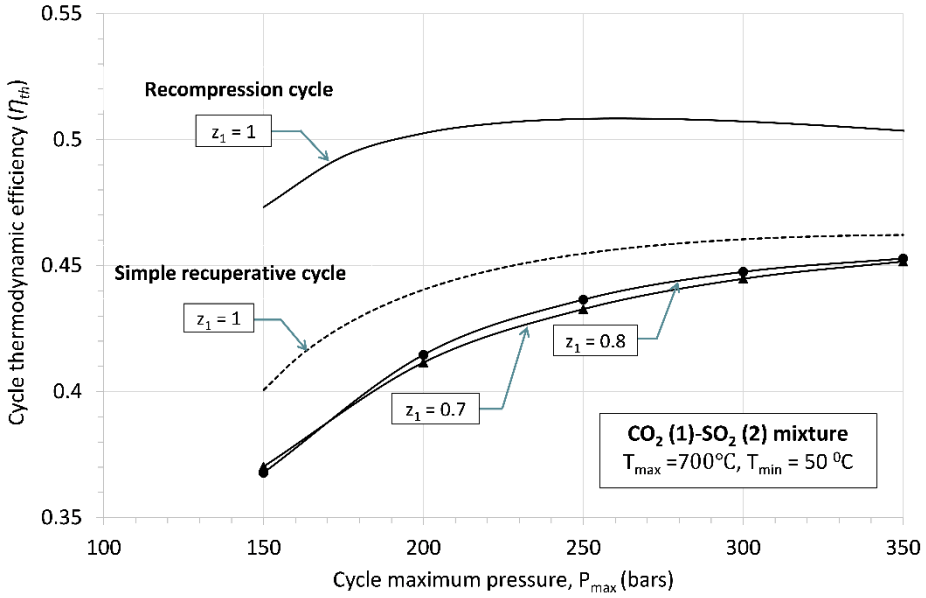

Figure 93: CO_2-SO_2 mixture cycle efficiency at varying cycle maximum pressure and mixture composition.

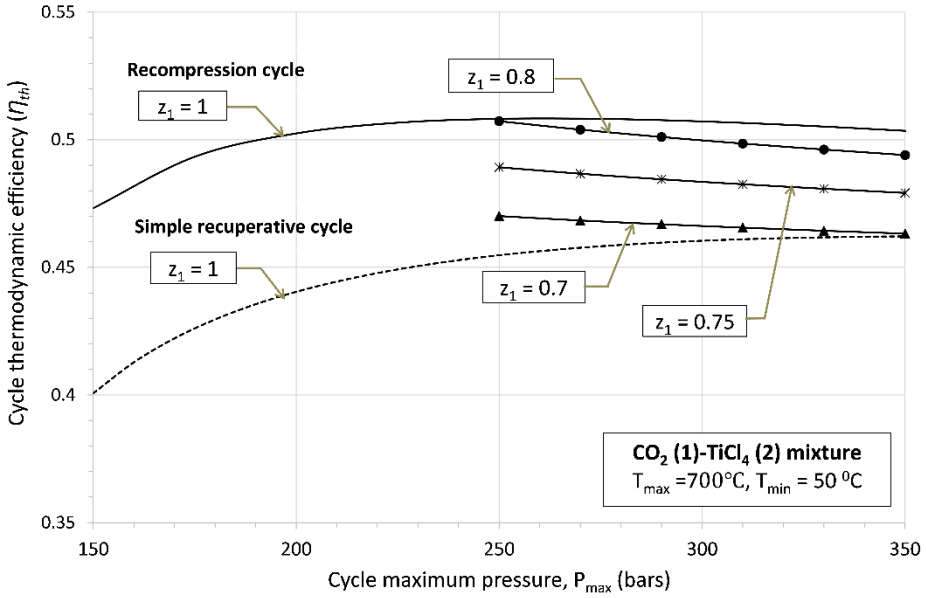

Figure 94: CO_2-$TiCl_4$ mixture cycle efficiency at varying cycle maximum pressure and mixture composition.

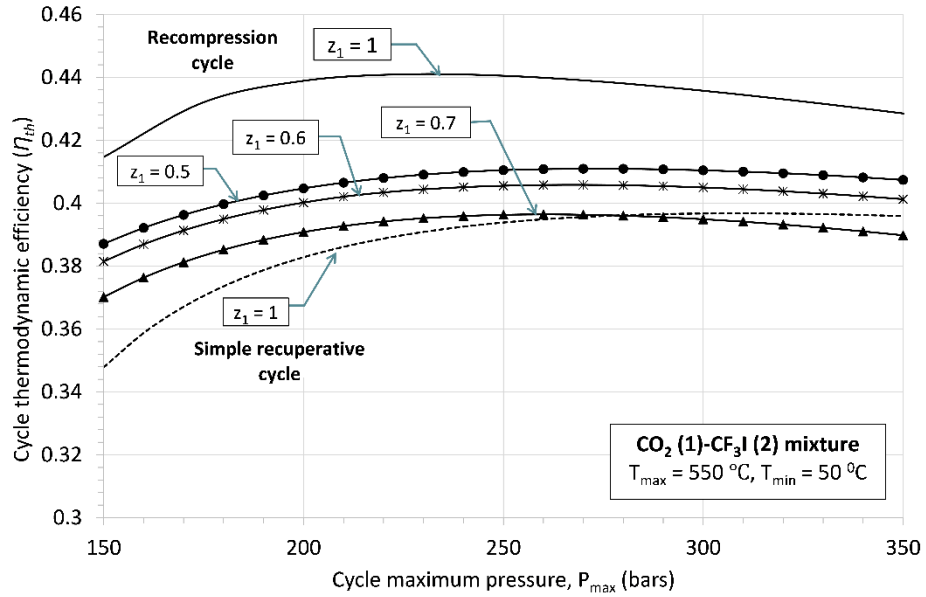

Figure 95: CO_2-CF_3I mixture cycle efficiency at varying cycle maximum pressure and mixture composition.

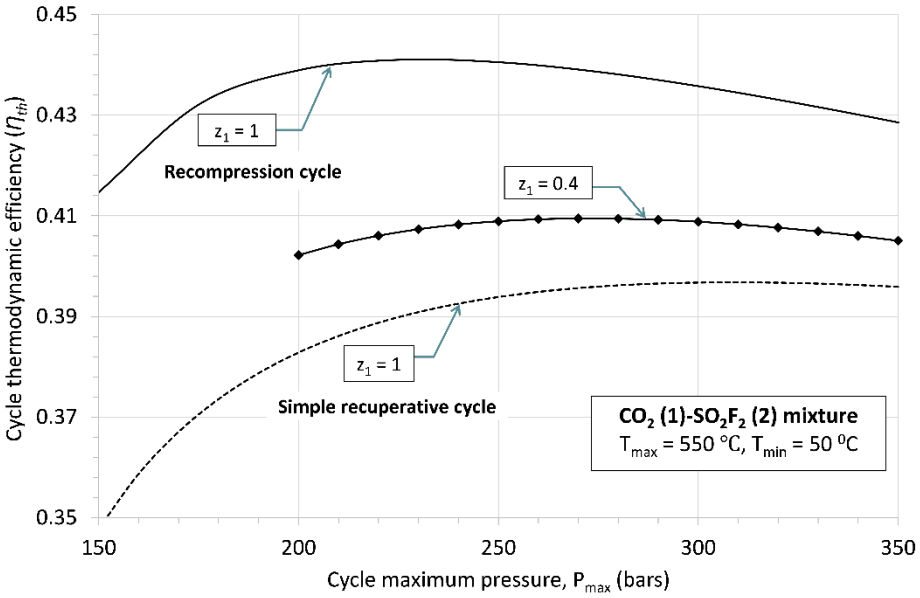

Figure 96: CO_2-SO_2F_2 mixture cycle efficiency at varying cycle maximum pressure and mixture composition.

From the evaluation of cycle efficiency at different P_{max} and composition, the mixture composition which enables higher cycle efficiency is selected for each CO_2 mixture and main thermodynamic performance indicators are assessed. The efficiency gain compared to sCO_2 simple recuperative cycle are shown in Figure 97 for all CO_2 mixtures operating in transcritical cycle at P_{max} of 250 bar.

Efficiency gain is defined as:

$$\Delta\eta_{th} = (\eta_{th})_{CO_2\ mixture} - (\eta_{th})_{CO_2} \qquad \text{Eq. 37}$$

Owing to well-known higher thermal stability of SO_2 and $TiCl_4$ dopants, cycle T_{max} of 700℃ is considered for mixtures with these dopants. However, T_{max} of 550 ℃ is considered for other mixtures because of two reasons: i) Thermal stability temperature of C_6F_6 is around 500℃ and ii) prospective thermal stability temperature of CF_3I and SO_2F_2 are expected to be around 500℃ based on the comparable values of standard enthalpy of formation per bond (as shown in Figure 70).

In perspective of cycle efficiency gain ($\Delta\eta_{th}$), CO_2-$TiCl_4$ gives maximum gain of +5.2%, CO_2-C_6F_6 comes on second priority with gain of +2.7% followed by CO_2-SO_2F_2 and CO_2-CF_3I mixtures with the gain of +1.5% and 1.1% respectively.

In addition to cycle efficiency gain, other thermodynamic cycle indicators are also assessed in order to explore full thermodynamic potential of CO_2 mixtures. The main

thermodynamic performance indicators which includes cycle specific work, pumping work, working fluid temperature at inlet of PHE, LMTD and UA of recuperator are compared among all CO_2 mixtures and pure CO_2 cycles as well. Table 48 reports the performance of CO_2 mixtures and pure CO_2 cycles considering constant P_{max} of 250 bar and T_{max} of 550℃ and Table 49 reports the performance at P_{max} of 250 bar and T_{max} of 700℃.

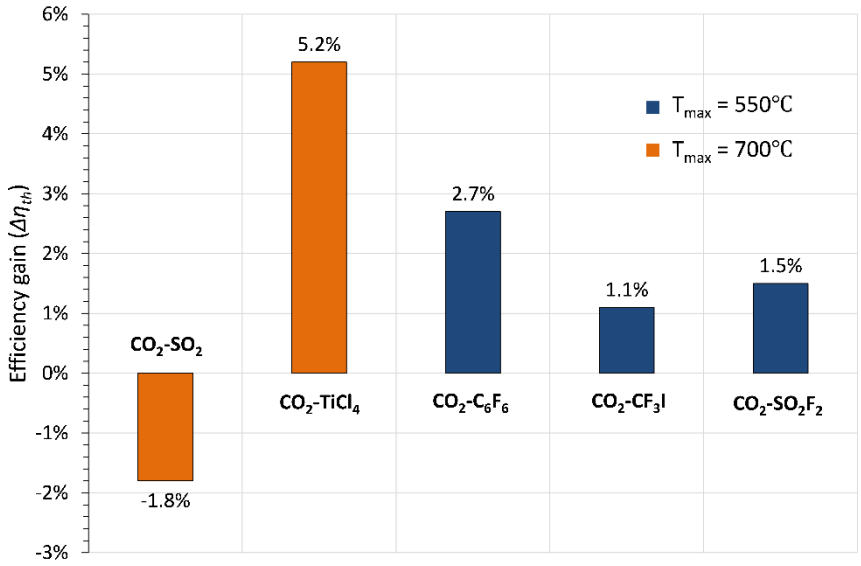

Figure 97: Gain in cycle efficiency of transcritical power cycles with CO_2 mixtures compared to sCO_2 simple recuperative power cycle

Table 48: Thermodynamic performance of cycles with CO_2 mixtures and pure CO_2 at T_{max} of 550 ℃ and P_{max} of 250 bar

Parameters	**CO_2-C_6F_6 [85%mol CO_2]**	**CO_2-CF_3I [60%mol CO_2]**	**CO_2-SO_2F_2 [40%mol CO_2]**	**sCO_2 simple recuperative cycle**	**sCO_2 Recompression cycle**
T_{max} [℃]	550	550	550	550	550
η_{th} [%]	42.1	40.6	40.8	39.4	44.1
$W_{turbine}$ [kJ/kg]	106.7	82.2	109.3	124.5	124.5
$W_{comp/pump}$ [kJ/kg]	21.8	19.3	25.7	37.1	45.4
$W_{specific}$ [kJ/kg]	84.9	62.9	83.6	87.4	79.1
$T_{in,PHE}$ [℃]	399.7	342	359.7	374.2	407.5
$LMTD_{recup}$ [℃]	18.2	21.9	24.8	28.8	6.5 (LTR) and 16.1 (HTR)
UA_{recup}/Q_{PHE} [1/K]	0.136	0.065	0.063	0.061	0.196

Table 49: Thermodynamic performance of cycles with CO_2 mixtures and pure CO_2 at T_{max} of 700 ℃ and P_{max} of 250 bar

Parameters	**CO_2-SO_2 [80%mol CO_2]**	**CO_2-$TiCl_4$ [80%mol CO_2]**	**sCO_2 simple recuperative cycle**	**sCO_2 Recompression cycle**
T_{max} [℃]	700	700	700	700
η_{th}	43.6	50.7	45.5	50.8
$W_{turbine}$ [kJ/kg]	168.2	91.2	149.6	149.6
$W_{comp/pump}$ [kJ/kg]	27.6	14.4	37.1	45.4
$W_{specific}$ [kJ/kg]	140.6	76.8	112.5	104.2
$T_{in,PHE}$ [℃]	427.9	541.3	505.5	538.98
$LMTD_{recup}$ [℃]	40.7	16.3	34.8	6.6 (LTR) and 19.9 (HTR)
UA_{recup}/Q_{PHE} [1/K]	0.039	0.227	0.064	0.196

Another important implication of adopting CO_2 mixtures in transcritical cycles is the reduction of power consumption in compression since compression is occurring below critical point compared to sCO_2 cycles in which compression is occurring above critical point (in supercritical phase). The adoption of mixtures enables the use of pump hence almost ten times reduction in compression work is achieved as evident from Table 48 and Table 49. Reduction in pumping work is a positive indication of reduction in CAPEX of power block.

Regarding expansion work, molecular weight and molecular complexity of the working fluid plays vital role. CO_2-SO_2 mixture possess lower molecular weight and lower molecular complexity than other mixtures which results in higher expansion work and consequently higher cycle specific work. Similar is the case of CO_2-SO_2F_2 mixture showing higher expansion work than CO_2-C_6F_6 and CO_2-CF_3I mixtures. In principle, higher cycle specific work demands lower mass flow rate of working fluid (for a constant power output) which leads to lower size of cycle components.

The significant part of size and CAPEX of power cycle is contributed by recuperators. Table 48 and Table 49 shows the parameter UA_{recup}/Q_{PHE} which is a relative indicator of size of recuperator in different cycles. Moreover, LMTD of recuperator is also shown to provide information about thermal match between and hot and cold streams in

recuperator. Lower value of LMTD implies good thermal match and larger size of the recuperator. As evident from results, CO_2-C_6F_6 and CO_2-$TiCl_4$ mixture which demonstrate higher gain in cycle efficiency demands larger recuperator size because of good thermal match and effective heat exchange in the recuperator compared to other mixtures. For better understanding of heat exchange in recuperators, Figure 98 and Figure 99 shows T-Q diagrams of recuperators for each CO_2 mixture.

Among all CO_2 mixtures, it is quite notable that log mean temperature difference (ΔT_{LM}) is the minimum in case of CO_2-C_6F_6 and CO_2-$TiCl_4$ mixtures. This is the manifestation of higher molecular weight and higher molecular complexity of such dopants which enable lower difference of heat capacities between hot and cold streams of recuperator. Another effect worth mentioning in these two CO_2 mixtures is the heat exchange in two-phase region i.e. inside the dome. In case of CO_2-C_6F_6, after 78% of heat exchange, minimum temperature difference (ΔT_{min}) occurs near dew point and then the hot stream enters two-phase region till point 6 (inlet of condenser). In case of CO_2-$TiCl_4$, hot stream enters two-phase region after 56% of heat exchange showing ΔT_{min} near dew point. This effect is also confirmed in T-s diagrams (Figure 100 and Figure 101) of the power cycles. In other CO_2 mixtures, heat exchange all through the recuperator is in vapor phase with ΔT_{min} occurring at cold side inlet (i.e. T_6-T_2). Recuperators in sCO_2 recompression cycle shows best heat exchange compared to sCO_2 simple recuperative cycle and transcritical cycles with CO_2 mixtures and this again confirms the importance of mass split and recompression in improving the thermodynamic performance of sCO_2 power cycles.

The working fluid temperature at the inlet of PHE (i.e. T_5) should be lower in order to achieve larger temperature differences (T_4-T_3) in PHE which leads to lower HTF mass flow rate for constant thermal power input and lower circulating pumping power of HTF. As seen from the T-s plots of cycles, CO_2 mixtures demonstrating lower cycle efficiency brings lower temperature at inlet of PHE and larger temperature difference (T_4-T_3). For example, CO_2-SO_2 mixture with cycle efficiency of 43.6% at T_{max} of 700℃ brings temperature difference of 272 ℃ across the PHE which is higher than temperature difference in CO_2-$TiCl_4$ cycle and CO_2-C_6F_6 cycle. Therefore, CO_2 mixtures showing lower cycle efficiency are beneficial in perspective of integration with solar receiver providing higher temperature difference in PHE which results in lower mass flow rate of HTF for constant thermal power input in PHE and higher thermal efficiency of receiver.

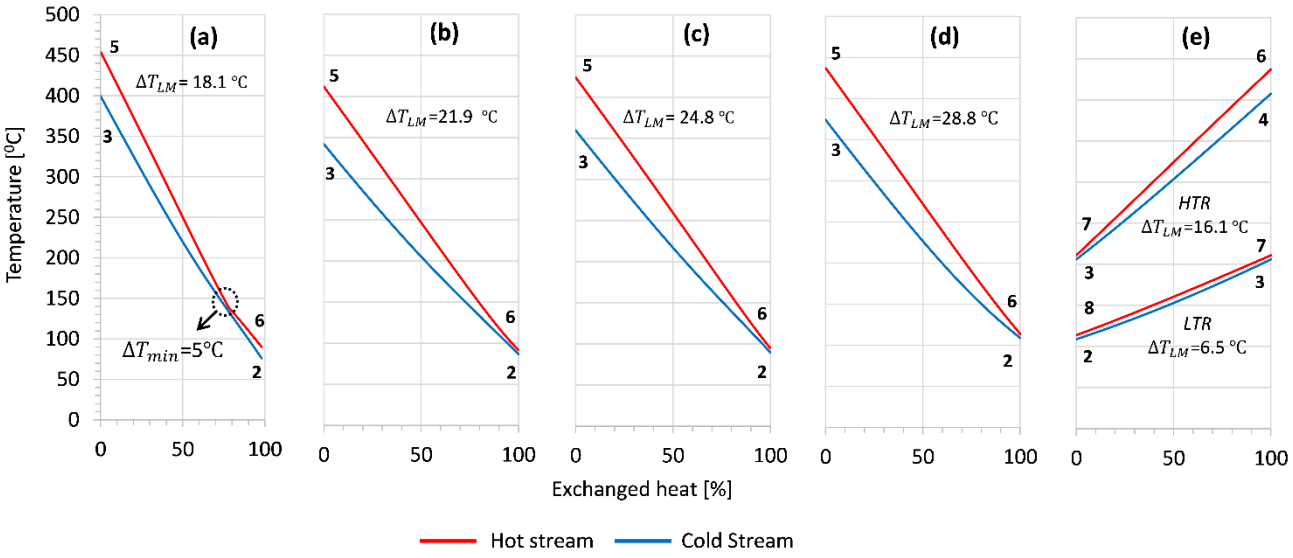

Figure 98: Temperature versus exchanged heat (T-Q) diagrams of recuperator of transcritical cycles with (a) CO_2-C_6F_6, (b) CO_2-CF_3I, (c) CO_2-SO_2F_2 working fluids compared to recuperator of (d) sCO_2 simple recuperative cycle and (e) sCO_2 recompression cycle. Turbine inlet temperature T_{max} is 550 °C for all working fluids.

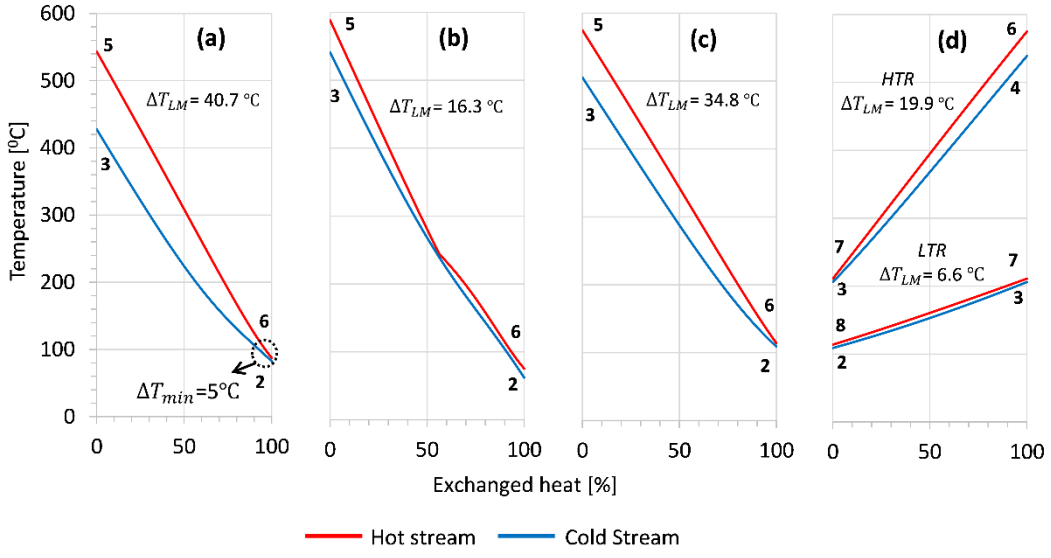

Figure 99: Temperature versus exchanged heat (T-Q) diagrams of recuperator of transcritical cycles with (a) CO_2-SO_2, (b) CO_2-$TiCl_4$ working fluids compared to recuperator of (c) sCO_2 simple recuperative cycle and (d) sCO_2 recompression cycle. Turbine inlet temperature T_{max} is 700 °C for all working fluids.

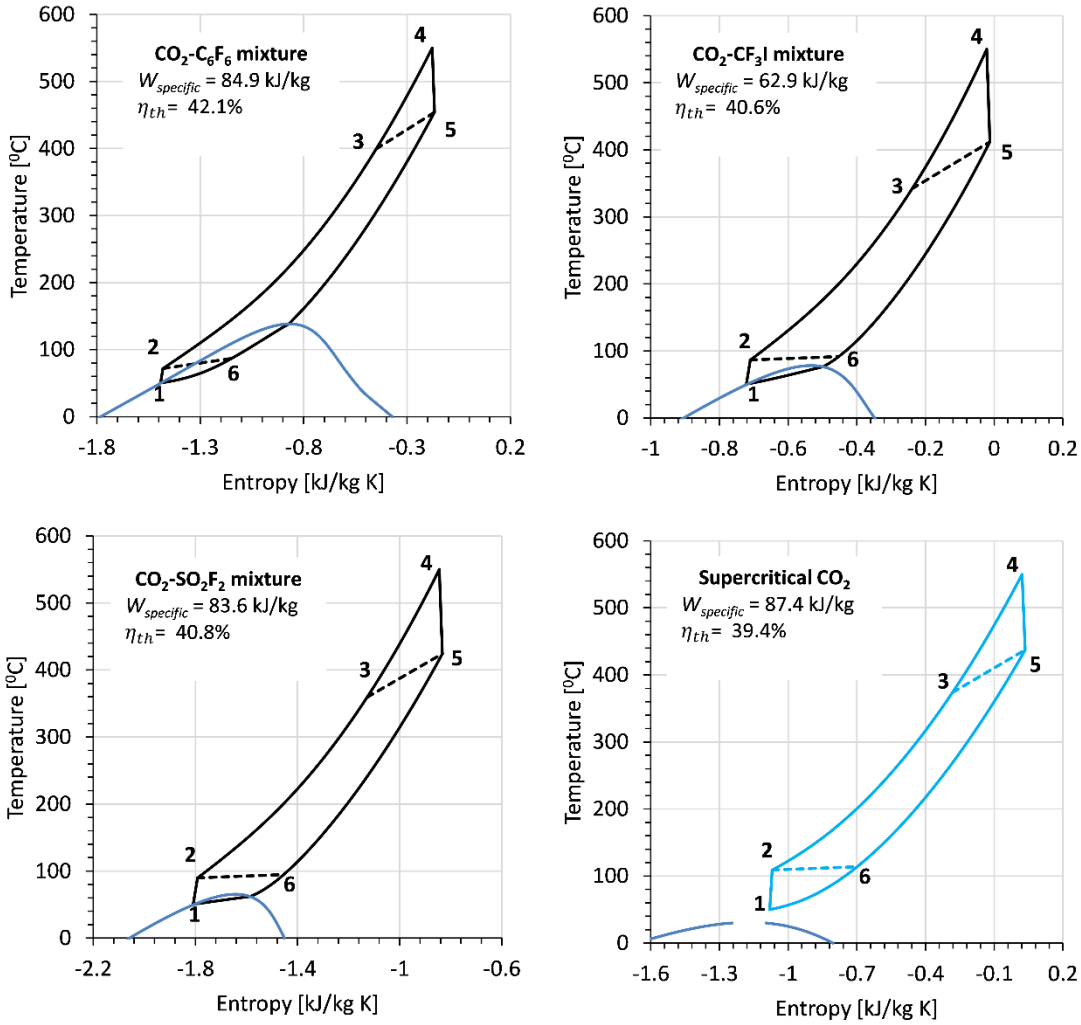

Figure 100: T-s diagrams corresponding to maximum efficiency point of CO_2 mixtures in simple recuperative transcritical power cycles compared with sCO_2 simple recuperative cycle (Blue shape diagram). Cycle maximum temperature is 550 ℃.

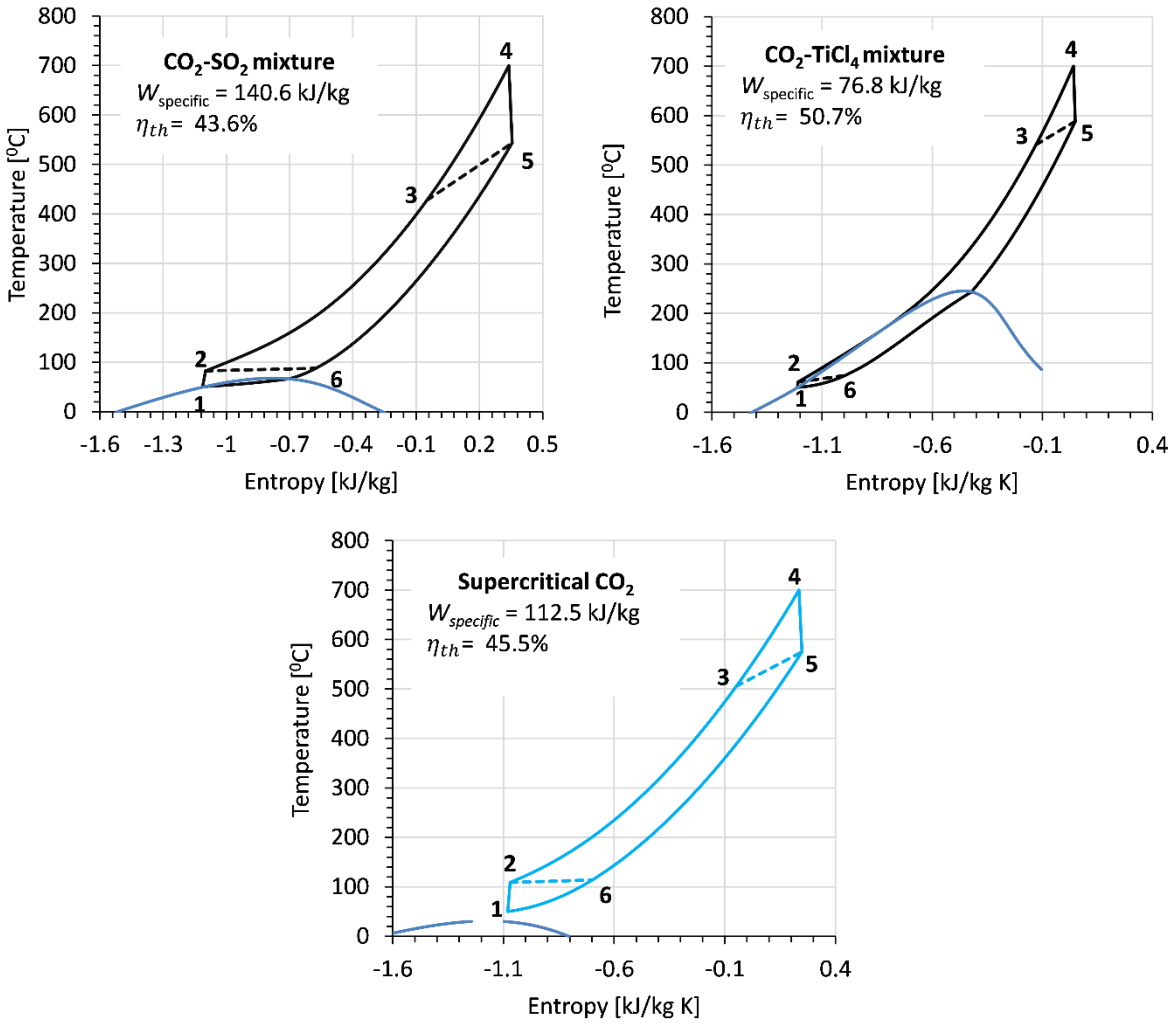

Figure 101: T-s diagrams corresponding to maximum efficiency point of CO_2 mixtures in simple recuperative transcritical power cycles compared with sCO_2 simple recuperative cycle (Blue shape diagram). Cycle maximum temperature is 700℃.

5.5 **Chapter Summary**

The primary goal of this chapter is to investigate the cycle efficiency of supercritical CO_2 cycles and transcritical CO_2-based mixture power cycles at high cycle minimum and maximum temperatures (T_{max}/T_{min} = 700°C/50°C). The presented thermodynamic analysis is relevant for concentrated solar power plants, which are typically installed in areas with high ambient temperatures (30 to 50 °C) as well as higher temperatures available at the solar receiver (500 to 700 °C).

The following are the key findings from the thermodynamic analysis:

- If pressure drops are neglected in the cycle components, the sCO_2 Recompression cycle can achieve maximum cycle efficiency of 50.8% considering T_{max}/T_{min} = 700℃/50℃ and 44.1% for T_{max}/T_{min} =550℃/50℃.
- sCO_2 Recompression cycle also demonstrates cycle efficiency higher than steam Rankine regenerative cycle with reheat at T_{max} of 500℃, 600℃ and 700℃.
- With the aim to enhance cycle efficiency of sCO_2 cycle, five CO_2-based binary mixtures are proposed as working fluids for transcritical power cycle. The first step in cycle thermodynamic analysis is to select equation of state and calibrate binary interaction parameter and validate the accuracy of equation of state. For this, Peng-Robinson EoS state is selected with van der Waals mixing rules (PR EoS-vdW) as property model to calculate thermodynamic phase behavior, enthalpy and entropy of CO_2-based mixture. Binary interaction parameter is determined using regression of VLE data with PR EoS-vdW as regression model.
- Binary interaction parameter for each CO_2-C_6F_6, CO_2-SO_2, CO_2-$TiCl_4$ and CO_2-CF_3I mixtures are obtained by regression of experimental VLE data. While, the binary interaction parameter of CO_2-SO_2F_2 mixture is obtained using the correlation developed in the chapter 2 (section 2.3) since No experimental VLE data corresponding to this mixture is currently available in the literature.
- Preliminary investigation of the five CO_2-based binary mixtures working fluids in transcritical simple recuperative cycle is performed in perspective of cycle efficiency, cycle specific work, size of recuperators (UA) and temperature at inlet of PHE.
- Gain in cycle efficiency in percentage points are +5.2, +2.7, +1.5, +1.1 for CO_2-$TiCl_4$, CO_2-C_6F_6, CO_2-CF_3I and CO_2-SO_2F_2 working fluid mixtures respectively compared to simple recuperative sCO_2 cycle.
- With the exception of the CO_2-$TiCl_4$ mixture, which has a cycle efficiency close to that of the sCO_2 recompression cycle (i.e. 50.7 percent), the cycle efficiency of all other mixtures is lower than that of the sCO_2 recompression cycle.
- In case of CO_2-SO_2 mixture working fluid in simple recuperative cycle, the cycle efficiency is lower than sCO_2 simple recuperative and sCO_2 recompression cycle. Albeit lower cycle efficiency, three positive impact of CO_2-SO_2 mixture compared to other CO_2 mixtures are: lower temperature at inlet of PHE (or *the higher temperature difference across PHE), higher cycle specific work and lower UA of recuperator when compared to sCO_2 cycles*.

- The cycle efficiency of a CO_2-SO_2 mixture can be improved by using a recompression cycle layout, and advanced cycle layouts such as precompression cycle layout and cycle layouts suggested in the literature for improved heat recovery should be investigated to determine the impact on cycle specific work, temperature difference across PHE, and size of recuperators.

In lieu of above considerations and results, the next chapter investigates cycle performance by incorporating the effect of advanced cycle layouts on thermodynamic performance adopting CO_2-SO_2 mixture working fluid in transcritical power cycle.

In addition to the primary goal of improving cycle efficiency, the other objectives are to improve cycle specific work, decrease the temperature of working fluid at the inlet of PHE (or increase the temperature difference across PHE), and reduce the size of recuperators; all these factors contribute towards lower cost of CSP power plant.

Chapter 6: Thermodynamic and economic assessment of transcritical power cycle operating with CO_2-SO_2 mixture as working fluid for CSP power plant

6.1 Introduction

In previous chapter, CO_2-$TiCl_4$ and CO_2-C_6F_6 are evidenced as promising working fluid mixtures because they show higher cycle efficiency compared to supercritical CO_2 simple recuperative cycle under same maximum and minimum temperatures. Albeit higher cycle efficiency, the main drawback in CO_2-$TiCl_4$ mixture is the reactivity of $TiCl_4$ with water; the violent reactivity of $TiCl_4$ in the presence of even small amount of moisture induce clogging in pipes due to formation of solid TiO_2 which is detrimental for cycle performance. Moreover, the CO_2-C_6F_6 mixture is also a promising working fluid mixture, but due to thermal stability limit, it can only be applicable for power cycles with maximum temperatures lower than 550 °C.

Sulphur dioxide (SO_2) is thermally stable at high temperature since it is produced from combustion of fossil fuels and from smelting of mineral ores containing sulphur, naturally it is produced from volcanic eruptions. The molecule of SO_2 consists of two strong S-O bonds with average bond energy of 522 kJ/mol. In addition, ozone depletion potential of SO_2 is negligible and it is a non-flammable gas, it does not react with water, air and CO_2. The only drawback of SO_2 is higher toxicity of level 3 according to NFPA 704 standard. However, it can be managed in closed cycle power plants where only limited amount of leakage are possible which can be handled by dedicated control system and by proper ventilation. Nevertheless, to ensure thermo-chemical stability at high temperatures, experimental tests are required to investigate the material compatibility of SO_2 with well-known Stainless steel and Inconel materials used in the fabrication of cycle components. The experimental activity to determine the thermo-chemical stability of CO_2-SO_2 is under-investigation in Fluid test Lab of University of Brescia.

Based on aforementioned characteristics of SO_2, it is qualified as promising candidate dopant for CO_2 based binary mixture and it can be applied to advanced solar power plants with maximum cycle temperature of 700 ℃ being its higher thermal stability.

In this chapter, CO_2-SO_2 mixture is investigated as working fluid in transcritical power cycle for advanced concentrated solar power (CSP) plant. The idea is to calculate cycle net efficiency of different cycle configurations and decide optimum mixture composition and cycle configuration assuming 100 MW net power output. The thermodynamic performance of transcritical power cycles with CO_2-SO_2 mixture working fluid is compared with supercritical carbon dioxide cycles under same operating conditions.

PC-SAFT EoS is used as property model due to comparatively higher accuracy of this model in computing thermodynamic properties of CO_2-SO_2 mixture as evidenced in Chapter 2. In contrast to the previous chapter, pressure drops in heat exchangers are also considered, and six different cycle layouts are examined.

6.2 Thermodynamic and economic model of power cycle

Property model

The identification of a property model for CO_2-SO_2 mixture and for pure CO_2 is the basic requirement for developing a thermodynamic cycle model. In Chapter 2, PC-SAFT EoS is chosen as the reference property model for CO_2-SO_2 mixture based on its accuracy in predicting thermodynamic properties when compared to PR EoS and GERG 2008 EoS. As a result, in this chapter, PC-SAFT EoS is used for thermodynamic cycle analysis with a CO_2-SO_2 mixture. For pure CO_2, Span and Wagner EoS is decided to conduct thermodynamic cycle analysis. The Span and Wagner EoS covers a wide temperature and pressure range and it has been proven to be the most accurate EoS for CO_2 [118].

Cycle boundary conditions and assumptions for simulation

Cycle thermodynamic simulation is carried out in Aspen plus v11 simulation environment. The cycle maximum temperature (or turbine inlet temperature) is fixed at 700°C both for the CO_2+SO_2 mixture and pure CO_2. As anticipated, this temperature represents the target for the next generation CSP solar tower power plants. Furthermore, design ambient temperature of 35°C is assumed in order to replicate hot and arid environment typical of CSP sites and a corresponding minimum cycle temperature of 51°C is set. Cycle maximum pressure (or turbine inlet pressure) is varied from 200 bar to 400 bar.

To deal with temperature differences in primary heat exchanger (PHE), it is not practical assumption to fix cold end temperature difference constant because the temperature of

working fluid entering PHE is varying depending on the cycle layout and working fluid composition. However, the temperature difference at hot end of PHE is maintained constant since the temperature of hot HTF and turbine inlet temperature are fixed. Therefore, the cold end temperature difference is computed by relationship given in *Figure 102*. As required, the temperature difference in cold side of PHE is higher at lower temperature of working fluid and the difference is lower at high temperature of working fluid at inlet of PHE. The positive effect of larger temperature at cold end is the larger log mean temperature difference (ΔT_{ML}) which would reduce the cost of PHE.

Other assumptions including pressure drops in heat exchangers, electro-mechanical efficiency of turbomachinery and auxiliary consumption in air cooled condenser are reported in Table 50.

Table 50: Assumptions in thermodynamic cycle analysis of power cycles considered in this chapter

Cycle minimum temperature	51°C
Cycle maximum temperature	700°C
Compression Isentropic efficiency	88%
Expansion Isentropic Efficiency	92%
MITA (Minimum Internal Temperature Approach) of PCHEs	5°C
DP/P Main PHE	2%
DP/P Secondary PHE	2%
DP/P PCHE HP Side	0.3%
DP/P PCHE LP Side	1.5%
DP/P Condenser	2%
Expander electromechanical efficiency	98.7%
Pump/compressor electromechanical efficiency	97%
Air-cooled condenser auxiliary consumption	1.5% QCOND

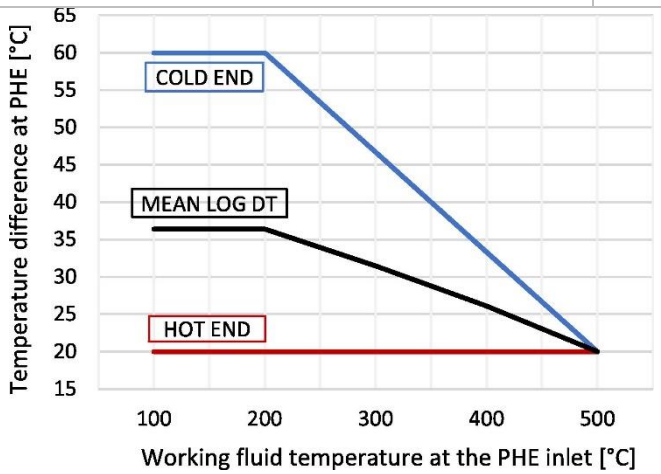

Figure 102: Temperature difference at hot end and cold end of PHE as a function of working fluid temperature at inlet of PHE.

Definition of CO_2-SO_2 mixture composition

The molar composition of the CO_2-SO_2 mixture is determined using the criterion established for the transcritical cycle. As described in Chapter 5, the criterion is to choose a mixture composition with a critical temperature that is at least 15°C higher than the cycle minimum temperature ($T_{cr,mix} - T_{min} \geq 15℃$). This criterion allows condensation of working fluid at inlet of compression phase thus enables reduction in compression work. Based on this criterion, the critical temperature of mixture should be greater than 65℃ when cycle minimum temperature is set at 51℃. The criterion allows for the selection of a mixture of 85% molar CO_2, 80% molar CO_2, 75% molar CO_2, and 70% molar CO_2. Table 51 reports the critical temperature, critical pressure and difference between critical temperature of mixture and cycle minimum temperature for different mixture molar composition.

Molar compositions greater than 85% molar CO_2 are not feasible because the critical temperature is too close to the cycle minimum temperature. Furthermore, molar compositions less than 70% molar CO_2 result in too high critical temperature and higher SO_2 content, which is undesirable knowing the toxicity of SO_2.

The same composition selection criteria were used in chapter 4 with PR EoS as the property model. The selection of CO_2 mixture composition is influenced by the use of different property models. As with PR EoS, 85% molar CO_2 is not a viable option, but PC-SAFT EoS allows for this composition based on the same criteria.

Table 51: Critical temperature, critical pressure and difference between $T_{cr,mix}$ and T_{min} for different molar compositions of CO_2-SO_2 mixture

Molar composition of CO_2	**$T_{cr,mix}$ (℃)**	**$P_{cr,mix}$ (bars)**	**$T_{cr,mix} - T_{min}$**
90% molar CO_2	57.7	97.9	6.7
85% molar CO_2	64.1	98.7	13.1
80% molar CO_2	70.4	101.5	19.4
75% molar CO_2	76.7	104.8	25.7
70% molar CO_2	84.1	107.4	33.1
60% molar CO_2	98.4	110.6	47.4
50% molar CO_2	111.7	111.2	60.7

Cycle layouts

In the literature, various cycle layouts are proposed with the goal of improving cycle efficiency and heat recovery. This chapter selects seven different cycle layouts from the best practice in the literature. The first layout, known as the simple recuperated cycle, is the most basic, in which a single recuperator is used to recover heat from turbine exhaust. In the second layout, a reheater and a turbine are added to raise the heat introduction temperature of the cycle, leading to high cycle efficiency. The third layout, known as the partial heating cycle, consists of two primary heat exchangers with the goal of recovering more heat from the heat source. Recompression cycle layout is a widely accepted cycle layout in literature for CSP and nuclear power plants due to its higher cycle efficiency. Precompression cycle is known for its higher turbine specific work because the pressure ratio of turbine in this layout is greater than pressure ratio of main compressor. Dual recuperated and cascade cycle are effective in heat recovery from heat source but with compromise of lower cycle efficiency. Every cycle layout has its own distinct characteristics, and the appropriate layout is determined by the working fluid, operating conditions and the purpose of the study. However, given the operating conditions of this study, it would be interesting to investigate the potential of these layouts using a CO_2-SO_2 mixture as the working fluid in perspective of thermodynamic performance and CAPEX of power cycle.

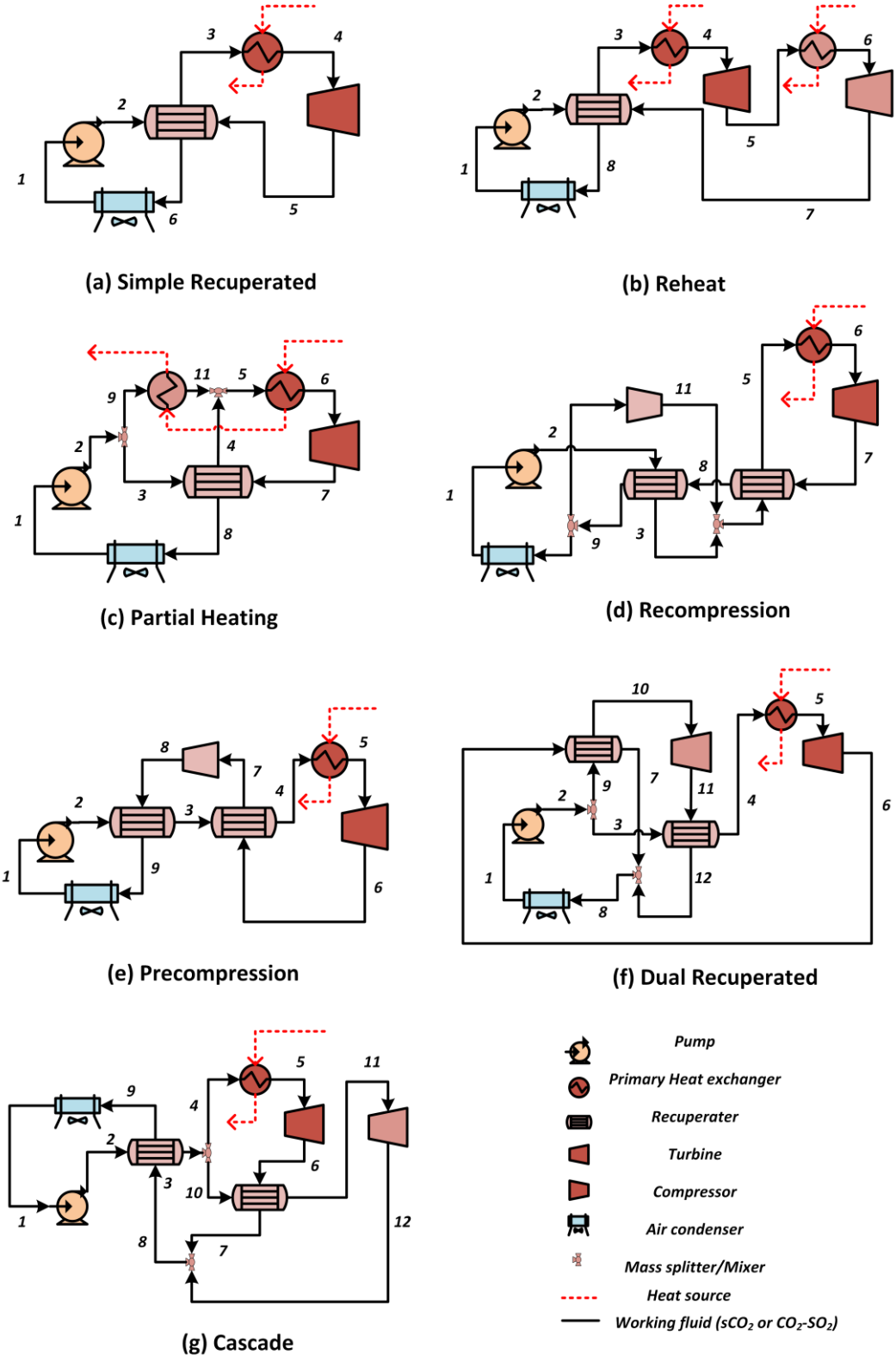

Figure 103: Cycle layouts considered in this work for power block of CSP power plant

Performance indicators

To evaluate thermodynamic performance of power cycles, four key performance indicators are decided. They are the gross cycle efficiency, the cycle specific work, the

temperature of the working fluid at the inlet of the PHE and the relative size of the recuperators.

Three of the four indicators are defined as:

$$\eta_{cycle} = \frac{Power_{Expansion} - Power_{Compression}}{Q_{IN,PHE}}$$

Eq. 38

$$w_{Specific,Cycle}\ [kJ/kg] = \frac{Power_{Expansion} - Power_{Compression}}{\dot{m}_{Cycle}}$$

Eq. 39

$$UA_{PCHE}/Q_{IN}\ [1/K] = \frac{\sum UA_{PCHE,i}}{Q_{IN,Cycle}}$$

Eq. 40

In definition of cycle efficiency, the power consumed or produced during the compression and expansion phase is computed using isentropic efficiencies of turbomachinery and $Q_{IN,PHE}$ is the thermal power introduced in the cycle by the hot source in PHE. In CSP power plants, cycle efficiency of power cycle is an important indicator which determines the size of solar field and specific CAPEX of power plant.

Cycle specific work is computed using the mass flow rate of working fluid during the compression phase ($\dot{m}_{Compression}$) to conduct a consistent comparison among all the plant layouts. The only exception is in recompression cycle layout, where two compression phases and only one expansion phase are present: in this case the specific work is computed using the mass flow rate in expansion phase ($\dot{m}_{Expansion}$). The cycle specific work plays key role in thermodynamic power cycle since it accounts for:

1. The overall working fluid inventory (generating an additional cost when non-conventional working fluids are considered).
2. The mass flow rate of the cycle (high mass flow rates increase the size of the cycle components and their cost),
3. The environmental impact of any leakage of the working fluid in case of leakages or damages.

The temperature of the working fluid at the inlet of the primary heat exchanger (PHE) is another important indicator of thermodynamic performance and costs in CSP power plants, because the lower the temperature of heat introduction, the greater the temperature difference of the HTF. High temperature differences of the HTF in CSP plants would result in:

1. An increase in receiver thermal efficiency due to a corresponding reduction in thermal losses between the receiver and the environment.
2. Lower HTF flow rates at constant thermal input, reducing the size and cost of the TES.

The final parameter, Overall heat transfer coefficient times area of heat exchanger (UA_{PCHE}) is computed in Aspen Plus by discretization of heat exchange domain into 200 steps and summing up UA in each step. The expression UA_{PCHE}/Q_{IN} accounts for the physical dimensions of the recuperators: because the various plant layouts differ significantly, this parameter indicates the relative size of recuperators.

Economic model

In a typical CSP plant, about 15% to 30% of overall plant CAPEX is shared by power cycle depending on the dimensions of TES and efficiency of power block. In this section, CAPEX of power cycle is considered as crucial indicator to study economic benefits of CO_2-SO_2 mixture cycle over sCO_2 cycle. To calculate CAPEX of power cycle, equipment cost of each component and direct costs are summed up. The equipment cost functions of cycle components proposed by Weiland *et* al [119] has been selected as, to the authors knowledge, it is one of the most updated and they are based on a detailed review of cost functions for sCO_2 power cycles considering data provided by real vendors. To calculate the CAPEX of a power cycle, the equipment cost of each component and the direct costs are added together. The equipment cost functions of cycle components proposed by Weiland *et* al [119] were chosen because, to the best of the authors' knowledge, they are the most up to date and are based on a thorough review of cost functions for sCO_2 power cycles using data provided by real vendors. Except for PHE, the cost function presented by Carlson *et* al [120] has been selected since it is based on UA of PHE unlike the cost function presented by Weiland *et* al. A more conservative results are hence expected on the PHE side for this reason. Lastly, the cost function of sCO_2 compressor presented by Weiland is used also adopted for pumps due to lack of available cost functions in literature which covers turbomachinery dealing with highly compressible liquids (slightly below

critical point of mixture). All cost functions with relevant references are shown in *Table 52*.

Table 52. Cost functions adopted in this work for the modelling of the CAPEX of CO_2-based power cycles

Component	Cost Function [M$]	Reference
Turbine	$3.49 \cdot 182600 \cdot W\ [MW]^{0.5561}$	Weiland, 2019 [119]
Compressor / Pump	$1.23 \cdot W\ [MW]^{0.3992}$	Weiland, 2019 [119]
PCHE	$49.45 \cdot UA\ [MW/K]^{0.7544}$	Weiland, 2019 [119]
PHE	$3.5 \cdot UA[MW/K]$	Carlson, 2017 [120]
Condenser	$32.88 \cdot UA[MW/K]^{0.75}$	Weiland, 2019 [119]
Generator	$0.1089 \cdot W[MW]^{0.5463}$	Weiland, 2019 [119]
Motor	$0.3994 \cdot W[MW]^{0.606}$	Weiland, 2019 [119]
Fraction of Direct Costs	All components except PCHE: 20% PCHE: 5%	Weiland, 2019 [119]

6.3 **Results**

Effect of working fluid mixture composition and cycle maximum pressure on thermodynamic performance of power block

In first step, thermodynamic performance indicators of sCO_2 cycle layouts and CO_2-SO_2 cycle layouts are studied varying molar composition of CO_2-SO_2 mixture and maximum cycle pressure. This necessary step enables to decide best cycle layout and composition of the working fluid. Figure 104 to Figure 107 illustrate effect of maximum cycle pressure and working fluid composition on four performance indicators of the power block defined in previous section.

Simple recuperative and reheat cycle layouts with CO_2-SO_2 mixture does not show significant improvement in cycle efficiency compared to sCO_2 cycle counterparts.

Recompression cycle layout with CO_2-SO_2 mixture show significant improvements in thermodynamic performance compared to sCO_2 cycle counterpart. Increase in gross cycle efficiency is 2 percentage points (i.e. 50.8% versus 48.8% at P_{max} of 250 bar and 85% molar CO_2). Depending upon composition, there is less than 40℃ drop in temperature at inlet of PHE, more than 20% reduction in relative size of recuperators and more than 20% gain in gross specific work of cycle.

In Precompression cycle layout, use of CO_2-SO_2 mixture enables 0.4 percentage points increase in cycle efficiency (i.e. 46.9% versus 46.5% at P_{max} of 250 bar and 85% molar CO_2). In addition, depending on composition, there is less than 70℃ drop in temperature at inlet of PHE, more than 40% decrease in relative size of recuperators and more than 30% gain in gross specific work of cycle.

It is also worth noting that highest cycle specific work among all layouts is given by Precompression cycle layout since in this layout expansion ratio of turbine is higher than compression ratio of the pump.

For all cycle layouts, overall trend shows that cycle specific work is increasing and relative size of recuperators is decreasing with increase in molar composition of SO_2 in the mixture.

The two cycle layouts which show lowest cycle efficiency are dual recuperated and cascade cycle layout. However, these layouts are way better than recompression and Precompression cycles in terms of temperature difference across PHE. For CO_2-SO_2 mixture, temperature at inlet of PHE for cascade and dual recuperated cycle is around 180 to 250℃ (see Figure 2) which results in temperature difference of working fluid in PHE around 450 to 520 ℃ (as turbine inlet temperature is fixed at 700℃). On other hand, this temperature difference in recompression cycle is within 150 to 200 ℃.

In the same way, compared to sCO_2 counterparts, dual recuperated and cascade cycle with CO_2-SO_2 mixture show comparable cycle efficiencies whereas considerable reduction in temperature at inlet of PHE (or gain in temperature difference in PHE). Around 100 to 130℃ reduction in temperature at inlet of PHE is enabled by adopting CO_2-SO_2 mixture in dual recuperated and cascade cycle layouts compared to sCO_2 counterparts. This reduction in temperature is mainly due to lower temperature difference in compression step of transcritical cycle compared to compression step in sCO_2 cycle.

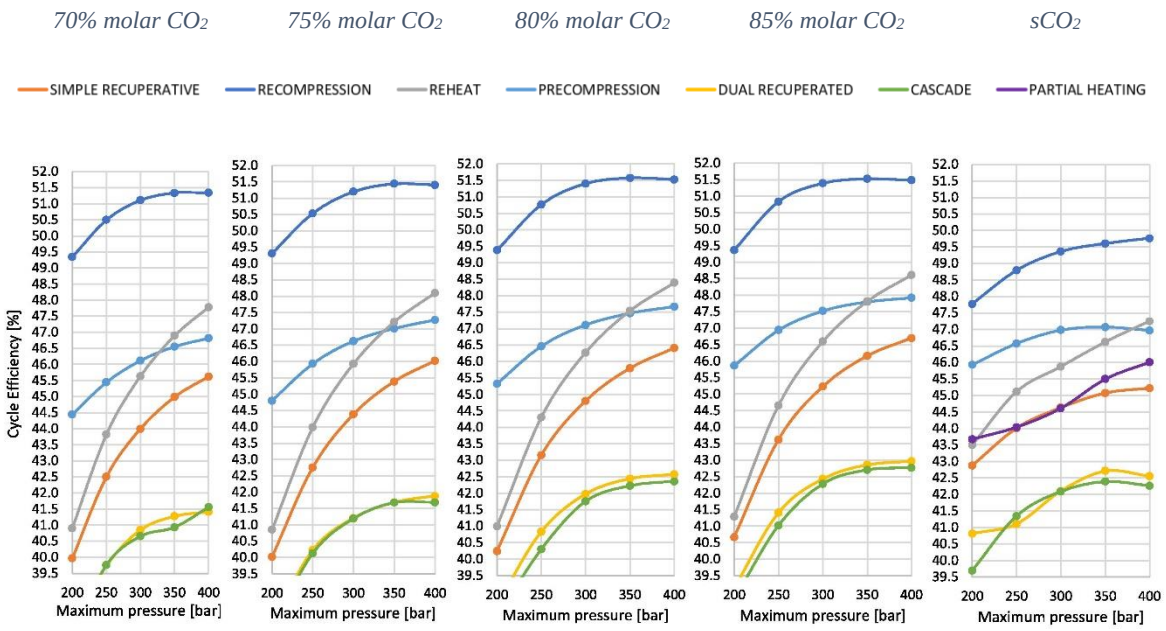

Figure 104: Effect of cycle maximum pressure and working fluid composition on cycle efficiency of power block for various cycle layouts.

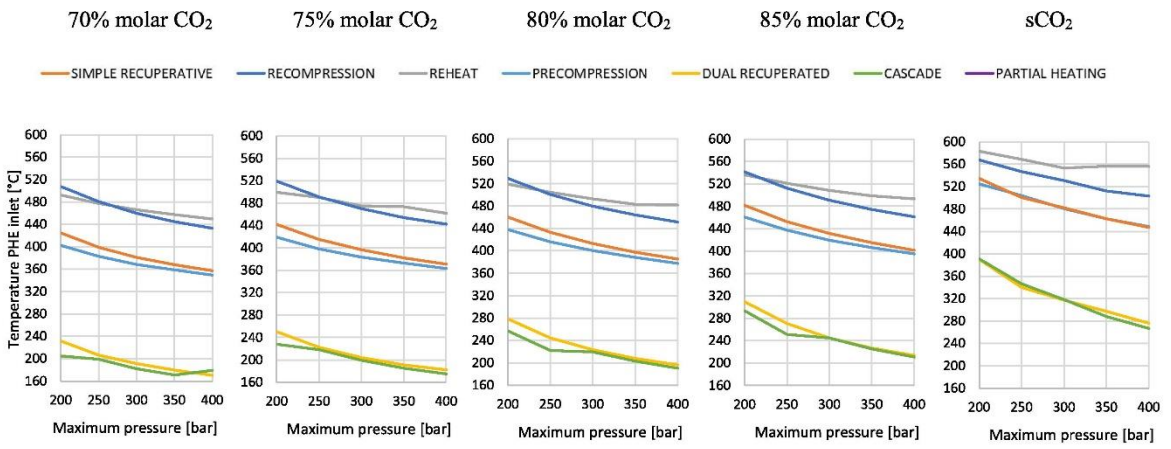

Figure 105: Effect of cycle maximum pressure and working fluid composition on temperature at inlet of PHE of the working fluid for various cycle layouts.

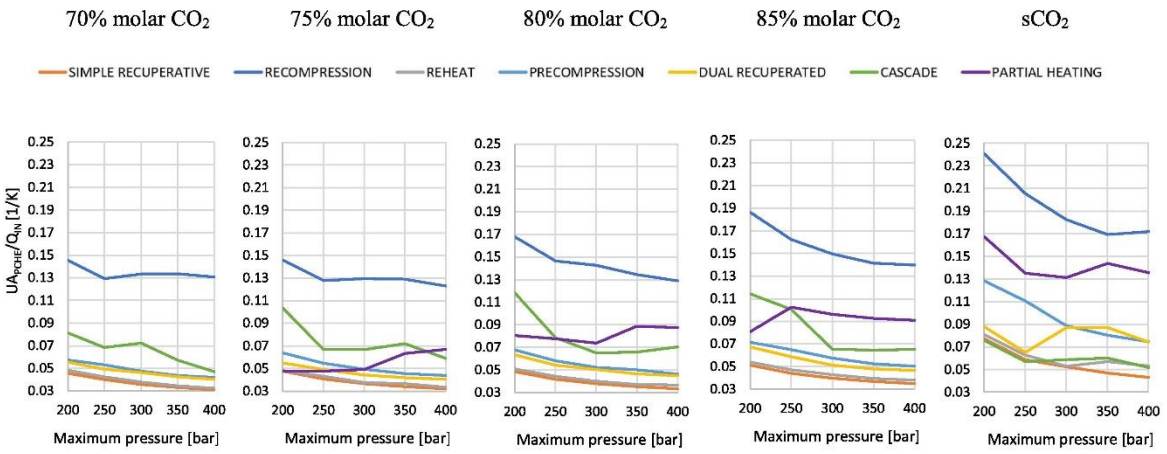

Figure 106: Effect of cycle maximum pressure and working fluid composition on relative size of recuperators of the power block for various cycle layouts.

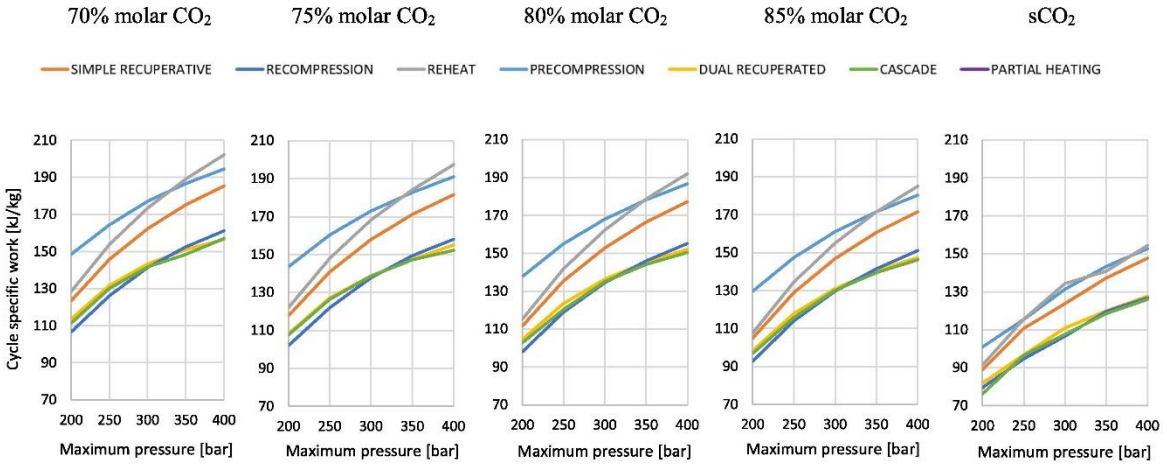

Figure 107: Effect of cycle maximum pressure and working fluid composition on gross specific work of the power block for various cycle layouts.

Analysis at optimal molar composition of working fluid mixture

Based on cycle efficiency, the most efficient mixture composition is 85% CO_2-15% SO_2 mixture for all cycle layouts therefore this composition is selected as optimal one. Unfortunately, relative size of recuperators is higher and cycle specific work is lower at this composition; this is attributed to reduction in molar mass of mixture with high CO_2 content and lower molecular complexity.

Once the thermodynamic indicators of sCO_2 cycles and CO_2-SO_2 mixture transcritical cycles have been studied, the potential benefits of transcritical cycles have been highlighted. The next step is to conduct a detailed analysis taking into account the optimal mixture composition and cycle maximum pressure at a state-of-the-art value of 250 bar.

All thermodynamic indicators and power balance of power cycle with CO_2-SO_2 mixture and sCO_2 are recorded in Table 53 and Table 54 respectively. The results shown corresponds to gross power output of 100 MW. The results also show power block electrical efficiency which is computed by incorporating electro/mechanical losses and heat rejection auxiliary consumption according to assumptions given in Table 50. In viewpoint of power block electrical efficiency, all cycle layouts with CO_2-SO_2 mixture outperforms sCO_2 cycle.

Pumping work of HTF in PHE is an important parameter in determining the net electrical efficiency of a CSP integrated power block. The temperature difference of the working fluid in PHE is greater in the CO_2-SO_2 mixture power block than in the sCO_2 power block, implying a lower mass flow rate of HTF in PHE (for constant thermal power input) and thus less pumping work. This feature enhances the advantages of CO_2-SO_2 mixture in power block over sCO_2 power block.

The cycle process diagram are plotted in temperature-entropy thermodynamic plane for all cycle layouts at optimal composition and P_{max} of 250 bar. For each cycle layout, comparison between CO_2-SO_2 mixture transcritical cycle and sCO_2 power cycle is presented. The lines of heat source are also shown to illustrate differences in temperature difference of HTF in PHE of all cycle layouts (See Figure 108 to Figure 114).

Table 53. Performance of the power cycles working with the innovative CO_2+SO_2 mixture for maximum pressure of 250 bar

	Transcritical CO_2+SO_2 Cycle – 85% Molar CO_2 – P_{max} = 250 bar						
	Simple Recuperative	Reheated	Recompression	Precompression	Cascade	Partial heating	Dual recuperated
Cycle Efficiency [%]	43.62	44.66	50.84	46.94	41.02	43.62	41.41
Specific Work [kJ/kg]	129	134	114	147	116	129	118
UA_{PCHE}/Q_{IN} [1/K]	0.044	0.047	0.162	0.065	0.101	0.102	0.059
UA_{PHE} [MW/K]	9.32	11.4	9.17	8.49	7.3	11.78	7.40
T inlet of PHE [°C]	453	521	513	437	251	-	270
Compression power [MW]	20.7	19.8	35.1	48.6	23.0	20.7	22.6
Expansion power [MW]	122.9	122.0	137.9	151.9	125.4	122.9	124.9
Heat rejected [MW]	132.1	126.6	99.5	116.7	147.1	132.2	144.8
Electro/mechanical losses [MW]	2.2	2.2	2.9	3.3	2.3	2.2	2.3
Heat rejection auxiliary [MW]	2	1.9	1.5	1.7	2.2	2	2.2
Power block electric efficiency [%]	41.81	43.87	48.67	44.65	39.22	41.81	39.58

Table 54. Performance of the sCO_2 power cycles for maximum pressure of 250 bar

	Supercritical CO_2 Cycle – P_{MAX} = 250 bar						
	Simple Recuperative	Reheated	Recompression	Precompression	Cascade	Partial heating	Dual recuperated
Cycle Efficiency [%]	44.01	45.11	48.79	46.57	41.34	44.04	41.10
Specific Work [kJ/kg]	111	115	95	115	97	112	97
UA_{PCHE}/Q_{IN} [1/K]	0.059	0.063	0.206	0.111	0.057	0.135	0.065
UA_{PHE} [MW/K]	11.7	11.3	10.6	11.2	8.6	11.75	8.6
T inlet PHE [°C]	501	569	547	504	347	-	340
Compression power [MW]	45.0	42.9	50.9	59.0	39.9	49.6	45.5
Expansion power [MW]	148.4	146.2	154.5	163.0	143.0	153.2	148.9
Heat rejected [MW]	131.4	125.6	108.7	119.2	146.3	131.5	148.1
Electro/mechanical losses [MW]	3.4	3.3	3.6	4	3.1	3.5	3.3
Heat rejection auxiliary [MW]	2.0	1.9	1.6	1.8	2.2	2.0	2.2
Power block electric efficiency [%]	41.75	42.88	46.34	44.00	39.20	41.69	38.89

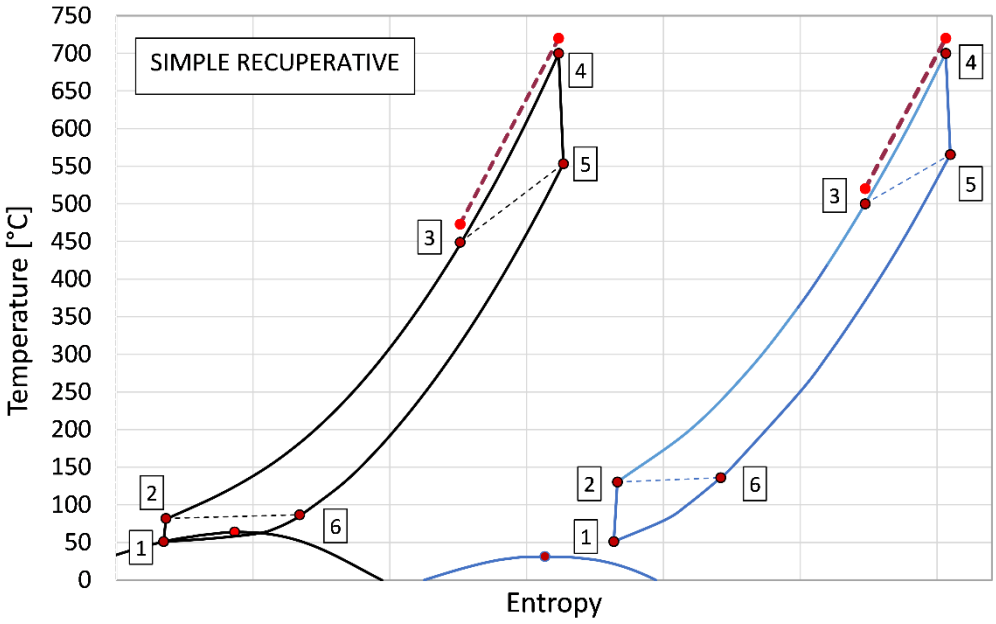

Figure 108: T-s diagram of simple recuperative cycle layout with CO_2-SO_2 mixture (on left) and supercritical CO_2 (on right). Dotted red line show heat source.

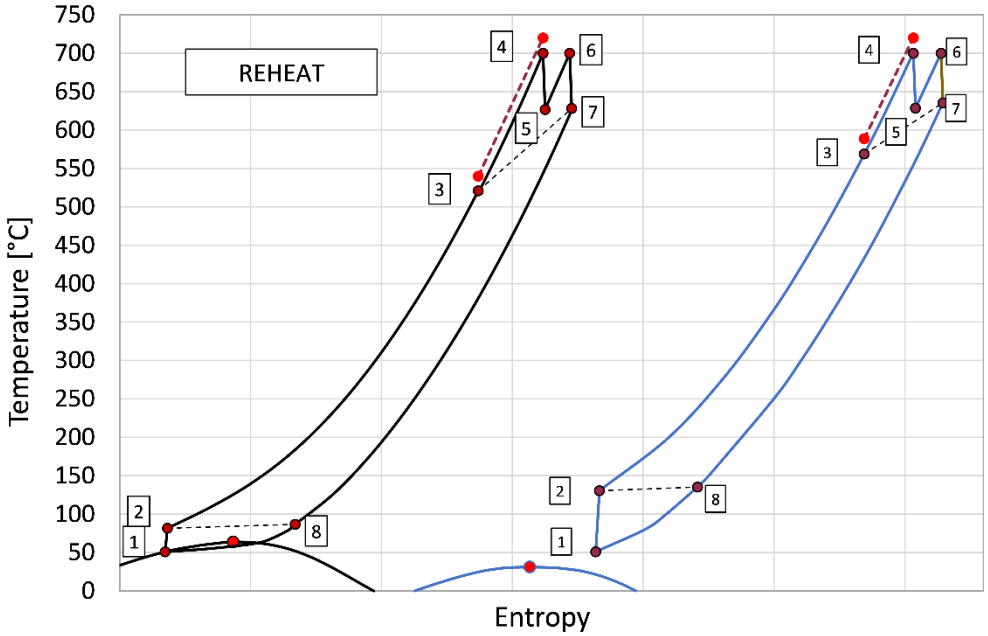

Figure 109: T-s diagram of reheat cycle layout with CO_2-SO_2 mixture (on left) and supercritical CO_2 (on right). Dotted red line show heat source.

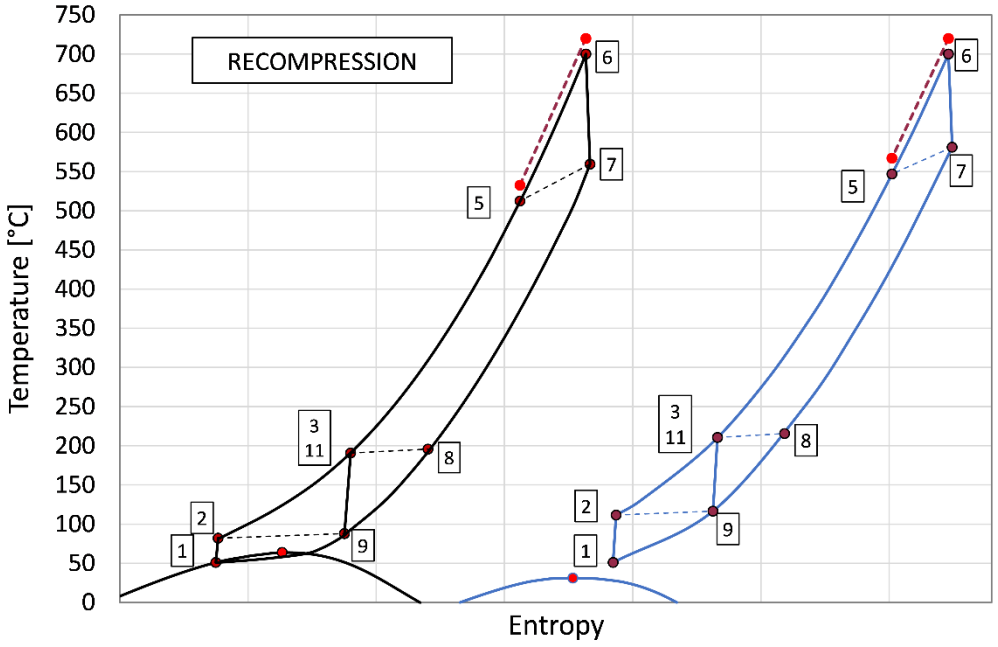

Figure 110: T-s diagram of recompression cycle layout with CO2-SO2 mixture (on left) and supercritical CO2 (on right). Dotted red line show heat source.

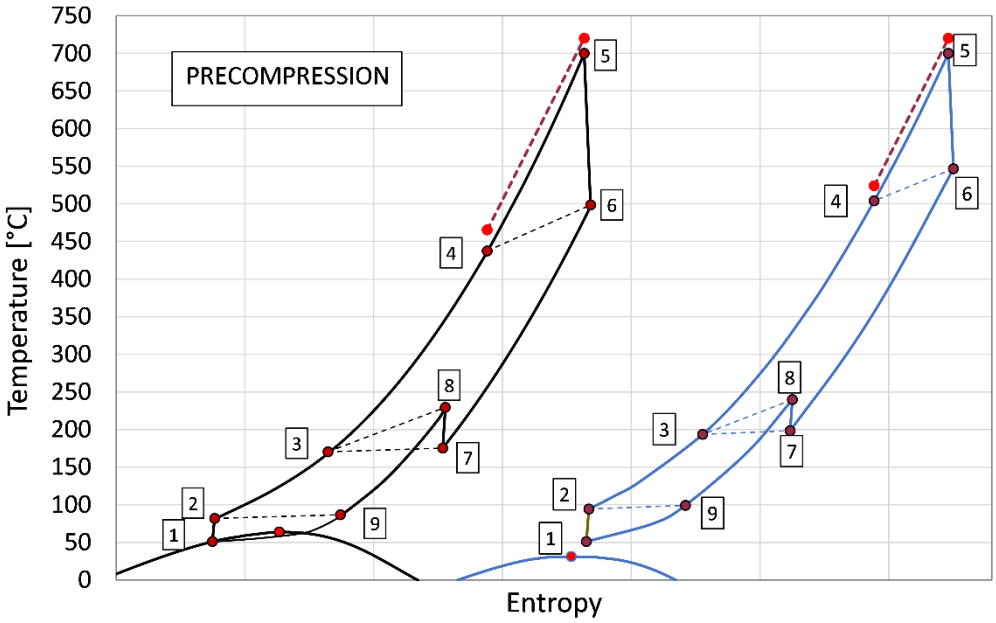

Figure 111: T-s diagram of Precompression cycle layout with CO_2-SO_2 mixture (on left) and supercritical CO_2 (on right). Dotted red line show heat source.

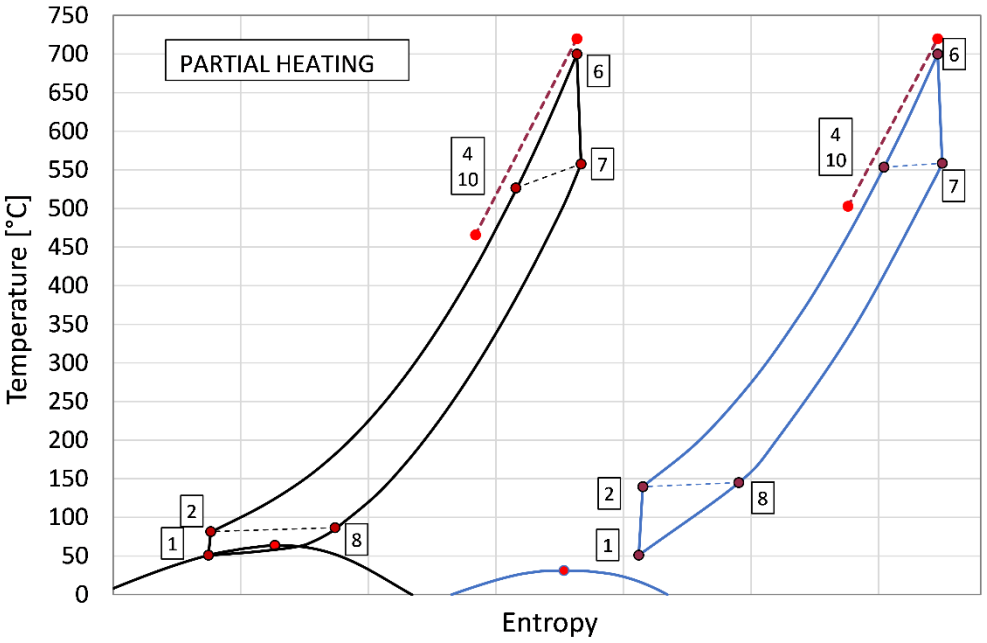

Figure 112: T-s diagram of Partial heating cycle layout with CO_2-SO_2 mixture (on left) and supercritical CO_2 (on right). Dotted red line show heat source.

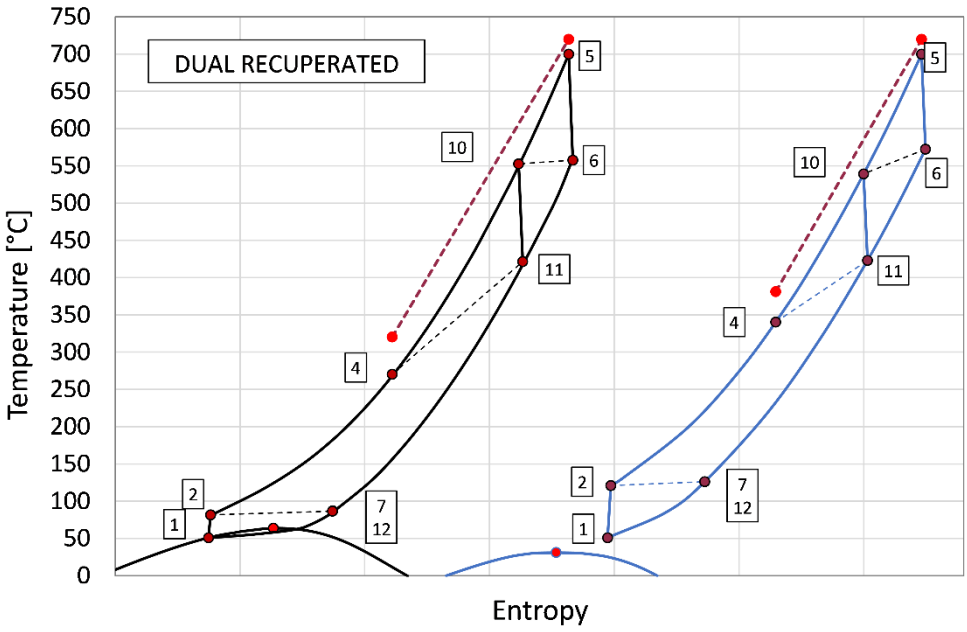

Figure 113: T-s diagram of dual recuperated cycle layout with CO_2-SO_2 mixture (on left) and supercritical CO_2 (on right). Dotted red line show heat source.

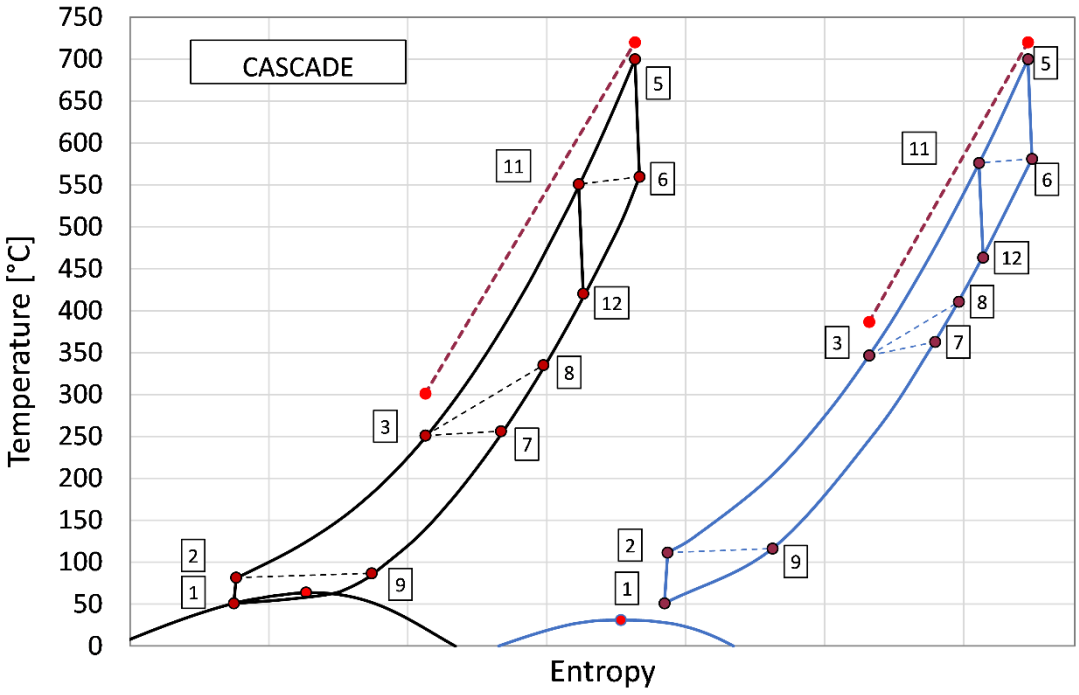

Figure 114: T-s diagram of cascade cycle layout with CO_2-SO_2 mixture (on left) and supercritical CO_2 (on right). Dotted red line show heat source

6.4 **Economic assessment**

This section presented the comparison of capital cost of transcritical power cycle with CO_2-SO_2 mixture and supercritical CO_2 power cycle. Figure 115 shows specific CAPEX

of all seven cycle layouts corresponding to optimal mixture composition and cycle maximum pressure of 250 bar. These specific costs are calculated for 100 MW electrical power output of power cycle. Adoption of CO_2-SO_2 mixture in transcritical cycle brings lower CAPEX compared to sCO_2 cycle. Following reasons can describe this trend:

1. Lower compression work in case of CO_2-SO_2 mixture than supercritical CO_2 which leads to less cost of turbomachinery.
2. Lower mass flow rate of working fluid owing to higher cycle specific work in case of CO_2-SO_2 transcritical cycle compared to sCO_2 counterparts.
3. Lower relative size of PCHE of CO_2-SO_2 transcritical cycles.
4. Lower temperature at inlet of PHE in case of CO_2-SO_2 transcritical cycle which leads to larger log mean temperature difference in PHE thus lower size and cost of PHE compared to sCO_2.

Due to the aforementioned reasons, transcritical power cycles with CO_2-SO_2 mixture experience lower CAPEX than sCO_2 cycles. Figure 116 depicts the CAPEX of a CO_2-SO_2 mixture transcritical cycle and a supercritical CO_2 cycle for various power sizes. When compared to sCO_2 power cycles, the mixture has a lower CAPEX trend at all power sizes. The analysis of power cycles from the points of view of thermodynamics and CAPEX enabled the selection of promising cycle layouts for CO_2-SO_2 mixtures. Recompression cycle layout is a promising layout for CO_2-SO_2 mixture in terms of higher cycle efficiency (above 50%). Dual recuperated cycle is also a promising layout since in perspective of lowest CAPEX and lowest temperature at inlet of PHE.

Figure 117 and Figure 118 show the effect of mixture molar composition and cycle maximum pressure on specific CAPEX of the two promising layouts. The specific CAPEX of a transcritical cycle with a CO_2-SO_2 mixture decreases as the SO_2 content in the mixture increases. This is primarily due to an increase in cycle specific work, which results in a lower mass flow rate of the working fluid mixture, resulting in a lower specific CAPEX of the power cycle. The increase in cycle maximum pressure improves cycle efficiency hence results in drop in specific CAPEX of power cycle.

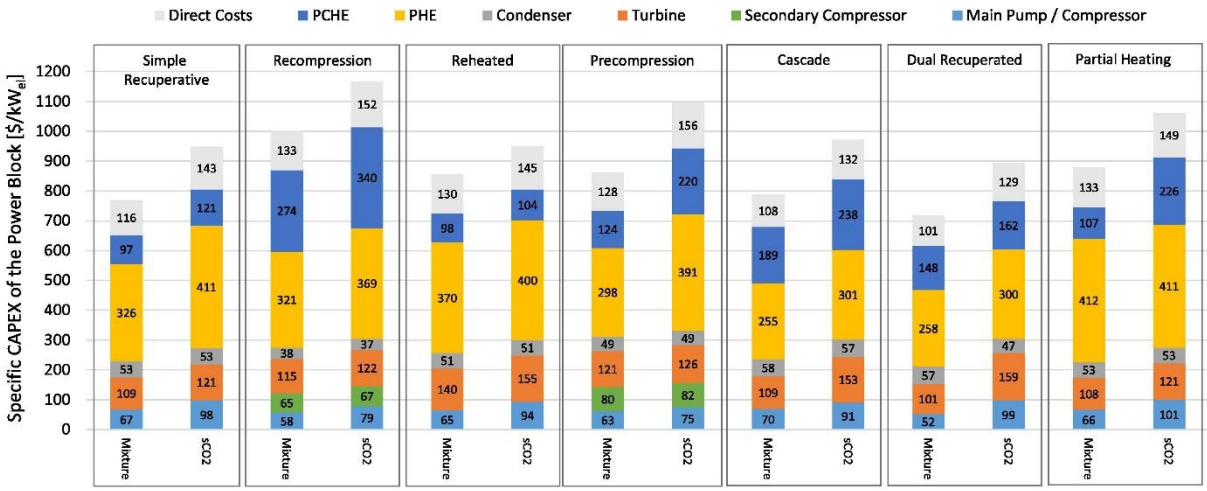

Figure 115: Breakdown of the power block capital cost in all the plant layouts proposed for sCO_2 and CO_2+SO_2 (85% CO_2 molar content) configurations. The calculations refer to 250 bar as maximum pressure and 100MWel of cycle net power

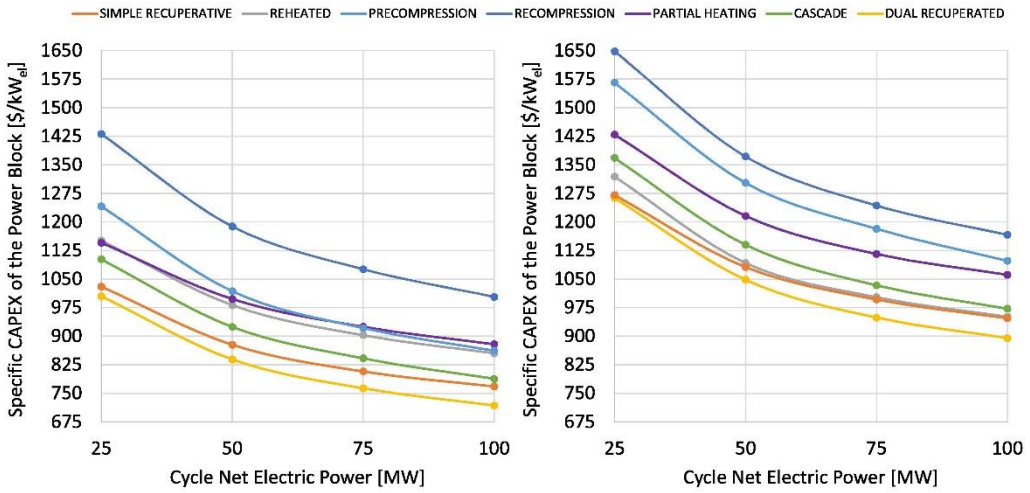

Figure 116: Sensitivity analysis of the power block specific CAPEX for various cycle net electric powers: transcritical CO_2+SO_2 (85% CO_2 molar content) cycle (left) and sCO_2 cycle (right)

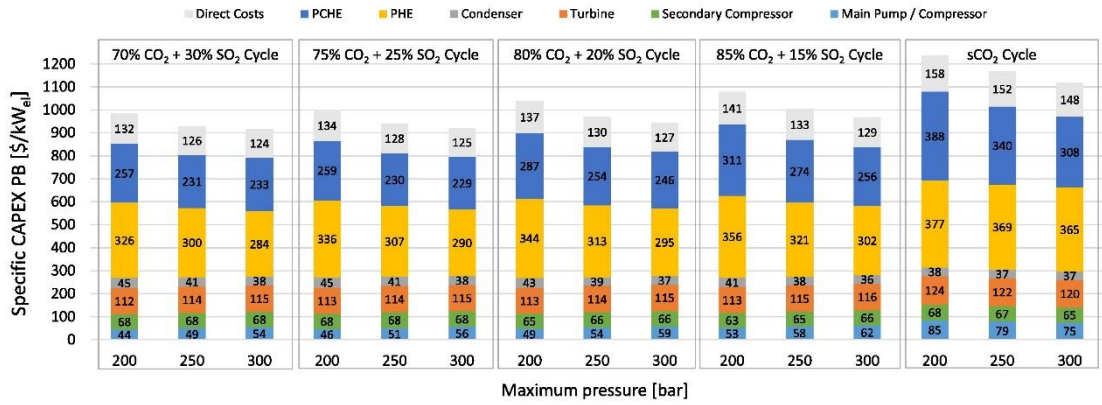

Figure 117: Breakdown of specific CAPEX for the recompression plant layout at various working fluid compositions and cycle maximum pressures for a cycle net power of 100MWel

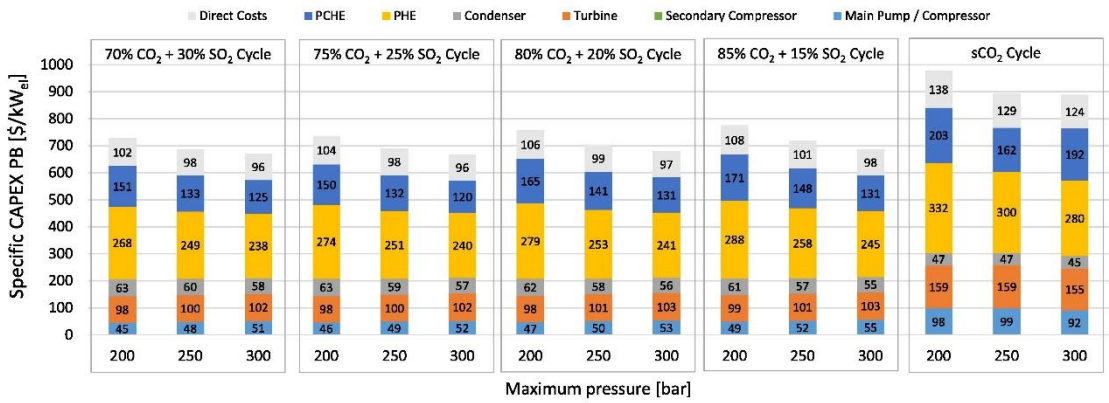

Figure 118: Breakdown of specific CAPEX for the dual recuperated plant layout at various working fluid compositions and cycle maximum pressures for a cycle net power of 100MWel

6.5 **Chapter Summary**

In this chapter, CO_2-SO_2 mixture is adopted as working fluid in transcritical power cycle operating in warm climate region with cycle minimum temperature of 51℃ and maximum temperature of 700℃. The typical application of such power cycles is in concentrated solar power where ambient conditions are hot and arid. Thermodynamic and preliminary economic assessment is carried out considering different cycle layouts.

At the same operating conditions and with the same cycle layouts, a comparison with a supercritical CO_2 cycle is performed to demonstrate the improvement in thermodynamic performance as well as the reduction in cycle specific CAPEX enabled by the use of a CO_2-SO_2 mixture.

The main findings of the analysis presented in this chapter are as follows:

- The use of CO_2-SO_2 mixture in transcritical power cycle enables decrease in heat introduction temperature (or temperature at inlet of PHE), rise in cycle specific work and reduction in relative size of recuperators as compared to sCO_2 cycle for all considered cycle layouts.
- From a cycle efficiency perspective, the recompression layout allows the most significant improvement in thermodynamic performances with respect to sCO_2 cycles,

  In the recompression configuration, the adoption of the mixture enables two percentage points increase in cycle efficiency (50.84% versus 48.79%) than sCO_2 recompression cycle.

- The dual recuperated cycle layout is presented as the promising one for heat recovery applications. In this layout, comparable values of cycle efficiency while a drop of 100 ℃ in the heat introduction temperature with CO_2-SO_2 mixture are obtained compared to analogous sCO_2 cycle layout.
- Considering reasonable values for the electromechanical and auxiliary losses, the transcritical CO_2+SO_2 cycles shows a higher net electric efficiency than the respective sCO_2 counterparts for a reference maximum pressure of 250 bar and a CO_2 molar fraction of 85%, for any cycle layout considered.
- In terms of cycle-specific CAPEX, the transcritical cycle with CO_2-SO_2 mixture once again outperforms the sCO_2 cycle. The recompression cycle with the optimal CO_2-SO_2 mixture has a specific CAPEX of 1000 $/kWel, while the sCO_2 cycle with the same cycle layout has a value of 1160 $/kWel. Similarly, the specific CAPEX of the dual recuperated cycle using the optimal CO_2-SO_2 mixture is 718 $/kWel, which is lower than the sCO_2 cycle, which has a value of 795 $/kWel for the same cycle layout.

Based on the results of this chapter, the CO_2+SO_2 mixture is demonstrated as a promising working fluid for closed power cycles. Because of higher thermal stability, this working fluid can also apply in other research fields: like high temperature heat recovery from exhaust gases of petrochemical, iron and steel industry. In this regard, a complete techno-economic assessment can be beneficial for industry and academia.

Chapter 7: Conclusion, Challenges and Future Work

In recent past, supercritical carbon dioxide (sCO_2) thermodynamic power cycles are introduced for power generation to replace conventional steam Rankine cycle technology. They key benefits of sCO_2 power cycle are compact size of heat exchangers and turbomachinery, higher cycle efficiency and the capability to integrate with high temperature heat sources (like CSP and nuclear) as well as low temperature heat sources (geothermal and low temperature heat recovery). Theoretically, a large body of research works and systematic review papers demonstrated the higher cycle thermodynamic efficiency (close to 48% at cycle T_{max} of 700℃) and smaller size foot print of sCO_2 power cycle compared to steam Rankine cycle.

7.1 **Application in waste heat recovery**

One of the major aims of this thesis is to explore thermodynamic potential of sCO_2 power cycles in high temperature waste heat recovery. The underpinning objective in waste heat recovery plants is to enhance total efficiency (*cycle efficiency* ***x*** *heat recovery effectiveness)* of thermodynamic power cycle and to keep cycle configuration simpler. Three sCO_2 cycle configurations are investigated to recover waste heat from flue gases at temperature of 450℃ as heat source and air coolant at inlet temperature of 15 ℃ as heat sink.

Thermodynamic analysis showed that in case of single flow split-dual expansion sCO_2 cycle, the maximum total efficiency of 15.4% is achieved with heat recovery effectiveness of 82% at cycle T_{max} of 400℃. On contrary, simple recuperative sCO_2 cycle and partial heating sCO_2 cycle showed maximum total efficiency of 13.2% (T_{max} = 400℃) and 14.6% (T_{max} = 350℃) respectively. The corresponding heat recovery effectiveness of simple recuperative sCO_2 cycle and partial heating sCO_2 cycle are 53.2% and 66.9% respectively.

Among the three sCO_2 cycle layouts, partial heating sCO_2 cycle demonstrated a good compromise between total efficiency and size of the power cycle. Though, the single flow-split dual expansion sCO_2 cycle is the best performing cycle for heat recovery from a thermodynamic standpoint, but the size of heat exchangers (*overall heat transfer coefficient* ***x*** *area of heat exchanger*) and number of components (cycle complexity) are larger, making it difficult to compete with simple recuperative sCO_2 cycle and partial

heating sCO_2 cycle since the rise in total efficiency is only around 2% points with the gross power output of 7.5 MW (i.e. smaller power size).

Organic Rankine cycles (ORC) are also analyzed in this thesis under same heat source and coolant air conditions in order to understand the difference in total efficiency compared to sCO_2 cycle technology. Considering cycle maximum temperature of 350℃, the total efficiency of transcritical organic Rankine cycles are rather higher than sCO_2 cycle. Transcritical ORC with CH_2Cl_2 working fluid demonstrated total efficiency of 20%, similarly in case of CH_3Cl working fluid the total efficiency is 19% and for NH_3 and CH_3OH working fluids the total efficiencies are 20% and 18% respectively. The higher total efficiency is mainly due to larger temperature drop in expansion process because the isentropic expansion exponent $(\gamma - 1/\gamma)$ of considered organic fluids is larger. The positive outcomes of larger isentropic expansion exponent are lower temperature at turbine outlet, greater power output and there is No need of recuperator for regeneration.

Transcritical ORCs with working fluids including C_4F_{10}, R134a and C_3H_8 showed lower temperature drop across the turbine owing to lower isentropic expansion exponent, as a result, recuperator is required to recover available heat at turbine outlet in order to enhance cycle efficiency. The total efficiencies achieved in case of C_4F_{10}, R134a and C_3H_8 working fluid at cycle maximum temperature of 350℃ are 11%, 15% and 14% respectively.

In a nutshell, Organic Rankine cycles (particularly transcritical ORCs) have been demonstrated to be a good fit for heat recovery from flue gases at 450℃ and cycle maximum temperature of 350℃.

7.2 **Challenges in sCO_2 cycles and ORCs for waste heat recovery**

The main challenges in ORCs are high cost of working fluid, high flammability, toxicity, and lower thermal stability of working fluids: CH_3Cl, CH_2Cl_2, NH_3, and CH_3OH. Some working fluids with good environmental characteristics (like negligible GWP and zero ODP) like hydrofluoroolefins including HFO1234yf and HFO1234ze (E) are thermally stable at maximum of 200℃ and therefore not suitable working fluid for cycle maximum temperature of 350℃.

Whereas, the main challenges to address in sCO_2 power cycles when applied to waste heat recovery plants are:

- Lower heat recovery effectiveness and total efficiency of sCO_2 power cycles compared to organic Rankine cycles at cycle maximum temperature of 350℃.
- Increase in the complexity of cycle layout to improve heat recovery effectiveness which results in larger size foot print (i.e. larger specific costs).
- Higher operating pressures (200 to 300 bar) which demands specialized materials and increase the cost.

7.3 **Advanced carbon dioxide power cycles for waste heat recovery**

This thesis proposed new CO_2-based binary mixtures as working fluids in transcritical power cycles to address challenges in ORCs and sCO_2 power cycles. CO_2-R134a and CO_2-C_3H_8 mixtures are employed as case studies to show how novel working fluid mixtures affect the total efficiency of the waste heat recovery power cycle.

From the analysis presented in Chapter 4, the following important conclusions are drawn from the thermodynamic analysis and comparison of transcritical ORC, sCO_2 cycles, and transcritical cycles with CO_2-based mixture working fluid:

- Total efficiency of transcritical power cycle with CO_2-R134a mixture [70% molar CO_2] considering cycle maximum temperature of 350℃ and cycle maximum pressure of 200 bar is 14.3%. This value of total efficiency is 1.52 percentage points higher together with simple cycle layout than complex single flow split-dual expansion sCO_2 cycle under cycle maximum temperature and cycle maximum pressure.
- At cycle maximum pressure of 150 bar, the gain in total efficiency with CO_2-R134a [70% molar CO_2] working fluid is 2.01 percentage points and in case of CO_2-R134a [80% molar CO_2], the gain is 1.3 percentage points compared to single flow split-dual expansion sCO_2 cycle.
- The total efficiency of the CO_2-R134a mixture is slightly lower than that of the transcritical ORC (14.3% versus 15%), but with a lower turbine expansion pressure ratio, 4 in the case of the CO_2-R134a mixture and 14.7 in the case of the ORC with R134a. Similarly, using a CO_2-C_3H_8 mixture working fluid, total efficiency attained is closer to transcritical ORC total efficiency (13.4% versus 13.9%), but the turbine

expansion ratio is lower, 3.33 in the case of CO_2-C_3H_8 and 11.56 in the case of C_3H_8 working fluid.

- Turbines of transcritical ORC have a larger size parameter (SP) and a higher volume expansion ratio (VFR), but turbine with CO_2-R134a mixtures have a lower VFR and SP. Lower turbine SP, on the other hand, is undesirable due to increase in tip leakage losses.

Overall, for heat recovery applications with T_{max} of 350℃, the CO_2-R134a and CO2-C_3H_8 mixture demonstrated a good compromise solution between sCO_2 and ORC technologies owing to two positive results:

1. Higher total efficiency is obtained (gain of 2 percentage points) along with a simpler cycle layout compared to complex layout of sCO_2 cycle (*this imply lower cycle specific costs*)
2. Comparable total efficiencies are obtained compared to ORC with only 30% percentage molar fraction of R134a that is an expensive fluid with a high GWP but good thermal stability (*this imply reduction in cost of working fluid and its harmful effects*).

7.4 **Application in concentrated solar power (CSP) plants**

The cycle maximum temperature of 700°C can be reached in cutting-edge concentrated solar power plants by using ternary solar salts as the heat transfer medium. Supercritical carbon dioxide (sCO_2) power cycles can be a good candidate as power block in CSP plants owing to its higher cycle efficiency at high turbine inlet temperatures compared to steam Rankine cycle technology as demonstrated in the works of Angelino [9] and Crespi *et* al [16].

Challenge in CSP power block

In CSP plants with dry cooling, the critical challenge is the significant decrease in cycle thermodynamic efficiency of sCO_2 cycle when compressor inlet temperature rises. As shown in Chapter 5, cycle efficiency of sCO_2 recompression cycle decreases by 6 points (52% to 46%) for rise in compressor inlet temperature from T_{cr} to $1.1xT_{cr}$. The increase in ambient air temperature in dry air-coolers at CSP sites is what causes the increase in compressor inlet temperature of the sCO_2 cycle. In reality, as the compressors inlet temperature rises above the critical point temperature, the benefits of real gas effects, such

as the benefit to obtain less compression work close to the critical point (owing to lower compressibility factor), are lost, which results in decline in cycle efficiency.

7.5 **Advanced carbon dioxide power cycles for concentrated solar power (CSP) plants**

This thesis proposed CO_2-based binary mixture as working fluids in sCO_2 power cycles in order to obtain higher cycle efficiency at high ambient temperature; Overall, the main objectives to adopt carbon dioxide based binary mixtures are:

1. To achieve cycle efficiency higher than supercritical CO_2 cycles at high ambient temperature. The value of ambient temperature assumed is 35℃ which represents the available ambient temperature at current operational CSP sites,
2. To reduce the temperature of working fluid at inlet of primary heat exchanger (or to enhance temperature difference across primary heat exchanger),
3. To increase cycle specific work,
4. To reduce size (UA) of recuperators,
5. To reduce capital expenditure (CAPEX) and operational expenditure (OPEX)

In the first phase of the analysis, as presented in the Chapter 5, five CO_2 based binary mixtures are selected and cycle simulations are performed for cycle maximum pressure of 150 to 300 bar and two representative values of cycle maximum temperature which includes 550℃ and 700℃. Moreover, 50℃ cycle minimum temperature is assumed since design approach temperature is 15℃ in air condenser (so that, $T_{min} = T_{amb} + 15$ ℃)

Simple recuperative cycle configuration for CO_2 mixtures working fluid is selected and thermodynamic cycle efficiency is compared with recompression sCO_2 cycle configuration and simple recuperative sCO_2 cycle configuration.

- According to the findings in Chapter 5, the CO_2-C_6F_6 mixture [85% molar CO_2] working fluid with cycle maximum temperature of 550°C demonstrated a cycle efficiency that is 2.7 percentage points higher than that of simple recuperative sCO_2 cycle layout. Compared to the sCO_2 recompression cycle layout, the cycle efficiency is 2 percentage points lower. But, with precompression cycle layout, a recent study

demonstrated 1.03 percentage points higher cycle efficiency with CO_2-C_6F_6 mixture compared to sCO_2 precompression cycle [96].

- The maximum cycle efficiency gain of 5.2 percentage points is obtained in CO_2-$TiCl_4$ mixture [80% molar CO_2] with simple recuperative cycle layout while cycle efficiency obtained is also close to the value obtained in recompression sCO_2 cycle layout considering cycle maximum temperature of 700℃.

- Furthermore, CO_2-SO_2F_2 [40% molar CO_2] and CO_2-CF_3I [60% molar CO_2] working fluids demonstrate 1.5 percentage points and 1.1 percentage points higher cycle efficiency respectively at cycle maximum temperature of 550℃ compared to sCO_2 simple recuperative layout.

Downsides of using CO_2-C_6F_6 and CO_2-$TiCl_4$ as working fluids

Some limitations and/or downside of CO_2 mixtures as working fluids should be highlighted. For example, in $TiCl_4$, the main difficulty is its higher reactivity with water, despite the fact that it has been tested as a thermally stable fluid at T>550℃. Small amounts of moisture cause the formation of TiO_2, which leads to clogging and serious issues during experiments.

CO_2-C_6F_6, on other hand, is a promising working fluid with high thermal stability; In a recent work[121], the experimental static test of CO_2-C_6F_6 mixture at different operating temperatures proofs maximum allowable thermal stability temperature of 600℃ in an Inconel 625 vessel. Yet, the disadvantage of C_6F_6 is its high global warming potential and larger cost of the fluid.

CO_2-SO_2 mixture for transcritical power cycle

CO_2-SO_2 working fluid is also chosen for its favorable properties, including high thermal stability of SO_2 at a maximum temperature of 700℃, high bond energy of the S-O bond compared to the C-F bond in perfluorocarbons, low flammability, low ODP, and negligible GWP. According to the NFPA-704 standard, one undesirable property of SO_2 is high toxicity, which can be mitigated by proper ventilation in power plants in the event of working fluid leakage.

The mixture of CO_2-SO_2 [80% molar CO_2] working fluid in simple recuperative cycle layout yield cycle efficiency of 43.6% at cycle maximum temperature of 700℃ and this efficiency value is 1.9 percentage points lower than sCO_2 cycle. However, the other

benefits of CO_2-SO_2 which cannot be overlooked are higher cycle specific work, lower temperature of working fluid at the inlet of PHE and lower size of recuperator (UA/Q_{in}) compared to sCO_2 power cycle. These advantages enable a more thorough investigation of the CO_2-SO_2 mixture; as a result, six additional cycle layouts in addition to the simple recuperative layout are selected for thermodynamic as well as economic assessment in Chapter 6.

According to results presented in Chapter 6, CO_2-SO_2 mixture [85% molar CO_2] with recompression cycle layout showed significant improvement in cycle efficiency compared to sCO_2 recompression cycle [50.84% versus 48.79%]. While the dual recuperated cycle with CO_2-SO_2 mixture compared to sCO_2 counterpart also show comparable cycle efficiency and the advantage of using this layout is lower temperature at inlet of PHE (270℃ versus 340℃) which results in higher temperature difference across PHE (which imply smaller size of thermal energy storage).

In additions to gain in cycle efficiency, transcritical power cycles with CO_2-SO_2 mixture working fluid also demonstrated superiority over sCO_2 cycles in terms of specific capital expenditure (CAPEX, $/kWel). It has been discovered that the specific CAPEX of transcritical power cycle reduced with increase in molar content of SO_2 in the mixture.

- With a recompression cycle layout, specific CAPEX for a CO_2-SO_2 mixture (85% molar CO_2) is 1000$/kWel, and for sCO_2, it is 1160$/kWel.
- Additionally, for a dual recovered cycle layout, specific CAPEX is 718 $/kWel using a CO_2-SO_2 mixture (85% molar CO_2) as opposed to 795 $/kWel for a sCO_2 cycle.

7.6 **Future Work**

The previous sections discussed the potential gains in thermodynamic performance that could be realized by using CO_2-based binary mixtures working fluids in carbon dioxide thermodynamic power cycles for two major applications: waste heat recovery plants and concentrated solar power plants. Furthermore, the use of a CO_2-based binary mixture with an appropriate cycle layout and optimal mixture composition results in lower specific CAPEX and better integration with thermal energy storage and the solar field.

However, it is also important to highlight and elaborate on the primary problems that need to be resolved in future in order to utilize novel working fluids in power cycles.

1. **Thermal stability of dopants for CO_2 mixtures:** There are many dopants for which information about thermal stability is required to ensure their use as working fluids in high temperature power cycles.

   For some dopants (including SO_2, SO_2F_2, Novec 649, Novec 5110 and CF_3I) with No evidence of thermal stability, this study used standard enthalpy of formation per bond ($\Delta H_B = \Delta H_f^o / n_B$) as a preliminary indicator to assess thermal stability relative to thermal stability of CO_2. However, it is important to determine thermal stability of new dopants by experiments at high temperature and for different vessel materials (Stainless steel and Inconel) as done for R134a, CH_2Cl_2, $TiCl_4$ and C_6F_6 in earlier works.

   In this regard, consortium of SCARABEUS project are working on determination of high temperature thermal stability of perfluorocarbons, sulphur dioxide, tin tetrachloride and some new refrigerants in Fluid Test Lab of Universita Degli Studi Di Brescia, Italy.

2. **Availability of experimental thermodynamic property data:** The research on CO_2-based binary mixture as working fluid in power plant is in early stages, due to which the experimental property data including density of mixture in liquid phase and near critical point, vapor liquid equilibrium (VLE) at different temperatures, speed of sound and specific heat data is not available for some CO_2 mixtures like CO_2-SO_2F_2, CO_2-CF_3I, CO_2-Novec5110, CO_2-$TiCl_4$ and CO_2-C_4F_{10}. As mentioned in Chapter 2, this data is required to determine binary interaction parameter ($k_{1,2}$) of equation of state (PR EoS and PC-SAFT EoS) by curve fitting. So, the need of the hour is to determine thermodynamic properties by doing experiments for required temperature and pressure range.

3. **More CO_2-based binary mixture as working fluids**: The thermodynamic benefit of using CO_2-R134a and CO_2-C_3H_8 binary mixtures in waste heat recovery power cycle is higher total efficiency with simple cycle layout and with only 30% molar content of R134a in the working fluid.

   In the light of this advantage, it is suggested to explore thermodynamic potential of more CO_2-based mixtures (like CO_2+aromatics, CO_2+SO_2, CO_2+siloxanes) and study

the effect of mixture composition on total efficiency, size and economics (specific cost and payback period) of the power cycle.

4. **Power cycle optimization in perspective of working fluid composition and cycle layout:** In CSP integrated power cycles, thermal efficiency gain is highly dependent on the particular mixture composition and the cycle layout. As in CO_2-$TiCl_4$, the optimum mixture composition and cycle layout is different from the CO_2-C_6F_6 mixture for maximum efficiency gain. Therefore, optimization study is required to determine the best suited cycle layout and mixture composition to achieve maximum efficiency. There are also other goals to achieve, such as increasing the temperature difference in PHE and reducing the size of recuperators. This demonstrates that the problem is multi-objective, and that finding an optimal solution is only possible when all objectives are considered, and multi-objective optimization should be performed.

Bibliography

[1] M. Marchionni, G. Bianchi, and S. A. Tassou, "Review of supercritical carbon dioxide (sCO2) technologies for high-grade waste heat to power conversion," *SN Appl. Sci.*, vol. 2, no. 4, p. 611, Apr. 2020, doi: 10.1007/s42452-020-2116-6.

[2] M. Usman, M. Imran, D. H. Lee, and B. S. Park, "Experimental investigation of off-grid organic Rankine cycle control system adapting sliding pressure strategy under proportional integral with feed-forward and compensator," *Appl. Therm. Eng.*, vol. 110, 2017, doi: 10.1016/j.applthermaleng.2016.09.021.

[3] M. Imran, F. Haglind, M. Asim, and J. Zeb Alvi, "Recent research trends in organic Rankine cycle technology: A bibliometric approach," *Renewable and Sustainable Energy Reviews*. 2018, doi: 10.1016/j.rser.2017.08.028.

[4] T. Tartière and M. Astolfi, "A World Overview of the Organic Rankine Cycle Market," *Energy Procedia*, vol. 129, pp. 2–9, 2017, doi: 10.1016/j.egypro.2017.09.159.

[5] C. M. Invernizzi and D. Bonalumi, *Thermal stability of organic fluids for Organic Rankine Cycle systems*. 2016.

[6] G. Manente and M. Costa, "On the Conceptual Design of Novel Supercritical CO2 Power Cycles for Waste Heat Recovery," *Energies*, vol. 13, no. 2, p. 370, Jan. 2020, doi: 10.3390/en13020370.

[7] F. Crespi, G. Gavagnin, D. Sánchez, and G. S. Martínez, "Analysis of the Thermodynamic Potential of Supercritical Carbon Dioxide Cycles: A Systematic Approach," *J. Eng. Gas Turbines Power*, vol. 140, no. 5, pp. 1–10, May 2018, doi: 10.1115/1.4038125.

[8] A. Ayub, N. A. Sheikh, R. Tariq, M. M. Khan, and C. M. Invernizzi, "Exergetic optimization and comparison of combined gas turbine supercritical CO 2 power cycles," *J. Renew. Sustain. Energy*, vol. 10, no. 4, p. 044703, Jul. 2018, doi: 10.1063/1.5038333.

[9] G. Angelino, "Carbon Dioxide Condensation Cycles For Power Production," *J. Eng. Power*, vol. 90, no. 3, pp. 287–295, Jul. 1968, doi: 10.1115/1.3609190.

[10] V. Dostal, M. J. Driscoll, and P. Hejzlar, "A Supercritical Carbon Dioxide Cycle

for Next Generation Nuclear Reactors," 2004.

[11] F. Crespi, D. Sánchez, G. S. Martínez, T. Sánchez-Lencero, and F. Jiménez-Espadafor, "Potential of supercritical carbon dioxide power cycles to reduce the levelised cost of electricity of contemporary concentrated solar power plants," *Appl. Sci.*, vol. 10, no. 15, p. 5049, Jul. 2020, doi: 10.3390/app10155049.

[12] D. Alfani, T. Neises, M. Astolfi, M. Binotti, and P. Silva, "Techno-economic analysis of CSP incorporating sCO2 brayton power cycles: Trade-off between cost and performance," in *AIP Conference Proceedings*, May 2022, vol. 2445, no. 1, p. 090001, doi: 10.1063/5.0086353.

[13] C. M. Invernizzi, "Prospects of mixtures as working fluids in real-gas Brayton cycles," *Energies*, vol. 10, no. 10, 2017, doi: 10.3390/en10101649.

[14] X. Liu, Z. Xu, Y. Xie, and H. Yang, "CO2-based mixture working fluids used for the dry-cooling supercritical Brayton cycle: Thermodynamic evaluation," *Appl. Therm. Eng.*, vol. 162, no. 17923, p. 114226, 2019, doi: 10.1016/j.applthermaleng.2019.114226.

[15] L. Wang, L. Pan, J. Wang, D. Chen, Y. Huang, and L. Hu, "Investigation on the temperature sensitivity of the S-CO2 Brayton cycle efficiency," *Energy*, vol. 178, pp. 739–750, Jul. 2019, doi: 10.1016/j.energy.2019.04.100.

[16] F. Crespi, G. Gavagnin, D. Sánchez, and G. S. Martínez, "Supercritical carbon dioxide cycles for power generation: A review," *Appl. Energy*, vol. 195, pp. 152–183, Jun. 2017, doi: 10.1016/j.apenergy.2017.02.048.

[17] G. Manente and F. M. Fortuna, "Supercritical CO2 power cycles for waste heat recovery: A systematic comparison between traditional and novel layouts with dual expansion," *Energy Convers. Manag.*, vol. 197, no. July, p. 111777, Oct. 2019, doi: 10.1016/j.enconman.2019.111777.

[18] M. Binotti, G. Di Marcoberardino, P. Iora, C. Invernizzi, and G. Manzolini, "SCARABEUS: Supercritical carbon dioxide/alternative fluid blends for efficiency upgrade of solar power plants," *AIP Conf. Proc.*, vol. 2303, no. 1, p. 130002, Dec. 2020, doi: 10.1063/5.0028799.

[19] L. Vesely, J. Kapat, S. Martin, S. Vasu, K. R. V. Manikantachari, and V. Dostal,

"Effect of Mixtures on Compressor and Cooler in Supercritical Carbon Dioxide Cycles," p. V009T38A010, 2018, doi: 10.1115/gt2018-75568.

[20] C. M. Invernizzi and T. Van Der Stelt, "Supercritical and real gas Brayton cycles operating with mixtures of carbon dioxide and hydrocarbons," *Proc. Inst. Mech. Eng. Part A J. Power Energy*, vol. 226, no. 5, pp. 682–693, 2012, doi: 10.1177/0957650912444689.

[21] S. A. Wright, P. S. Pickard, M. E. Vernon, and R. F. Radel, "Enhancing power cycle efficiency for a supercritical Brayton cycle power system using tunable supercritical gas mixtures. Patent Application Pub. No. US20130033044A1.," 2013.

[22] J. Q. Guo, M. J. Li, J. L. Xu, J. J. Yan, and K. Wang, "Thermodynamic performance analysis of different supercritical Brayton cycles using CO2-based binary mixtures in the molten salt solar power tower systems," *Energy*, vol. 173, pp. 785–798, 2019, doi: 10.1016/j.energy.2019.02.008.

[23] W. S. Jeong, J. I. Lee, and Y. H. Jeong, "Potential improvements of supercritical recompression CO2Brayton cycle by mixing other gases for power conversion system of a SFR," *Nucl. Eng. Des.*, vol. 241, no. 6, pp. 2128–2137, 2011, doi: 10.1016/j.nucengdes.2011.03.043.

[24] D. Bonalumi, S. Lasala, and E. Macchi, "CO2-TiCl4 working fluid for high-temperature heat source power cycles and solar application," *Renew. Energy*, vol. 147, pp. 2842–2854, Mar. 2020, doi: 10.1016/j.renene.2018.10.018.

[25] G. Manzolini, M. Binotti, D. Bonalumi, C. Invernizzi, and P. Iora, "CO2 mixtures as innovative working fluid in power cycles applied to solar plants. Techno-economic assessment," *Sol. Energy*, vol. 181, no. January, pp. 530–544, Mar. 2019, doi: 10.1016/j.solener.2019.01.015.

[26] O. A. Aqel, M. T. White, M. A. Khader, and A. I. Sayma, "Sensitivity of transcritical cycle and turbine design to dopant fraction in CO2-based working fluids," *Appl. Therm. Eng.*, vol. 190, no. February, p. 116796, May 2021, doi: 10.1016/j.applthermaleng.2021.116796.

[27] J. S. Lopez-Echeverry, S. Reif-Acherman, and E. Araujo-Lopez, "Peng-Robinson

equation of state: 40 years through cubics," *Fluid Phase Equilib.*, vol. 447, pp. 39–71, 2017, doi: 10.1016/j.fluid.2017.05.007.

[28] J. Gross and G. Sadowski, "Perturbed-chain SAFT: An equation of state based on a perturbation theory for chain molecules," *Ind. Eng. Chem. Res.*, vol. 40, no. 4, pp. 1244–1260, Feb. 2001, doi: 10.1021/ie0003887.

[29] S. W. Løvseth *et al.*, "Thermodynamics of the carbon dioxide plus argon (CO2 + Ar) system: An improved reference mixture model and measurements of vapor-liquid, vapor-solid, liquid-solid and vapor-liquid-solid phase equilibrium data at the temperatures 213–299 K and pressures up," *Fluid Phase Equilib.*, vol. 466, pp. 48–78, 2018, doi: 10.1016/j.fluid.2018.02.009.

[30] T. Neumann, "Development of New Helmholtz Models for Binary Mixture Relevant for CCS," Ruhr-Universität Bochum, 2017.

[31] B. Gimeno, M. Artal, I. Velasco, J. Fernández, and S. T. Blanco, "Influence of SO2 on CO2 Transport by Pipeline for Carbon Capture and Storage Technology: Evaluation of CO2/SO2 Cocapture," *Energy and Fuels*, vol. 32, no. 8, pp. 8641–8657, 2018, doi: 10.1021/acs.energyfuels.8b01666.

[32] M. Nazeri, A. Chapoy, A. Valtz, C. Coquelet, and B. Tohidi, "New experimental density data and derived thermophysical properties of carbon dioxide – Sulphur dioxide binary mixture (CO2 - SO2) in gas, liquid and supercritical phases from 273 K to 353 K and at pressures up to 42 MPa," *Fluid Phase Equilib.*, vol. 454, pp. 64–77, 2017, doi: 10.1016/j.fluid.2017.09.014.

[33] C. Coquelet, A. Valtz, and P. Arpentinier, "Thermodynamic study of binary and ternary systems containing CO2+impurities in the context of CO2 transportation," *Fluid Phase Equilib.*, vol. 382, pp. 205–211, Nov. 2014, doi: 10.1016/j.fluid.2014.08.031.

[34] C. J. Noriega Sanchez, L. Gosselin, and A. K. da Silva, "Designed binary mixtures for subcritical organic Rankine cycles based on multiobjective optimization," *Energy Convers. Manag.*, vol. 156, no. July 2017, pp. 585–596, 2018, doi: 10.1016/j.enconman.2017.11.050.

[35] R. Smith, H. Inomata, and C. Peters, "Underlying Thermodynamics and Practical

Expressions," in *Supercritical Fluid Science and Technology*, vol. 4, 2013, pp. 275–332.

[36] R. Smith, H. Inomata, and C. Peters, "Phase Equilibria and Mass Transfer," in *Introduction to Supercritical Fluids A Spreadsheet-based Approach*, vol. 4, 2013, pp. 481–556.

[37] R. A. Heidemann and A. M. Khalil, "The calculation of critical points," *AIChE J.*, vol. 26, no. 5, pp. 769–779, Sep. 1980, doi: 10.1002/aic.690260510.

[38] R. Smith, H. Inomata, and C. Peters, "Phase Equilibria and Mass Transfer," in *Supercritical Fluid Science and Technology*, vol. 4, Elsevier B.V., 2013, pp. 481–556.

[39] P. H. V. Konynenburg and R. L. Scott, "Critical Lines and Phase Equilibria in Binary Van Der Waals Mixtures," *Philos. Trans. R. Soc. A Math. Phys. Eng. Sci.*, vol. 298, no. 1442, pp. 495–540, 2006, doi: 10.1098/rsta.1980.0266.

[40] D. -y Peng and D. B. Robinson, "A rigorous method for predicting the critical properties of multicomponent systems from an equation of state," *AIChE J.*, vol. 23, no. 2, pp. 137–144, Mar. 1977, doi: 10.1002/aic.690230202.

[41] M. L. Michelsen and R. A. Heidemann, "Calculation of critical points from cubic two-constant equations of state," *AIChE J.*, vol. 27, no. 3, pp. 521–523, May 1981, doi: 10.1002/aic.690270326.

[42] W. Jia, C. Li, and X. Wu, "Computation of liquid-vapor critical points for multi-component mixtures," *Int. J. Thermodyn.*, vol. 15, no. 3, pp. 149–156, 2012, doi: 10.5541/ijot.380.

[43] P. Dimitrakopoulos, W. Jia, and C. Li, "An improved computational method for the calculation of mixture liquid-vapor critical points," *Int. J. Thermophys.*, vol. 35, no. 5, pp. 865–889, 2014, doi: 10.1007/s10765-014-1680-7.

[44] B. A. Stradi, J. F. Brennecke, P. Kohn, and M. A. Stadtherr, "Reliable computation of mixture critical points," *AIChE J.*, vol. 47, no. 1, pp. 212–221, 2001, doi: 10.1002/aic.690470121.

[45] B. A. Stradi-Granados, "Interval Arithmetic for Nonlinear Problem Solving," *Int.*

J. Eng. Math., vol. 2013, pp. 1–11, 2013, doi: 10.1155/2013/768474.

[46] N. Henderson, W. F. Sacco, N. E. Barufatti, and M. M. Ali, "Calculation of critical points of thermodynamic mixtures with differential evolution algorithms," *Ind. Eng. Chem. Res.*, vol. 49, no. 4, pp. 1872–1882, 2010, doi: 10.1021/ie900948z.

[47] H. Hoteit, E. Santiso, and A. Firoozabadi, "An efficient and robust algorithm for the calculation of gas-liquid critical point of multicomponent petroleum fluids," *Fluid Phase Equilib.*, vol. 241, no. 1–2, pp. 186–195, 2006, doi: 10.1016/j.fluid.2005.12.019.

[48] S. M. Rump, "INTLAB — INTerval LABoratory," in *Developments in Reliable Computing*, E. Tibor Csendes, Ed. Dordrecht: Springer Netherlands, 1999, pp. 77–104.

[49] A. Aasen, M. Hammer, G. Skaugen, J. P. Jakobsen, and Wilhelmsen, "Thermodynamic models to accurately describe the PVTxy-behavior of water / carbon dioxide mixtures," *Fluid Phase Equilib.*, vol. 442, pp. 125–139, 2017, doi: 10.1016/j.fluid.2017.02.006.

[50] F. H. Poettmann and D. L. Katz, "Phase Behavior of Binary Carbon Dioxide-Paraffin Systems," *Ind. Eng. Chem.*, vol. 37, no. 9, pp. 847–853, Sep. 1945, doi: 10.1021/ie50429a017.

[51] H. H. Reamer, B. H. Sage, and W. N. Lacey, "Phase Equilibria in Hydrocarbon Systems. Volumetric and Phase Behavior of the Propane-Carbon Dioxide System," *Ind. Eng. Chem.*, vol. 43, no. 11, pp. 2515–2520, Nov. 1951, doi: 10.1021/ie50503a035.

[52] J. G. Roof and J. D. Baron, "Critical Loci Of Binary Mixtures Of Propane With Methane, Carbon Dioxide, and Nitrogen," *J. Chem. Eng. Data*, vol. 12, no. 3, pp. 292–293, 1967, doi: 10.1021/je60034a003.

[53] N. Juntarachat, S. Bello, R. Privat, and J. N. Jaubert, "Validation of a new apparatus using the dynamic method for determining the critical properties of binary gas/gas mixtures," *J. Chem. Eng. Data*, vol. 58, no. 3, pp. 671–676, 2013, doi: 10.1021/je301209u.

[54] A. Valtz, X. Courtial, E. Johansson, C. Coquelet, and D. Ramjugernath,

"Isothermal vapor-liquid equilibrium data for the carbon dioxide (R744)+decafluorobutane (R610) system at temperatures from 263 to 353K," *Fluid Phase Equilib.*, vol. 304, no. 1–2, pp. 44–51, 2011, doi: 10.1016/j.fluid.2011.01.017.

[55] D. Bonalumi, S. Lasala, and E. Macchi, "CO2-TiCl4 working fluid for high-temperature heat source power cycles and solar application," *Renew. Energy*, pp. 1–13, 2018, doi: 10.1016/j.renene.2018.10.018.

[56] J. T. Reaves, A. T. Griffith, and C. B. Roberts, "Critical Properties of Dilute Carbon Dioxide + Entrainer and Ethane + Entrainer Mixtures," *J. Chem. Eng. Data*, vol. 43, no. 4, pp. 683–686, Jul. 1998, doi: 10.1021/je9702753.

[57] C. P. Hicks and C. L. Young, "The Gas-Liquid Critical Properties of Binary Mixtures," *Chem. Rev.*, vol. 75, no. 2, pp. 119–175, 1975, doi: 10.1021/cr60294a001.

[58] G. S. Gurdial, N. R. Foster, S. L. J. Yun, and K. D. Tilly, "Phase Behavior of Supercritical Fluid—Entrainer Systems," pp. 34–45, 2009, doi: 10.1021/bk-1992-0514.ch003.

[59] Y. Sun, Y. Li, J. Zhou, R. Zhu, and Y. Tian, "Experimental determination and calculation of the critical curves for the binary systems of CO2 containing ketone, alkane, ester and alcohol, respectively," *Fluid Phase Equilib.*, vol. 307, no. 1, pp. 72–77, 2011, doi: 10.1016/j.fluid.2011.05.005.

[60] S. Takenouchi and G. C. Kennedy, "The binary system H2O-CO2 at high temperatures and pressures," *Am. J. Sci.*, 2010, doi: 10.2475/ajs.262.9.1055.

[61] K. Tödheide and E. U. Franck, "Das zweiphasengebiet und die kritische kurve im system kohlendioxid-wasser bis zu drucken von 3500 bar," *Zeitschrift fur Phys. Chemie*, 1963, doi: 10.1524/zpch.1963.37.5_6.387.

[62] J. S. Gallagher, R. Crovetto, and J. M. H. levelt Sengers, "The Thermodynamic Behavior of the CO2-H2O System from 400K to 1000K, upt o 100 MPa and 30% Mole fraction of CO2," *J. Phys. Chem. Ref. Data*, vol. 22, no. 2, pp. 431–513, 1993, [Online]. Available: https://www.nist.gov/sites/default/files/documents/srd/jpcrd452.pdf.

[63] A. Valtz, A. Chapoy, C. Coquelet, P. Paricaud, and D. Richon, “Vapour-liquid equilibria in the carbon dioxide-water system, measurement and modelling from 278.2 to 318.2 K,” *Fluid Phase Equilib.*, vol. 226, no. 1–2, pp. 333–344, 2004, doi: 10.1016/j.fluid.2004.10.013.

[64] G. P. Panayiotou *et al.*, “Preliminary assessment of waste heat potential in major European industries,” *Energy Procedia*, vol. 123, no. April, pp. 335–345, Sep. 2017, doi: 10.1016/j.egypro.2017.07.263.

[65] G. Bianchi *et al.*, “Estimating the waste heat recovery in the European Union Industry,” *Energy, Ecol. Environ.*, vol. 4, no. 5, pp. 211–221, Oct. 2019, doi: 10.1007/s40974-019-00132-7.

[66] O. Kizilkan, “Performance assessment of steam Rankine cycle and sCO 2 Brayton cycle for waste heat recovery in a cement plant: A comparative study for supercritical fluids,” *Int. J. Energy Res.*, no. September 2019, p. er.5138, Jan. 2020, doi: 10.1002/er.5138.

[67] R. Scaccabarozzi, M. Tavano, C. M. Invernizzi, and E. Martelli, “Comparison of working fluids and cycle optimization for heat recovery ORCs from large internal combustion engines,” *Energy*, vol. 158, pp. 396–416, 2018, doi: 10.1016/j.energy.2018.06.017.

[68] F. Aziz, R. Mudasar, and M. H. Kim, “Exergetic and heat load optimization of high temperature organic Rankine cycle,” *Energy Convers. Manag.*, vol. 171, no. March, pp. 48–58, 2018, doi: 10.1016/j.enconman.2018.05.094.

[69] H. Chen, D. Y. Goswami, and E. K. Stefanakos, “A review of thermodynamic cycles and working fluids for the conversion of low-grade heat,” *Renew. Sustain. Energy Rev.*, vol. 14, no. 9, pp. 3059–3067, 2010, doi: 10.1016/j.rser.2010.07.006.

[70] P. Bombarda, C. M. Invernizzi, and C. Pietra, “Heat recovery from Diesel engines: A thermodynamic comparison between Kalina and ORC cycles,” *Appl. Therm. Eng.*, vol. 30, no. 2–3, pp. 212–219, Feb. 2010, doi: 10.1016/j.applthermaleng.2009.08.006.

[71] A. Uusitalo, J. Honkatukia, and T. Turunen-Saaresti, “Evaluation of a small-scale waste heat recovery organic Rankine cycle,” *Appl. Energy*, vol. 192, pp. 146–158,

Apr. 2017, doi: 10.1016/j.apenergy.2017.01.088.

[72] M. Astolfi, M. C. Romano, P. Bombarda, and E. Macchi, “Binary ORC (organic Rankine cycles) power plants for the exploitation of medium–low temperature geothermal sources – Part A: Thermodynamic optimization,” *Energy*, vol. 66, pp. 423–434, Mar. 2014, doi: 10.1016/j.energy.2013.11.056.

[73] F. A. Al-Sulaiman, I. Dincer, and F. Hamdullahpur, “Energy and exergy analyses of a biomass trigeneration system using an organic Rankine cycle,” *Energy*, vol. 45, no. 1, pp. 975–985, 2012, doi: 10.1016/j.energy.2012.06.060.

[74] C. Invernizzi, P. Iora, and P. Silva, “Bottoming micro-Rankine cycles for micro-gas turbines,” *Appl. Therm. Eng.*, vol. 27, no. 1, pp. 100–110, 2007, doi: 10.1016/j.applthermaleng.2006.05.003.

[75] E. Bellos and C. Tzivanidis, “Parametric analysis and optimization of an Organic Rankine Cycle with nanofluid based solar parabolic trough collectors,” *Renew. Energy*, vol. 114, pp. 1376–1393, 2017, doi: 10.1016/j.renene.2017.06.055.

[76] M. T. White, G. Bianchi, L. Chai, S. A. Tassou, and A. I. Sayma, “Review of supercritical CO2 technologies and systems for power generation,” *Appl. Therm. Eng.*, vol. 185, p. 116447, Feb. 2021, doi: 10.1016/j.applthermaleng.2020.116447.

[77] Y. Ahn *et al.*, “Review of supercritical CO2 power cycle technology and current status of research and development,” *Nucl. Eng. Technol.*, vol. 47, no. 6, pp. 647–661, 2015, doi: 10.1016/j.net.2015.06.009.

[78] M. Astolfi, D. Alfani, S. Lasala, and E. Macchi, “Comparison between ORC and CO2 power systems for the exploitation of low-medium temperature heat sources,” *Energy*, vol. 161, pp. 1250–1261, Oct. 2018, doi: 10.1016/j.energy.2018.07.099.

[79] P. Danieli, S. Rech, and A. Lazzaretto, “Supercritical CO2 and air Brayton-Joule versus ORC systems for heat recovery from glass furnaces: Performance and economic evaluation,” *Energy*, vol. 168, pp. 295–309, 2018, doi: 10.1016/j.energy.2018.11.089.

[80] M. Marchionni, G. Bianchi, and S. A. Tassou, “Techno-economic assessment of Joule-Brayton cycle architectures for heat to power conversion from high-grade heat sources using CO2 in the supercritical state,” *Energy*, vol. 148, pp. 1140–

1152, Apr. 2018, doi: 10.1016/j.energy.2018.02.005.

[81] G. Di Marcoberardino, E. Morosini, and G. Manzolini, “Preliminary investigation of the influence of equations of state on the performance of CO2 + C6F6 as innovative working fluid in transcritical cycles,” *Energy*, vol. 238, p. 121815, Jan. 2022, doi: 10.1016/j.energy.2021.121815.

[82] D. Alfani, M. Astolfi, M. Binotti, E. Macchi, and P. Silva, “Optimization of the Part-load Operation Strategy of sCO2 Power Plants,” *5th Int. Semin. ORC Power Syst.*, no. i, pp. 1–10, 2019.

[83] X. Lin, Z. Cui, Z. Geng, J. Zhang, Z. Zhang, and J. Xu, “Calculation of Thermodynamic Physical Parameters of C5F10O/CO2 and C6F12O/CO2 Mixtures,” in *Proceedings of the 2019 5th International Conference on Electric Power Equipment - Switching Technology: Frontiers of Switching Technology for a Future Sustainable Power System, ICEPE-ST 2019*, Oct. 2019, pp. 55–59, doi: 10.1109/ICEPE-ST.2019.8928679.

[84] C. M. Invernizzi, “Closed power cycles: Thermodynamic fundamentals and applications,” *Lect. Notes Energy*, vol. 11, 2013, doi: 10.1007/978-1-4471-5140-1.

[85] 3M Canada Company, “3M safety data sheet, 3M Novec 649 Engineered Fluid,” 2018.

[86] 3M Canada Company, “3M safety datasheet, 3M Novec 5110 Engineered fluid,” 2020.

[87] J. M. Calm and G. C. Hourahan, “Physical, safety, and environmental data for current and alternative refrigerants,” in *23rd International congress of refrigeration, ICR 2011, Prague, Czech Republic*, 2011, pp. 1–22.

[88] J. Nouman, “Comparative studies and analyses of working fluids for Organic Rankine Cycles - ORC, Master of Science Thesis, EGI-2012-086MSC,” KTH Industrial Engineering and Management, 2012.

[89] National Fire Protection Association, *NFPA 704 - Standard System for the Identification of the Hazards of Materials for Emergency Response*. 2007.

[90] L. Calderazzi and P. Colonna di Paliano, “Thermal stability of R-134a, R-141b, R-13I1, R-7146, R-125 associated with stainless steel as a containing material,” *Int. J. Refrig.*, vol. 20, no. 6, pp. 381–389, Jan. 1997, doi: 10.1016/S0140-7007(97)00043-1.

[91] C. M. Invernizzi, P. Iora, M. Preßinger, and G. Manzolini, “HFOs as substitute for R-134a as working fluids in ORC power plants: A thermodynamic assessment and thermal stability analysis,” *Appl. Therm. Eng.*, vol. 103, no. January 2015, pp. 790–797, Jun. 2016, doi: 10.1016/j.applthermaleng.2016.04.101.

[92] M. Z. Irriyanto, H. S. Lim, B. S. Choi, A. A. Myint, and J. Kim, “Thermal stability and decomposition behavior of HFO-1234ze(E) as a working fluid in the supercritical organic Rankine cycle,” *J. Supercrit. Fluids*, vol. 154, p. 104602, Dec. 2019, doi: 10.1016/j.supflu.2019.104602.

[93] E. Santacesaria, A. Morini, and S. Carrá, “Influence of metallic surfaces on decomposition of methylene chlorine,” *La Termotec.*, vol. 29, pp. 443–449, 1975.

[94] E. Santacesaria, A. Morini, and S. Carrá, “Research on thermal decomposition of methylene chlorine,” *La Chim. e l’Industria*, vol. 56, pp. 443–449, 1974.

[95] Y. Li, X. Zhang, S. Tian, S. Xiao, Y. Li, and D. Chen, “Insight into the decomposition mechanism of C6F12O-CO2 gas mixture,” *Chem. Eng. J.*, vol. 360, no. 299, pp. 929–940, Mar. 2019, doi: 10.1016/j.cej.2018.10.167.

[96] F. Crespi *et al.*, “Thermal efficiency gains enabled by using CO2 mixtures in supercritical power cycles,” *Energy*, vol. 238, p. 121899, Jan. 2022, doi: 10.1016/j.energy.2021.121899.

[97] G. Silva-Oliver and L. A. Galicia-Luna, “Vapor-liquid equilibria for carbon dioxide + 1,1,1,2-tetrafluoroethane (R-134a) systems at temperatures from 329 to 354 K and pressures upto 7.37 MPa,” in *Fluid Phase Equilibria*, Jun. 2002, vol. 199, no. 1–2, pp. 213–222, doi: 10.1016/S0378-3812(01)00816-0.

[98] J. S. Lim, J. M. Jin, and K.-P. Yoo, “VLE measurement for binary systems of CO2+1,1,1,2-tetrafluoroethane (HFC-134a) at high pressures,” *J. Supercrit. Fluids*, vol. 44, no. 3, pp. 279–283, Apr. 2008, doi: 10.1016/j.supflu.2007.09.025.

[99] C. Duran-Valencia, G. Pointurier, A. Valtz, P. Guilbot, and D. Richon,

"Vapor−Liquid Equilibrium (VLE) Data for the Carbon Dioxide (CO2) + 1,1,1,2-Tetrafluoroethane (R134a) System at Temperatures from 252.95 K to 292.95 K and Pressures up to 2 MPa," *J. Chem. Eng. Data*, vol. 47, no. 1, pp. 59–61, Jan. 2001, doi: 10.1021/JE010075Y.

[100] H. Saravanamuttoo, G. Rogers, H. Cohen, S. PV, and A. Nix, *Gas Turbine Theory*. Pearson, 2017.

[101] S. I. Salah, M. A. Khader, M. T. White, and A. I. Sayma, "Mean-Line Design of a Supercritical CO2 Micro Axial Turbine," *Appl. Sci.*, vol. 10, no. 15, p. 5069, Jul. 2020, doi: 10.3390/app10155069.

[102] E. Keneth and P. E. Nichols, "How to Select Turbomachinery For Your Application," *Barber-Nichols Inc.*, pp. 1–10.

[103] W. M. Kays and M. E. Crawford, *Convective Heat and Mass Transfer*, 3rd ed. McGraw-Hill, 1993.

[104] M. Kulhánek and V. Dostál, "Thermodynamic Analysis and Comparison of Supercritical Carbon Dioxide Cycles," in *Proceedings of SCCO2 Power Cycle Symposium*, 2011, pp. 1–7, [Online]. Available: http://www.sco2powercyclesymposium.org/resource_center/system_concepts/thermodynamic-analysis-and-comparison-of-supercritical-carbon-dioxide-cycles.

[105] M. Binotti, C. M. Invernizzi, P. Iora, and G. Manzolini, "Dinitrogen tetroxide and carbon dioxide mixtures as working fluids in solar tower plants," *Sol. Energy*, vol. 181, no. September 2018, pp. 203–213, 2019, doi: 10.1016/j.solener.2019.01.079.

[106] G. Angelino and C. Invernizzi, "Binary conversion cycles for concentrating solar power technology," *Sol. Energy*, vol. 82, no. 7, pp. 637–647, Jul. 2008, doi: 10.1016/j.solener.2008.01.003.

[107] C. Craig, "Kirk-Othmer Encyclopedia of Chemical Technology and Ullmann's Encyclopedia of Industrial Chemistry," *Issues Sci. Technol. Librariansh.*, no. 46, p. 7, 2006, Accessed: Jun. 10, 2021. [Online]. Available: https://journals.library.ualberta.ca/istl/index.php/istl/article/view/2063.

[108] M. D. Koplow, L. R. DiNanno, and F. A. DiBella, "AN RC-1 ORGANIC RANKINE BOTTOMING CYCLE FOR AN ADIABATIC DIESEL ENGINE.,"

1984.

[109] C. M. Invernizzi, P. Iora, D. Bonalumi, E. Macchi, R. Roberto, and M. Caldera, “Titanium tetrachloride as novel working fluid for high temperature Rankine Cycles: Thermodynamic analysis and experimental assessment of the thermal stability,” *Appl. Therm. Eng.*, vol. 107, pp. 21–27, 2016, doi: 10.1016/j.applthermaleng.2016.06.136.

[110] C. M. Invernizzi and D. Bonalumi, “Thermal stability of organic fluids for Organic Rankine Cycle systems,” in *Organic Rankine Cycle (ORC) Power Systems*, Elsevier, 2017, pp. 121–151.

[111] G. Di Marcoberardino *et al.*, “Experimental and analytical procedure for the characterization of innovative working fluids for power plants applications,” *Appl. Therm. Eng.*, vol. 178, no. May, p. 115513, Sep. 2020, doi: 10.1016/j.applthermaleng.2020.115513.

[112] Aspen Technology Inc., “Aspen Plus. The Chemical Industry’s Leading Process Simulation Software.” Bedford, Massachusetts 01730, USA, [Online]. Available: https://www.aspentech.com/en/products/engineering/aspen-plus.

[113] M.F.Caubet, “Liquéfaction des mélanges gazeux,” Université de Bordeaux, 1901.

[114] A. M. A. Dias *et al.*, “Vapor - Liquid equilibrium of carbon dioxide - Perfluoroalkane mixtures: Experimental data and SAFT modeling,” *Ind. Eng. Chem. Res.*, vol. 45, no. 7, pp. 2341–2350, Mar. 2006, doi: 10.1021/ie051017z.

[115] Z. Yuan, Y. Tu, C. Wang, Y. Zhao, and X. Dong, “Experimental research on (vapor + liquid) equilibria for the {trifluoroiodomethane (CF3I) + carbon dioxide (CO2)} system from 243.150 to 273.150 K,” *J. Chem. Thermodyn.*, vol. 101, pp. 49–53, Oct. 2016, doi: 10.1016/j.jct.2016.05.012.

[116] W. K. Tolley, R. M. Izatt, and J. L. Oscarson, “Titanium tetrachloride-supercritical carbon dioxide interaction: A solvent extraction and thermodynamic study,” *Metall. Trans. B*, vol. 23, no. 1, pp. 65–72, Jan. 1992, doi: 10.1007/BF02654038.

[117] F. Crespi *et al.*, “Thermal efficiency gains enabled by using supercritical CO2 mixtures in Concentrated Solar Power applications,” in *4th European sCO2 Conference for Energy Systems: March 23-24, 2021, Online Conference*, Mar.

2021, pp. 291–300, doi: 10.17185/DUEPUBLICO/73972.

[118] M. Bertini, D. Fiaschi, G. Manfrida, P. H Niknam, and L. Talluri, “Evaluation of the property methods for pure and mixture of CO2 for power cycles analysis,” *Energy Convers. Manag.*, vol. 245, p. 114568, Oct. 2021, doi: 10.1016/j.enconman.2021.114568.

[119] N. T. Weiland, B. W. Lance, and S. R. Pidaparti, “SCO2 power cycle component cost correlations from DOE data spanning multiple scales and applications,” in *Proceedings of the ASME Turbo Expo*, 2019, vol. 9, doi: 10.1115/GT2019-90493.

[120] M. D. Carlson, B. M. Middleton, and C. K. Ho, “Cycles Using Component Cost Models Baselined With Vendor Data,” *Proc. ASME 2017 Power Energy Conf.*, pp. 1–7, 2017.

[121] G. Di Marcoberardino *et al.*, “Experimental characterisation of CO2 + C6F6 mixture: Thermal stability and vapour liquid equilibrium test for its application in transcritical power cycle,” *Appl. Therm. Eng.*, vol. 212, no. May, p. 118520, Jul. 2022, doi: 10.1016/j.applthermaleng.2022.118520.